

JYU DISSERTATIONS 123

Markus Vilén

Mass Measurements and Production of Ions at IGISOL for the Astrophysical *r*- and *rp*-Processes



UNIVERSITY OF JYVÄSKYLÄ
FACULTY OF MATHEMATICS
AND SCIENCE

JYU DISSERTATIONS 123

Markus Vilén

**Mass Measurements and Production
of Ions at IGISOL for the Astrophysical
r- and *rp*-Processes**

Esitetään Jyväskylän yliopiston matemaattis-luonnontieteellisen tiedekunnan suostumuksella
julkisesti tarkastettavaksi yliopiston Ylistönrinteen salissa FYS1
syyskuun 20. päivänä 2019 kello 12.

Academic dissertation to be publicly discussed, by permission of
the Faculty of Mathematics and Science of the University of Jyväskylä,
in Ylistönrinne, auditorium FYS1, on September 20, 2019 at 12 o'clock noon.



JYVÄSKYLÄN YLIOPISTO
UNIVERSITY OF JYVÄSKYLÄ

JYVÄSKYLÄ 2019

Editors

Anu Kankainen

Department of Physics, University of Jyväskylä

Ville Korkiakangas

Open Science Centre, University of Jyväskylä

Copyright © 2019, by University of Jyväskylä

Permanent link to this publication: <http://urn.fi/URN:ISBN:978-951-39-7838-9>

ISBN 978-951-39-7838-9 (PDF)

URN:ISBN:978-951-39-7838-9

ISSN 2489-9003

ABSTRACT

Vilén, Markus

Mass measurements and production of ions at IGISOL for the astrophysical r - and rp -processes

Jyväskylä: University of Jyväskylä, 2019, 86 p.(+included articles)

(JYU Dissertations

ISSN 2489-9003; 123)

ISBN 978-951-39-7838-9 (PDF)

Diss.

The masses of 27 nuclear ground states and three isomeric states have been measured with the JYFLTRAP double Penning trap mass spectrometer at the Ion Guide Isotope Separator On-Line (IGISOL) facility. The studied nuclides are located in two separate regions of the nuclear chart, the neutron-rich rare-earth region around $A \approx 160$ and the neutron-deficient $A \approx 80$ region near the $N = Z$ line. The mass measurements were performed using the the Time-of-Flight Ion-Cyclotron Resonance and Phase-Imaging Ion-Cyclotron Resonance techniques. The impact of the measured masses on the astrophysical rapid neutron capture process (r -process) was studied for several trajectories representing a neutron-star merger scenario. The masses of two nuclides near the $N = Z$ line were predicted using mirror displacement energies and the masses of their mirror partners measured in this work. Additionally, the effects of the measured masses on nuclear structure and the mass surface in both regions of the nuclear chart were studied. An upgraded version of the Heavy-ion Ion Guide Isotope Separator On-Line (HIGISOL) system for the production of radioactive ions using heavy-ion beams has been commissioned and successfully used in its first on-line experiment. The new off-line ion source facility has been brought into routine use at the IGISOL facility and used in various experiments. Systematic studies on the effect of ion count rate on mass measurements at JYFLTRAP have been performed using stable ion beams from the new ion source station.

Keywords: Penning trap, r -process, nuclear structure, IGISOL, off-line ion beams, systematic uncertainty

Author

M.Sc Markus Vilén
Department of Physics
University of Jyväskylä
Finland

Supervisors

Associate Prof. Dr. Anu Kankainen
Department of Physics
University of Jyväskylä
Finland

Prof. Dr. Ari Jokinen
Department of Physics
University of Jyväskylä
Finland

Reviewers

Dr. Sergey Eliseev
Max Planck Institute for Nuclear Physics
University of Heidelberg
Germany

Adjunct Prof. Dr. Iris Dillmann
Physical Science Division
TRIUMF
Canada
Department of Physics and Astronomy
University of Victoria
Canada

Opponent

Prof. Dr. Dan Melconian
Department of Physics & Astronomy
Texas A&M University
The United States of America

PREFACE

On a seemingly normal day during my early years as a physics student, I walked into a class room with a group of friends. It was the first lecture of a new course and the lecturer introduced himself. He welcomed us to his class, saying he will be our Sauron and the classroom his Mordor for the course. That marked the beginning of four courses in Mordor and one of the longest years I spent at the university. As time passed, the shadow of Mordor slowly retreated and a path forward started to become clear. With the completion of this thesis, I will have finally found my way out of Mordor and now I wish to thank those who helped me find my path and those who made it easier to travel.

I wish to thank my supervisor Associate Prof. Anu Kankainen. She paved the way for me to graduate ahead of schedule through careful planning of all the experiments performed in this work. She was always easy to approach and helped me whenever I needed guidance. I wish to thank Dr. Tommi Eronen for his encouragement and guidance with the ion traps at IGISOL. I also wish to thank him for the wisdom he offered related to the life of a young researcher. I wish to thank Dr. Sami Rinta-Antila for his expertise on all technical matters and for making me feel welcome at IGISOL as a new student. He introduced me to the technical side of the IGISOL facility as well as to the mechanical and electrical workshops, all of which turned out to play a major role in this work. I wish to thank Prof. Ari Jokinen and Prof. Iain Moore for their support when I applied for my next position. Without the letters of recommendation from them and Associate Prof. Anu Kankainen, my future would look very different. I also wish to thank my fellow students and post docs, Antoine, Dmitrii, Laetitia, Sarina, Ilkka, Ruben and Wouter for their help with various tasks around the lab and for their company.

I also wish to thank my friends, Jarkko, Juho, Jukka and Oula, who walked through Mordor with me. You made the journey much lighter and often even enjoyable. I wish to thank my mother and sister for encouraging me to pursue a career sciences. You nudged me in the right direction on several occasions along the way and have given me confidence to think I have achieved something to be proud of. Finally, I wish to thank M.Sc. Maija Keskinen for her continued support and understanding. I must have not been an easy person to live with as I was searching for my path through Mordor and yet you stayed by my side all these years.

The work presented in this thesis has been carried out in the Exotic Nuclei and Beams group at the IGISOL facility in the JYFL Accelerator Laboratory at the Department of Physics at the University of Jyväskylä, Finland, between August 2016 and September 2019.

ACKNOWLEDGEMENTS

This project has been supported by the Academy of Finland under the Finnish Centre of Excellence Programme 2012–2017 (Nuclear and Accelerator Based Physics Research at JYFL). This project has received funding from the European Union's Horizon 2020 research and innovation programme under grant agreement No 771036 (ERC CoG MAIDEN).

CONTENTS

ABSTRACT

PREFACE

ACKNOWLEDGEMENTS

CONTENTS

LIST OF INCLUDED ARTICLES

1	INTRODUCTION	9
2	THEORY	12
2.1	Nuclear binding energies and astrophysical processes	12
2.1.1	Atomic mass and nuclear binding energy	12
2.1.2	Stellar evolution and astrophysical sites for the rapid neutron and proton capture processes	15
2.1.3	Rapid neutron capture process (<i>r</i> -process)	20
2.1.4	Rapid proton capture process (<i>rp</i> -process)	24
2.2	Penning traps	26
3	EXPERIMENTAL METHODS	31
3.1	Radioactive isotope production	32
3.1.1	Fission ion guide	33
3.1.2	Heavy-ion ion guide and development of the HIGISOL system	34
3.2	Off-line production of stable ions	36
3.2.1	The new off-line ion source facility	36
3.2.2	Future plans for the ion source station	39
3.3	Ion beam formation and manipulation	41
3.4	JYFLTRAP double Penning trap	43
3.5	Penning trap mass measurement techniques	45
3.5.1	Ion sample purification	45
3.5.2	Time-of-Flight Ion Cyclotron Resonance (TOF-ICR)	48
3.5.3	Phase-Imaging Ion-Cyclotron-Resonance (PI-ICR)	51
4	RESULTS AND DISCUSSION	56
4.1	Mass measurements in the neutron rich rare-earth region	56
4.2	Mass measurements of neutron deficient nuclei near the $N = Z$ line	63
4.3	Systematic studies on the effect of count rate on PI-ICR mass measurements	68
5	SUMMARY AND OUTLOOK	75
	REFERENCES	78

INCLUDED ARTICLES

LIST OF INCLUDED ARTICLES

- PI M. Vilén, J.M. Kelly, A. Kankainen, M. Brodeur, A. Aprahamian, L. Canete, T. Eronen, A. Jokinen, T. Kuta, I.D. Moore, M.R. Mumpower, D.A. Nesterenko, H. Penttilä, I. Pohjalainen, W.S. Porter, S. Rinta-Antila, R. Surman, A. Voss, J. Äystö. Precision Mass Measurements on Neutron-Rich Rare-Earth Isotopes at JYFLTRAP: Reduced Neutron Pairing and Implications for r-Process Calculations. *Physical Review Letters* 120, 262701, 2018.
- PII M. Vilén, J.M. Kelly, A. Kankainen, M. Brodeur, A. Aprahamian, L. Canete, R. de Groote, A. de Roubin, T. Eronen, A. Jokinen, I.D. Moore, M.R. Mumpower, D.A. Nesterenko, J. O'Brien, A. Pardo Perdomo, H. Penttilä, M. Reponen, S. Rinta-Antila, R. Surman. Exploring the mass surface near the rare-earth abundance peak via precision mass measurements. *Submitted to Physical Review C*, 2019.
- PIII M. Vilén, A. Kankainen, P. Bączyk, L. Canete, J. Dobaczewski, T. Eronen, S. Geldhof, A. Jokinen, M. Konieczka, J. Kostensalo, I.D. Moore, D.A. Nesterenko, H. Penttilä, I. Pohjalainen, M. Reponen, S. Rinta-Antila, A. de Roubin, W. Satuła, J. Suhonen. High-precision mass measurements and production of neutron-deficient isotopes using heavy-ion beams at IGISOL. *Submitted to Physical Review C*.
- PIV M. Vilén, L. Canete, B. Cheal, A. Giatzoglou, R. de Groote, A. de Roubin, T. Eronen, S. Geldhof, A. Jokinen, A. Kankainen, I.D. Moore, D.A. Nesterenko, H. Penttilä, I. Pohjalainen, M. Reponen, S. Rinta-Antila, J. Äystö. A new off-line ion source facility at IGISOL . *Accepted for publication in Nuclear Instruments and Methods in Physics Research Section B: Beam Interactions with Materials and Atoms* (DOI: 10.1016/j.nimb.2019.04.051).

1 INTRODUCTION

All elements heavier than lithium have been produced exclusively in stellar environments. There are a number of astrophysical sites and scenarios in which nucleosynthesis takes place and among them are processes that have seemingly very little in common. There are steady burning processes in stellar interiors lasting for millions or billions of years that are known to produce many of the elements we see around us on a daily basis. On the other hand, there are also extremely fast and energetic processes lasting only for mere seconds that are considered to produce a large portion of nuclides known today. Runaway processes in individual stars can result in explosions that outshine entire galaxies for a brief moment and, at the same time, there are stars whose brightness steadily fades away over vast time scales exceeding the current age of the Universe and ultimately end up as cool and dim objects on the sky. There are also several types of star systems that undergo events of thermonuclear runaway, surviving each event only to repeat it all over again.

Regardless of the seemingly large differences between various astrophysical events, they can be, in many cases, studied using similar theoretical and experimental tools. Theoretical models describing these processes are often based on established properties of nuclear matter and are supplemented with experimental data. The models range from describing entire nucleosynthesis processes that take place in various astrophysical events to describing the structure of individual nuclides. Various quantities that enter these models can be determined experimentally, providing valuable feedback for refining the theories and helping predict properties of matter beyond what can be reached in experiments. One of the most influential quantities entering theoretical nucleosynthesis models are nuclear masses. In this work the masses of 27 nuclear ground states and three isomeric states were measured, see figure 1, and their effect on the rapid neutron capture process (r -process) and the rapid proton capture process (rp -process) was studied. Even though these processes take place in highly different astrophysical environments, they can be studied using very similar theoretical and experimental tools. Experimental masses enter theoretical models of both of these processes through quantities such as reaction rates, half-lives and branching ratios [1–4].

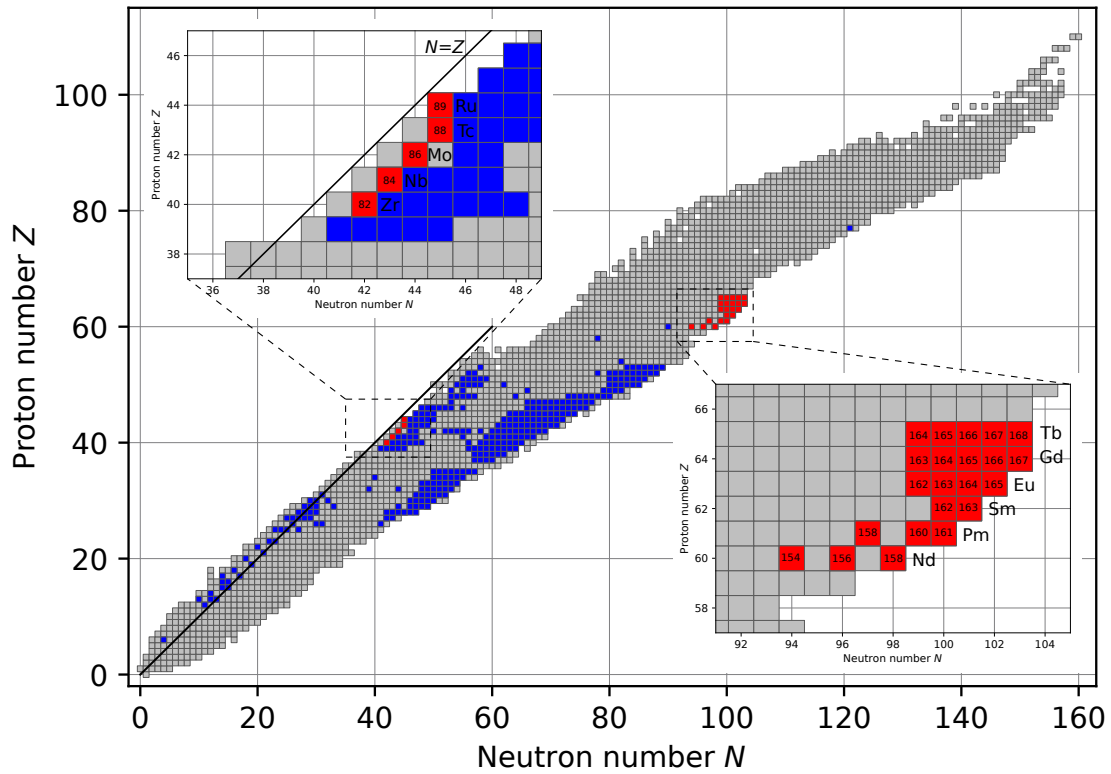


FIGURE 1 Nuclides whose masses have been experimentally determined. Masses listed in the the AME2016 atomic mass evaluation are presented in gray, masses measured in this work in red and other masses measured at JYFLTRAP in blue. Nuclides measured in this work are labeled with their mass numbers A .

These processes and the effect atomic masses have on them, together with the astrophysical sites that house the processes, will be discussed in more detail in section 2.1.

Any experimental facility aiming to provide new information on nuclides relevant to the r - and rp -process must be equipped to produce and study exotic nuclides. In this work 16 out of the 30 measured masses were determined experimentally for the first time and much of the work in this thesis is related to improving the experimental setup at the Ion-Guide Isotope Separator On-Line (IGISOL) facility [5–7]. The ion guide platform used to produce radioactive ions in the heavier $N = Z$ region was upgraded, see section 3.1.2. It was used in an on-line experiment where the masses of two nuclear states, $^{88}\text{Tc}^m$ and ^{89}Ru , were measured for the first time [PIII]. Additionally, the off-line ion source station for producing stable ion beams was fully commissioned [PIV], see section 3.2. The new station was mostly used to produce reference ion samples for mass measurements at the double Penning trap mass spectrometer JYFLTRAP [8]. Most of the mass measurements presented in this work were conducted using the Time-of-Flight Ion-Cyclotron Resonance (TOF-ICR) [9, 10] technique. The Phase-Imaging Ion-Cyclotron Resonance (PI-ICR) [11–13] technique was used for the measurements of ^{88}Tc and ^{162}Eu , both of which have low-lying isomeric states. Acquired

results will be discussed in sections [4.1](#) and [4.2](#). As a part of the measurement campaigns of [\[PI\]](#) and [\[PII\]](#) systematic uncertainties related to the measurements done with the PI-ICR method in this work were studied, see section [4.3](#).

Penning traps are the most precise tools currently available for mass measurements. They are also suitable for measuring radioactive ions down to half-lives of the order of 100 ms. Therefore, the IGISOL facility with JYFLTRAP and the newly commissioned upgrades to the facility offer a valuable possibility to extend the list of experimentally-known atomic masses, improve their precisions and to study the effect of atomic masses on nuclear astrophysics. Here an overview of the theoretical concepts relevant for the performed measurements will be given in chapter [2](#). The technical development related to the production of radioactive and stable ion beams at the IGISOL facility done in this work will be presented in sections [3.1](#) and [3.2](#). The development was instrumental for the experiments presented in Sections [4.1](#) and [4.2](#).

2 THEORY

In this section the theoretical framework behind this work will be introduced. Focus will be on aspects of nuclear astrophysics that provide the motivation for the measurements performed in this work and theoretical treatment of the single most important tool available for mass measurements at the IGISOL facility, a double Penning trap JYFLTRAP. Basic concepts related to mass in nuclear physics will be introduced and the evolution of stars of different masses will be discussed. Astrophysical environments believed to house the nuclear processes responsible for the production of the majority of isotopes on the nuclear chart will be introduced. Focus will be on the r and rp -processes, relevant for the included articles [PI, PII] and [PIII], respectively. Finally, a brief description of an ideal Penning trap is given.

2.1 Nuclear binding energies and astrophysical processes

2.1.1 Atomic mass and nuclear binding energy

The mass of an atom can be expressed using the masses of its individual constituents. One of the first things taught to an aspiring nuclear physics student is that the sum of the masses of the individual components is not equal to the mass of the atom. A small portion of the sum of the individual masses is lost as the components are assembled into an atom. The difference between the masses has come to be known as binding energy. As the terminology implies, there is an equivalence between mass and energy that can be expressed as $E = mc^2$, where E is energy, m is mass and c is the speed of light in vacuum. With this definition the total mass of an atom can be written as

$$m_{atom} = Zm_p + Nm_n + Zm_e - B/c^2, \quad (1)$$

where m_p is the mass of a proton, m_n the mass of a neutron, m_e the mass of an electron and B the total binding energy. The binding energy can be further separated

into two parts, $B = B_{nuclear} + B_e$, where $B_{nuclear}$ is the nuclear binding energy due to interactions between nucleons and B_e the electron binding energy resulting from interactions between electrons and the nucleus. The magnitude of the electron binding energy is several orders of magnitude smaller than the nuclear binding energy. In this work the significance of the electron binding energy is negligible compared to the nuclear binding energy and, for example, in the analysis process of mass measurements performed in this work the electron binding energies were neglected. On the other hand, the nuclear binding energy (and hence the total binding energy) is of utmost relevance in this work. Henceforth, the term binding energy is used to refer to the nuclear binding energy $B_{nuclear}$, unless otherwise stated.

The total binding energy can be expressed in several ways and it is often useful to present the same underlying information on binding energies through various different quantities in order to highlight some particular properties of nuclei. A common way of expressing the binding energy is to calculate a quantity called atomic mass excess ME , given by

$$ME = (m_{atom} - Am_u)c^2, \quad (2)$$

where A is the integer mass number of an atom and m_u represents the atomic mass unit, traditionally defined as one-twelfth of the mass of a neutral ^{12}C atom. In many cases the difference of binding energies between nuclei is of interest. It can be used to evaluate the amount of energy that can be gained in a nuclear reaction or how much energy needs to be provided to a system to enable a certain reaction. In many situations this amount of energy is referred to as the Q value of a reaction. Depending on the reaction, the Q value might have come to be known by a dedicated name, such neutron separation energy S_n ,

$$S_n = [m(Z, N - 1) + m_n - m(Z, N)] c^2, \quad (3)$$

which describes the amount amount of energy needed to remove one neutron from a given nuclide. Neutron separation energies are of particular interest in section 2.1.3, where they have a crucial role in shaping the path the astrophysical rapid neutron capture process takes on the nuclear chart.

In the context of this work, one especially important aspect of binding energy is that the binding energy per nucleon B/A reaches its maximum value at a relatively low mass number. The binding energy per nucleon initially increases as we move towards more massive stable nuclei but reaches its peak value around the $A = 60$ region known as the iron peak. This has a profound effect on the nuclear processes that take place in stellar environments due to the fact that beyond the $A = 60$ region additional energy is required to fuse nuclei. This means that even the most massive stars can only generate energy via nuclear fusion up to a certain point, after which they will inevitably experience radical changes to their energy generation and even their stability, as will be discussed in section 2.1.2. Binding energy per nucleon is presented in figure 2, where the most tightly bound isotope of each isotopic chain is plotted. The name "iron peak" highlights

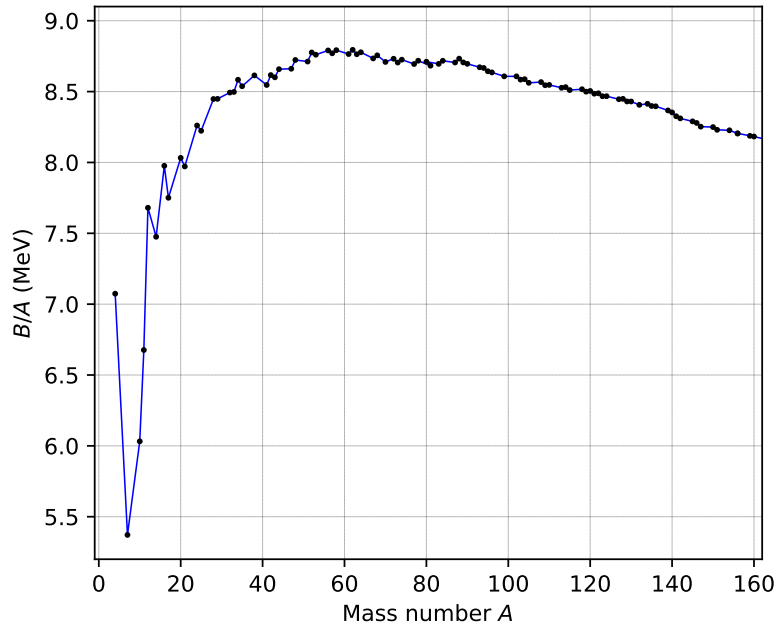


FIGURE 2 Binding energy per nucleon as a function of the mass number A . Only the isotope with the highest binding energy per nucleon is plotted for each isotope chain.

the significance of iron isotopes on nuclear fusion in stellar environments, where ^{56}Fe , located at the top of the peak in figure 2, is the heaviest isotope produced via fusion. The region around iron nuclides also stands out in solar system abundances at the time of the formation of the solar system presented in figure 3. The peak is a result of nucleosynthesis in stars of earlier generations than the Sun.

Changes in binding energy affect the production of nuclei also beyond the iron peak. There are several processes that extend nucleosynthesis in stellar environments far beyond what can be reached via nuclear fusion alone. The majority of nuclides heavier than iron are produced via two distinct neutron capture processes, the slow (s -process) and rapid (r -process) neutron capture processes. In this work focus will be on the r -process which will be discussed in more detail in section 2.1.3. Some sections of the nuclear chart cannot be reached via any neutron capture process. The production of nuclides in these regions relies on various proton-capture processes, such as the rapid proton-capture process (rp -process). The rp -process will be discussed in more detail in section 2.1.4. Nuclear masses, and thus binding energies, play a crucial role in modeling these processes where several quantities, including reaction rates, half-lives and branching ratios, are affected by nuclear masses [1–4]. Additionally, nuclear masses affect the path taken by these processes through the nuclear chart and affect the energy generation in stars [2]. Especially in the case of the r -process [1, 14, 15] but also in the case of the rp -process [4, 16] there is a large amount of important nuclear masses that have either not been measured or have high uncertainties that can considerably affect the abundance distributions resulting from theoretical models of the processes.

Nuclear masses can be estimated using various mass models. There are

several types of models, ranging from fully theoretical approaches to partially experimental models. In the latter ones, experimental data is used to fit parameters of an underlying model in order to reproduce observed properties of the mass surface. Mass models used in this work are the microscopic Hartree-Fock-based model by Duflo and Zuker (henceforth referred to as Duflo-Zuker or D-Z) [17], Hartree-Fock-Bogoliubov model (HFB24) [18], Universal Nuclear Energy Density Functional (UNEDF0) [19] and two Weizsäcker-Skyrme models WS3 [20] and WS4 [21]. These models reproduce known masses typically within root-mean-square errors of the order of hundreds of keV. This accuracy is not satisfactory in many astrophysical nucleosynthesis models and more accurate values are desirable. Many modern mass measurement techniques, such as Penning traps, offer considerably smaller uncertainties than current mass models. Mass measurements can, therefore, provide valuable information for testing mass models and experimental mass data can also be used directly in nucleosynthesis models.

The biggest difficulties in current experimental work are in producing sufficient amounts of the experimentally unknown nuclei to enable precise measurements. There are several ongoing development projects at various facilities around the globe, such as FAIR at GSI Darmstadt, FRIB at MSU, ISOLDE at CERN, SPIRAL II at GANIL and IGISOL at Jyväskylä, that aim to push the boundaries of what nuclei can be reached in experiments. In this work a total of 27 atomic ground state masses were measured along with three isomeric state masses and their effect on both astrophysical nucleosynthesis and nuclear structure were studied. The conclusions reached in this work are all based on measured atomic masses, see included articles [PI, PII, PIII], which goes to show that masses are a highly relevant quantity in a wide range of situations. More detailed discussion on the r and rp -processes and the way in which masses affect the processes will be given in the following sections 2.1.3 and 2.1.4.

2.1.2 Stellar evolution and astrophysical sites for the rapid neutron and proton capture processes

This section will serve as an introduction into the production mechanisms of different elements. All elements heavier than lithium have been produced in stellar environments via a wide range of nuclear processes. Perhaps the most well known nucleosynthesis process is nuclear fusion which produces elements up to the iron peak presented in figure 3, centered around ^{56}Fe . However, beyond this point fusion is no longer energetically favorable and other production mechanisms are needed to synthesize heavier nuclides. This section will discuss the stages of stellar evolution that are needed to create the environments necessary for the additional nucleosynthesis processes extending the nuclear chart beyond iron. In some cases, suitable conditions are created within a single star of suitable mass but in many cases a binary star system is required where at least one of the participants has evolved past its main sequence. Astrophysical nucleosynthesis processes relevant to this work will be discussed in the following sections 2.1.3 and 2.1.4.

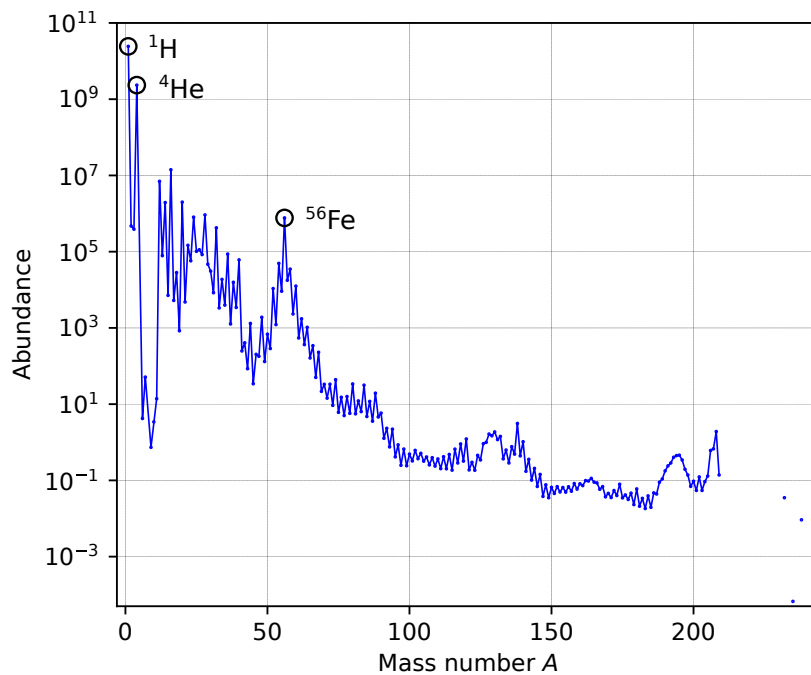


FIGURE 3 Solar system abundances at the time of the formation of the solar system on a scale where Si has been set at 10^6 . Hydrogen, helium and the iron region are highlighted with black circles.

The life of a star begins as a cloud of interstellar gas consisting mainly of hydrogen and helium produced in the primordial nucleosynthesis. In the case of the Sun, for example, hydrogen and helium were several orders of magnitude more abundant than any other element at the time of the formation of the Sun [22], see figure 3. The gravitational pull of the gas could slowly increase the density of the gas, raising its temperature and creating radiation. As the gas cloud contracts, radiation is trapped more and more efficiently due to the increase in density. This in turn further increases the temperature and pressure within the central region of the cloud, leading to slowing down of the contraction. Material from the outer regions of the cloud keeps accumulating around the central region and eventually the resulting increase in temperature leads to dissociation of hydrogen molecules into atoms, and finally ionization of hydrogen and helium atoms. Ionized matter is more efficient in trapping radiation than neutral atoms, which leads to a further increase in temperature and pressure in the central region. As the contraction of the gas cloud continues the pressure becomes sufficient to halt the collapse of the central region. The source of energy supporting the core region up to this point is gravitational contraction.

Once the temperature of the central region reaches a few million kelvin the first nuclear reactions start to occur. Initially, primordial deuterium and hydrogen start to fuse and primordial lithium ${}^7\text{Li}$ can break into two alpha particles via fusing with hydrogen. Energy released in these nuclear processes is still very small. As the temperature rises further and reaches several million kelvin, hydrogen nuclei start to fuse into helium. This increases the total energy output

and eventually becomes the only source of energy in the core region. The gas cloud has now reached a hydrostatic and thermal equilibrium and has become what is known as a zero age main sequence star.

Further evolution of a new star depends on its mass and can result in a variety of different outcomes. Stars in the mass range $0.013M_{\odot} \lesssim M \lesssim 0.08M_{\odot}$ [23], where M_{\odot} is the mass of the sun, have insufficient mass to reach central temperatures needed to sustain hydrogen fusion. This leads to the star not being able to support the pressure exerted by the gravitational pull of the gas and the star collapses into what is known as a brown dwarf. The collapse of the star is halted by electron degeneracy pressure in the core region and the star slowly radiates its thermal energy into space.

Degeneracy pressure is a purely quantum mechanical property of fermion systems, ultimately caused by the requirement that the wave function two of identical fermions must be anti-symmetric under the exchange of particles. That is, if $\psi_a(\mathbf{r})$ is the wave function of particle 1 and $\psi_b(\mathbf{r})$ of particle 2 their combined wave function $\psi(\mathbf{r}_1, \mathbf{r}_2) = \psi_a(\mathbf{r}_1)\psi_b(\mathbf{r}_2)$ must obey

$$\psi(\mathbf{r}_1, \mathbf{r}_2) = -\psi(\mathbf{r}_2, \mathbf{r}_1). \quad (4)$$

In the case of electron degeneracy pressure, electrons being spin 1/2 particles, this results in the limitation that only two electrons can occupy the same quantum state. Therefore, only a limited number of states is available in the contracting core region of the star. As the volume of the core region decreases the energy of the quantum mechanical system formed by the electron gas increases, resulting in a pressure [24] that works to halt the collapse of the core region.

Slightly more massive stars in the mass range $0.08M_{\odot} \lesssim M \lesssim 0.4M_{\odot}$ [23] are the lightest stars that have sufficient mass to sustain a hydrostatic equilibrium through fusing hydrogen to helium. As such, they are the least massive stars belonging to the group of main sequence stars and have come to be known as red dwarfs. Red dwarfs are among the longest living stars, spending time in the main sequence, according to theoretical models, in excess of the current age of the Universe. For example, a $0.1M_{\odot}$ star with solar metallicity is expected to spend around 6000 Gy in the main sequence. Therefore, given that the age of the Universe is only approximately 14 Gy, all red dwarfs that we observe must still be in the main sequence [23]. Red dwarfs have insufficient mass to fuse helium to heavier nuclei and, in large part, share the fate of stars with lower mass. Once red dwarfs run out of hydrogen fuel they collapse until electron degeneracy pressure sets in, becoming what is known as a helium white dwarf. All true stars (brown dwarfs are not considered true stars) that end their life cycle in a collapse halted by electron degeneracy pressure are called white dwarfs.

Stars in the mass range $0.4M_{\odot} \lesssim M \lesssim 11M_{\odot}$ [23] have a much richer variety of possible paths of evolution. The exact course of events that stars in this mass range experience is determined by several factors, such as metallicity of the gas cloud that formed the star and the initial mass of the star. A common property of these stars is that they are all massive enough to ignite helium in their cores and fuse it to carbon and oxygen. However, the process responsible for fusing

hydrogen to helium differs between stars of different masses. In lighter stars the dominant forms of energy production, i.e. way of fusing hydrogen into helium, are the pp chains. A total of three pp chains have been identified, all of which have the end result of converting four hydrogen nuclei to one ${}^4\text{He}$. Fusing four protons via a single collision event to ${}^4\text{He}$ is statistically improbable. Therefore, the pp chains all have several intermediate steps, nuclear reactions, that finally add up to converting four protons into one helium.

In heavier stars with higher metallicity the pp chains are supplanted by CNO or hot CNO cycles. In these cycles certain C, N, O, F and Ne isotopes act as catalysts in fusing hydrogen to helium. Several intermediate nuclear reactions are involved in all of the reaction cycles with the end result being the same as in the pp chains, four protons fusing to form a ${}^4\text{He}$ nuclide. As the amount of hydrogen fuel reduces and helium increases in the core of the star, the hydrogen burning moves to a thick shell around the core. At this time the star leaves the main sequence and its core contracts in order to generate enough energy to counter gravitational pressure. This results in an increase in temperature in the hydrogen burning shell which eventually leads to the envelope of the star becoming fully convective. As a result, energy output of the hydrogen burning shell increases significantly causing the surface of the star to expand. In the case of the Sun, the expansion is estimated to reach beyond the orbit of Mercury. Stars in this stage of their evolution are called red giants.

The following stages of the evolution of a star depend, again, on its mass. If the star is massive enough the helium core will start to fuse helium into heavier elements without the core becoming electron degenerate. The main products of this helium burning are carbon and oxygen, the fourth and third most abundant elements in the solar system. If the core region reaches electron degeneracy before the beginning of helium burning the star will undergo a core helium flash as the helium burning begins caused by a thermonuclear runaway due to electron degeneracy. Subsequently, the star will alternate between producing its energy via hydrogen and helium burning in a series of helium shell flashes. More massive stars may undergo additional convection events, or dredge-ups, and in addition to fusing helium they may also be massive enough to eventually start fusing carbon into heavier elements. Similarly as with helium shell flashes, the primary source of energy of the star alternates between carbon burning and helium burning. In all of these cases the star will end up losing a large portion of its mass due to solar winds. When the surface of the star reaches a high enough temperature it will ionize the gas ejected by solar winds and the residual core of the star will become the center of a fluorescent planetary nebula, a planetary nebula nucleus. In this final stage of stellar evolution in this mass range, the remaining core is electron degenerate and will slowly radiate its energy into space as a white dwarf. The elemental composition of the white dwarf depends of the evolutionary path of the star and can vary from consisting mainly of carbon and oxygen to oxygen and neon [23].

Stars even more massive than the previous cases with $M \gtrsim 11M_{\odot}$ have clearly different final stages of stellar evolution. Initially, these stars go through

similar burning stages as stars with lower mass, fusing hydrogen, helium and carbon. However, in this mass range the stars will be able to ignite additional burning stages known as neon burning, oxygen burning and silicon burning. These processes result in the core of the star consisting of the heaviest and most stable nuclei, the most abundant being ^{56}Fe which is located near the top of the binding energy per nucleon chart (see figure 2). As a result, further burning stages fusing ^{56}Fe are not energetically favorable regardless of whether conditions in the core region would provide sufficient energy to individual nuclei to overcome the Coulomb barrier.

The way in which energy is transported away from the stellar interior changes as the burning advances to the latter stages. In the initial burning stages the dominant form of energy transport is electromagnetic radiation, but in the advanced burning stages the energy carried by neutrino-antineutrino pairs becomes the most significant form of transport. Neutrinos interact with solar matter much more weakly than light and as a result the nuclear reaction rate must increase in the burning region to provide sufficient support against gravitational pressure. Therefore, the durations of the latter burning stages are considerably shorter than those of the initial burning stages. For example, in a $25M_{\odot}$ star of solar composition the silicon burning is estimated to last for only about one day [23].

Once the core region of a star reaches the end of silicon burning it has no more sources of energy available. Nuclear burning will still continue in the shells surrounding the core and additional material is accumulated on the core region. When the gravitational pressure due to the mass of the core exceeds the limit of what the electron degeneracy pressure can support, the Chandrasekhar limit ($\approx 1.4M_{\odot}$), the core collapses. During the collapse, electron density reaches sufficiently high levels to allow electrons to be captured onto the iron peak nuclei. This further reduces the pressure support provided by the electron degeneracy pressure, accelerating the collapse. Additionally, as temperature increases during the collapse thermal radiation becomes energetic enough to photodisintegrate the iron peak nuclei. Given that iron peak nuclei have the highest binding energies per nucleon, energy is removed from the core in the process, which reduces the pressure even further.

As the core collapse advances and density reaches values of the order of nuclear density, the strong force between nucleons begins to provide pressure support. However, density of the core overshoots the nuclear density by approximately a factor of two [25] and the strong force, which is strongly repulsive at short distances, causes the core to rebound. An outward moving shock wave is created around a dense inner core region that survives the rebound. The remaining inner core region is called a proto-neutron star.

As the shock wave moves through the outer core region, photodisintegration of iron peak nuclei removes energy from the shock wave together with emission of neutrinos. The energy loss is sufficient to cause the shock wave to lose all its kinetic energy by the time it reaches the outer edge of the core, resulting in the shock stalling. It is believed that the shock is revived through some process but the exact mechanism is still unknown. It is thought that neutrinos and an-

neutrinos emitted by the proto-neutron star could provide the necessary energy to revive the shock as they are absorbed in the surrounding layers [25]. Revival of the shock is considered to create suitable conditions for a range of nuclear reactions and to result in the production of significant amounts of nuclei up to ^{56}Ni which is the dominant species contributing to observed light curves emanating from this type of core collapse events. The brief phase of nucleosynthesis initiated by the revival of the shock is known as explosive nuclear burning. In addition to producing elements up to the iron peak, large amounts of free neutrons are ejected from the core, which is believed to result in the production of a wide range of heavier elements in the rapid neutron capture process (*r*-process) [23].

Stellar explosion scenario described above is referred to as a core collapse supernova. In many cases events such as this result in a neutron star being created. However, the explosion mechanism is not fully understood and it is considered that also another outcome is possible, where a black hole is created instead of a neutron star. In this work the focus will be on neutron stars, regardless of the details of other possible outcomes. Neutron stars are a recurring theme in this work. The astrophysical production mechanisms behind isotopes measured in included articles [PI, PII, PIII] are all thought to be connected to some path of stellar evolution involving neutron stars.

Details of the process that result in the creation of a neutron star are, naturally, highly relevant in the case of the neutrino-driven revival of the shock that is considered to give rise to the *r*-process. However, there are also situations where the creation process of the neutron star plays a less significant role but the presence of the neutron star is still of critical importance for this work. In these situations the neutron star is a part of a binary star system, where two stars orbit each other at a close distance. Resulting nuclear processes depend on the composition of the two stars. Two particularly interesting cases in the context of this work are binary neutron star systems and systems where a neutron star accretes material from a companion star. These two cases and the resulting nucleosynthesis will be discussed in more detail in sections 2.1.3 and 2.1.4, respectively.

2.1.3 Rapid neutron capture process (*r*-process)

The production of heavier nuclei in fusion reactions in stellar environments is at first limited and eventually inhibited by the Coulomb barrier. As fusion products reach higher proton numbers Z the electrostatic repulsion between nuclei becomes ever higher. Fusion of nuclides reaches only up to the iron peak, see figure 2, where the binding energy per nucleon reaches its maximum value. This prevents fusion reactions from producing heavier elements by fusing electrically charged nuclei. One way to circumvent the Coulomb barrier and to produce elements beyond the iron peak is to fuse nuclei with neutrons. Neutrons, being electrically neutral, are not affected by the Coulomb barrier and can therefore fuse with nuclei regardless of their electrical charge. The distribution of isotopes that can be produced by subjecting seed nuclides to free neutrons depends on the conditions at the reaction site. Most importantly, the resulting abundances de-

pend on the amount of free neutrons. Neutron capture reactions responsible for the production of elements beyond the iron peak are can be divided into two distinct processes depending on the amount of available neutrons, the slow (*s*) and rapid (*r*) neutron capture process. Even though these two processes have many properties in common, here the discussion will be limited to the *r*-process due to its relevance to the included articles [PI, PII].

In short, the term *r*-process is used to describe successive capture of neutrons on seed nuclei (typically iron peak nuclei) in a highly neutron-rich environment. The series of neutron captures continues until the β^- rates become comparable to the neutron capture rate. Following the β^- decay, the daughter nuclei then capture additional neutrons and the process repeats itself, producing heavier and heavier nuclei with higher proton numbers [26]. Once the flux of free neutrons becomes too low for the process to continue the produced nuclei decay towards the valley of stability, resulting in the final *r*-process abundance distribution. There are several factors that affect the path taken by the *r*-process, such as density of free neutrons and temperature of the astrophysical site.

The most simple description of the *r*-process is the classical *r*-process model. In the classical model an initial assumption of constant temperature and neutron flux is made requiring them to be sufficiently high to make both (n, γ) and (γ ,n) reactions much faster than β^- decays. In such conditions the abundance of a given nuclide is determined solely by neutron capture and photodisintegration rates. The abundance of a given species ${}^A_Z X$ can be expressed as

$$\frac{dN(Z, A)}{dt} = -N_n N(Z, A) \langle \sigma v \rangle_{Z, A} + N(Z, A + 1) \lambda_\gamma(Z, A + 1), \quad (5)$$

where N are the number densities of nuclei with given Z and A , N_n is the neutron number density, $\langle \sigma v \rangle_{Z, A}$ is the neutron capture reaction rate per particle pair and $\lambda_\gamma(Z, A + 1)$ the photodisintegration decay constant [23]. If the neutron capture and photodisintegration rates are high enough a thermal equilibrium is reached within each isotopic chain, resulting in the number densities of nuclides being constant. The ratio of the number densities is then given by the Saha equation

$$\frac{N(Z, A + 1)}{N(Z, A)} = N_n \left(\frac{h^2}{2\pi m_{An} kT} \right)^{3/2} \frac{(2j_{Z, A+1} + 1)}{(2j_{Z, A} + 1)(2j_n + 1)} \frac{G_{Z, A+1}^{\text{norm}}}{G_{Z, A}^{\text{norm}}} e^{\frac{Q_{n\gamma}}{kT}}, \quad (6)$$

where m_{An} is the reduced mass $m_A m_n / (m_A + m_n)$, j are the spins of the nuclei, G the normalized partition functions and $Q_{n\gamma}$ is the Q value for the neutron capture reaction [23]. Here it is worth highlighting that the number ratio is proportional to the neutron number density N_n and inversely proportional to temperature T . Also, the neutron capture Q value $Q_{n\gamma}$ for ${}^A_Z X$ can also be expressed as neutron separation energy S_n for ${}^{A+1}_Z X$. These three quantities have the strongest effect on isotopic abundance distributions in the *r*-process.

Using equation (6) it is possible to find all isotopic abundances of relevance to the *r*-process in an isotopic chain. The equation can also be used to give a approximate description of the shape of the abundance distribution by approximating the spins j and normalized partition functions G as equal to unity. The

resulting number density ratio is only a function of the neutron number density and temperature, which are assumed to be constant in the classical r -process model. Therefore, it is possible to solve the equation for the Q value and find which value Q_0 would produce equal abundances for the neighboring nuclides. Actually, this solution suggests that the abundance is the same for all isotopes in a given chain. However, the Q -values in reality are not constant and the abundances vary along the isotopic chain. On average the Q -values decrease as the neutron number N increases and the nuclides become less stable. This gives rise to an interesting result that near the valley of stability the number density ratio is larger than unity and near the neutron drip line it is less than unity. In other words, it results in the isotopic abundance distribution having a maximum near Q_0 where the number density ratio is equal to unity.

This approximation, however, neglects one important factor, the odd-even staggering of the Q -values. The staggering results in nuclides with an even neutron number N having a higher abundance than the neighboring odd- N nuclides. The most abundant isotopes in any chain are, therefore, found at an even N near the nuclide where the Q value goes below Q_0 . In practice the abundance distributions are rather sharp and only a few isotopes exist in significant amounts.

Once a thermal equilibrium between neutron capture and photodisintegration reactions is established throughout an isotopic chain, the r -process must continue via a β^- decay. Given that only a few isotopes are present in significant amounts, the process will have to continue through the decays of those nuclides, known as waiting point nuclides. Due to the high free neutron density and temperature the β^- decays are slow compared to (n,γ) and (γ,n) reactions and the abundance distribution within an isotopic chain remains unchanged. The assumption of $(n,\gamma)\leftrightarrow(\gamma,n)$ equilibrium, which gives rise to the significant waiting point nuclei abundances, is known as the waiting point approximation [23].

The accumulation of material at the waiting point nuclides together with their β^- decay half-lives determine the elemental abundances produced in the r -process. Each isotopic chain is fed by the decays of the waiting point nuclides in the previous isotopic chain and depleted by the decays of its own waiting point nuclides. Elemental abundances together with the location of waiting points in each isotopic chain is of relevance for the final r -process abundance distribution since all produced radioactive material will decay back towards the valley of stability, typically along their isobaric chains once the neutron flux ends.

Shell closures can have a significant effect on the location of the abundance maximum of an isotopic chain and, therefore, the final abundance distribution. This is most clearly seen at the magic neutron numbers $N = 50, 82, 126$, where the energetically favorable neutron configurations of nuclei cause the Q -values of the (n,γ) reaction to change strongly. Q -values of the neutron-capture reactions producing nuclei at the magic numbers are relatively large while the Q -values of the following neutron-capture reactions are relatively low. This sudden change in Q -value results in the nuclei at magic neutron numbers being likely waiting points. As a result, the r -process proceeds via subsequent β^- decays and neutron captures at the magic numbers, pushing the process path closer to the valley

of stability towards more tightly bound nuclei. Eventually, the produced nuclei have high enough Q-values to move the waiting point of an isotopic chain beyond the magic neutron number, allowing the r -process path to once again move closer to the neutron drip line. This results in the r -process accumulating relatively large amounts of material near the magic neutron numbers, giving rise to several peaks in the final abundance distribution.

There are also other mechanisms which affect the shape of the final abundance distribution but are not included in the classical r -process model. For example, in the mass region near $A \approx 165$ nuclear deformation together with peculiar β^- decay properties are considered to accumulate the r -process nuclei into a peak during the final stages of the r -process when the number of free neutrons rapidly declines [27, 28]. The final shape of the $A \approx 165$ peak is also believed to be affected by spontaneous or β -delayed fission reactions of heavier r -process nuclei. Fission fragments of the heavier elements become seed nuclei and return to the r -process path lower in the nuclear chart and, therefore, alter the final abundance distribution. The $A \approx 165$ region is of particular interest in this work due to the fact that several nuclides in the mass region have become accessible to mass measurements using Penning traps for the first time. In this work the masses of a range of nuclides in the $A \approx 165$ mass region were determined, many of which had not been directly measured prior to this work, and the acquired results were used as inputs in r -process modeling. For further details, see [PI, PII].

The above description of the classical r -process model provides a useful overall picture but it omits several significant factors. For example, the assumptions made in the classical model over-simplify the properties of the astrophysical site by assuming a constant temperature and a constant neutron flux with an instantaneous end. Without the assumption of constant temperature and neutron flux, the waiting point approximation does not hold true and additional factors such as the β^- decay half-lives and (n, γ) and (γ, n) reaction rates need to be evaluated carefully. Additionally, some waiting point nuclei may decay to neutron-unbound states resulting in β -delayed neutron emission. Such decays make the final r -process abundance distribution smoother. Also, nuclides near the heaviest isotopes produced in the r -process can decay via emission of α particles, which is not taken into account in the above discussion. More sophisticated r -process models have been developed that include, for example, multiple subsequent nucleosynthesis events and dynamical modeling of the characteristics of the astrophysical site. For a more detailed discussion, the reader is referred to, for example, [25, 29].

There are two astrophysical sites where the r -process is believed to take place. One possible site are the neutrino-driven winds of a core collapse supernova. A significant amount of free neutrons is ejected from the deeper regions of the rebounding core region of the collapsing massive star. These neutrons together with the iron peak nuclei created in the explosive nuclear burning provide the necessary material for the r -process. It is thought that suitable conditions for the r -process could be formed as the revived shock wave passes through the layers of matter that surrounds the proto-neutron star. However, difficulties have

been encountered in simulations in reproducing the explosions assumed here, which casts doubt on the neutrino-driven winds being sites for the r -process [25]. Also, there are indications that the neutrino driven winds, even in cases where the r -process occurs, might not a suitable location for producing the heaviest r -process nuclei above $A = 140$ [30].

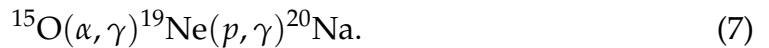
The r -process has also been thought to take place during neutron star merger events. In fact, it was confirmed in August 2017 that the r -process does indeed take place in neutron star mergers by the gravitational wave event GW170817 [31,32] and the respective kilonova [30,33]. The observed afterglow, known as a kilonova, changed its color from blue to red within a few days of the event, which was interpreted as an indication of the presence of lanthanide-rich high-opacity isotopes produced in the r -process [30,33].

2.1.4 Rapid proton capture process (rp -process)

The second astrophysical nucleosynthesis process of particular relevance to this work is the rapid proton capture process (rp -process). It has many similarities with the r -process described in section 2.1.3. Instead of transforming seed nuclei via successive neutron captures, the rp -process operates mainly via proton captures. Also, instead of β^- decays, the process relies on β^+ decays to allow nucleosynthesis to proceed beyond nuclides that are proton-unbound or undergo very fast photodisintegrations via the (γ, p) reaction. Even though the processes have many similarities, they take place in very different astrophysical environments and produce nuclei in separate regions of the nuclear chart.

The rp -process takes place on the opposite side of the valley of stability than the r -process. The process relies on the hot CNO cycles (HCNO) to provide it with necessary seed nuclei. Initiation of the rapid proton capture is preceded by stable operation hot CNO cycles until temperature of the stellar environment exceeds approximately 0.5 GK. After this point, a number of new reaction processes involving captures of α -particles, protons and photodisintegrations start to become likely alternatives to the hot CNO cycles. As a result, nuclides needed as catalysts in the HCNO processes escape the cycles and undergo further processing into heavier nuclides. The exact reaction channels depend on the conditions of the environment. Eventually these new reaction processes, called breakout sequences, lead to the production of a varying range of heavier nuclides via the rp -process, ranging from the CNO nuclides up to the SnSbTe region [23,34].

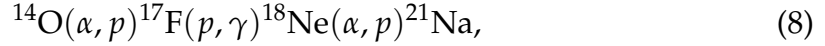
In environments characterized by temperature $T = 0.5$ GK, density $\rho = 10^4$ g/cm³ and reaction process time scale $t = 100$ s, breakout from the HCNO cycles happens via



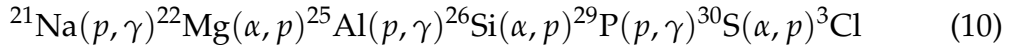
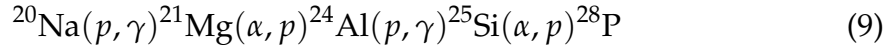
This is followed by successive proton captures until a nuclide is synthesized that undergoes such fast (γ, p) photodisintegrations that it becomes favorable for the rp -process to continue via the β^+ decay channel. Following a β^+ decay the process will repeat and either more protons are added to a nuclide or it undergoes additional radioactive decays [23,35]. This is known as the rp -process. It is worth

noting that the proton capture rate does not necessarily determine whether β^+ decays are the dominant path forward. It is possible that regardless of a high proton capture rate $\lambda_{p\gamma}$ leading to more exotic species, the reverse photodisintegration reaction rate is even higher, and β^+ decay dominates the process even if it is the least probable reaction among the three ($\lambda_{\beta^+} < \lambda_{p\gamma} < \lambda_{\gamma p}$). This can lead the rp -process to nuclei with long β^+ decay half-lives and very low proton capture Q value. As a result, (γ, p) reactions will force the process to proceed via the slow β^+ decay. These nuclides are the waiting points of the rp -process.

At a temperature of approximately 1 GK a second break out sequence from the HCNO cycles,



starts to affect the rp -process, pushing the end point of nucleosynthesis higher up the nuclear chart [23]. At a temperature of 1.5 GK a third break out sequence becomes active ${}^{14}\text{O}(\alpha, p){}^{17}\text{F}(\gamma, p){}^{16}\text{O}(\alpha, \gamma){}^{20}\text{Ne}$. In these conditions all three sequences operate at the same time. However, the initial abundance flow after break out follows a different path via the



reaction sequences known as the αp -process. These break out sequences provide the rp -process with its seed nuclei that are subsequently processed into heavier nuclides, in many cases even up to the SnSbTe region [34].

The rp -process is thought to take place in binary star systems where a neutron star accretes material rich in hydrogen and helium from its companion star. When material is transferred from the companion star it is accumulated in an accretion disk around the neutron star. Eventually, the material will fall onto the neutron star gaining a significant amount of energy as it moves deeper into the gravitational potential well. The material is heated to such high temperatures that it will begin to emit thermal radiation in the X-ray wave lengths. Temperature and density at the surface are high enough to allow the star to continuously fuse hydrogen into helium via the HCNO cycles. The environment is not, however, initially suitable for fusing helium into carbon via the triple- α process and the neutron star will continue to accrete material. As time passes, the star will accumulate enough material to initiate the helium burning under electron degenerate conditions, resulting in a thermonuclear runaway accompanied with a burst of X-ray radiation. It is believed that the thermonuclear runaway initiates the rp -process on the surface of the neutron star [34]. The neutron star is not destroyed in the runaway and the process will repeat itself as new material is accreted. This is the thermonuclear runaway model of a type I X-ray burst [3, 23]. The scenario presented here is not the only possible explanation for the origin of the bursts. For example, if the neutron star at the center of the event is strongly magnetized, it is believed that it will accumulate material at its magnetic poles at higher localized accretion rates [3].

Numerous direct observations of X-ray bursts have been made ever since the first ones were detected in 1976 [36,37]. This has provided valuable opportunities to compare theoretical models of type I X-ray bursts and the resulting *rp*-process to direct observations. Similarly as in the case of the *r*-process, theoretical models of the *rp*-process rely on knowledge of a wide range of nuclear properties across the entire *rp*-process region, such as reaction rates and half-lives [38], many of which are affected by nuclear masses. As was already mentioned in section 2.1.1, there are several unknown masses of high importance to the *rp*-process with large uncertainties [4,16]. More precise measurements of such masses could possibly lead to significant changes in elemental abundances resulting from theoretical *rp*-process models. Variations of the masses of individual nuclides were shown to change the final abundances of a single mass number A by up to a factor of ten, when comparing calculations with masses shifted by $\pm 3\sigma$ [4]. In this work mass measurements were performed in the proton-rich $A = 82 - 89$ region near the $N = Z$. ^{89}Ru and $^{88}\text{Tc}^m$ were measured for the first time and the precisions of ^{82}Zr , ^{84}Nb and ^{88}Tc were significantly improved. Their effect on the mass surface was studied. However, due to the fact that no radical changes were seen in the mass surface compared to the Atomic Mass Evaluation 2016 [39], which includes recent storage-ring measurements [40] in the region, detailed *rp*-process modeling was not performed using the new masses. For additional details, see included article [PIII].

2.2 Penning traps

This section will provide the reader an overview of the theoretical framework for the measurements performed at the JYFLTRAP double Penning trap mass spectrometer. Ideal Penning traps are discussed in order to give the reader sufficient information to understand the experimental methods utilized in this work. A full in-depth description of real ion traps will not be given. For more exhaustive discussion on deviations from ideality, further references are provided.

Confinement of ions in a Penning trap is achieved via superimposing a uniform magnetic field with an electrostatic quadrupole field. The second component of the trapping potential, the electrostatic quadrupole field, can be generated using several electrode geometries, the most common of which are hyperbolic and cylindrical geometries. The simplest way to describe an ideal Penning trap is to make use of three hyperboloids of revolution that form two endcap electrodes and one ring electrode, see figure 4 (a). In an ideal case the three electrodes would extend infinitely far creating an ideal electric quadrupole potential within the trap providing axial confinement of ions. Additionally, in an ideal case a homogenous magnetic field aligned with the axis of rotational symmetry of the trap would provide confinement in the radial direction. Naturally, such an ideal device is not possible to construct in real life due to a range of limitations, such as the finite size of electrodes, limitations in machining precision and misalignment

of electrodes. As a result, hyperbolic traps, as well as all other trap designs, are prone to imperfections.

Theoretical studies have been conducted in an effort to find ways of reducing the imperfections in several trap geometries, see for example [41,42]. Both hyperbolic and cylindrical traps can be equipped with correction electrodes that can be used to fine-tune the trapping potential and reduce its anharmonicity. However, cylindrical traps have proven to be easier to manufacture due to their more simple electrode geometry. Additionally, the more simple structure makes theoretical modeling of the trap design easier and offers practical advantages, such as easier loading of particles into the trap and improved pumping efficiency due to the more open structure [42]. The open cylindrical electrode design used at JYFLTRAP is presented in figure 4. For the purpose of this work, it is sufficient to assume that both trap designs can be designed and manufactured with a high enough accuracy that the resulting trapping potential can be approximated as harmonic. For simplicity, we shall use the hyperbolic trap design as an example in the following treatment.

In an ideal hyperbolic Penning trap ions are confined in the radial direction by a uniform magnetic field of the form $\mathbf{B} = B_z \hat{\mathbf{e}}_z$, where vector quantities are denoted in bold. This results in cyclotron frequency

$$\omega_c = \frac{qB}{m}, \quad (11)$$

where q and m are the charge and mass of a trapped ion, respectively. Axial confinement is achieved via superimposing an electric quadrupole field of the form

$$U = \frac{U_0}{2d^2} \left(z^2 - \frac{\rho^2}{2} \right) \quad (12)$$

with the magnetic field, see for example [41]. Here z and ρ are the axial and radial

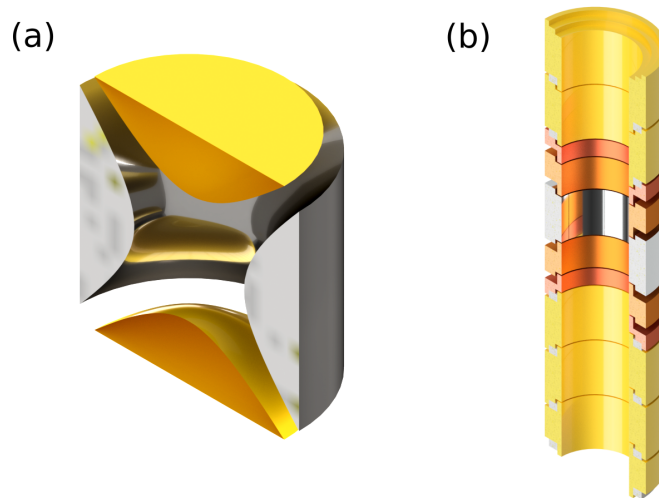


FIGURE 4 Hyperbolic (a) and cylindrical (b) Penning trap designs. Endcap electrodes are presented in yellow, ring electrodes in gray and in (b) correction electrodes in red and orange.

distance from the trap center, respectively, U_0 is the potential difference between endcap and ring electrodes and d is the characteristic trap dimension

$$d = \sqrt{\frac{1}{2}(z_0^2 + \rho_0^2/2)}, \quad (13)$$

where z_0 and ρ_0 are the minimum axial and radial distance from the trap center to the electrodes. In case $qU_0 > 0$, the electrostatic potential gives rise to a harmonic oscillation in the z direction at the frequency

$$\omega_z = \sqrt{\frac{4qU_0}{m(2z_0^2 + \rho_0^2)}}. \quad (14)$$

Motion of a particle in the trap can then be described using Newtonian equations of motion for each dimension as,

$$\ddot{x} - \omega_c \dot{y} - \frac{1}{2} \omega_z^2 x = 0 \quad (15)$$

$$\ddot{y} + \omega_c \dot{x} - \frac{1}{2} \omega_z^2 y = 0 \quad (16)$$

$$\ddot{z} + \omega_z^2 z = 0. \quad (17)$$

The first two equations yield roots for bound motion that can be expressed as

$$\omega_{\pm} = \frac{1}{2} \left[\omega_c \pm \sqrt{\omega_c^2 - 2\omega_z^2} \right], \quad (18)$$

where ω_+ is the reduced (or modified) cyclotron frequency and ω_- the magnetron frequency [41, 43]. Equations (14) and (18) define the three eigenmotion frequencies of ions confined into a Penning trap.

There are three aspects to these eigenmotions that are especially noteworthy in the context of this work and are critical to understand in order to be able to appreciate the full set of techniques utilized in mass measurements at JYFLTRAP. The first noteworthy aspect is the magnitude and hierarchy of the frequencies, $\omega_c \approx \omega_+ \gg \omega_z \gg \omega_-$. The corresponding frequencies $\nu_i = \omega_i/2\pi$ at JYFLTRAP for $^{133}\text{Cs}^{1+}$ ions are $\nu_+ \approx 807$ kHz, $\nu_z \approx 52$ kHz and $\nu_- \approx 1.7$ kHz. The fact that $\omega_+ \gg \omega_z \gg \omega_-$ turns out to be a critical component in operating the purification trap introduced in section 3.4 and also dictates some of the steps taken in determination of the ν_c frequencies of ions. JYFLTRAP consists of two cylindrical Penning trap located inside a 7 T superconducting coil. The two traps have almost identical potentials and geometries and, therefore, the approximate frequencies presented above apply to both traps.

The second noteworthy aspect is that the magnetron motion is mass-independent to first order. This property is utilized in both purifying ion samples and measuring their masses. The weak mass dependency of the magnetron frequency can be

shown starting with the radial eigenmotions defined in equation (18). It directly follows that

$$\omega_{\pm} = \frac{\omega_c}{2} \pm \frac{1}{2} \sqrt{\omega_c^2 \left(1 - \frac{2\omega_z^2}{\omega_c^2}\right)} \quad (19)$$

$$\omega_{\pm} = \frac{\omega_c}{2} \pm \frac{\omega_c}{2} \sqrt{1 - \frac{2\omega_z^2}{\omega_c^2}}. \quad (20)$$

Given that $\omega_c \gg \omega_z$, we can expand this as a Taylor series according around to

$$f(x) = \sum_{n=0}^{\infty} \frac{f^{(n)}(a)}{n!} (x - a)^n \quad (21)$$

with $x = \omega_z/\omega_c$ around $a = \omega_z/\omega_c = 0$. This results in

$$\omega_{\pm} = \frac{\omega_c}{2} \pm \frac{\omega_c}{2} \left[1 - \left(\frac{\omega_z}{\omega_c}\right)^2 - \frac{1}{2} \left(\frac{\omega_z}{\omega_c}\right)^4 + \mathcal{O}\left(\frac{\omega_z}{\omega_c}\right)^6 \right], \quad (22)$$

leading to

$$\omega_- = 0 + \frac{1}{2} \frac{\omega_z^2}{\omega_c} + \frac{1}{4} \frac{\omega_z^4}{\omega_c^3} + \frac{\omega_c}{2} \mathcal{O}\left(\frac{\omega_z}{\omega_c}\right)^6 \quad (23)$$

$$\omega_+ = \omega_c - \frac{1}{2} \frac{\omega_z^2}{\omega_c} - \frac{1}{4} \frac{\omega_z^4}{\omega_c^3} - \frac{\omega_c}{2} \mathcal{O}\left(\frac{\omega_z}{\omega_c}\right)^6. \quad (24)$$

These definitions give us, together with equations (11) and (14),

$$\omega_- = 0 + \frac{U}{z_0^2 + \frac{1}{2}r_0^2} + \frac{mU^2}{(z_0^2 + \frac{1}{2}r_0^2)^2 qB^3} + \frac{\omega_c}{2} \mathcal{O}\left(\frac{\omega_z}{\omega_c}\right)^6 \quad (25)$$

$$\omega_+ = \frac{qB}{m} - \frac{U}{z_0^2 - \frac{1}{2}r_0^2} - \frac{mU^2}{(z_0^2 + \frac{1}{2}r_0^2)^2 qB^3} - \frac{\omega_c}{2} \mathcal{O}\left(\frac{\omega_z}{\omega_c}\right)^6. \quad (26)$$

Based on equation (25) it is clear that the 0th and 1st order terms in the expression of the magnetron frequency ω_- are mass-independent. On the other hand, already the 0th order term of the reduced cyclotron motion ω_+ has a mass dependence. Also, equation (19) gives us a useful result that can be used as an approximate relation when working with real Penning traps

$$\omega_c = \omega_+ + \omega_-. \quad (27)$$

The third noteworthy aspect of the three eigenmotions is the dependence of the amplitude of each eigenmotion on the total energy of the corresponding motion. The total energy of an ion bound in a Penning trap can be described with Hamiltonians in the axial and radial directions, see [41],

$$H_z = \hbar\omega_z \left(a_z^\dagger a_z + \frac{1}{2} \right) \quad (28)$$

$$H_\rho = \hbar\omega_+(a_+^\dagger a_+ + \frac{1}{2}) - \hbar\omega_-(a_-^\dagger a_- + \frac{1}{2}) \quad (29)$$

with eigenvalues of the number operators of the form $a^\dagger a |j\rangle = j |j\rangle$. Therefore, eigenvalues of the total Hamiltonian $H = H_z + H_\rho$, given a state $|k, n, l\rangle$, can be expressed as

$$E = E_k + E_n + E_l = \hbar\omega_z(k + \frac{1}{2}) + \hbar\omega_+(n + \frac{1}{2}) - \hbar\omega_-(l + \frac{1}{2}), \quad (30)$$

where k, n, l are the quantum numbers describing axial, reduced cyclotron and magnetron motions, respectively. Equation 30 shows that the energy of the magnetron motion is inversely correlated with the quantum number l . Consequently, as an ion orbiting in the magnetron mode loses energy its quantum number l increases. This corresponds to the ion moving farther from the trap center where the electric quadrupole potential presented in equation 12 has its maximum value [41]. On the other hand, axial and reduced cyclotron eigenmotions gain energy with an increase in their quantum numbers. The radii of all three eigenmotions are proportional to the square root of their quantum numbers [44]. Therefore, when ions trapped in a Penning trap experience losses in energy the axial and reduced cyclotron motion are bound whereas the magnetron motion is unbound. Fortunately, in practical situations the energy losses are so slow that the magnetron motion can be considered to be bound. However, this sets the magnetron motion apart from the other eigenmotions in the sense that it cannot be cooled away just by allowing the ions to dissipate their energy in the trap [41]. Therefore, other methods for cooling the magnetron motion are necessary. Cooling methods employed at JYFLTRAP will be discussed in section 3.5.1.

The treatment presented here applies for an ideal Penning trap, i.e. one without any misalignments, machining imperfections or field inhomogeneities. The purpose of this section is to serve as an introduction and a first approximation to real Penning traps. For more information on deviations from ideality typically encountered in Penning traps the reader is referred to, for example, [41, 43, 45].

3 EXPERIMENTAL METHODS

This section gives a broad overview of the experimental methods and apparatuses utilized in this work. The layout of the IGISOL facility is presented in figure 5 together with the MCC30/15 cyclotron (A) [46] and the beam line delivering primary beams from the K130 cyclotron (B) [46]. Radioactive isotope production at the IGISOL target area (D) and production of stable ion beams at the off-line ion source station (C) will be discussed in sections 3.1 and 3.2, respectively. Ion beams from these two locations are formed into a beam, mass separated using the dipole magnet (E), guided through the switchyard (F) and injected into the RFQ (G). This part of the system will be discussed in section 3.3. In this work the ions were then injected into JYFLTRAP (I), which will be discussed in section 3.4.

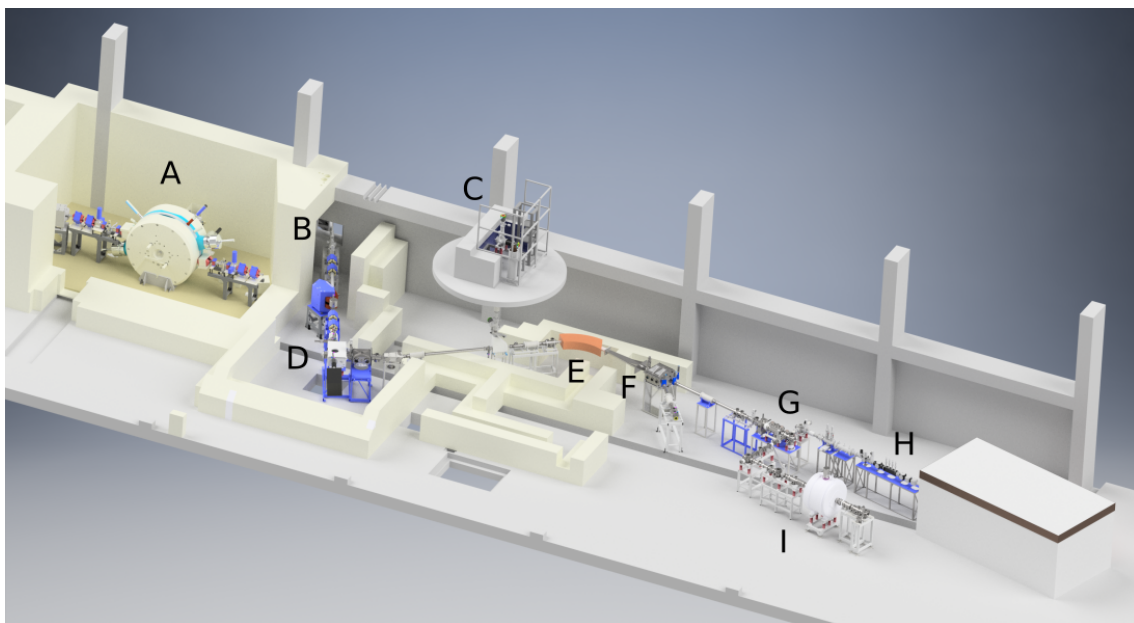


FIGURE 5 Layout of the IGISOL facility: MCC30/15 cyclotron (A), beam line from the K130 cyclotron (B), off-line ion source station (C), radioactive isotope production (D), dipole magnet (E), switchyard (F), RFQ (G), laser spectroscopy line (H), JYFLTRAP (I).

3.1 Radioactive isotope production

Samples of radioactive ions used in experiment at IGISOL are produced using the ion guide method [5] where a primary beam impinges upon a thin target inducing nuclear reactions. The type of reaction is chosen based on the needs of each individual experiment. Reaction products are ejected from the target due to residual kinetic energy, left over from the nuclear reaction, and captured in an ion guide. An ion guide comprises a volume of buffer gas, typically helium, enclosed in a casing optimized for efficient evacuation and a nozzle that is used to direct the gas flow out of the ion guide. The primary purpose of the buffer gas is to slow down created reaction products and capture them. As the produced ions enter the gas volume they start to collide with buffer gas atoms and gradually lose their energy. As a result reaction products are stopped, thermalized and finally extracted from the ion guide as the buffer gas flows through the exit nozzle. The exit nozzle also serves as a pumping barrier. In this work buffer gas pressure inside the ion guide was typically 200 – 300 mbar and $5 \cdot 10^{-2} - 7 \cdot 10^{-2}$ mbar right outside the ion guide.

This method can be used to produce a large variety of radioactive ion samples through a range of nuclear reaction processes, such as proton induced fission and heavy-ion or light-ion induced fusion-evaporation. The use of some particular reaction processes necessitates making modifications to the IGISOL target area. For example, heavy-ion induced fusion-evaporation reactions require a target that is separated from the ion guide, in contrast to the proton induced fission, where the target is located inside the ion guide. Regardless of the choice of reaction process, the method relies on creating electrically charged samples of desired elements and stopping, thermalizing and extracting them while retaining their charge. This is of critical importance due to the fact that separation of the reaction products from the buffer gas relies on the presence of an electrical charge. In this work, all on-line experiments were conducted using singly-charged ions.

There are several factors that affect the likelihood of produced ions conserving their electrical charge. These include, for example, cleanliness of the ion guide and the surrounding vacuum system and type and purity of buffer gas. These factors have an effect on the probability of an ion regaining its missing electrical charge through charge exchange reactions with any material it comes into contact with. Helium is a favorable choice of buffer gas since it has a high ionization potential. This results in low likelihood of charge exchange reactions between buffer gas atoms and reaction products. However, composition of the buffer gas is never pure helium due to practical limitations. There is always some amount of contamination in the system, resulting in an increased chance of neutralization of reaction products via charge exchange reactions with the impurities. This can be minimized through baking the system prior to experiments and using a cryogenic buffer gas purification system, a cold trap, during on-line operations. The gas handling system used at IGISOL is introduced in detail in [47]. As a part of this work the cold trap design utilized in [47] was adopted in construct-

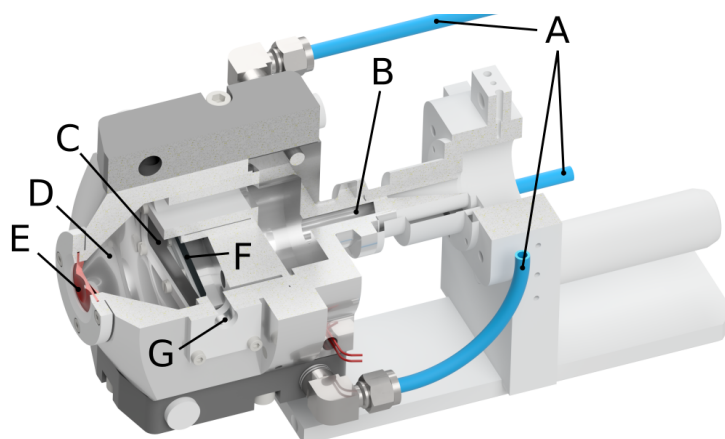


FIGURE 6 Fission ion guide design used at the IGISOL facility: A: coolant lines, B: buffer gas input, C: chamber separation foil, D: stopping volume, E: extraction nozzle, F: target foil, G: primary beam entrance.

ing a gas purification system for an off-line ion source station that was recently commissioned at IGISOL. The new ion source station is discussed in section 3.2. In this work proton induced fission and heavy-ion induced fusion-evaporation reactions were used to produce studied nuclides. Ion guides and specific modifications to the IGISOL target area used in these reactions are discussed in the following sections 3.1.1 and 3.1.2.

3.1.1 Fission ion guide

The most common reaction for the production of radioactive ions at IGISOL is nuclear fission. Typically, fission is induced by impinging a proton beam on a natural uranium target, as was the case in included articles [PI, PII]. In fission reactions at IGISOL the target is mounted inside the fission ion guide [7, 48, 49] presented in figure 6. The target is separated from the buffer gas in its own volume allowing the primary beam to pass through the ion guide without coming into contact with the buffer gas. This is done in order to minimize ionization of the buffer gas that would adversely affect fission fragment yield. The target is set at an angle with respect to the beam axis, increasing the effective thickness of the target. As a result, the probability of proton induced fission is increased but at the same time the likelihood of fission fragments escaping the target material remains high due to the low actual thickness of the target. Emission of fission fragments from the target foil is nearly isotropic [7]. A portion of emitted fragments enter the buffer gas volume through a thin chamber separation foil and are thermalized and extracted with the buffer gas flow. The most common reaction for producing radioactive ions utilized in this work was proton induced fission of natural uranium using the fission ion guide.

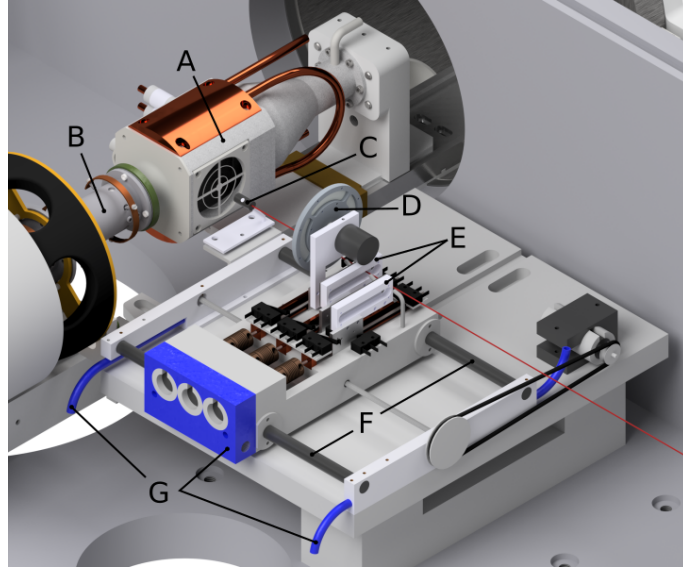


FIGURE 7 The new HIGISOL system: A: Ion guide gas cell, B: SPIG, C: Beam dump, D: Target wheel, E: Degrader holder, F: Rails for distance adjustment, G: Coolant line

3.1.2 Heavy-ion ion guide and development of the HIGISOL system

In addition to fission fragments, mass measurements were also performed on neutron-deficient nuclides in the $N = Z$ region. These nuclei cannot be produced in fission, and production via light-ion fusion-evaporation reactions is also challenging since the stable nuclei are located far from the $N = Z$ line at heavier mass numbers. For this purpose a dedicated ion production system was used that is known as the Heavy-ion Ion Guide Isotope Separator On-Line (HIGISOL) system [6, 50–52]. It consists of an ion guide specifically optimized for the heavy-ion induced reactions and an additional platform housing the target and a beam dump. The HIGISOL system is presented in figure 7.

In the HIGISOL system the target is separated from the ion guide and a beam dump for primary beam is placed between the target and the ion guide. This is done to prevent the primary beam from entering the buffer gas volume and causing excessive ionization. The ion guide itself consist of a single gas-filled volume with a large entrance window covered with a thin foil (typically around $2 \mu\text{m}$ thick havar). Once ions enter the ion guide they come into direct contact with the buffer gas, thermalize and exit the ion guide with the flowing buffer gas. Due to the fact that the target is separated from the ion guide, the distance between the two needs to be adjusted in such a way that the dimensions of the cone of reaction products from the target matches the size of the entrance window. This is achieved using the new control system developed in this work.

The platform itself, see figure 7, houses a total of three foil holders, one for the target and two for degrader foils to reduce the primary beam energy if needed. All three can be remotely moved parallel to the primary beam axis to adjust their distance to the ion guide. The new control system monitors the position of the foils using a resistive wire and a voltage readout circuit. The three

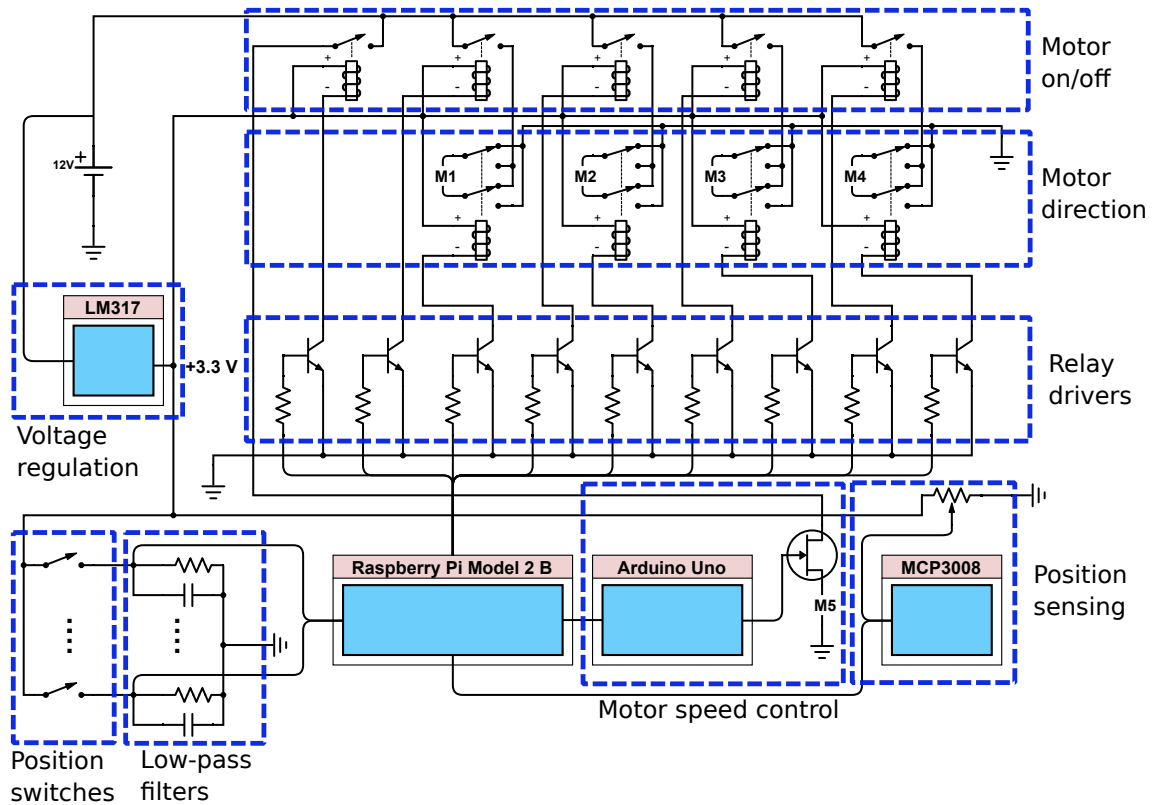


FIGURE 8 Schematic of the control system developed for the HIGISOL platform. Different sections of the system are highlighted based on their functionality.

foils can also be remotely moved in and out of the path of the primary beam. The target is a wheel rotating at a remotely adjustable angular speed. The system also houses several switches that are used to monitor various parts of the apparatus. This system is described in detail in included article [PIII].

Prior to this work the mechanical structure of the system was largely similar to the one presented in figure 7. In this work all components of the electrical system were replaced with higher quality components, including new switches and more powerful direct current (DC) motors. Some upgrades were made to the mechanical design, such as improvements to cooling and mechanical stability, while keeping the operating principle of the previous version of the system. The most significant upgrade to the HIGISOL platform was the development of a fully computerized control system. Previously the system was controlled using a combination of mechanical switches and relays without any remote control or readout capabilities. The lack of remote controls was problematic since operating the manual controls required a person to break the radiation and high-voltage interlocks and to enter the IGISOL target area with elevated radiation levels.

The new control system is built around a Raspberry Pi 2 Model B computer [53] equipped with 40 general-purpose input/output channels and 4 USB ports. The Raspberry Pi is used together with a custom-built electronics circuit and an Arduino Uno [54] microcontroller to monitor and control the HIGISOL system. A schematic illustrating the different parts of the control system and their functions is presented in figure 8. The Raspberry Pi is directly used to read states

of the mechanical switches in the system and to monitor the distance between the target and gas cell through an MCP3008 analog-to-digital converter. The Arduino is used to drive a transistor which is in turn used to adjust the speed of the target wheel motor via pulse-width modulation (PWM). Communication between the Raspberry Pi and Arduino Uno is performed via a serial connection through a USB port. It was decided to implement the pulse-width modulation using an Arduino Uno microcontroller instead of a Raspberry Pi due to the fact that the former offers hardware-based PWM. This was considered to be a more robust solution compared to any necessarily software-based PWM implementation using a Raspberry Pi computer.

The new control system has a graphical user interface (GUI) program that provides users with all necessary information and remote controls to operate the HIGISOL system. The control program is executed by the Raspberry Pi computer in order to minimize any possible issues in transferring information between the input/output hardware and the control program. Due to the fact that the IGISOL frontend is located on a 30 keV high-voltage platform there is a need to provide users access to the control software without directly connecting the control unit to a monitor and keyboard. For this reason, the GUI program is executed on the Raspberry Pi and remotely viewed on a client computer via SSH tunneling using X11 forwarding. The Raspberry Pi is connected to the internal network of the facility using optical-to-ethernet converters in order to overcome the potential difference between parts of the system.

3.2 Off-line production of stable ions

3.2.1 The new off-line ion source facility

The ion guide method discussed in section 3.1 is the primary way of producing ion beams at the IGISOL facility. In the past it has served as a source of both stable and radioactive ion species for various experiments ranging from Penning trap mass measurements [55] to atom trap experiments [56] and decay and laser spectroscopy [57] using several experimental set-ups. In most cases producing and studying radioactive ions has been the primary goal and stable isotopes have served as reference samples for calibrating parts of the system. Often the choice of reference ion has been made during an online experiment based on factors such as measured yields and presence of other ions close in mass to the reference ion and their mass numbers and half-lives. Nuclear reaction processes utilized in this work for the production of radioactive ions are such that they also produce a wide range of isotopes in the surrounding region of the nuclear chart. As a result, availability of suitable, pure beams of reference ions with unambiguous identification were found to present challenges in on-line experiments.

As a part of this work, commissioning of a new off-line ion source facility,

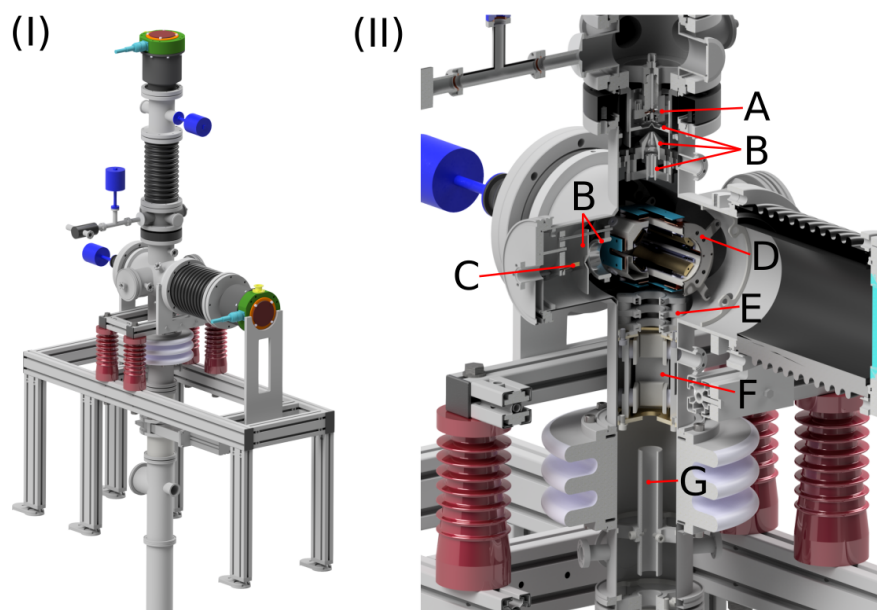


FIGURE 9 The new off-line ion source station (I) and its internal structure (II) where (A) is the glow discharge ion source, (B) ion optics for beam formation, (C) surface ion source, (D) bending ion optics, (E) Einzel lens, (F) steering electrodes and (G) extraction electrode.

which can be used as an alternative source of stable ions, was finalized at IGISOL, see included article [PIV]. The work was started as a M.Sc. project, see [58], and fully taken into use as a part of this work. The new facility consists of an ion source station located on the second floor of the IGISOL facility and a beam line connecting the station to the pre-existing mass separator. The new ion source facility is presented in figures 5 and 9. The new ion source facility and its location upstream of the mass separator introduces the possibility of producing reference ion samples with a dedicated ion source in parallel with the IGISOL front end used to produce radioactive isotopes. This makes it possible to overcome many of the challenges encountered in using the beam from IGISOL for reference samples.

Two ion sources have been commissioned at the off-line station, a surface ion source based on thermal emission of ions and a glow discharge ion source. The thermal emission ion source is, in its simplicity, a small cylinder with a built-in resistor for heating. One end of the cylinder is covered with a mixture of materials that is ionized as the source is heated. The source is commercially available with a range of element mixtures [59]. In this work a combination of ^{39}K , ^{85}Rb , ^{87}Rb and ^{133}Cs was used. The second ion source, the glow discharge ion source, consist of two electrodes approximately 5 mm apart placed in a small volume of flowing helium buffer gas. A voltage is applied between the electrodes to initiate an electrical breakdown. Resistance and voltage of the circuit are tuned to limit power dissipation in the circuit. A steady glow discharge is established where positive ions created in the discharge are accelerated to the cathode, sputtering material upon impact. Sputtered atoms are then ionized in the discharge and

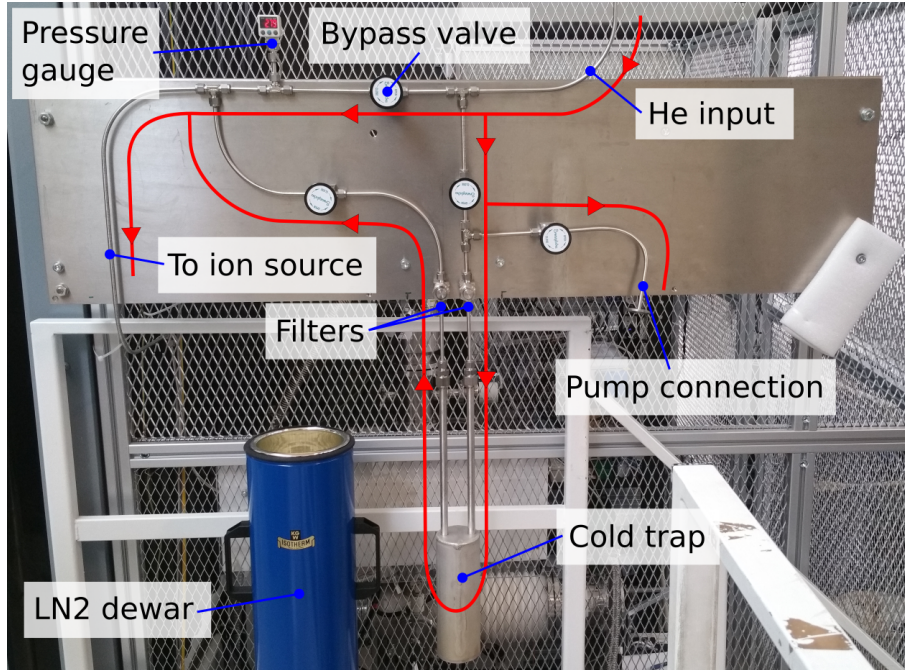


FIGURE 10 Cryogenic gas purifier constructed at the off-line ion source station. Parts of the system are highlighted and the direction of gas flow is indicated with arrows.

transported out of the ion source in the buffer gas flow. Produced ions are separated from the buffer gas using a skimmer electrode and differential pumping. Ion beam from one of the sources is then directed down the connecting beam line to the mass separator where a single isobar can be selected.

Initial tests of the glow discharge ion source were already performed in [58] followed by installation of the surface ion source as a summer student project at IGISOL. In this work the new system was used in on-line experiments for the first time. Typically the ion source station was used to provide $^{133}\text{Cs}^{1+}$ from the surface ion source to be used as a mass reference in atomic mass measurements at JYFLTRAP. This ensured the availability of ions with well-known atomic mass whenever needed and, additionally, provided definite identification of the reference species. As mentioned earlier, one of the challenges in using the ion guide method for producing reference ions is the possibility to have other ions present with mass close to the atomic mass of the intended reference isotope. For example, it was discovered in [PII] that ^{163}Eu and ^{163}Gd initially measured in [PI] using what was thought to be $^{163}\text{Dy}^{1+}$ as a reference ion were, in fact, measured using a molecular ion as a reference. The most likely candidate for the wrongly-identified reference was found to be $^{146}\text{La}^{16}\text{O}^{1}\text{H}^{1+}$ [PII]. Confirmation of the misidentification was done by remeasuring the masses of ^{163}Eu and ^{163}Gd using $^{133}\text{Cs}^{1+}$ ions from the off-line station as a reference. Unambiguous identification of the reference isotope was possible due to the fact that the surface ion source uses a mixture of material with no other isotopes within 46 atomic mass units from ^{133}Cs . This combined with the location of the ion source station upstream of the IGISOL mass separator allowed a definite identification of the reference isotope.

The off-line ion source station was used to provide other types of experiments with stable ions, as well. $^{89}\text{Y}^{2+}$ ions were produced to be used as a reference in a collinear laser spectroscopy experiment on radioactive yttrium isotopes [60]. Previously, reference ions for this kind of experiments have been produced by placing a foil of the desired material at injection aperture of the SPIG [61] so that it partly overlaps with the gas jet coming from the ion guide. However, it was discovered in [60] that the method did not produce ^{89}Y in the required doubly-charged state. Therefore, the glow discharge ion source was used to provide the necessary $^{89}\text{Y}^{2+}$ samples. In another experiment the new system was used to ionize natural palladium using the glow discharge ion source. The Q-value for the neutrinoless double electron capture on ^{102}Pd , i.e. the mass difference between ^{102}Pd and ^{102}Ru was measured in [62], where two sources of the same type were used to produce two beams of stable ions. The off-line station provided the $^{102}\text{Pd}^{1+}$ ions and another glow discharge ion source located in the IGISOL target chamber produced the $^{102}\text{Ru}^{1+}$ ions. The possibility to operate two sources simultaneously enabled the experiment to be conducted fully off-line so that the system was tuned to accept one or the other beam at any given time.

In addition to yttrium [60], palladium [62] and copper used in the initial test in [58], several other elements have been ionized using the glow discharge ion source at the offline ion source station, including Ba and Nd. In preparation to a need to ionize elements that are more chemically active, a cryogenic gas purification system, referred to as cold trap, was constructed for the off-line ion source station in order to minimize the loss of ions via charge-exchange reactions with impurities. The gas purification system is presented in figure 10. Design of the cold trap and the choice of porous filling material were adopted from [47].

3.2.2 Future plans for the ion source station

The development of the off-line ion source station has been on-going ever since the initial tests of the system in 2016. Ion yields have been improved via refining the current design of the glow-discharge ion source through adjusting the dimensions of the buffer gas volume and exit nozzle. Also, a new buffer gas purification system has been constructed. Operating the system has become a routine part of experiments at the IGISOL facility and a considerable amount of experience has been acquired with the new ion source station. Several ways to improve the system have been identified. Therefore, an upgraded version of the system was designed, see figures 11 and 12, as a part of this work. The upgraded off-line ion source station design will broaden the selection of ion sources it can accommodate and it will also provide practical benefits to its use.

The current version of the system, presented in figure 9, is fully functional and has been proven to be capable of producing ion beams from a wide range of elements using two ions sources. However, the mechanical design of the part of the system surrounding the glow discharge ion source has set some limitations to the use of the system. The most significant limitation of the very compact current design is buffer gas removal via pumping. The reason behind this is two-fold.

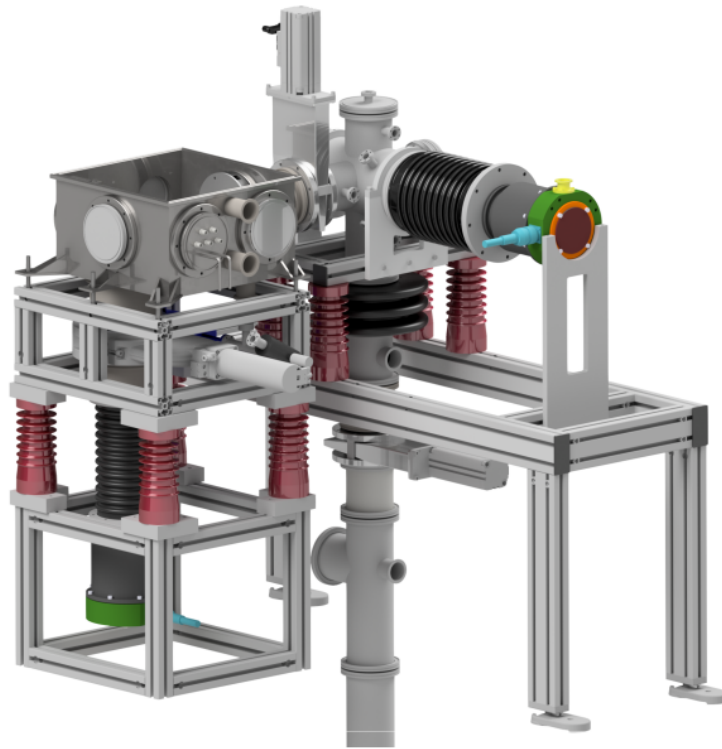


FIGURE 11 The planned upgrade to the off-line ion source station.

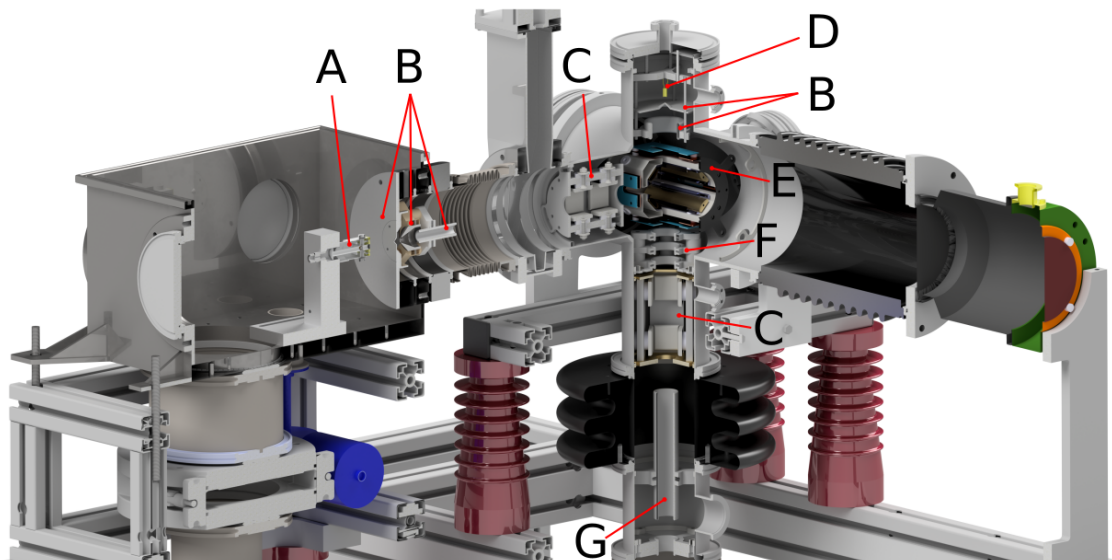


FIGURE 12 Internal structure of the planned upgrade to the off-line ion source station where (A) is the glow discharge ion source, (B) ion optics for beam formation, (C) steering electrodes, (D) surface ion source, (E) bending ion optics, (F) Einzel lens and (G) extraction electrode.

This design does not have a lot of free volume for the buffer gas to expand into, resulting in the extraction region of the ion source having an undesirably high pressure. Also, the system cannot accommodate much larger vacuum pumps in its current configuration. As a result, ion beam intensities are limited by the vacuum and pumping systems. Based on experience with a similar ion source mounted in the IGISOL target chamber, which is equipped with considerably more pumping capacity, the possibility to use higher buffer gas pressures would offer significant improvements to beam intensities.

Another factor, held in high value during the design process of the new version of the ion source station, was easy access to both ion sources. In the current version removal of the glow discharge ion source or replacing its electrodes requires a considerable amount of effort due to the fact that much of the vacuum system has to be removed before the source becomes accessible. In the new design the source is located in a spacious vacuum chamber directly underneath a hinged lid. Additionally, in the new design no ion optical elements need to be removed for accessing the ion source. This is expected to improve the efficiency of the ion optical system and also reduce the amount of time needed for retuning the system after replacing the electrodes inside the ion source.

The upgraded system is designed to accommodate either the vacuum pump currently in use or a new pump with higher pumping capacity. Gate valves were added on both sides of the chamber in order to allow venting the chamber without having to vent neighboring sections of the system at the same time. Additionally, this removes the need to stop any of the vacuum pumps for venting the ion source chamber. The rectangular vacuum chamber was designed with a large number of flanges that can be used to provide access into the chamber. In particular, installation of a laser ablation ion source was considered and sufficient laser beam access was a requirement in the design process.

3.3 Ion beam formation and manipulation

Once reaction products have been evacuated from the ion guide they are separated from the remaining buffer gas with the help of a sextupole ion beam guide (SPIG) [61] which is a linear Paul trap with sextupole electrode configuration. The benefit of using such a device is that its open geometry allows for efficient removal of neutral buffer gas via pumping while confining electrically charged reaction products to a small region within the trap. The SPIG transports collected ions to an extraction electrode system which is used to accelerate the ions with a static total potential of 30 kV. This concludes the initial formation of the secondary beam at IGISOL. Subsequently, the ion beam is guided to a mass separator dipole magnet with mass resolving power $M/\Delta M = 500$. Achieved mass resolution is sufficient for separation of different isobars in the secondary beam.

After the secondary beam has been isobarically separated, the ions are injected into a radiofrequency quadrupole cooler buncher (RFQ) [63]. The RFQ is a

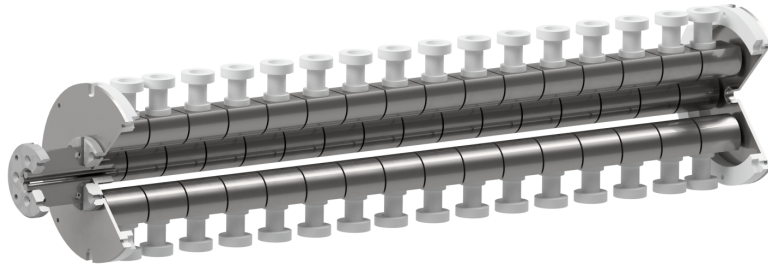


FIGURE 13 Internal structure of the RFQ used at IGISOL as it was at the time of the measurement campaigns of this work. An updated design was commissioned following the measurement campaigns. One quarter section has been removed in the figure for better visibility.

linear Paul trap used to cool and bunch the secondary beam. The device consists of four circular rods that have been segmented along the beam axis, see figure 13. A radiofrequency (RF) voltage is applied to the rods together with a set of DC voltages that are applied to individual axial segments. The DC voltages are used to generate a voltage gradient along the beam axis with a local minimum near the far end of the device. Together these voltages provide both radial and axial confinement for ions with kinetic energies not exceeding the depth of the effective static pseudo potential of the device.

In order to inject ions into the Paul trap without having them bounce back out, helium buffer gas is used. Energy of incident particles is adjusted to be barely sufficient for the ions to climb over the effective pseudo potential in the RFQ. This is achieved by supplying an adjustable static voltage, approximately 30 kV, to the RFQ and surrounding pieces of infrastructure, including deceleration electrodes, for example. As the ions pass through the device they lose energy via elastic collisions with helium atoms and become trapped in the potential well. Neutral helium atoms are not affected by the effective pseudo potential and therefore, on average, carry their kinetic energy away from the trapping region. This leads to cooling of the secondary beam and eventually formation of ion bunches as the ions fall deeper into the potential well guided by the DC voltage gradient along the beam axis. Finally, the ions can be extracted as bunches by lowering the potential wall on the extraction side of the RFQ.

The RFQ was a critical component of all measurements in this work. It was used to create well defined ion bunches that were then injected into the JYFLTRAP [8] double Penning trap for the purpose of high-precision mass measurements (see included articles [PI, PII, PIII]) or systematic characterization of the detector system used in the mass measurements (see section 4.3).

3.4 JYFLTRAP double Penning trap

The most significant part of the IGISOL facility for this work was the JYFLTRAP [8] double Penning trap. It was either directly utilized or served as a source of motivation throughout this work. Direct usage came in the form of high-precision mass measurements during three measurement campaigns where both TOF-ICR and PI-ICR techniques were used, see included articles [PI,PI,PIII]. Additionally, mass measurements at JYFLTRAP served as perhaps the single strongest argument for developing the new off-line ion source station discussed in the included article [PIV].

JYFLTRAP consists of two cylindrical Penning traps located within the bore of a single superconducting magnet, see figure 14. JYFLTRAP and all electronics needed for its operation are located on a 30 kV platform after the RFQ presented in section 3.3. The two traps primarily serve two separate purposes, purification of ion samples and high precision mass measurements. The first of the two traps is the gas-filled purification trap. It is filled with helium buffer gas, typically $2 \cdot 10^{-2} - 4 \cdot 10^{-2}$ mbar, for the purpose of utilizing the mass-selective buffer gas cooling method [44]. The purification trap can be used to provide the second trap with isobarically pure ion samples. If there are other strongly produced ions, other than the ion-of-interest additional cleaning might be required. In cases like that, the second trap can be utilized together with the purification trap to perform an additional cleaning step.

The second trap is the measurement trap. It is separated from the gas-filled purification trap with a small cylindrical channel, 2 mm in diameter and approximately 5 cm long, that allows ions to be transported between the traps and simultaneously functions as a pumping barrier, see figure 15. Any residual gas in the second trap is unwanted as it limits the precision achievable in the determination of the ν_c frequency. Extraction side of the trap has an open geometry for

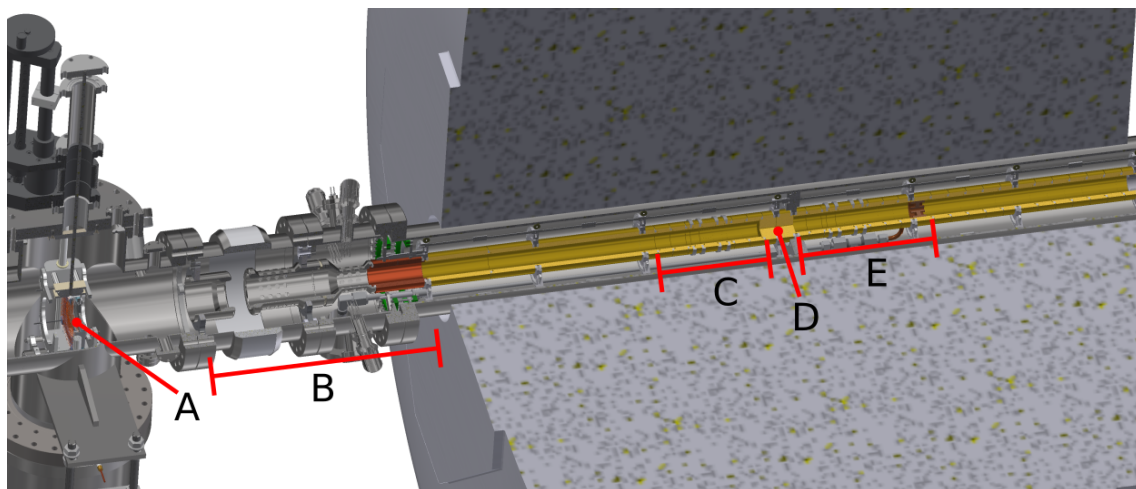


FIGURE 14 Internal structure of JYFLTRAP and its extraction region, where (A) is the delay-line MCP detector, (B) extraction ion optics, (C) measurement trap, (D) pumping barrier and (E) purification trap.

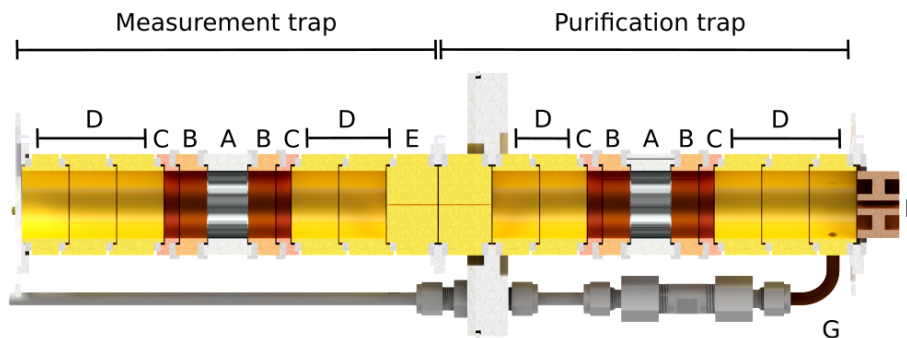


FIGURE 15 JYFLTRAP electrode and pumping barrier geometry. Here (A) are the eight-fold segmented ring electrodes, (B) and (C) the two-fold segmented and non-segmented correction electrodes, (D) the endcap electrodes, (E) and (F) purification trap pumping barriers and (G) is the buffer gas line.

improved pumping.

The two traps have the same electrode geometry. Both consist of a eight-fold segmented ring electrode, two sets of correction electrodes and endcap electrodes. The segmented ring electrodes are used for all manipulations of radial eigenmotions in the traps using a simplified excitation scheme. In the simplified excitation scheme quadrupole excitations are performed via applying an RF signal to two opposite quadrants of the ring electrode while applying a static voltage to the remaining two quadrants. Similarly, dipole excitations are applied to only a single quadrant while the remaining sections are kept at a fixed voltage [8]. Electrodes closest to the ring electrode are the two-fold segmented correction electrodes which were effectively used as a non-segment electrodes in this work. These are followed by set of non-segmented correction electrodes and endcap electrodes. Together these electrodes can be used to tune the potential in the traps to approximate an ideal harmonic potential. For a more thorough discussion on the technical details of JYFLTRAP the reader is referred to [8, 13].

A set of extraction electrodes is located after the measurement trap that accelerates ions to 30 keV. The extraction optics is designed to guide ions onto a microchannel plate detector (MCP) and magnifying the image created by the ions to better match the dimensions of the detector. The MCP is equipped with a delay line anode which is used to measure the position of each ion hitting the detector. A position sensitive detector is a critical component for the PI-ICR method but it can also be used in the TOF-ICR method. The model of the MCP used at JYFLTRAP is DLD40 from RoentDek GmbH [64]. As a part of this work it was discovered that the performance of the MCP detector is of high importance to the measurements with JYFLTRAP not only via the need to collect sufficient statistics but it was also found to introduce a systematic shift in ν_c frequency determination. This effect was studied in great detail in this work as a part of a measurement campaign in the neutron-rich rare-earth region of the nuclear chart, see section 4.3.

3.5 Penning trap mass measurement techniques

Penning trap mass measurements at JYFLTRAP were an integral part of this PhD thesis work. All results presented in included articles [PI, PII, PIII] were directly measured using JYFLTRAP. It also served as a motivation for the commissioning of the new off-line ion source facility at IGISOL, discussed in section 3.2. Due to the great importance of JYFLTRAP for this work, understanding of available ion sample purification and mass measurement techniques is instrumental. In this section methods that were utilized in the successful measurement campaigns of this thesis work will be presented.

3.5.1 Ion sample purification

Any measurement at JYFLTRAP starts with the injection of an ion bunch into the purification trap presented in section 3.4. This is achieved via alternating a voltage on the injection side endcaps of the purification trap labeled D in figure 14. At first, the voltages are lowered to slightly below the potential of the incoming ion bunch. Once the ion bunch has passed the endcap electrodes the voltages are raised and the ions are trapped. The timing of the changes in the voltages is determined by the distance between the source of the ion sample (the RFQ) and JYFLTRAP together with the energy and mass of the ion beam as it is transported through the intermediate beam line between RFQ and JYFLTRAP.

Once a bunch of ions has been captured in the purification trap the ions are allowed to dissipate their remaining axial energy in the buffer gas. The remaining axial amplitude is a sum of the potential difference between the RFQ and the purification trap and the amount of energy the ion bunch acquired due to the raising of the injection side potential in the trap. If an ion bunch has not fully passed the endcap electrodes before the voltage is raised at least a part of the ion sample will receive an increase in their axial amplitude from the raising potential wall. This effect is also to be considered in any other situation where an ion bunch is captured in either of the traps, most notably in the case of the PI-ICR method when ions are transported into the measurement trap.

Having cooled sufficiently, the ions are excited with a short RF pulse applied to one quadrant of the trap at the ν_- frequency, which corresponds to the dipole excitation in the simplified excitation scheme described in section 3.4. According to equation 25 the magnetron motion is first-order mass independent. Therefore, excitation of the magnetron motion amplitude will enlarge the radius of all ions irrespective of their mass. Using a sufficiently high excitation pulse amplitude this results in a situation where all ions are lost when extracting them from the trap as they collide with the diaphragm located between the two traps, see figure 15. However, ions can be mass-selectively recentered by converting their motion into the high-frequency ν_+ mode using a quadrupole excitation at the ν_c frequency.

As discussed in section 2.2, the magnetron motion has the lowest frequency

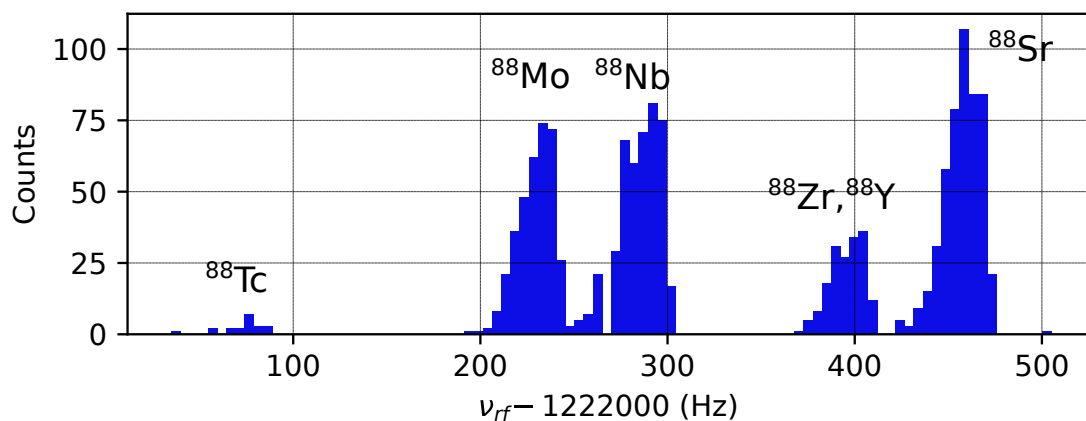


FIGURE 16 Scan of the quadrupole excitation frequency at mass number $A = 88$. The scan was performed as a part of the measurement campaign of article [PIII] where the isomeric and ground states of ^{88}Tc were measured. The cyclotron frequencies ν_c for the isobars are determined from the locations of the highlighted peaks.

out of the three eigenmotion. Additionally, both axial and reduced cyclotron motion have radii that are proportional to energy of the motion. Therefore, if the induced magnetron motion were to be converted into the reduced cyclotron motion there would be a considerable increase in energy dissipation due to an increase in collisions with buffer gas and, therefore, the ions would fall closer to the center of the trap. It was shown in [65] that such a conversion from one eigenmotion to another is, in fact, possible. It can be achieved via applying a quadrupole excitation at the sum frequency $\nu_+ + \nu_- = \nu_c$ to the ring electrode. This causes the amplitudes of the magnetron and reduced cyclotron motion to oscillate in between being purely magnetron to purely reduced cyclotron. Given that the ν_+ component of the sum frequency used for the conversion has a leading order mass dependence, see equation 26, this method is also mass-selective. The method is known as the sideband cooling technique [44].

The sideband cooling technique is the primary tool at JYFLTRAP for removing isobaric contaminants from ion samples. Each mass measurement starts with exciting the magnetron motion amplitude of the full ion sample injected into the purification trap. Then the quadrupole excitation frequency is scanned and at the end of each cycle the centered ions are extracted onto an MCP detector. An example of a quadrupole excitation scan is presented in figure 16, where isobars from ^{88}Tc to the stable ^{88}Sr have been identified based on expected cyclotron frequencies. ^{88}Zr and ^{88}Y are separated by only 10 Hz and therefore appear here only as a single peak, assuming that both were produced in detectable amounts in the used reaction process.

In order to select the ion of interest, the quadrupole excitation frequency is fixed to the ν_c frequency determined from the corresponding peak in the excitation scan (see figure 16). The ion sample is then extracted from the purification trap and recaptured in the measurement trap. Most often this procedure offers

sufficient mass resolving power to remove all unwanted ion species. However, this is not always the case. For example, the mass difference between ^{88}Zr and ^{88}Y is so small (670 keV [39]) that they cannot be resolved from each other (see figure 16). There are two additional methods that can be utilized in the second, measurement trap of JYFLTRAP in case further cleaning is required, the so-called Ramsey cleaning [66] and phase-dependent cleaning methods.

In this work only the Ramsey cleaning was used in addition to the sideband cooling technique. The so-called Ramsey cleaning method utilizes a dipole RF excitation in the measurement trap at the ν_c frequency to excite the unwanted ions into large radii. At the same time the ion of interest needs to remain centered. This is achieved via selecting the RF excitation timings in such a way that the unwanted ions are maximally and the ions of interest minimally excited. This method requires sufficient knowledge of the ν_c frequencies of all ion species beforehand. Once the unwanted ions have been excited to a large radius the ions are extracted back towards the purification trap where the ions of interest are recaptured. Simultaneously, the contaminant ions hit the diaphragm separating the traps. The recaptured ions are usually re-cooled and centered in the purification trap and the remaining ions moved back into the measurement trap for determination of the ν_c frequency or transported directly to a post-trap spectroscopy set-up. For a more detailed discussion, the reader is referred to [66].

The second method for additional cleaning that has been tested at JYFLTRAP is the phase-dependent cleaning method [13]. Phase-dependent cleaning can be performed in two ways, both of which are mainly suitable for cleaning an ion sample from contaminants close in mass to the desired ion species in preparation to transporting the ions to a post-trap spectroscopy set-up. Both methods begin with capturing a sample of ions in the measurement trap and applying a short wide-band dipole excitation at the ν_+ frequency. This ensures that all ion species are excited. Sufficient time is allowed to pass in order to accumulate a phase difference between ion species. A quadrupole pulse is then applied at the ν_c frequency to convert the ions to the ν_- mode, followed by extraction of the ions. This produces two separate images on the MCP detector. Movable slits are then placed in front of the detector in such a way that only the ions of interest pass through the slit, resulting in a clean ion sample. Once the detector is retracted from the beam line the ions can be transported to a post-trap spectroscopy set-up.

The phase difference accumulated in the process can also be used to remove contaminants without the use of a slit system. The phase accumulation time can be adjusted so that a phase difference of π separates ions of interest and contaminants. Applying a dipole pulse at the ν_- frequency after the conversion excitation it is possible to push the ions of interest towards the center of the trap. Simultaneously, contaminant ions are moved in the same direction resulting in them gaining a larger radius. If the timing and amplitude of the additional RF pulse are suitable, it is possible to excite contaminants so far that they either hit trap electrodes or are not transported to any subsequent measurement set-up while pushing the desired ions towards the trap center.

3.5.2 Time-of-Flight Ion Cyclotron Resonance (TOF-ICR)

Two mass measurement techniques have been used at JYFLTRAP, the Time-of-Flight Ion Cyclotron Resonance technique (TOF-ICR) [9,10] and the Phase-Imaging Ion-Cyclotron-Resonance (PI-ICR) [11–13] technique. The latter was commissioned only recently [13] whereas the TOF-ICR technique has been in active use ever since JYFLTRAP was commissioned and it still maintains an important role in mass measurements. Both techniques have their strengths and in many cases they are used to complement each other, as was the case, for example, in the included article [PIII].

The TOF-ICR technique is based on using the time-of-flight (TOF) of ions from the measurement trap onto the MCP detector as a method of detecting conversions between the two radial eigenmotions of ions in Penning traps. The time-of-flight of ions depends on three factors: initial axial speed, shape of the extraction potential after the traps and interaction between the ions and the magnetic field of the superconducting solenoid housing the two Penning traps. The first two are kept constant for the duration of a measurement but the third can be affected mass-selectively via increasing the amplitudes of their radial eigenmotions. This effect can be described conveniently using the magnetic moment

$$\mu = IA = \frac{\omega}{2\pi} q\pi r^2 = \frac{1}{2} \omega q r^2. \quad (31)$$

Starting from Newtonian equations for a singly charged particle moving in a uniform magnetic field perpendicular to the field we can derive two intermediate results

$$m \frac{v^2}{r} = evB \quad (32)$$

$$\omega = \frac{eB}{m} \quad (33)$$

and

$$r = \frac{\sqrt{2E_\theta m}}{eB}, \quad (34)$$

where v is the speed, ω the angular speed and E_θ the kinetic energy of the ion's angular motion. Plugging these two results into equation (31) we get

$$\mu = \frac{E_\theta}{B}. \quad (35)$$

Here $E_\theta \approx E_\theta(\omega_{rf})$ and $B \approx B(z)$ leading to $\vec{B}(z) = B(z)\hat{e}_z$ and

$$\vec{\mu}(\omega_{rf}, z) = \frac{E_r(\omega_{rf})}{B(z)} \hat{e}_z. \quad (36)$$

As ions pass through the gradient of the magnetic field they experience an axial force

$$\vec{F}(\omega_{rf}, z) = -\nabla \left(\vec{\mu}(\omega_{rf}, z) \cdot \vec{B}(z) \right). \quad (37)$$

This force leads to a reduction in the time-of-flight of ions as a function of their radial kinetic energy. More specifically, this results in different time-of-flights for ions in the magnetron and reduced cyclotron motion due to the fact that the cyclotron eigenmotion is much more energetic than the magnetron. The total time-of-flight T can be expressed as

$$T(\omega_{rf}) = \int_{z_0}^{z_1} \sqrt{\frac{m}{2[E_0 - q \cdot V(z) - \mu(\omega_{rf}, z) \cdot B(z)]}} dz, \quad (38)$$

where E_0 is the total energy of the ion, q the electrical charge of the ion, $V(z)$ the electrical potential and $B(z)$ the magnetic field strength at point z along the path from the measurement trap at $z = z_0$ to the MCP detector at $z = z_1$ [10, 67].

TOF-ICR measurements are performed by first increasing the amplitude of the magnetron motion of ions in the measurement trap. A quadrupolar conversion RF pulse is then applied to convert the motion of ions from the ν_+ mode into the ν_- mode and the ions are extracted onto the detector. This process is repeated while the conversion frequency is scanned. This results in varying degrees of conversion from the magnetron mode into the reduced cyclotron mode depending on the ν_c frequency of the ions. When the conversion frequency matches the ν_c frequency of the ions, the time-of-flight will reach its minimum. In case a single conversion pulse is used, there will be a single local minimum with a smaller time-of-flight than any other minima. An example of a time-of-flight spectrum resulting from the use of a single conversion pulse is presented in figure 17. There will also be several other local minima, but with longer time-of-flights than the central minimum. A TOF-ICR spectrum collected in such a scan can be fitted with a theoretical function describing the line shape, where frequency of the central minimum is one of the fitted parameters. Therefore, fitting the data enables experimental determination of the cyclotron frequency ν_c .

TOF-ICR measurements can also be performed using more complex RF conversion schemes. In this work the so-called Ramsey method [68, 69] was also utilized. There the conversion pulse is divided into parts separated by a period without excitation. In this work, two excitation pulses were used with 25 – 350 – 25 ms (On-Off-On) and 25 – 750 – 25 ms (On-Off-On) timing patterns, where the RF excitations were applied for the duration of the 25 ms sections. The benefit of the Ramsey method is the reduction of the full width at half-maximum (FWHM) of a central TOF minimum, i.e. uncertainty of the measured ν_c frequency. The improvement has been experimentally determined to be about a factor of 3 [69] in the case of the two-pulse Ramsey excitation. Alternatively, the improvement can be seen via a reduced length of excitation needed to reach a given level of resolution. In the case of measuring radioactive isotopes, which was the case in included articles [PI, PII, PIII], reduction in the excitation time gives a two-fold gain in statistics: more measurement cycles can be performed and less ions are lost due to radioactive decays. For these reasons the Ramsey method was utilized on several occasions in this work.

The Ramsey method is based on the principle of using the TOF of ions to determine the ν_c frequency of ions in the same manner as with the single con-

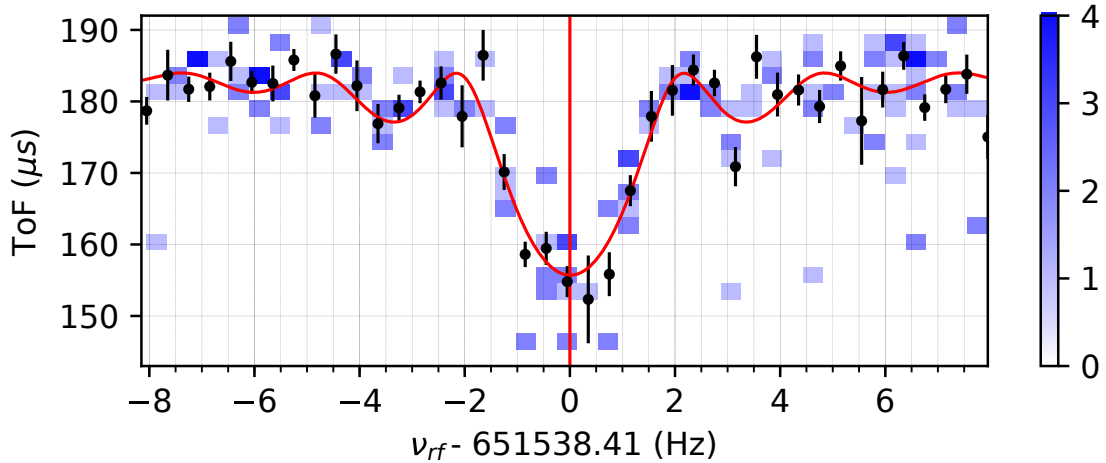


FIGURE 17 A time-of-flight resonance spectrum for $^{165}\text{Tb}^{1+}$ measured as a part of the work presented in [PII] using a 400 ms quadrupole excitation in the measurement trap. Center frequency and fitted theoretical lineshape are presented as red solid lines. The color of background shading indicates the number of ions.

version excitation. However, resulting TOF spectra have a different line shape. An example of a TOF spectrum measured with the Ramsey method using two RF excitation pulses is presented in figure 18. The figure illustrates the different line shape but also shows that the Ramsey method cannot be used on its own to determine the ν_c frequency due to the fact that all TOF minima are roughly of the same depth. As a result, distinguishing which minimum corresponds to the ν_c frequency is not reliable based solely on the two-pulse Ramsey method. For this reason, each measurement using the Ramsey method was accompanied with another measurement using a single conversion pulse. The resonance presented in figure 17 was used during the measurement campaign of [PII] to verify which minimum in figure 18 corresponds to the ν_c frequency.

The Ramsey method was used in a large portion of TOF-ICR measurements performed in this work. However, full measurements using only a single conversion pulse were also necessary. Two types of situation were encountered where the Ramsey method was not a viable option. The line shape resulting from the two-pulse conversion in the Ramsey method becomes difficult to fit with a theoretical line shape in case a background of unwanted ions is present. Even a comparably small number of contaminant ions is sufficient to blur out a resonance and make it difficult to distinguish TOF minima and maxima, or possibly even verify if the ion-of-interest is present. In such cases, the use of a single conversion pulse is preferable since it makes a successful conversion at the central TOF minimum easy to distinguish from background. This applies also to cases where more than one nuclear state of the ion-of-interest are injected into the measurement trap. Given a sufficiently long excitation time, the central minima of different states can be separated if a single conversion pulse is used. On the other hand, in the Ramsey method different states are likely to either form separate

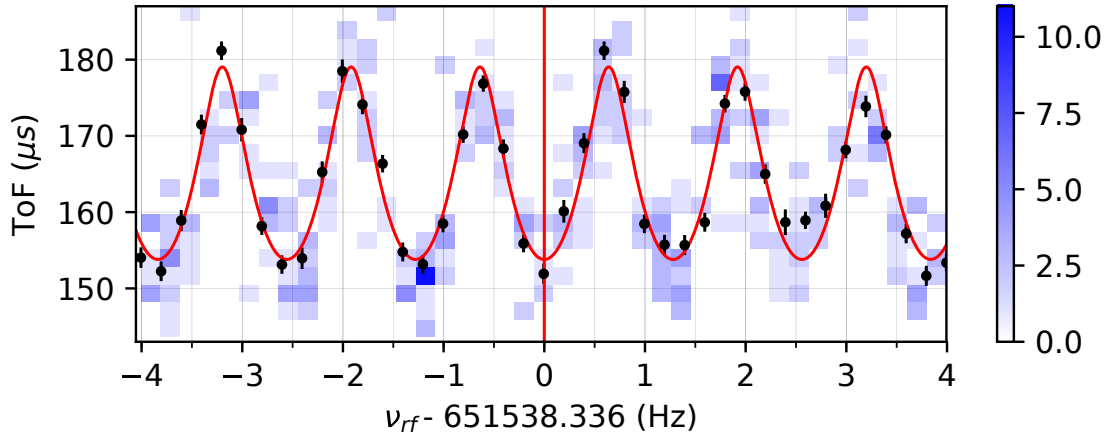


FIGURE 18 A time-of-flight resonance for $^{165}\text{Tb}^{1+}$ measured with the Ramsey method as a part of the work presented in [PII] using 25 – 750 – 25 ms (On-Off-On) excitation cycle. Center frequency and fitted theoretical lineshape are presented as red solid lines. The color of background shading indicates the number of ions.

central minima and overlap with each others line shapes, resulting in a failure to identify the separate states, or blur out the resonance. Such a case was discovered in the attached article [PII], where it was found that a combination of ^{162}Eu and $^{162}\text{Eu}^m$ was mistakenly labeled as a single state during the measurement campaign of [PI]. The presence of two states was verified in [PII] using both TOF-ICR and PI-ICR techniques. For a more detailed discussion the reader is referred to [PII].

3.5.3 Phase-Imaging Ion-Cyclotron-Resonance (PI-ICR)

The Phase-Imaging Ion-Cyclotron-Resonance (PI-ICR) method [11, 12] is based on determination of the cyclotron frequency ν_c via direct measurement of the accumulated phases of the magnetron ν_- and reduced cyclotron ν_+ motions after a certain accumulation time. This basic principle makes the method rather straight-forward to comprehend on a general level. However, an actual measurement using the method requires careful manipulation of an ion sample using a somewhat complex timing pattern. Compared to the TOF-ICR method, an individual measurement using the PI-ICR method is more time consuming to set up, regardless of the simpler basic idea behind the measurement technique, but it offers significant gains in mass resolution and measurement precision.

In the PI-ICR method the ion samples are prepared in the purification trap the same way as in the TOF-ICR method, as discussed in section 3.5.1. Once a purified ion sample is captured in the measurement trap the amplitude of any coherent ion motion is damped using dipolar RF excitations. As ions are injected into the measurement trap, they can acquire non-zero amplitudes for the axial ν_z and magnetron ν_- eigenmotions, here referred to as residual motion. The main source of the residual axial motion is the process of transferring ions from the pu-

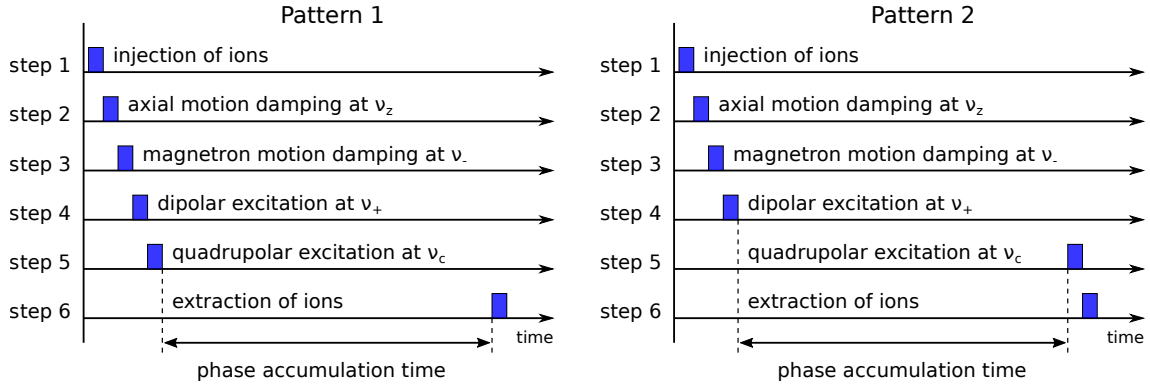


FIGURE 19 Excitation pulse timing patterns used in the PI-ICR method for the determination of the ν_c frequency in this work. Pattern 1 corresponds to the angle accumulated in the magnetron mode ϕ_- and pattern 2 to the angle accumulated in the reduced cyclotron mode ϕ_+ .

rification trap into the measurement trap, where voltage of the endcap electrodes separating the two traps, see figure 15, are lowered to allow ions to pass from one trap into the next. As the voltages are raised back to their original values, some ions may be affected by the changing electrical field and receive an increase in their potential energy. Once these ions reach the measurement trap they begin to oscillate in the approximately harmonic potential well with an increased axial motion amplitude. The gain in axial motion amplitude can be minimized through careful tuning of the release and capture times of ions when they are transferred between the two traps.

Even though tuning the transfer timings is a standard procedure in any measurement at JYFLTRAP, ions still acquire a non-zero axial motion amplitude as they are captured in the measurement trap. Given that the measurement trap is not filled with buffer gas, only coherent motion of ions can be addressed. This is done via scanning the timing of the extraction of ions over the period of the axial motion. This results in an oscillating time-of-flight pattern as a function of the extraction time that can be used as a diagnostic tool in setting up a suitable RF excitation to damp the motion. Both the phase and amplitude of the RF excitation need to be tuned to match the phase and amplitude of the residual axial motion in order to achieve optimal damping of the coherent residual motion. Damping of the residual axial motion corresponds to step 2 in figure 19.

The other residual motion type can be addressed in a similar manner. Any ion sample transferred from the purification trap into the measurement trap receives a non-zero magnetron motion amplitude. The main reason behind this is misalignment of the two traps compared to each other. Any ion that is injected into a Penning trap at a non-zero radius with respect to the center of the trap will assume a magnetron motion amplitude equal to the injection radius. As in the case of damping residual axial motion, only coherent residual magnetron motion can be damped in the measurement trap. Here the timing of extraction of ions from the measurement trap onto the position-sensitive MCP detector is scanned over the period of the magnetron motion. This results in a number of ion sam-

ple projections on the detector that surround the projection of the center of the trap. Scanning the extraction timing evenly throughout the period of the magnetron motion allows the determination of the location of the trap center which is calculated as the average position of all detected ions.

Once the coordinates corresponding to the center of the measurement trap have been determined, a scan of the extraction time over the magnetron period can be used as a diagnostic tool in setting up a suitable RF excitation for damping the residual magnetron motion. Again, both the phase and amplitude of the excitation must be tuned to match those of the coherent motion of ions. Damping of the residual magnetron motion corresponds to step 3 in figure 19. The order of steps 2 and 3 can be interchanged without affecting the measurement process.

After both the residual axial and magnetron motions have been damped the ion sample is ready for the actual determination of the ν_c frequency which is done in two parts. Ions are allowed to accumulate a phase angle in both of the two radial motion types, magnetron ν_- and reduced cyclotron ν_+ . In both cases the procedure starts with increasing the ν_+ radius of the damped ion bunches using a dipolar RF pulse, labeled step 4 in figure 19. Then the ions are either allowed to accumulate phase in the ν_+ (pattern 2) mode or they are subjected to a broad-band conversion pulse at the presumed ν_c frequency (pattern 1). Using a high amplitude and a short duration for the conversion pulse results in a large band-width of the excitation, which removes the need to have precise knowledge of the ν_c frequency - the quantity that is actually being measured. In the case of accumulating phase in the ν_+ mode, a conversion pulse is applied before extracting the ions from the measurement trap. Therefore, the two patterns presented in figure 19 differ only in the location of the conversion pulse and they share the same phase accumulation time.

These two patterns result in two phase angles, $\phi_- + 2\pi n_- = 2\pi\nu_-t$ in the case of the magnetron mode and $\phi_+ + 2\pi n_+ = 2\pi\nu_+t$ in the case of the reduced cyclotron mode, where n are the numbers of full revolutions completed in phase accumulation time t and ϕ are the additional angles accumulated on top of the full revolutions. Combining the two expression gives us

$$2\pi(\nu_+ + \nu_-)t = \phi_+ + \phi_- + 2\pi(n_+ + n_-). \quad (39)$$

Here it needs to be noted that projections of the accumulated phase angles on the detector evolve in opposite directions as the phase accumulation time t is changed. This is due to the fact that the ν_+ phase angle is accumulated prior to the conversion pulse which effectively reverses the sign of the projected angle. Taking into account the handedness of a standard cartesian coordinate system, equation (39) can be expressed using equation (27) together with $\omega_{\pm} = 2\pi\nu_{\pm}$ as

$$2\pi\nu_c t = \phi_+ - \phi_- + 2\pi(n_+ + n_-) \equiv \phi + 2\pi(n_+ + n_-), \quad (40)$$

leading to

$$\nu_c = \frac{\phi + 2\pi(n_+ + n_-)}{2\pi t}, \quad (41)$$

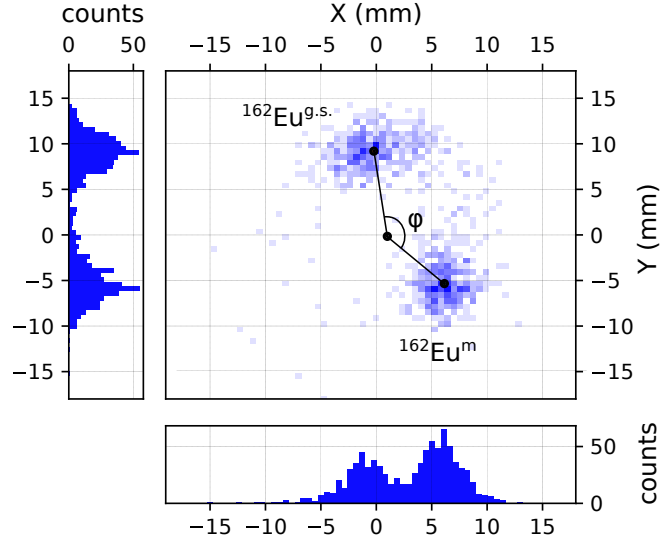


FIGURE 20 An example of ν_+ phases accumulated using a 600 ms phase accumulation time in the PI-ICR method where the singly-charged ions belonging to the ground and isomeric state of ^{162}Eu are separated. In the middle figure background shading indicates the total number of ions, where darker shading indicates more ions. Center point of the two states and the center of the measurement trap are marked as black dots and the angle between the two states as ϕ . Figures on the left and bottom present projections of the middle figure onto the Y and X axes, respectively.

where ϕ is the angle between the projections of the phase angles on the detector. An example of ν_+ phases of ^{162}Eu and $^{162}\text{Eu}^m$ projected onto the detector are presented in figure 20. Expression (41) also reveals one challenge inherent to this measurement technique: the ν_+ and ν_- frequencies need to be known precisely enough to guarantee that the numbers of full revolutions for each eigenmotion is determined correctly. In the case of the first-order mass-independent magnetron motion (see equation (25)) this is not an issue. However, the strongly mass-dependent reduced cyclotron motion (see equation (26)) is more prone to errors in this regard. To overcome this issue, a brief measurement with the TOF-ICR technique can be used to verify the ν_c frequency with sufficient precision to guarantee correct assignment of the integer number of revolutions in the ν_+ mode. In principle, measurement of the angle between the ν_+ projection and any fixed reference point on the detector using several accumulation times could be used to deduce the ν_+ frequency with sufficient precision. However, the TOF-ICR method has proven to be the more convenient choice in practice.

For further discussion on the PI-ICR method in general the reader is referred to [12]. For a detailed discussion on the use of the method at JYFLTRAP the reader is referred to [13] where, among other things, the main sources of systematic uncertainty in PI-ICR measurements at JYFLTRAP were estimated. However, more recently, additional sources of systematic uncertainties have been studied. For example the effect of the magnitude of the angle ϕ on the resulting ν_c frequency has been studied. Additionally, as a part of this work a new source of systematic

uncertainty relevant to both the TOF-ICR and PI-ICR methods was discovered, see section 4.3. A publication detailing findings on all discovered sources of systematic uncertainty is to follow this work [70].

4 RESULTS AND DISCUSSION

This section is dedicated to discussing results obtained in this work. Included articles [PI, PII, PIII] contain detailed discussion on each measurement campaign and present the most important findings from each campaign. Therefore, it is recommended that the reader consults the included articles prior to reading this section. Here in sections 4.1 and 4.2 the discussion will be limited to details that could not be included in the articles. Additionally, systematic studies on the effect of count rate on PI-ICR mass measurements will be discussed in section 4.3.

4.1 Mass measurements in the neutron rich rare-earth region

A total of 22 ground-state masses ($^{154,156,158}\text{Nd}$, $^{158,160,161}\text{Pm}$, $^{162,163}\text{Sm}$, $^{162-165}\text{Eu}$, $^{163-167}\text{Gd}$, $^{164-168}\text{Tb}$) and two isomeric state masses ($^{162}\text{Eu}^m$, $^{163}\text{Gd}^m$) were measured in the neutron-rich rare-earth region of the nuclear chart as a part of this work, see included articles [PI, PII]. Mass measurement results from the two publications are presented in table 1. Out of the measured nuclides, 14 were measured for the first time and the precisions of many of the other masses were improved considerably. In this work we measured some of the heaviest neutron-rich nuclei ever produced as fission fragments at the IGISOL facility. In fact, ^{168}Tb measured in this work is the heaviest fission fragment measured at JYFLTRAP to date.

The effect of the results on the mass surface was studied using several metrics probing various properties of the nuclei. In general, all studied quantities are derivatives of the mass surface which is a contour spanned by plotting atomic masses as a function of neutron (N) and proton (Z) numbers. The surface exhibits staggering between neighboring points across the nuclear chart, known as odd-even staggering. It can be studied via calculating quantities between successive points, such as neutron (S_n) and proton (S_p) separation energies or the neutron (D_n) and proton (D_p) pairing energy metrics. Quantities sensitive to the odd-even staggering can be used to study how individual nucleons pair with each other. In

this work the neutron separation energies S_n were the most significant derivatives of the mass surface due to their importance to the used nucleosynthesis models.

The mass surface acquires a smooth shape if the plotted masses are chosen in such a way that the pairing effect causing the odd-even staggering is neglected. This can be achieved by plotting nuclei with only even-even, odd-odd, even-odd or odd-even neutron and proton numbers. Studying the mass surface using such carefully limited subsets of atomic masses can reveal a wealth of information and interesting properties of individual nuclei and regions of the nuclear chart. In this work several quantities insensitive to the odd-even staggering were studied, such as two-neutron separation energies (S_{2n}) and two-neutron shell gap energies (D_{2n}). Such metrics are useful in studying general trends in nuclear structure otherwise easily masked by the odd-even staggering. In addition to studying the behavior of nucleons of a single type, either protons or neutrons, also the interaction between the two can be probed via calculating double differences of binding energies, called δV_{pn} . For definitions of these quantities, the reader is referred to [PI, PII].

Together metrics such as these form a set of tools that can be used to study the mass surface and extract new information on nuclear structure. In the case of included articles [PI] and [PII] focusing on the neutron-rich side of the nuclear chart, the primary focus was on studying properties of nuclei with differing neutron numbers N through the use of quantities such as S_n , S_{2n} , D_n and D_{2n} . Additionally, the effect of the measured atomic masses on the r -process was studied via simulations of a neutron-star merger. The new masses resulted in reduced staggering of simulated r -process abundances and in a better agreement between the simulation and observed solar abundances. In the simulations, the most significant metrics derived from the results of this work was the neutron separation energy S_n . It is the primary way in which our results affect the simulations due to the fact that the neutron separation energies affect both neutron-capture and photo-dissociation rates, both of which are highly important for the r -process in the astrophysical conditions of a neutron star merger.

The simulations relied on theoretical mass models in regions of the nuclear chart that have not been reached in experiments. Therefore, the measurements of atomic masses that previously needed to be extracted from theoretical mass models provides a two-fold benefit: a lower number of simulation input values rely on theoretical mass values and more data are available to test existing theoretical models which can be developed further. In the simulations performed in this work the FRDM12 [71] was used to supplement experimentally-known masses. However, there are several other theoretical models that could have been used instead, some of which, in fact, match the results from this work better than FRDM12. The reason why FRDM12 was used in this work is that it has been shown to result in isotopic abundances that match the solar data more precisely than other models [72], regardless of local mismatches with experimental data.

The primary quantity determined in a mass measurement at JYFLTRAP is the frequency ratio between two ion species, from which the typically reported mass excess values can be calculated. The mass excess values can be further used

to calculate any derivative of the mass surface, such as the neutron separation energies. Figures 21–26 present the mass excesses (ME) and neutron separation energies S_n determined in this work in the neutron-rich rare-earth region for the isotopic chains of Nd, Pm, Sm, Eu, Gd and Tb, respectively. Several theoretical mass models are included in the figures: microscopic Hartree-Fock-based model by Duflo and Zuker (henceforth referred to as Duflo-Zuker or D-Z) [17], Hartree-Fock-Bogoliubov model (HFB24) [18], Universal Nuclear Energy Density Functional (UNEDF0) [19] and two Weizsäcker-Skyrme models WS3 [20] and WS4 [21].

In the mass-excess figures (see figures (a) in figures 21–26) it can be seen that most of the mass models reproduce the trends of the mass surface rather well where there is experimental data available. However, the models start to diverge strongly as the neutron number N reaches a region where there is no experimental data to constrain the theories. It is noteworthy that FRDM12 does not reproduce the behavior of the mass surface seen as a peak in all of the figures around $N = 90$, attributed to the onset of strong prolate deformation [73,74], as well as many of the other theories. Additionally, the new experimental masses seem to indicate that there is a trend of growing under-estimation of mass excesses by FRDM12. On the other hand, this trend is not visible in the neutron separation energy figures (see figures (b) in figures 21–26). Interestingly, the diverging of theories seen in the mass-excess values is also not present so strongly in neutron-separation energies. WS3 and WS4 produce a dip in neutron separation energies compared to the FRDM12 around $N = 106$ not seen with other models, but still do not show signs of a long-term trend. Also, even though there is a clear over-estimation of mass-excesses by the UNEDF0 model throughout the region studied in this work, there is no clear over or under-estimation of neutron separation energies.

The most clear changes introduced into the mass surface by this work can be seen in the isotopic chain of neodymium, presented in figure 21. Both the mass excesses and neutron separation energies show clear changes to the literature values from the most recent atomic mass evaluation AME2016 [39]. As discussed in included articles [PI,PII], the new mass values reveal that there is an over-estimation of the odd-even staggering in all isotopic chains for all studied models. The new mass values produced a smoother abundance in the r -process simulations than the baseline calculations using mass values from AME16 and FRDM12. Additionally, the new masses resulted in a better agreement with the observed solar abundance pattern of the r -process, quantified here as

$$\chi^2 = \sum_A \left(\frac{Y(A)_{solar} - Y(A)_{calc}}{Y(A)_{solar}} \right)^2 \quad (42)$$

which reduced from 18.9 to 10.7 after the first measurement campaign, see [PI], and dropping further down to 9.6 after the second measurement campaign, see [PII], indicating that the new masses result in better agreement between the r -process simulations and solar abundances.

TABLE 1 Frequency ratios (r) and mass-excess values (ME) determined in this work in the rare-earth region with JYFLTRAP and corresponding AME16 values. All measurements were done with singly-charged ions. The reference masses were adopted from AME16 and # signs indicate extrapolated values therein. For more details on these results, see included articles [PI, PII].

Isotope	Reference	$r = \nu_{c,ref}/\nu_c$	$ME_{JYFL}(\text{keV})$	$ME_{AME16}(\text{keV})$
^{154}Nd	^{133}Cs	1.158 189 215(203)	-65601.2(25.1)	-65825(53)
^{156}Nd	^{136}Xe	1.147 366 924(19)	-60210(2)	-60470(200)
^{158}Nd	^{136}Xe	1.162 132 772(290)	-53897(37)	-54060(200)#
^{158}Pm	^{158}Gd	1.000 078 752(9)	-59104(2)	-59089(13)
^{160}Pm	^{136}Xe	1.176 857 014(130)	-52851(16)	-53000(200)#
^{161}Pm	^{136}Xe	1.184 236 679(468)	-50107.6(59.3)	-50235(298)#
^{162}Sm	^{136}Xe	1.191 560 914(39)	-54381(5)	-54530(200)#
^{163}Sm	^{136}Xe	1.198 949 148(286)	-50552.3(36.2)	-50720(298)#
^{162}Eu	see [PII]	see [PII]	-58720.4(3.1)	-58703(35)
$^{162}\text{Eu}^m$	^{133}Cs	1.218 439 459(13)	-58565.7(7.6)	-58540(40)
^{163}Eu	^{133}Cs	1.225 979 710(30)	-56575.7(3.8)	-56485(66)
^{164}Eu	^{136}Xe	1.206 285 979(29)	-53231.1(3.7)	-53381(114)#
^{165}Eu	^{136}Xe	1.213 663 750(48)	-50726.9(6.0)	-50724(138)#
^{163}Gd	^{136}Xe	1.198 863 600(81)	-61382.4(10.2)	-61314(8)
$^{163}\text{Gd}^m$	^{136}Xe	1.198 864 872(106)	-61221.3(13.4)	-61176(8)
^{164}Gd	^{171}Yb	0.959 046 522(14)	-59694(3)	-59770(100)#
^{165}Gd	^{171}Yb	1.058 489 243(23)	-56522(4)	-56450(120)#
^{166}Gd	^{136}Xe	1.220 992 828(29)	-54387(4)	-54530(200)#
^{167}Gd	^{136}Xe	1.228 379 286(97)	-50783.4(12.3)	-50813(298)#
^{164}Tb	^{171}Yb	0.959 031 473(21)	-62090(4)	-62080(100)
^{165}Tb	^{136}Xe	1.213 585 800(31)	-60595.1(3.9)	-60566(102)#
^{166}Tb	^{136}Xe	1.220 965 810(30)	-57807.6(3.7)	-57885(70)
^{167}Tb	^{136}Xe	1.228 338 998(30)	-55883.7(3.8)	-55927(196)#
^{168}Tb	^{136}Xe	1.235 721 496(33)	-52781.2(4.1)	-52723(298)#

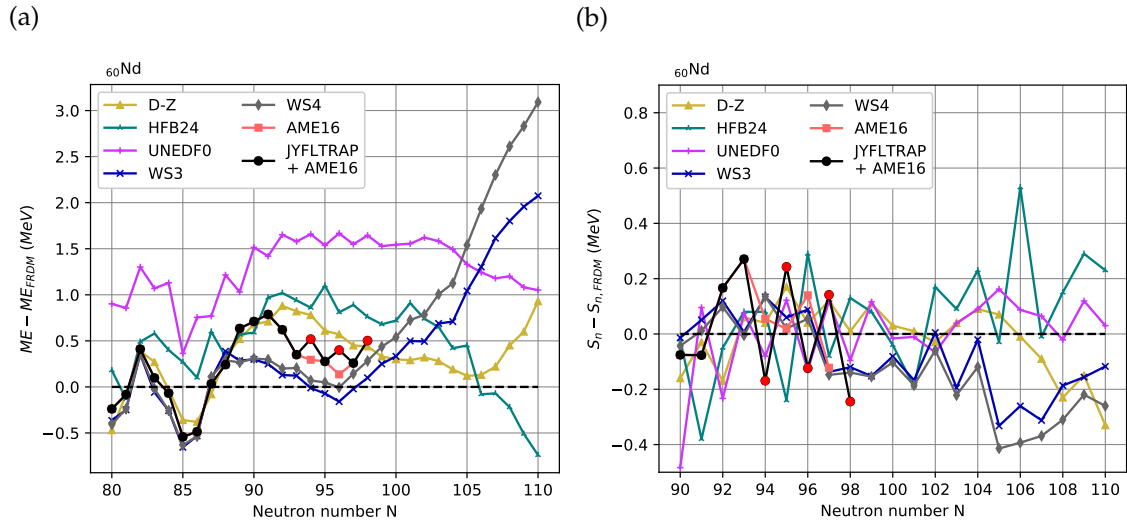


FIGURE 21 Experimental and theoretical mass excess values ME (a) and neutron separation energies S_n (b) of neodymium ($Z = 60$) isotopes compared to the FRDM12 mass model. Values affected by this work are highlighted with red markers.

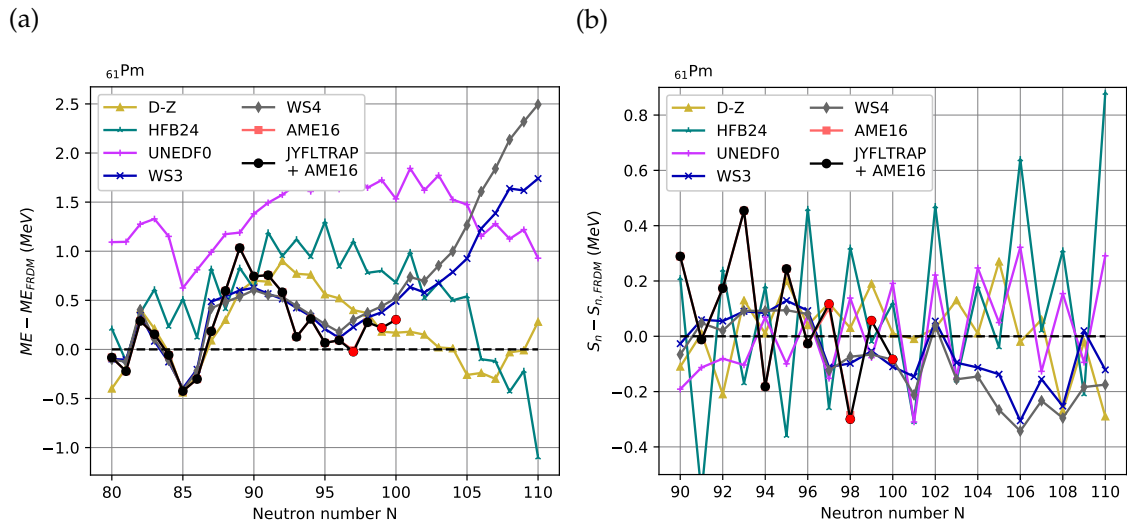


FIGURE 22 Experimental and theoretical mass excess values ME (a) and neutron separation energies S_n (b) of promethium ($Z = 61$) isotopes compared to the FRDM12 mass model. Values affected by this work are highlighted with red markers.

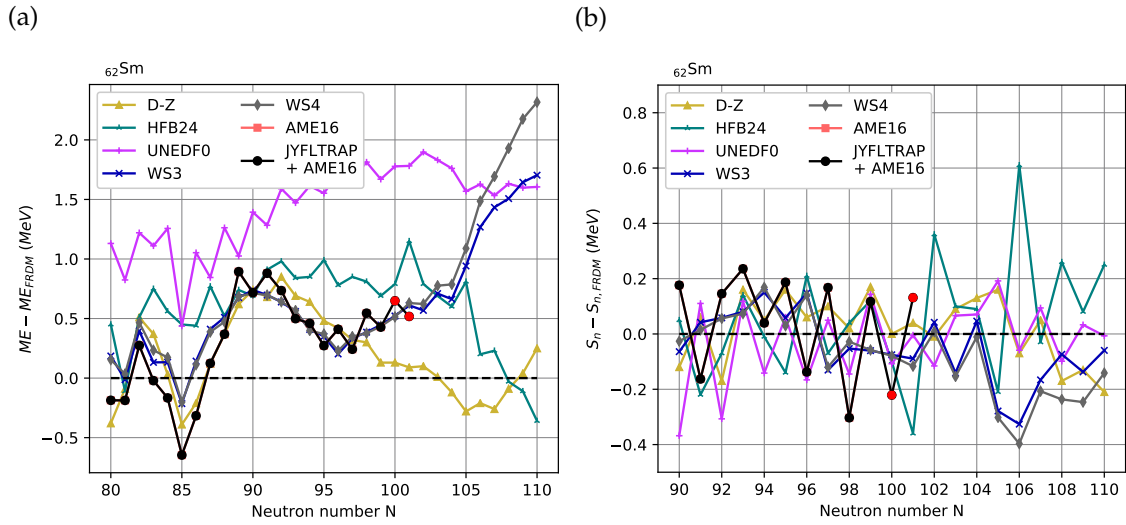


FIGURE 23 Experimental and theoretical mass excess values ME (a) and neutron separation energies S_n (b) of samarium ($Z = 62$) isotopes compared to the FRDM12 mass model. Values affected by this work are highlighted with red markers.

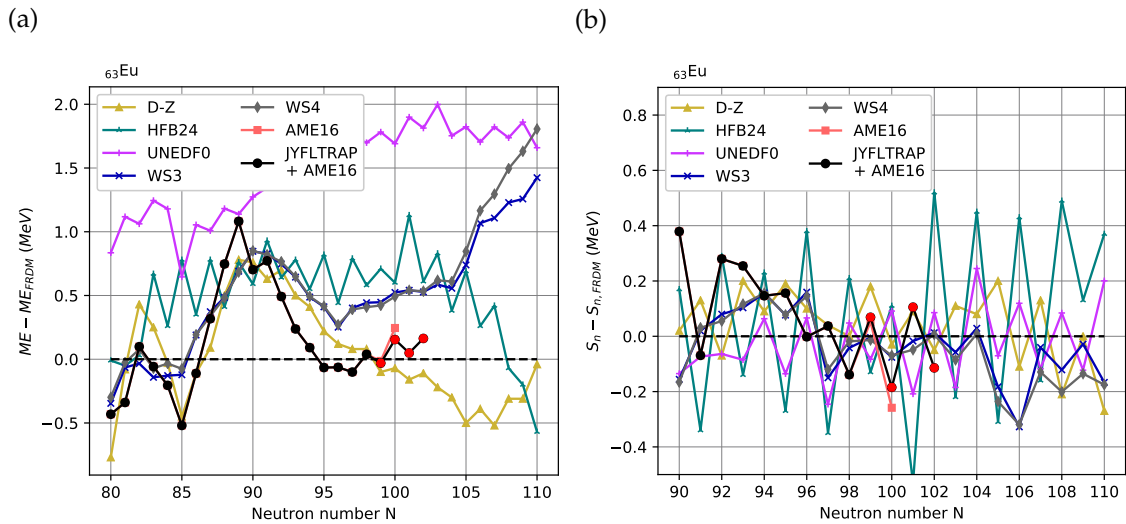


FIGURE 24 Experimental and theoretical mass excess values ME (a) and neutron separation energies S_n (b) of europium ($Z = 63$) isotopes compared to the FRDM12 mass model. Values affected by this work are highlighted with red markers.

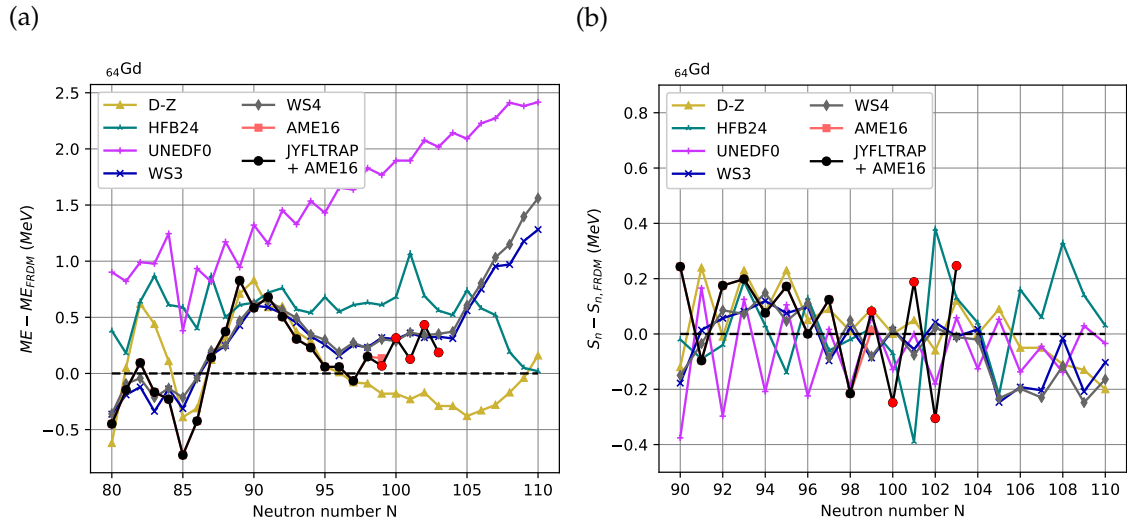


FIGURE 25 Experimental and theoretical mass excess values ME (a) and neutron separation energies S_n (b) of gadolinium ($Z = 64$) isotopes compared to the FRDM12 mass model. Values affected by this work are highlighted with red markers.

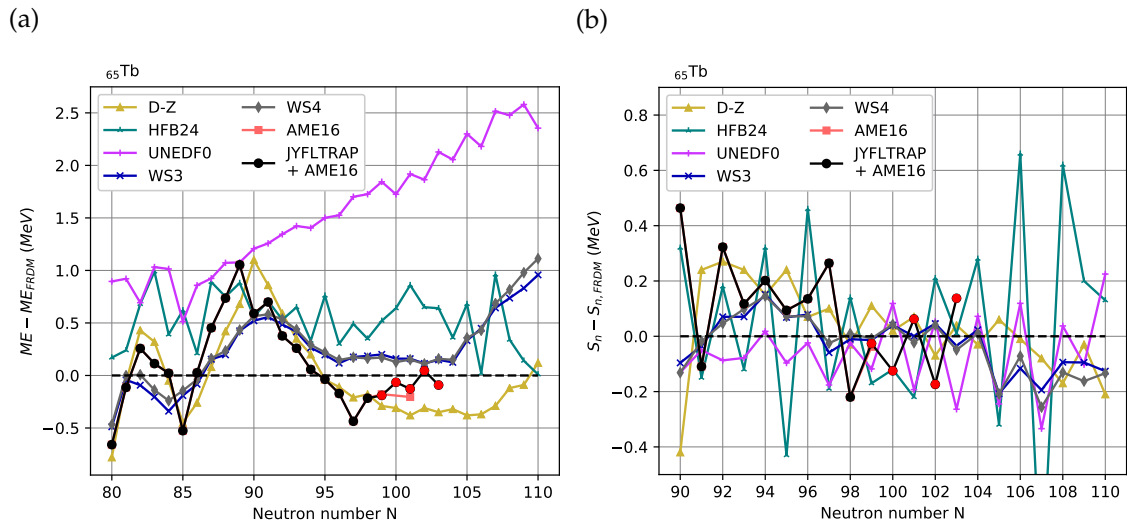


FIGURE 26 Experimental and theoretical mass excess values ME (a) and neutron separation energies S_n (b) of terbium ($Z = 65$) isotopes compared to the FRDM12 mass model. Values affected by this work are highlighted with red markers.

4.2 Mass measurements of neutron deficient nuclei near the $N = Z$ line

In this work the upgraded ion-guide system for producing neutron-deficient isotopes with heavy-ion beams was commissioned, see the included article [PIII]. It was used in its first on-line experiment to produce neutron-deficient isotopes close to the $N = Z$ line. The mass measurements were performed using JYFLTRAP and masses of five nuclear ground states (^{82}Zr , ^{84}Nb , ^{86}Mo , ^{88}Tc , ^{89}Ru) and one isomeric state ($^{88}\text{Tc}^m$) were measured, see table 2. Out of these, two masses were measured for the first time and the precisions of three other masses were improved. Heavier proton-rich nuclei have been studied at JYFLTRAP using previous versions of the commissioned system in, for example, [75].

Similarly to the measurements in the neutron-rich rare-earth region, the effect of the results on the mass surface was studied. Given that the number of measured masses in this region is much lower than in the rare-earth region and that no large changes in the mass values were observed (see table 2) compared to the most recent atomic mass evaluation AME16 [39], which includes recent storage-ring measurements [40] in this region, no new trends on the mass surface could be established. Most of the measured masses introduced only minor changes to the mass surface. However, the measurement of the mass of ^{89}Ru enabled us to extend the experimental mass surface next to the $N = Z$ line. Similarly as in section 4.1, figures 27–31 present mass excess values (ME) and proton separation energies (S_p) determined in this work for isotopic chains of Zr, Nb, Mo, Tc and Ru. In this case, proton separation energies are of higher relevance than the neutron separation energies discussed in section 4.1 due to the close proximity of the proton drip line and relevance for the rp -process.

The mass excess figures (see figures (a) in figures 27–31) show that the FRDM12 mass model does not reproduce the behavior of the mass surface as closely as most of the other models. Out of the theories used here, UNEDF0 seems to have the highest deviation with respect to the experimental data. As the neutron number N goes lower and reaches the last experimentally known mass values in any of the isotopic chains, the theoretical models start to diverge strongly. Many of the isotopes near the low neutron numbers in the figures are likely to be proton-unbound making experimental determination of those masses highly difficult by Penning trap mass spectrometry. In the proton separation energy figures (see figures (b) in figures 27–31) it can be seen that the FRDM12 model deviates from the experimental data and other mass model less than in the case of mass excesses. Again, where there are experimental data available theoretical mass models agree with each other better than beyond the last experimentally known masses. Interestingly, even though WS3 and WS4 models diverge from the other mass models in the ME figures with low neutron numbers, they produce proton separation energies that closely match Duflo-Zuker and in many cases HFB24. Due to the relatively small changes introduced into the mass surface by the new masses, their effect on the rp -process was not studied in this work. In general, proton

separation energies S_p hold a similar role in the modeling of the rp -process as the neutron separation energies S_n in the r -process modeling.

The level structure of ^{88}Tc was studied using the mass of the isomeric state that was measured for the first time in this work. Additional constraints were placed on the order of the three lowest states. The masses of ^{86}Ru and ^{82}Mo were predicted using measured masses of their mirror partners, ^{86}Mo and ^{82}Zr , and theoretical mirror displacement energies, resulting in ^{86}Ru and ^{82}Mo being more tightly bound nuclei with smaller uncertainties than in literature.

TABLE 2 Frequency ratios (r) and mass-excess values (ME) determined in this work near the $N = Z$ line with JYFLTRAP and corresponding AME16 values. All measurements were done with singly-charged ions. The reference masses were adopted from AME16 and # signs indicate extrapolated values therein. For more details on these results, see included article [P111].

Isotope	Reference	$r = \nu_{c,ref}/\nu_c$	ME_{JYFL} (keV)	ME_{AME16} (keV)
^{82}Zr	^{85}Rb	0.96490356(2)	-63613(2)	-63631(12)
^{84}Nb	^{85}Rb	0.988488167(5)	-61193.8(4)	-61219(13)
^{86}Mo	^{85}Rb	1.01200528(6)	-64112(5)	-64113(5)
^{88}Tc	^{87}Rb	1.01178955(5)	-61670(4)	-61681(149)
$^{88}\text{Tc}^m$	^{88}Tc	1.00000086(4)	-61600(5)	-61680(340)#
^{89}Ru	^{85}Rb	1.0474089(3)	-58372(21)	-58260(298)#

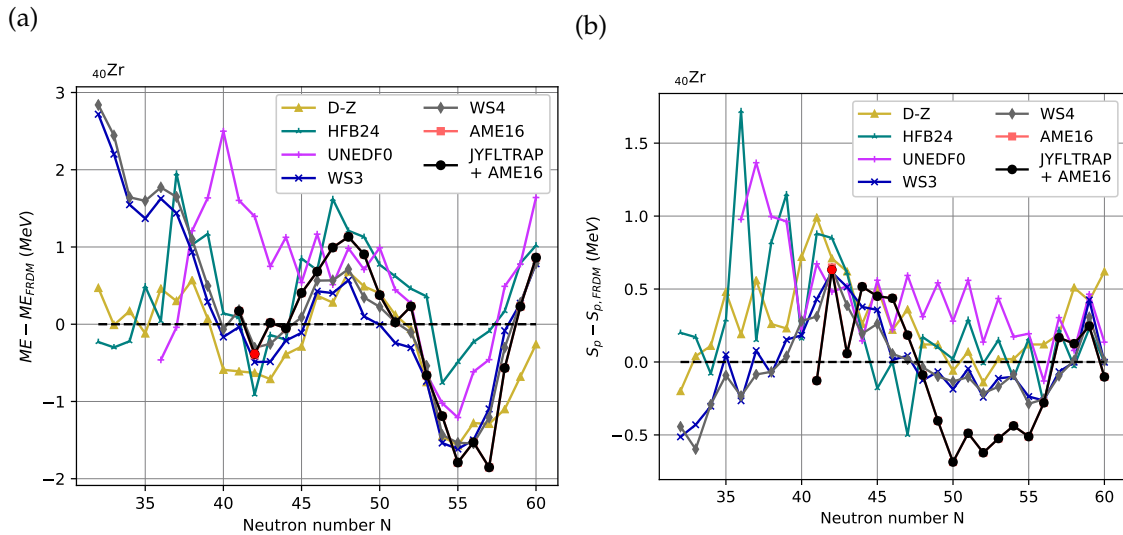


FIGURE 27 Experimental and theoretical mass excess values ME (a) and proton separation energies S_p (b) of zirconium ($Z = 40$) isotopes compared to the FRDM12 mass model. Values affected by this work are highlighted with red markers.

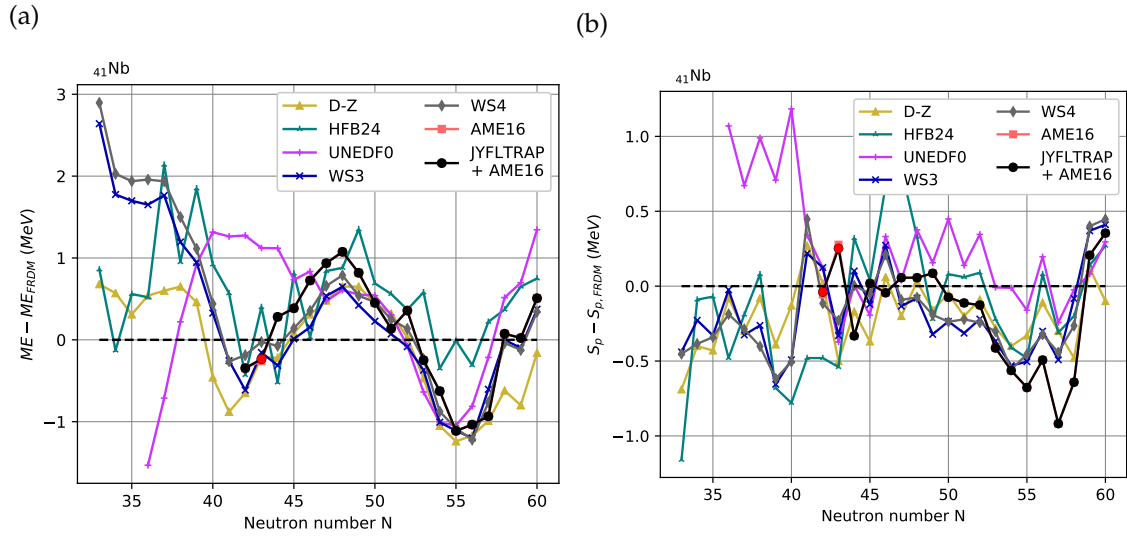


FIGURE 28 Experimental and theoretical mass excess values ME (a) and proton separation energies S_p (b) of niobium ($Z = 41$) isotopes compared to the FRDM12 mass model. Values affected by this work are highlighted with red markers.

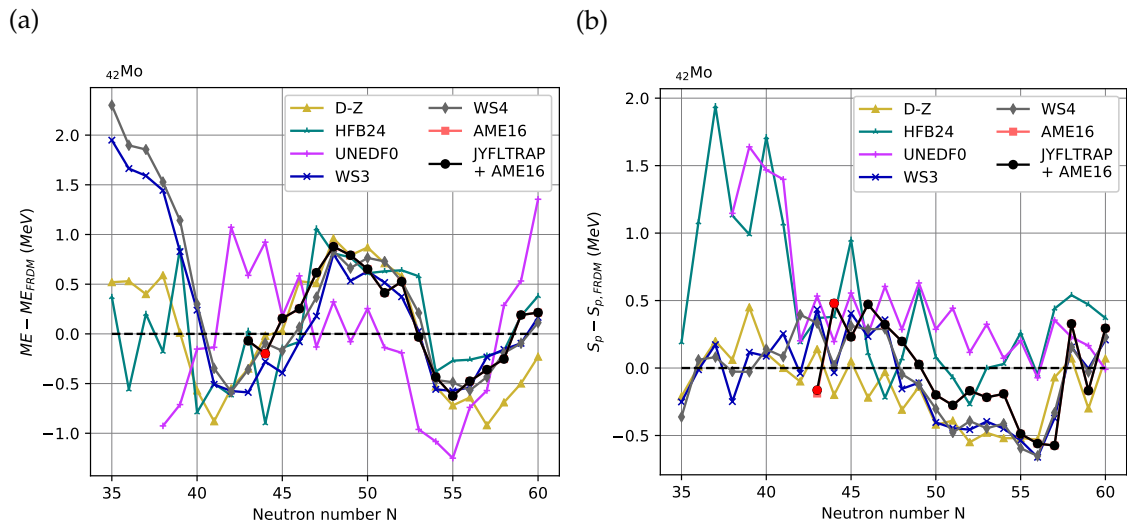


FIGURE 29 Experimental and theoretical mass excess values ME (a) and proton separation energies S_p (b) of molybdenum ($Z = 42$) isotopes compared to the FRDM12 mass model. Values affected by this work are highlighted with red markers.

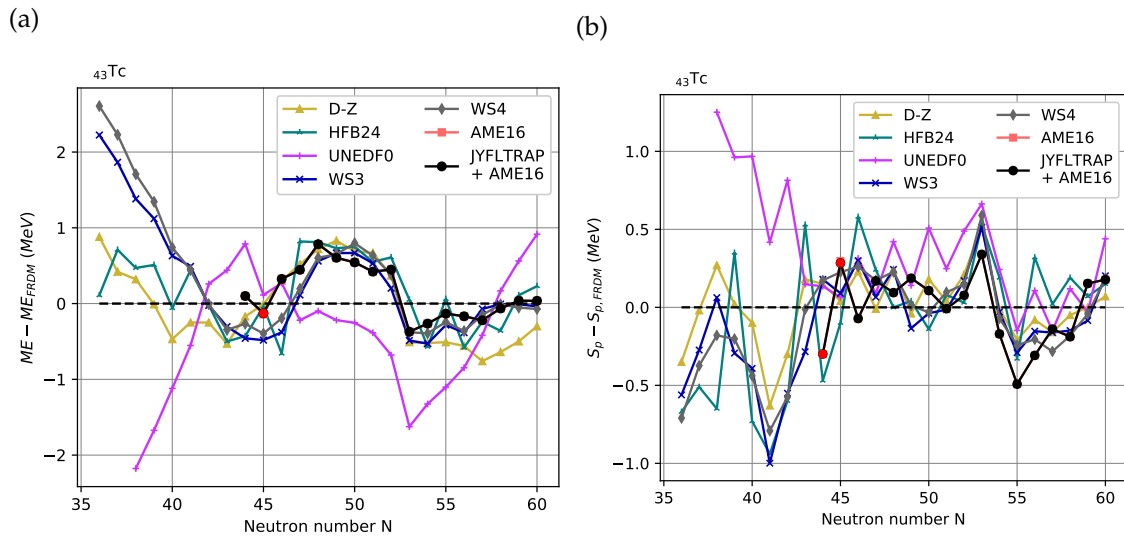


FIGURE 30 Experimental and theoretical mass excess values ME (a) and proton separation energies S_p (b) of technetium ($Z = 43$) isotopes compared to the FRDM12 mass model. Values affected by this work are highlighted with red markers.

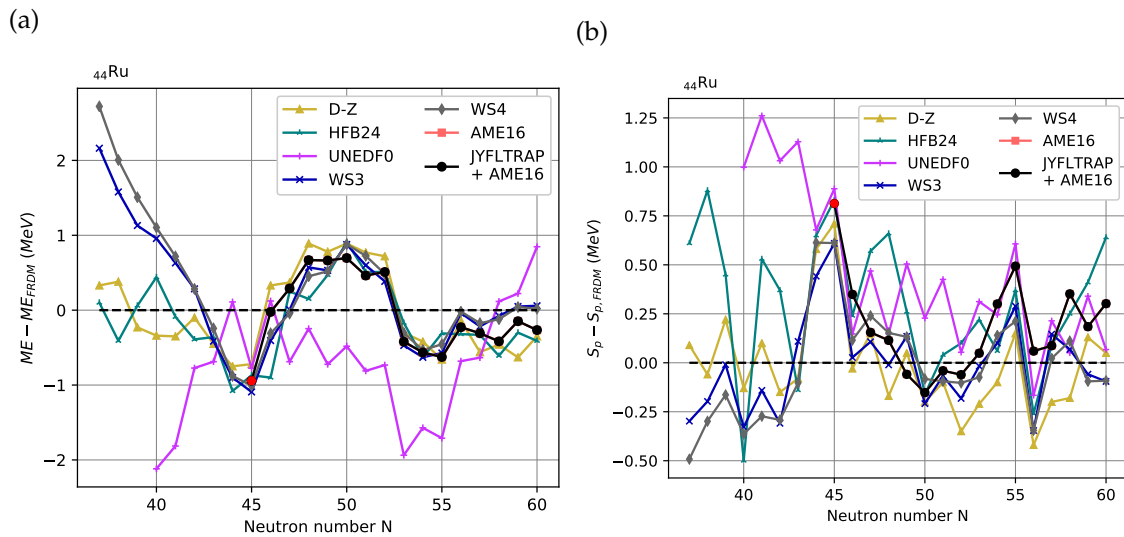


FIGURE 31 Experimental and theoretical mass excess values ME (a) and proton separation energies S_p (b) of ruthenium ($Z = 44$) isotopes compared to the FRDM12 mass model. Values affected by this work are highlighted with red markers.

4.3 Systematic studies on the effect of count rate on PI-ICR mass measurements

The PI-ICR method was commissioned recently at JYFLTRAP [13]. For the PI-ICR mass measurements, a new detection system consisting of a Time-to-Digital Converter (TDC) and a position-sensitive delay line MCP detector, was installed at JYFLTRAP. Also, the extraction region of JYFLTRAP, see figure 14, was redesigned to optimally magnify the projections of ion motions in the measurement trap. Together these modifications introduce various sources of systematic uncertainty that need to be quantified in order to guarantee the accuracy of measurements at JYFLTRAP.

Prior to this work, it was expected that there are at least two sources of systematic uncertainty related to the detector system that need to be accounted for in mass measurements: distortion of the projections of ion motions in the measurement trap and the detector efficiency. The former is relevant due to the fact that in the PI-ICR method the ν_c frequency is determined based on the difference between ion motion projections, as discussed in section 3.5.3. In an ideal case, projection of ions orbiting in the measurement trap would form a perfect circle on the detector. However, in practice the projected image can suffer from distortion due to imperfections of the extraction ion optics and tilt of the detector with respect to the plane of radial motion of ions within the measurement trap, leading to ion motion being projected into an ellipse rather than a circle. Any distortion in the projection of ion motion can lead to systematic shifts in the determination of angles using the detector system, which in turn will lead to shifts in mass measurement results.

The other source of systematic uncertainty that was expected to be relevant, the detector efficiency, can be taken into account in the data analysis process. In the past it has been done as a part of the process used to account for the simultaneous presence of multiple particles in the measurement trap, originally introduced in [76]. In that process the data are divided into separate classes based on the number of ions detected per measurement cycle and each of the classes is analyzed separately. Due to the fact that the detector system has an efficiency smaller than unity, each number of detected ions represents only a fraction of the actual number of ions that were present in the measurement trap. Ideally, determination of the ν_c frequency should be performed on individual ions to avoid any systematic shifts due to ion-ion interactions during the measurement process. For this reason, the cyclotron frequencies ν_c from the separate count-rate classes are fitted with a linear function and the function is extrapolated down to the value corresponding to detector efficiency. This process approximates the ν_c frequency that would result if only individual ions were measured. This process has been a routine procedure at JYFLTRAP.

One of the first direct comparisons between the TOF-ICR and PI-ICR methods at JYFLTRAP was performed as a part of the measurement campaign presented in the included article [PII], where ^{162}Eu and $^{162}\text{Eu}^m$ were measured using

TABLE 3 Mass excesses (ME) of ^{162}Eu and $^{162}\text{Eu}^m$ from this work without count-rate class analysis (PI-ICR_{method 1}), with a fixed detector efficiency in the count-rate class analysis (PI-ICR_{method 2}) and with a count-rate dependent detector efficiency (PI-ICR_{method 3}). For reference, values from CPT and from a TOF-ICR measurement at JYFLTRAP are also listed.

	$ME(\text{keV})$	
	^{162}Eu	$^{162}\text{Eu}^m$
TOF-ICR	-58717.2(5.5) [PII]	-58560.3(7.6) [PII]
PI-ICR _{method 1}	-58709.6(1.6)	-58576.8(1.3)
PI-ICR _{method 2}	-58716.2(3.0)	-58567.2(2.0)
PI-ICR _{method 3}	-58721.8(3.7) [PII]	-58566.0(2.2) [PII]
CPT	-58723.9(1.5) [77]	-58563.7(1.9) [77]

TABLE 4 Mass excesses differences (ΔME) of ^{162}Eu and $^{162}\text{Eu}^m$ between different mass measurement techniques, analysis methods and results from CPT in units of keV and standard deviation σ . Analysis was repeated without count-rate class analysis (PI-ICR_{method 1}), with a fixed detector efficiency in the count-rate class analysis (PI-ICR_{method 2}) and with a count-rate dependent detector efficiency (PI-ICR_{method 3}).

	^{162}Eu		$^{162}\text{Eu}^m$	
	$\Delta ME(\text{keV})$	$\Delta ME(\sigma)$	$\Delta ME(\text{keV})$	$\Delta ME(\sigma)$
PI-ICR _{method3} - PI-ICR _{method1}	12.2(4.1)	3.0	10.8(2.6)	4.2
PI-ICR _{method3} - PI-ICR _{method2}	5.6(3.4)	1.6	1.2(3.0)	0.4
PI-ICR _{method1} - TOF-ICR	7.6(5.8)	1.3	-16.5(7.8)	-2.1
PI-ICR _{method2} - TOF-ICR	1.0(6.3)	0.2	-6.9(7.9)	-0.9
PI-ICR _{method3} - TOF-ICR	-4.6(6.7)	-0.7	-5.7(8.0)	-0.7
TOF-ICR - CPT	6.7(5.7)	1.2	3.4(7.9)	0.4
PI-ICR _{method1} - CPT	14.3(2.2)	6.5	-13.1(2.3)	-5.7
PI-ICR _{method2} - CPT	7.7(3.4)	2.3	-3.5(2.8)	-1.3
PI-ICR _{method3} - CPT	2.1(4.0)	0.5	-2.3(2.9)	-0.8

both techniques. The two long-living states in ^{162}Eu were successfully resolved from each other using both methods. However, initial analysis revealed that the two techniques did not fully agree with each other. Additionally, they did not agree with the measurements done at the Canadian Penning Trap (CPT) [77]. The initial PI-ICR results did not include any corrections due to ion-ion interactions in the measurement trap due to a lack of software capable of taking the effect into account. The first PI-ICR results are presented in tables 3 and 4 as PI-ICR_{method 1}. It should be noted here that the TOF-ICR results presented in the tables do not include any corrections due to ion-ion interactions due to insufficient statistics in the performed measurement. To minimize possible systematic count-rate effects, the number of ions was limited to 1-3 ions per bunch in the TOF-ICR data analysis.

In an effort to solve the discrepancies observed for ^{162}Eu and $^{162}\text{Eu}^m$ between the initial PI-ICR results and values from CPT, 6.5 and 5.7 standard deviations, respectively, and between the PI-ICR and TOF-ICR results, 1.3 and 2.1 standard deviations, respectively, further development of the analysis software was undertaken. A software tool for performing similar extrapolation of measured quantities as originally described in [76] was developed. In this case, the extrapolated quantity was the x and y coordinates of images projected onto the detector. This resulted in a significant change to the results, see PI-ICR_{method 2} in tables 3 and 4. However, a discrepancy larger than what can be explained solely by statistical fluctuation still remained between the PI-ICR results and values from CPT, 2.3 and 1.3 standard deviations for ^{162}Eu and $^{162}\text{Eu}^m$, respectively.

At this stage the assumption of a linear relationship between the extrapolated quantity and the number of ions per measurement cycle was suspected to be causing the discrepancy. In order to investigate this further, the analysis tool was then further developed to optionally perform the extrapolations using a linear relationship in a radial coordinate system. The change of coordinate system effectively modifies the way in which the x and y coordinates depend on the number of detected ions. Analysis was repeated with the modified program, but no significant change was observed and the discrepancy remained.

Another approach was then taken and attention was turned to the detector system, the detector and TDC, used in the measurements. If the efficiency of the detector system is not constant with all count rates the extrapolations would have to be performed using a non-linear function in the count-rate class analysis [76]. Efficiency of the detector system was studied using stable $^{133}\text{Cs}^{1+}$ ions from the off-line ion source station, see attached article [PIV]. The number of ions per measurement cycle was controlled by changing the time ions were accumulated in the RFQ [63] before they were injected into JYFLTRAP. Ions were cooled similarly as during on-line measurements, extracted onto the MCP detector and the number of detected ions was recorded. Varying the accumulation time in the RFQ allowed the efficiency of the detector system to be studied as a function of the accumulation time - or in other words, the number of ions but without an absolute scale. Previous measurements with the RFQ using radioactive ions and a silicon detector at JYFLTRAP have shown that there is no considerable loss of ions within the

time scales typically used in mass measurements. The off-line studies resulted in an efficiency curve in arbitrary units for the detector system as a whole. The absolute efficiency was determined during an online experiment by comparing the detected MCP counts to the number of beta particles observed with a silicon detector with a well-known efficiency. The absolute efficiency measured during the on-line experiment was then used to calibrate the off-line data, resulting in the final efficiency curve. The efficiency was studied both on- and off-line in order to reduce the statistical uncertainty of the final efficiency curve. Performing the off-line studies made it possible to collect most of the statistics without the need for a primary beam from a cyclotron.

With the new efficiency function it became possible to test the assumption of a linear relationship in the extrapolations for the second time. The count-rate class analysis was repeated with the new efficiency function added in the software tool. Each count-rate class was corrected by the detector efficiency according to the efficiency function, i.e. the extrapolation was performed using the number of ions in the measurement trap rather than the number of detected ions. The extrapolation was then correspondingly modified to go down to unity instead of the detector efficiency. Additionally, the analysis software was modified to include both x (number of ions) and y (ion spot location on the detector) coordinate errors in the fits used in the extrapolation. Effectively, this introduced a new systematic uncertainty into the calculations, uncertainty of the detector system efficiency function (i.e. x coordinate), which is also a function of the number of ions trapped per measurement cycle. This process transforms the non-linear dependency between the number of detected ions and ion spot location on the detector into a linear relationship between the number of ions in the measurement trap and ion spot location on the detector.

The analysis process was repeated using these modifications, see PI-ICR_{method 3} in tables 3 and 4. The modifications brought the difference between this work and CPT down to 0.5 and 0.8 standard deviations for ^{162}Eu and $^{162}\text{Eu}^m$, respectively. Additionally, the difference between the TOF-ICR and PI-ICR methods remained within variation expected based on statistical fluctuations, at 0.7 standard deviations for both ion species. Interestingly, in the case of ^{162}Eu the difference between the two measurement techniques changed its sign with the last modifications to the analysis process but still remained within one standard deviation.

The determination of the detector system efficiency provided valuable information on the system, not only due to the changes seen in mass measurement results, but also thinking of the performance of the IGISOL facility and JYFLTRAP as a whole. It was discovered that the system suffered from a significant loss of efficiency with low ion count rates. This was an unexpected result since the detector itself is only prone to suffer at high count rates due to dead times needed in position information acquisition using delay lines. The efficiency of the detector system used in the PI-ICR measurements of the measurement campaign of [PII] is presented in figure 32. It should be noted that the efficiency curve is not the same for the TOF-ICR technique due to the fact that it does not make use of the position information provided by the system. Therefore, all detected ions with

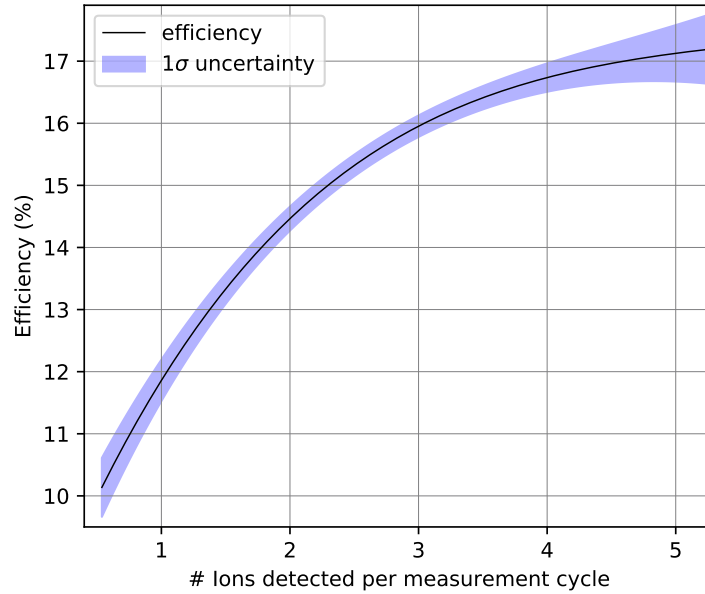


FIGURE 32 Efficiency of the data acquisition system (the delay-line MCP detector and RoentDek TDC) in PI-ICR measurements at JYFLTRAP as a function of the number of ions detected per measurement cycle at the beginning of the systematic studies.

time-of-flight information can be used in the TOF-ICR method, even if the reconstruction of the position of the ion is not successful. On the other hand, in the PI-ICR method the position information is required. According to preliminary estimates, the difference between the efficiencies for the two methods, at count-rates typically used in mass measurements, was approximately two percentage points, in the favor of the TOF-ICR technique.

The reason for the unexpected drop of efficiency at low count rates was found to be in the Time-to-Digital Conversion (TDC) system, manufactured by RoentDek Handels GmbH, used to interpret signals from the MCP detector via comparing it against two other TDC systems, one commercially available system from Cronologic GmbH and one that was built in-house. A comparison between the three TDC systems was performed by splitting the signal coming from the detector to all three TDCs and measuring the number of ions registered by each system using various accumulation times in the RFQ. The accumulation time controls the amount of ions injected into JYFLTRAP, and therefore the number of ions detected by the TDC systems. Only the RoentDek TDC system was capable of handling position information from the delay lines of the detector. Therefore, the position information was neglected in the case of the RoentDek TDC. Results from the comparison are presented in figure 33 where it can be seen that the RoentDek system clearly suffered from lower efficiency than the other two systems.

It was discovered that the reason for the lower efficiency at low ion numbers was in a piece of software developed in-house that was used to reconstruct events of ions impacting the detector. The issue was rectified in two ways: the

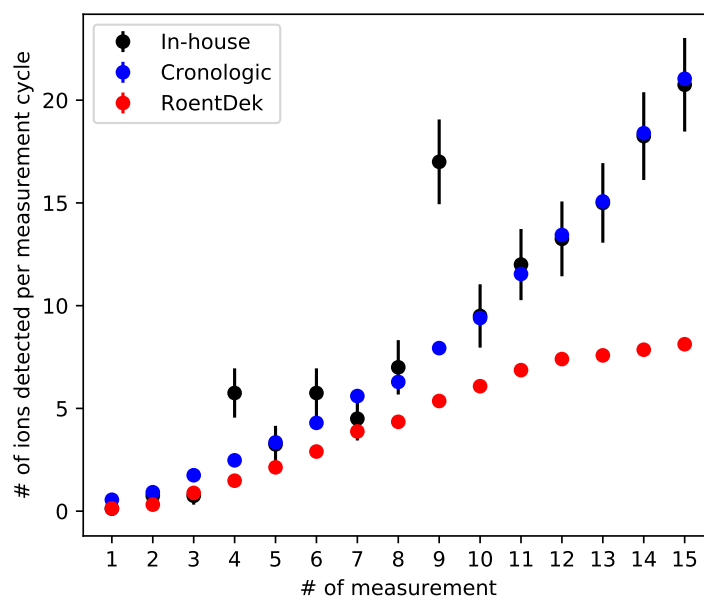


FIGURE 33 The number of ions detected per measurement cycle measured using three different TDC systems. Accumulation time of the RFQ was increased after each measurement to increase the number of ions detected.

event reconstruction code was fully rewritten and also the original code was inspected carefully and the source of the issue was located and the issue fixed. These two event reconstruction codes were then compared and identical results were acquired. Additionally, the RoentDek TDC system was compared to the other two systems using the new event reconstruction code and all three systems were found to agree with each other.

Determination of the efficiency function was then repeated using the new event reconstruction code. The shape of the efficiency function changed dramatically, see figure 34. The strong drop in efficiency observed with the old event reconstruction code at low count rates was removed and the function acquired a shape that was closer to the behavior expected from the MCP detector. The improvement of the detection efficiency at low count rates will be of high importance for future measurements at JYFLTRAP. As the measurements move towards more exotic ion species the number of ions available at JYFLTRAP, naturally, decreases. In a large portion of experiments the yield of exotic isotopes has been a limiting factor. Using the old event reconstruction code this would have also meant that the efficiency of the data acquisition system goes down simultaneously, compounding the problem and resulting in an experiment becoming even more challenging. The new event reconstruction code increased the efficiency of the system at the detection rate of one ion per measurement cycle by approximately 40%, or from the original efficiency of 12% to 17%. However, observed data acquisition system efficiency, even using the new event reconstruction code, is far away from the absolute efficiency of up to 81% [64] reported by the detector manufacturer. Reaching the efficiency reported by the manufacturer would give at least a factor-of-four improvement, which would enable studying even more

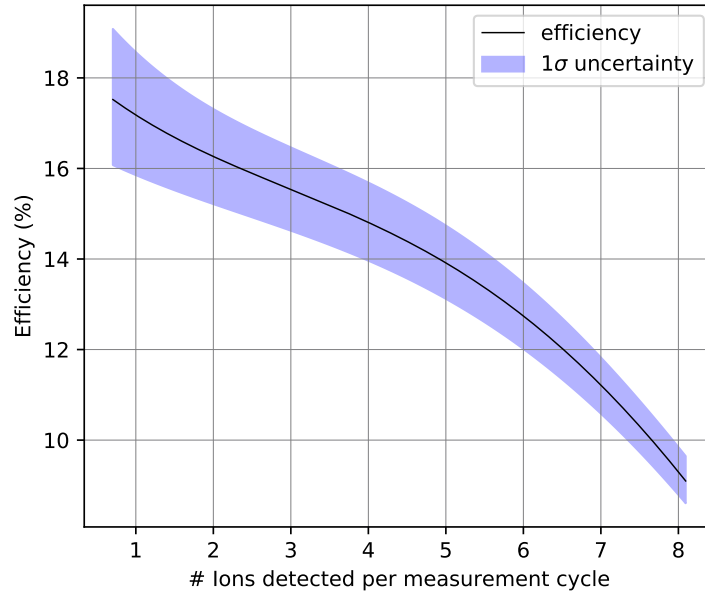


FIGURE 34 Preliminary efficiency of the data acquisition system (the delay-line MCP detector and RoentDek TDC) in PI-ICR measurements used at JYFLTRAP as a function of the number of ions detected per measurement cycle using the new event reconstruction code.

exotic ion species in the future. Further studies on the efficiency of the system have already been undertaken and a detailed report on the findings will follow this work [70].

The commissioning of the PI-ICR method at JYFLTRAP has generated much interest in studying low-lying isomeric states in various parts of the nuclear chart through mass measurements. While the increase in efficiency seen in this work is going to provide improved possibilities in measuring exotic isotopes, it is also of great significance to the accuracy of the results, as demonstrated by the measurements performed on ^{162}Eu and $^{162}\text{Eu}^m$. Initial results suggest that the effect seen in this work is more pronounced in cases where there are several nuclear states or isotope species present in the measurement trap simultaneously. Therefore, systematic studies on the efficiency of the data acquisition system performed as a part of this work are especially relevant in future studies on low-lying isomeric states. It should be noted, however, that the count-rate effect seen with ^{162}Eu and $^{162}\text{Eu}^m$ in this work would most likely have been weaker if the corrected event reconstruction code had been in use.

5 SUMMARY AND OUTLOOK

In this work the masses of 27 nuclear ground states and three isomeric states were measured, see figure 1 and tables 1 and 2. Measurements were performed in two separate regions of the nuclear chart, neutron-rich rare-earth region and the $A \approx 80$ region near the $N = Z$ line. Both of these regions are of interest to nuclear astrophysics and, more specifically, nucleosynthesis in the r - and rp -processes. The impact on the r -process was studied for several trajectories representing a neutron-star merger scenario. The two measurement campaigns of [PI] and [PII] resulted each in a better agreement between the observed solar system r -process abundances and those predicted by the models.

In the case of the mass measurement results of [PIII] relevant to the rp -process, similar theoretical modeling of the corresponding nucleosynthesis was not performed due to the limited number of measured masses. Also, the results were, in most cases, in such a close agreement with literature values that the new results were not expected to produce significant changes in the rp -process modeling. The effect on nuclear structure was also studied for all mass measurement results of this work, see [PI,PII,PIII]. The new data in the rare-earth region, which extends the experimentally-known mass surface by several nuclides, revealed an increasing over-estimation of the odd-even staggering by theoretical mass models. The presence of a proposed subshell closure at $N = 100$ [78] was also studied. It was found that the new data does not offer support to the existence of the subshell closure. The new data measured near the $N = Z$ line extended the experimentally-known masses by one nuclide towards the proton drip line, which is insufficient to reveal new trends. However, the first successful measurement of the $^{88}\text{Tc}^m$ isomeric provided new information on its level scheme, see the included article [PIII] for more details. The masses of two additional nuclides, ^{82}Mo and ^{86}Ru , were estimated using theoretical mirror displacement energies and the masses of their mirror partners measured in this work.

The mass measurements presented in this work involved several technical developments, ranging from the production of radioactive and stable ion beams to systematic studies of the detector system used at JYFLTRAP. The HIGISOL heavy-ion ion guide platform used to produce radioactive ions in [PIII] was up-

graded. A new control system was developed that allowed, for the first time, remote control of the position and rotational speed of the target together with remote position information readout. The upgraded HIGISOL platform was successfully commissioned in this work [PIII]. It was the first on-line experiment with HIGISOL at the new IGISOL facility, also known as IGISOL-4. The previous HIGISOL experiments [50, 51] had been done at the decommissioned IGISOL-3 facility (see for example [6]) more than a decade ago. The new HIGISOL system was modified after the measurement campaign of [PIII] for use in multi-nucleon transfer (MNT) reactions at IGISOL. Following initial tests of the MNT reactions using a ^{136}Xe beam on ^{nat}Bi target, there is a continued interest to utilize a HIGISOL type of a system in future MNT work. With the recent commissioning of the PI-ICR method, the HIGISOL system is still an interesting tool for producing and studying nuclides near the $N = Z$ line. Previous work in the region has been performed using the TOF-ICR method which is not optimal for studying low-lying isomeric states and, therefore, the recent upgrades to the IGISOL facility offer a possibility to revisit already measured nuclides and refine their masses via separating and studying low-lying isomeric states.

As a part of this work the new off-line ion source station [PIV] was brought into routine use at the IGISOL facility. Following upgrades after the initial tests of the system in [58], the ion source station was used to provide stable ion samples for various experiments, including collinear laser spectroscopy using doubly-charged $^{89}\text{Y}^{2+}$ [60], production of ultra-cold samples of cesium [56] and several Penning trap mass measurement campaigns, such as [PII]. Some limitations in the current design of the ion source station were identified in this work. In order to address them, an upgraded version of the station was designed, offering a highly versatile platform for installing new types of ion sources and improving the usability of the ion sources currently in use. However, the new ion source station design was not taken into use in this work due to time constraints. The construction and commissioning of the upgraded design could serve, for example, as a suitable M.Sc. thesis project for a future student. See section 3.2.2 for further details on the upgraded ion source station design.

The off-line ion source station was used in systematic studies on the effect of ion count rate in PI-ICR mass measurements. It was discovered that the event reconstruction code used at the time of the ^{162}Eu measurement at JYFLTRAP lost some events in the reconstruction process, resulting in a considerable loss of efficiency at low count rates. As a result, the PI-ICR measurements of ^{162}Eu , which involved both the ground- and isomeric-state ions simultaneously in the measurement trap, were found to present a strong ion count-rate dependence. After the introduction of a new event reconstruction code, however, the efficiency of the detector system remained substantially lower than what is to be expected based on efficiency reported by the manufacturer. Compared to the manufacturer's estimate, even with the updated software, the system is up to a factor of four less efficient than it could be. This is such a large factor that further investigation into the cause of the difference in efficiency is highly justified. If the cause of the loss of efficiency turns out to be the a problem or a fault in the detector itself, which

is plausible given the fact that with the new event reconstruction code all three TDCs agree with each other, it is worth considering replacing the detector. However, there are no clear indications of problems with the detector, other than the unexpected level of efficiency. Therefore, consulting with the manufacturer and possibly comparing the detector to another with similar design would be beneficial. In case the efficiency of the detector system can be raised by a factor of four, a number of new exotic nuclides are likely to become reachable in mass measurements at JYFLTRAP – simply due to improved performance of the detector system.

REFERENCES

- [1] M. R. Mumpower, R. Surman, D.-L. Fang, M. Beard, P. Möller, T. Kawano, and A. Aprahamian. [Impact of individual nuclear masses on \$r\$ -process abundances](#). *Phys. Rev. C*, 92:035807, Sep 2015.
- [2] M.R. Mumpower, R. Surman, G.C. McLaughlin, and A. Aprahamian. [The impact of individual nuclear properties on \$r\$ -process nucleosynthesis](#). *Progress in Particle and Nuclear Physics*, 86:86 – 126, 2016.
- [3] A. Parikh, J. José, G. Sala, and C. Iliadis. [Nucleosynthesis in type I X-ray bursts](#). *Progress in Particle and Nuclear Physics*, 69:225 – 253, 2013.
- [4] H. Schatz and W.-J. Ong. [Dependence of X-Ray Burst Models on Nuclear Masses](#). *The Astrophysical Journal*, 844(2):139, aug 2017.
- [5] J. Ärje, J. Äystö, H. Hyvönen, P. Taskinen, V. Koponen, J. Honkanen, A. Hautjärvi, and K. Vierinen. [Submillisecond On-Line Mass Separation of Non-volatile Radioactive Elements: An Application of Charge Exchange and Thermalization Processes of Primary Recoil Ions in Helium](#). *Phys. Rev. Lett.*, 54:99–101, Jan 1985.
- [6] I. D. Moore, P. Dendooven, and J. Ärje. [The IGISOL technique—three decades of developments](#). *Hyperfine Interactions*, 223(1):17–62, Jan 2014.
- [7] Juha Äystö. [Development and applications of the IGISOL technique](#). *Nuclear Physics A*, 693(1):477 – 494, 2001. Radioactive Nuclear Beams.
- [8] T. Eronen, V. S. Kolhinen, V. V. Elomaa, D. Gorelov, U. Hager, J. Hakala, A. Jokinen, A. Kankainen, P. Karvonen, S. Kopecky, I. D. Moore, H. Penttilä, S. Rahaman, S. Rinta-Antila, J. Rissanen, A. Saastamoinen, J. Szerypo, C. Weber, and J. Äystö. [JYFLTRAP: a Penning trap for precision mass spectroscopy and isobaric purification](#). *The European Physical Journal A*, 48(4):46, Apr 2012.
- [9] G. Gräff, H. Kalinowsky, and J. Traut. [A direct determination of the proton electron mass ratio](#). *Zeitschrift für Physik A Atoms and Nuclei*, 297(1):35–39, Mar 1980.
- [10] M. König, G. Bollen, H.-J. Kluge, T. Otto, and J. Szerypo. [Quadrupole excitation of stored ion motion at the true cyclotron frequency](#). *International Journal of Mass Spectrometry and Ion Processes*, 142(1):95 – 116, 1995.
- [11] S. Eliseev, K. Blaum, M. Block, C. Droese, M. Goncharov, E. Minaya Ramirez, D. A. Nesterenko, Yu. N. Novikov, and L. Schweikhard. [Phase-Imaging Ion-Cyclotron-Resonance Measurements for Short-Lived Nuclides](#). *Phys. Rev. Lett.*, 110:082501, Feb 2013.

- [12] S. Eliseev, K. Blaum, M. Block, A. Dörr, C. Droese, T. Eronen, M. Goncharov, M. Höcker, J. Ketter, E. Minaya Ramirez, D. A. Nesterenko, Yu. N. Novikov, and L. Schweikhard. [A phase-imaging technique for cyclotron-frequency measurements](#). *Applied Physics B*, 114(1):107–128, Jan 2014.
- [13] D. A. Nesterenko, T. Eronen, A. Kankainen, L. Canete, A. Jokinen, I. D. Moore, H. Penttilä, S. Rinta-Antila, A. de Roubin, and M. Vilen. [Phase-Imaging Ion-Cyclotron-Resonance technique at the JYFLTRAP double Penning trap mass spectrometer](#). *The European Physical Journal A*, 54(9):154, Sep 2018.
- [14] S. Brett, I. Bentley, N. Paul, R. Surman, and A. Aprahamian. [Sensitivity of the r-process to nuclear masses](#). *The European Physical Journal A*, 48(12):184, Dec 2012.
- [15] A. Aprahamian, I. Bentley, M. Mumpower, and R. Surman. [Sensitivity studies for the main r process: nuclear masses](#). *AIP Advances*, 4(4):041101, 2014.
- [16] A. Parikh, J. José, C. Iliadis, F. Moreno, and T. Rauscher. [Impact of uncertainties in reaction Q values on nucleosynthesis in type I x-ray bursts](#). *Phys. Rev. C*, 79:045802, Apr 2009.
- [17] J. Duflo and A.P. Zuker. [Microscopic mass formulas](#). *Phys. Rev. C*, 52:R23–R27, Jul 1995.
- [18] S. Goriely, N. Chamel, and J. M. Pearson. [Further explorations of Skyrme-Hartree-Fock-Bogoliubov mass formulas. XIII. The 2012 atomic mass evaluation and the symmetry coefficient](#). *Phys. Rev. C*, 88:024308, Aug 2013.
- [19] M. Kortelainen, T. Lesinski, J. Moré, W. Nazarewicz, J. Sarich, N. Schunck, M. V. Stoitsov, and S. Wild. [Nuclear energy density optimization](#). *Phys. Rev. C*, 82:024313, Aug 2010.
- [20] Ning Wang and Min Liu. [An improved nuclear mass formula: WS3](#). *Journal of Physics: Conference Series*, 420:012057, mar 2013.
- [21] Ning Wang, Min Liu, Xizhen Wu, and Jie Meng. [Surface diffuseness correction in global mass formula](#). *Physics Letters B*, 734:215 – 219, 2014.
- [22] Katharina Lodders. [Solar System Abundances and Condensation Temperatures of the Elements](#). *The Astrophysical Journal*, 591(2):1220–1247, jul 2003.
- [23] Christian Iliadis. [Nuclear Physics of Stars](#). Wiley-WHC, Weinheim, second, revised and enlarged edition edition, 2015.
- [24] David J. Griffiths. [Introduction to quantum mechanics](#). Pearson Prentice Hall, Upper Saddle River, NJ, 2nd edition, 2005.
- [25] M. Arnould, S. Goriely, and K. Takahashi. [The r-process of stellar nucleosynthesis: Astrophysics and nuclear physics achievements and mysteries](#). *Physics Reports*, 450(4):97 – 213, 2007.

- [26] A.G.W. Cameron. [Stellar evolution, nuclear astrophysics, and nucleogenesis](#), 1957. Chalk River Report CLR-41. Publisher: Atomic Energy of Canada Limited.
- [27] Rebecca Surman, Jonathan Engel, Jonathan R. Bennett, and Bradley S. Meyer. [Source of the Rare-Earth Element Peak in \$r\$ -Process Nucleosynthesis](#). *Phys. Rev. Lett.*, 79:1809–1812, Sep 1997.
- [28] Matthew R. Mumpower, G. C. McLaughlin, and Rebecca Surman. [Formation of the rare-earth peak: Gaining insight into late-time \$r\$ -process dynamics](#). *Phys. Rev. C*, 85:045801, Apr 2012.
- [29] C. J. Horowitz, A. Arcones, B. Côté, I. Dillmann, W. Nazarewicz, I. U. Roederer, H. Schatz, A. Aprahamian, D. Atanasov, A. Bauswein, T. C. Beers, J. Bliss, M. Brodeur, J. A. Clark, A. Frebel, F. Foucart, C. J. Hansen, O. Just, A. Kankainen, G. C. McLaughlin, J. M. Kelly, S. N. Liddick, D. M. Lee, J. Lippuner, D. Martin, J. Mendoza-Temis, B. D. Metzger, M. R. Mumpower, G. Perdikakis, J. Pereira, B. W. O’Shea, R. Reifarth, A. M. Rogers, D. M. Siegel, A. Spyrou, R. Surman, X. Tang, T. Uesaka, and M. Wang. [\$r\$ -process nucleosynthesis: connecting rare-isotope beam facilities with the cosmos](#). *Journal of Physics G: Nuclear and Particle Physics*, 46(8):083001, jul 2019.
- [30] N. R. Tanvir, A. J. Levan, C. González-Fernández, O. Korobkin, I. Mandel, S. Rosswog, J. Hjorth, P. D’Avanzo, A. S. Fruchter, C. L. Fryer, T. Kangas, B. Milvang-Jensen, S. Rosetti, D. Steeghs, R. T. Wollaeger, Z. Cano, C. M. Copperwheat, S. Covino, V. D’Elia, A. de Ugarte Postigo, P. A. Evans, W. P. Even, S. Fairhurst, R. Figuera Jaimes, C. J. Fontes, Y. I. Fujii, J. P. U. Fynbo, B. P. Gompertz, J. Greiner, G. Hodosan, M. J. Irwin, P. Jakobsson, U. G. Jørgensen, D. A. Kann, J. D. Lyman, D. Malesani, R. G. McMahon, A. Melandri, P. T. O’Brien, J. P. Osborne, E. Palazzi, D. A. Perley, E. Pian, S. Piranomonte, M. Rabus, E. Rol, A. Rowlinson, S. Schulze, P. Sutton, C. C. Thöne, K. Ulaczyk, D. Watson, K. Wiersema, and R. A. M. J. Wijers. [The Emergence of a Lanthanide-rich Kilonova Following the Merger of Two Neutron Stars](#). *The Astrophysical Journal*, 848(2):L27, oct 2017.
- [31] B. P. Abbott, LIGO Scientific Collaboration, and Virgo Collaboration. [GW170817: Observation of Gravitational Waves from a Binary Neutron Star Inspiral](#). *Phys. Rev. Lett.*, 119:161101, Oct 2017.
- [32] B. P. Abbott *et al.* [Multi-messenger Observations of a Binary Neutron Star Merger](#). *The Astrophysical Journal*, 848(2):L12, oct 2017.
- [33] Daniel Kasen, Brian Metzger, Jennifer Barnes, Eliot Quataert, and Enrico Ramirez-Ruiz. [Origin of the heavy elements in binary neutron-star mergers from a gravitational-wave event](#). *Nature*, 551:80–84, 2017.
- [34] H. Schatz, A. Aprahamian, V. Barnard, L. Bildsten, A. Cumming, M. Ouellette, T. Rauscher, F.-K. Thielemann, and M. Wiescher. [End Point of the \$rp\$ Process on Accreting Neutron Stars](#). *Phys. Rev. Lett.*, 86:3471–3474, Apr 2001.

- [35] R. K. Wallace and S. E. Woosley. [Explosive hydrogen burning](#). *ASTROPHYS J SUPPL S*, 45:389–420, Feb 1981.
- [36] J. Grindlay, H. Gursky, H. Schnopper, D. R. Parsignault, J. Heise, A. C. Brinkman, and J. Schrijver. [Discovery of intense X-ray bursts from the globular cluster NGC 6624](#). *ASTROPHYS J SUPPL S*, 205:L127–L130, May 1976.
- [37] R. D. Belian, J. P. Conner, and W. D. Evans. [The discovery of X-ray bursts from a region in the constellation Norma](#). *ASTROPHYS J SUPPL S*, 206:L135–L138, Jun 1976.
- [38] R. H. Cyburt, A. M. Amthor, A. Heger, E. Johnson, L. Keek, Z. Meisel, H. Schatz, and K. Smith. [DEPENDENCE OF X-RAY BURST MODELS ON NUCLEAR REACTION RATES](#). *The Astrophysical Journal*, 830(2):55, oct 2016.
- [39] Meng Wang, G. Audi, F. G. Kondev, W.J. Huang, S. Naimi, and Xing Xu. [The AME2016 atomic mass evaluation \(II\). Tables, graphs and references](#). *Chinese Physics C*, 41(3):030003, mar 2017.
- [40] Y.M. Xing, K.A. Li, Y.H. Zhang, X.H. Zhou, M. Wang, Yu.A. Litvinov, K. Blaum, S. Wanajo, S. Kubono, G. Martnez-Pinedo, A. Sieverding, R.J. Chen, P. Shuai, C.Y. Fu, X.L. Yan, W.J. Huang, X. Xu, X.D. Tang, H.S. Xu, T. Bao, X.C. Chen, B.S. Gao, J.J. He, Y.H. Lam, H.F. Li, J.H. Liu, X.W. Ma, R.S. Mao, M. Si, M.Z. Sun, X.L. Tu, Q. Wang, J.C. Yang, Y.J. Yuan, Q. Zeng, P. Zhang, X. Zhou, W.L. Zhan, S. Litvinov, G. Audi, T. Uesaka, Y. Yamaguchi, T. Yamaguchi, A. Ozawa, C. Frhlich, T. Rauscher, F.-K. Thielemann, B.H. Sun, Y. Sun, A.C. Dai, and F.R. Xu. [Mass measurements of neutron-deficient Y, Zr, and Nb isotopes and their impact on \$rp\$ and \$\nu p\$ nucleosynthesis processes](#). *Physics Letters B*, 781:358 – 363, 2018.
- [41] Lowell S. Brown and Gerald Gabrielse. [Geonium theory: Physics of a single electron or ion in a Penning trap](#). *Rev. Mod. Phys.*, 58:233–311, Jan 1986.
- [42] G. Gabrielse, L. Haarsma, and S.L. Rolston. [Open-endcap Penning traps for high precision experiments](#). *International Journal of Mass Spectrometry and Ion Processes*, 88(2):319 – 332, 1989.
- [43] Martin Kretschmar. [Single particle motion in a Penning trap: description in the classical canonical formalism](#). *Physica Scripta*, 46(6):544–554, dec 1992.
- [44] G. Savard, St. Becker, G. Bollen, H.-J. Kluge, R.B. Moore, Th. Otto, L. Schweikhard, H. Stolzenberg, and U. Wiess. [A new cooling technique for heavy ions in a Penning trap](#). *Physics Letters A*, 158(5):247 – 252, 1991.
- [45] Jochen Ketter, Tommi Eronen, Martin Hocker, Sebastian Streubel, and Klaus Blaum. [First-order perturbative calculation of the frequency-shifts caused by static cylindrically-symmetric electric and magnetic imperfections of a Penning trap](#). *International Journal of Mass Spectrometry*, 358:1 – 16, 2014.

- [46] Accelerator laboratory website. <https://www.jyu.fi/science/en/physics/research/infrastructures/accelerator-laboratory/accelerators-and-ion-sources>. Accessed: 2019-07-24.
- [47] I. Pohjalainen, I. D. Moore, T. Eronen, A. Jokinen, H. Penttilä, and S. Rinta-Antila. [Gas purification studies at IGISOL-4](#). *Hyperfine Interactions*, 227(1-3):169–180, January 2014.
- [48] H. Penttilä, V. V. Elomaa, T. Eronen, J. Hakala, A. Jokinen, A. Kankainen, I. D. Moore, S. Rahaman, S. Rinta-Antila, J. Rissanen, V. Rubchenya, A. Saastamoinen, C. Weber, and J. Äystö. [Fission yield studies at the IGISOL facility](#). *The European Physical Journal A*, 48(4):43, Apr 2012.
- [49] A. Al-Adili, K. Jansson, M. Lantz, A. Solders, D. Gorelov, C. Gustavsson, A. Mattera, I. Moore, A. V. Prokofiev, V. Rakopoulos, H. Penttilä, D. Tarrío, S. Wiberg, M. Österlund, and S. Pomp. [Simulations of the fission-product stopping efficiency in IGISOL](#). *The European Physical Journal A*, 51(5):59, May 2015.
- [50] Viki-Veikko Elomaa. [Mass measurements for explosive nucleosynthesis in stars](#). PhD thesis, University of Jyväskylä, 2009.
- [51] J. Huikari, P. Dendooven, A. Jokinen, A. Nieminen, H. Penttilä, K. Peräjärvi, A. Popov, S. Rinta-Antila, and J. Äystö. [Production of neutron deficient rare isotope beams at IGISOL; on-line and off-line studies](#). *Nuclear Instruments and Methods in Physics Research Section B: Beam Interactions with Materials and Atoms*, 222(3):632 – 652, 2004.
- [52] R. Béraud, G. Canchel, A. Emsallem, P. Dendooven, J. Huikari, W. Huang, Y. Wang, K. Peräjärvi, S. Rinta-Antila, A. Jokinen, V. S. Kolhinen, A. Nieminen, H. Penttilä, J. Szerypo, J. Äystö, B. Bruyneel, and A. Popov. [Status of HIGISOL, a New Version Equipped with SPIG and Electric Field Guidance](#). *Hyperfine Interactions*, 132(1):481–486, Jan 2001.
- [53] The Raspberry Pi Foundation website. <https://www.raspberrypi.org/>. Accessed: 2019-06-25.
- [54] Arduino website. <https://www.arduino.cc/>. Accessed: 2019-06-25.
- [55] Tommi Eronen, Anu Kankainen, and Juha Äystö. [Ion traps in nuclear physics – Recent results and achievements](#). *Progress in Particle and Nuclear Physics*, 91:259 – 293, 2016.
- [56] Alexandros Giatzoglou, Tanapoom Poomaradee, Ilkka Pohjalainen, Sami Rinta-Antila, Iain D. Moore, Philip M. Walker, Luca Marmugi, and Ferruccio Renzoni. [A facility for production and laser cooling of cesium isotopes and isomers](#). *Nuclear Instruments and Methods in Physics Research Section A: Accelerators, Spectrometers, Detectors and Associated Equipment*, 908:367 – 375, 2018.

- [57] P. Campbell, I.D. Moore, and M.R. Pearson. [Laser spectroscopy for nuclear structure physics](#). *Progress in Particle and Nuclear Physics*, 86:127 – 180, 2016.
- [58] M. Vilén. [New off-line ion source infrastructure at IGISOL](#). Master's thesis, University of Jyväskylä, 2016.
- [59] HeatWave Labs, Inc. <https://www.cathode.com/>. Accessed: 2019-06-17.
- [60] L. J. Vormawah, M. Vilén, R. Beerwerth, P. Campbell, B. Cheal, A. Dicker, T. Eronen, S. Fritzsche, S. Geldhof, A. Jokinen, S. Kelly, I. D. Moore, M. Reponen, S. Rinta-Antila, S. O. Stock, and A. Voss. [Isotope shifts from collinear laser spectroscopy of doubly charged yttrium isotopes](#). *Phys. Rev. A*, 97:042504, Apr 2018.
- [61] P. Karvonen, I.D. Moore, T. Sonoda, T. Kessler, H. Penttilä, K. Peräjärvi, P. Ronkanen, and J. Äystö. [A sextupole ion beam guide to improve the efficiency and beam quality at IGISOL](#). *Nuclear Instruments and Methods in Physics Research Section B: Beam Interactions with Materials and Atoms*, 266(21):4794–4807, November 2008.
- [62] D.A. Nesterenko, L. Canete, T. Eronen, A. Jokinen, A. Kankainen, Yu.N. Novikov, S. Rinta-Antila, A. de Roubin, and M. Vilen. [High-precision measurement of the mass difference between \$^{102}\text{Pd}\$ and \$^{102}\text{Ru}\$](#) . *International Journal of Mass Spectrometry*, 435:204 – 208, 2019.
- [63] A. Nieminen, J. Huikari, A. Jokinen, J. Äystö, P. Campbell, and E.C.A. Cochrane. [Beam cooler for low-energy radioactive ions](#). *Nuclear Instruments and Methods in Physics Research Section A: Accelerators, Spectrometers, Detectors and Associated Equipment*, 469(2):244 – 253, 2001.
- [64] MCP delay line detector, RoentDek Handels GmbH. <http://www.roentdek.de/detectors/>. Accessed: 2019-06-06.
- [65] G. Bollen, R. B. Moore, G. Savard, and H. Stolzenberg. [The accuracy of heavy ion mass measurements using time of flight ion cyclotron resonance in a Penning trap](#). *Journal of Applied Physics*, 68(9):4355–4374, 1990.
- [66] T. Eronen, V.-V. Elomaa, U. Hager, J. Hakala, A. Jokinen, A. Kankainen, S. Rahaman, J. Rissanen, C. Weber, and J. Äystö. [Preparing isomerically pure beams of short-lived nuclei at JYFLTRAP](#). *Nuclear Instruments and Methods in Physics Research Section B: Beam Interactions with Materials and Atoms*, 266(19):4527 – 4531, 2008. Proceedings of the XVth International Conference on Electromagnetic Isotope Separators and Techniques Related to their Applications.
- [67] G Bollen, S Becker, H.-J Kluge, M König, R.B Moore, T Otto, H Raimbault-Hartmann, G Savard, L Schweikhard, and H Stolzenberg. [ISOLTRAP: a tandem Penning trap system for accurate on-line mass determination of short-lived isotopes](#). *Nuclear Instruments and Methods in Physics Research Section*

A: Accelerators, Spectrometers, Detectors and Associated Equipment, 368(3):675 – 697, 1996.

- [68] Martin Kretschmar. [The Ramsey method in high-precision mass spectrometry with Penning traps: Theoretical foundations](#). *International Journal of Mass Spectrometry*, 264(2):122 – 145, 2007.
- [69] S. George, K. Blaum, F. Herfurth, A. Herlert, M. Kretschmar, S. Nagy, S. Schwarz, L. Schweikhard, and C. Yazidjian. [The Ramsey method in high-precision mass spectrometry with Penning traps: Experimental results](#). *International Journal of Mass Spectrometry*, 264(2):110 – 121, 2007.
- [70] M. Vilén, D.A. Nesterenko, T. Eronen, A. Kankainen, et al. *To be submitted*, 2019.
- [71] P. Möller, A.J. Sierk, T. Ichikawa, and H. Sagawa. [Nuclear ground-state masses and deformations: FRDM\(2012\)](#). *Atomic Data and Nuclear Data Tables*, 109-110:1 – 204, 2016.
- [72] M R Mumpower, G C McLaughlin, R Surman, and A W Steiner. [Reverse engineering nuclear properties from rare earth abundances in the process](#). *Journal of Physics G: Nuclear and Particle Physics*, 44(3):034003, feb 2017.
- [73] Peter Brix. [Zum Isotopieverschiebungseffekt in den Atomspektren der Seltenen Erden](#). *Zeitschrift für Physik*, 132(5):579–607, Oct 1952.
- [74] B. R. Mottelson and S. G. Nilsson. [Classification of the Nucleonic States in Deformed Nuclei](#). *Phys. Rev.*, 99:1615–1617, Sep 1955.
- [75] V.-V. Elomaa, G. K. Vorobjev, A. Kankainen, L. Batist, S. Eliseev, T. Eronen, J. Hakala, A. Jokinen, I. D. Moore, Yu. N. Novikov, H. Penttilä, A. Popov, S. Rahaman, J. Rissanen, A. Saastamoinen, H. Schatz, D. M. Seliverstov, C. Weber, and J. Äystö. [Quenching of the SnSbTe Cycle in the \$rp\$ Process](#). *Phys. Rev. Lett.*, 102:252501, Jun 2009.
- [76] A. Kellerbauer, K. Blaum, G. Bollen, F. Herfurth, H.-J. Kluge, M. Kuckein, E. Sauvan, C. Scheidenberger, and L. Schweikhard. [From direct to absolute mass measurements: A study of the accuracy of ISOLTRAP](#). *The European Physical Journal D - Atomic, Molecular, Optical and Plasma Physics*, 22(1):53–64, Jan 2003.
- [77] D. J. Hartley, F. G. Kondev, R. Orford, J. A. Clark, G. Savard, A. D. Ayangeakaa, S. Bottoni, F. Buchinger, M. T. Burkey, M. P. Carpenter, P. Copp, D. A. Gorelov, K. Hicks, C. R. Hoffman, C. Hu, R. V. F. Janssens, J. W. Klimes, T. Lauritsen, J. Sethi, D. Seweryniak, K. S. Sharma, H. Zhang, S. Zhu, and Y. Zhu. [Masses and \$\beta\$ -Decay Spectroscopy of Neutron-Rich Odd-Odd \$^{160,162}\text{Eu}\$ Nuclei: Evidence for a Subshell Gap with Large Deformation at \$N = 98\$](#) . *Phys. Rev. Lett.*, 120:182502, May 2018.

- [78] S. K. Ghorui, B. B. Sahu, C. R. Praharaj, and S. K. Patra. [Examining the stability of Sm nuclei around \$N = 100\$](#) . *Phys. Rev. C*, 85:064327, Jun 2012.



ORIGINAL PAPERS

I

PRECISION MASS MEASUREMENTS ON NEUTRON-RICH RARE-EARTH ISOTOPES AT JYFLTRAP: REDUCED NEUTRON PAIRING AND IMPLICATIONS FOR R-PROCESS CALCULATIONS

by


M. Vilén, J.M. Kelly, A. Kankainen, M. Brodeur, A. Aprahamian, L. Canete, T. Eronen, A. Jokinen, T. Kuta, I.D. Moore, M.R. Mumpower, D.A. Nesterenko, H. Penttilä, I. Pohjalainen, W.S. Porter, S. Rinta-Antila, R. Surman, A. Voss, J. Äystö
2018

Physical Review Letters 120, 262701

Reproduced with kind permission of Physical Review Letters.

Precision Mass Measurements on Neutron-Rich Rare-Earth Isotopes at JYFLTRAP: Reduced Neutron Pairing and Implications for r -Process Calculations

M. Vilen,^{1,*} J. M. Kelly,^{2,†} A. Kankainen,¹ M. Brodeur,² A. Aprahamian,² L. Canete,¹ T. Eronen,¹ A. Jokinen,¹ T. Kuta,² I. D. Moore,¹ M. R. Mumpower,^{2,3} D. A. Nesterenko,¹ H. Penttilä,¹ I. Pohjalainen,¹ W. S. Porter,² S. Rinta-Antila,¹ R. Surman,² A. Voss,¹ and J. Äystö¹
¹*University of Jyväskylä, P.O. Box 35, FI-40014 University of Jyväskylä, Finland*
²*University of Notre Dame, Notre Dame, Indiana 46556, USA*
³*Theory Division, Los Alamos National Lab, Los Alamos, New Mexico 87544, USA*

 (Received 3 August 2017; revised manuscript received 17 February 2018; published 29 June 2018)

The rare-earth peak in the r -process abundance pattern depends sensitively on both the astrophysical conditions and subtle changes in nuclear structure in the region. This work takes an important step towards elucidating the nuclear structure and reducing the uncertainties in r -process calculations via precise atomic mass measurements at the JYFLTRAP double Penning trap. ^{158}Nd , ^{160}Pm , ^{162}Sm , and $^{164-166}\text{Gd}$ have been measured for the first time, and the precisions for ^{156}Nd , ^{158}Pm , $^{162,163}\text{Eu}$, ^{163}Gd , and ^{164}Tb have been improved considerably. Nuclear structure has been probed via two-neutron separation energies S_{2n} and neutron pairing energy metrics D_n . The data do not support the existence of a subshell closure at $N = 100$. Neutron pairing has been found to be weaker than predicted by theoretical mass models. The impact on the calculated r -process abundances has been studied. Substantial changes resulting in a smoother abundance distribution and a better agreement with the solar r -process abundances are observed.

DOI: 10.1103/PhysRevLett.120.262701

The astrophysical rapid neutron capture process (r process) [1–3] is responsible for the production of around half of the elements heavier than iron. The r process and its astrophysical site have driven research not only in nuclear astrophysics but in multiple fields, including nuclear structure [4,5] and theory [6,7], accelerator mass spectrometry [8], and observational astronomy [9,10]. Various astrophysical sites have been proposed over the years, e.g., neutrino-driven winds from the remnants of core-collapse supernovae [3,11], magnetohydrodynamic supernovae [12], and neutron-star mergers [13–18]. The recent, seminal multimessenger observations of a neutron-star merger [19,20], namely, the gravitational waves from GW170817 [21] followed by a kilonova (AT 2017 gfo) powered by the radioactive decay of r -process nuclei synthesized in the ejecta [22,23], provide direct evidence that the r process takes place in neutron-star mergers. For the first time, this allows the testing of r -process abundance models using an unpolluted sample [24]. Hence, there is now a strong impetus to have accurate nuclear physics inputs to ensure the reliability of the abundance calculations. With their high opacity, lanthanides play a central role in the diagnostics of heavy r -process ejecta from such mergers [25,26]. In this Letter, we present results for nuclear binding energies that affect the calculated r -process abundances of lanthanides in the rare-earth region.

Because the r -process path traverses uncharted and largely inaccessible regions of the chart of nuclides, there is a scarcity of experimental information with which to

constrain the astrophysical calculations. Detailed r -process sensitivity studies performed in recent years [27–32] have shown that, among the various quantities entering into their calculations, e.g., neutron-capture and photodisintegration rates, beta-decay half-lives, and beta-delayed neutron emission and fission probabilities, it is the quantities most strongly derivative of nuclear mass, namely, binding energies, that proved to be the most sensitive [29]. However, the masses of the most relevant r -process nuclei have never been measured, leaving nuclear abundance calculations to rely on theoretical mass models such as FRDM12 [33], HFB-24 [34], Duflo-Zuker [35], or Skyrme energy-density functionals [7] for these critical inputs. While the mass models agree closely with one another in regions with existing measurements, they diverge strongly in the absence of such empirical data, which has profound impacts on abundance peak formation simulations [29].

The formation of the rare-earth abundance peak is very sensitive to nuclear structure in the neutron-rich rare-earth region. A confluence of nuclear deformation and β -decay properties peculiar to nuclei surrounding $A = 165$ is understood to create a funneling effect that draws the nuclei towards the peak as neutron captures dwindle and existing radionuclides decay towards stability [36,37]. Furthermore, fission recycling is believed to augment this process, as the fragments of heavier, unstable nuclides beyond the third ($A \approx 195$) peak could cycle back into the rare-earth region

[17,37,38]. Fortunately, the rare-earth abundances are some of the most precisely known in the Solar System and in metal-poor stars [39].

The rare-earth region, located in the midshell bounded by $Z = 50$ – 82 and $N = 82$ – 126 , incorporates several interesting nuclear structure features that can affect the r process. A surge of research was triggered by the discovery of the onset of strong prolate deformation at $N = 88$ – 90 in the 1950s [40,41]. Proton-neutron interactions enhanced in nuclei with approximately equal numbers of valence protons and neutrons have been found to play a key role in the evolution of nuclear structure and collectivity in this region [42–44]. A local minimum in the $E(2^+)$ energies and a local maximum of moment of inertia have been observed for the Gd isotopes at $N = 98$ via γ -ray spectroscopy at Gammasphere [45]. Jones *et al.* [45] found ^{164}Gd ($N = 100$) to be more rigid and to show less stretching than ^{162}Gd , suggesting a possible change in structure. Recently, γ -ray spectroscopy on ^{164}Sm and ^{166}Gd with EURICA at the Radioactive Isotope Beam Factory (RIBF) revealed an increase in the $E(2^+)$ and $E(4^+)$ energies at $N = 100$ in comparison with the $N = 98$ cases for Gd and Sm isotopes, supporting an implied subshell closure at $N = 100$ proffered by the Hartree-Fock calculations of Ref. [46]. Interestingly, recent half-life measurements performed at RIKEN [47] did not find any supporting evidence for the $N = 100$ subshell closure. Additionally, the systematics of the new K isomers found in the neutron-rich $N = 100$ isotones ^{162}Sm , ^{163}Eu , and ^{164}Gd at RIKEN could be explained without the predicted $N = 100$ shell gap [48].

Although information on beta-decay half-lives [47] and level structures [45,49] of rare-earth nuclei has increased substantially in recent years, nuclear binding energies—i.e., masses—have not been pursued so intensively. The Canadian Penning trap (*CPT*) has explored some rare-earth nuclei in the past [50], and some Q_β measurements have been performed using a total absorption Clover detector [51]. In this Letter, we present the first mass measurements of several rare-earth nuclei close to $N = 100$ of significance for the astrophysical r process while providing further information on the nuclear structure which is of direct relevance for the r process.

The studied neutron-rich rare-earth nuclei were produced at the Ion Guide Isotope Separator On-Line (IGISOL) facility [52], employing a 25 MeV, 10–15 μA proton beam impinging on a 15 mg/cm²-thick natural uranium target. The fission fragments were thermalized in helium buffer gas and extracted from the gas cell with a typical charge state of $q = +e$ by a radio-frequency sextupole ion guide [53]. Subsequently, the ions were accelerated to 30 keV before mass separation with a dipole magnet. The continuous beam was cooled and bunched in a radio-frequency quadrupole cooler buncher [54] prior to injection into the double Penning trap mass spectrometer JYFLTRAP [55].

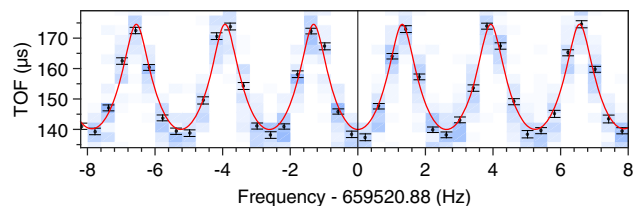


FIG. 1. Time-of-flight spectrum for $^{163}\text{Eu}^+$. Background shading indicates the total number of ions, where darker shading indicates more ions.

Isobarically pure ion samples were prepared in the purification trap via the mass-selective buffer gas cooling method [56]. For ^{156}Nd , ^{158}Pm , ^{162}Sm , $^{162,163}\text{Eu}$, $^{163-166}\text{Gd}$, and ^{164}Tb , an additional cleaning phase employing dipolar Ramsey excitations [57] in the second trap was required. The mass measurements were performed by determining the cyclotron frequency, $\nu_c = qB/(2\pi m)$, for an ion with mass m and charge q in a magnetic field B using the time-of-flight-ion-cyclotron resonance method (TOF-ICR) [58,59] (see Fig. 1). A 400-ms quadrupolar excitation scheme was applied for ^{158}Nd and ^{160}Pm . To more accurately determine the frequency, separated oscillatory fields [60,61] with excitation patterns of 25-350–25 ms and 25-750–25 ms (on-off-on) were applied for ^{156}Nd , ^{158}Pm , ^{162}Sm , $^{162,163}\text{Eu}$, $^{163-166}\text{Gd}$, and ^{164}Tb .

The magnetic field strength was precisely determined by interleaving measurements of a well-known reference ion ($\nu_{c,\text{ref}}$) just before and after an ion of interest (ν_c). The mass ratios and atomic masses were then calculated from the ratio of frequencies $r = \nu_{c,\text{ref}}/\nu_c$, which equals the ratio of the ion masses. Data analysis followed the procedure described in Refs. [55,62]. Temporal fluctuations of the B field, $\delta_B(\nu_{\text{ref}})/\nu_{\text{ref}} = \Delta t \times 8.18 \times 10^{-12}/\text{min}$ [63], where Δt is the time between consecutive reference measurements, and a mass-dependent uncertainty $\delta_m(r)/r = \Delta m \times 2.2(6) \times 10^{-10}/u$, determined soon after the experiment, were taken into account.

The measured frequency ratios and the corresponding mass-excess values are presented in Table I. Six isotopes, namely, ^{158}Nd , ^{160}Pm , ^{162}Sm , and $^{164-166}\text{Gd}$, were measured for the first time. The precision of the mass values has been improved considerably for all studied isotopes. The new values agree with the extrapolations of AME16 [64], which have generally overestimated the nuclear binding energies in this region by about 150 keV.

Most of the previously known mass values were based on β -decay Q -value measurements, such as ^{156}Nd [65], $^{162,163}\text{Eu}$ [51], and ^{164}Tb [66]. Although the Q_β values yield lower mass values than the present Penning trap measurement, only ^{156}Nd [65] deviates by more than 1σ from this work. In fact, it has been suggested [67] that, based on the trends on the mass surface, ^{156}Nd might actually be 70 keV less bound.

Two of the studied isotopes, ^{158}Pm and ^{163}Gd , have been measured by the *CPT* [50]. While the results for ^{158}Pm

TABLE I. Frequency ratios (r) and mass-excess values (ME) determined in this work with JYFLTRAP compared with AME16 [64]. All measurements were done with singly charged ions. The reference masses, ^{136}Xe , ^{158}Gd , ^{163}Dy , and ^{171}Yb , were adopted from AME16, and # signs indicate extrapolated values therein.

Isotope	Reference	ME _{REF} (keV)	$r = \nu_{c,\text{ref}}/\nu_c$	ME _{JYFL} (keV)	ME _{AME16} (keV)	$\Delta\text{ME}_{\text{JYFL-AME16}}$ (keV)
^{156}Nd	^{136}Xe	-86429.159(7)	1.147 366 924(19)	-60210(2)	-60470(200)	260(200)
^{158}Nd	^{136}Xe	-86429.159(7)	1.162 132 772(290)	-53897(37)	-54060(200)#	160(200)#
^{158}Pm	^{158}Gd	-70689.5(12)	1.000 078 752(9)	-59104(2)	-59089(13)	-15(13)
^{160}Pm	^{136}Xe	-86429.159(7)	1.176 857 014(130)	-52851(16)	-53000(200)#	149(201)#
^{162}Sm	^{136}Xe	-86429.159(7)	1.191 560 914(39)	-54381(5)	-54530(200)#	149(200)#
^{162}Eu	^{136}Xe	-86429.159(7)	1.191 527 132(28)	-58658(4)	-58700(40)	42(40)
^{163}Eu	^{163}Dy	-66381.2(8)	1.000 065 633(23)	-56420(4)	-56480(70)	60(70)
^{163}Gd	^{163}Dy	-66381.2(8)	1.000 034 135(22)	-61200(4) ^a	-61314(8)	114(9)
^{164}Gd	^{171}Yb	-59306.810(13)	0.959 046 522(14)	-59694(3)	-59770(100)#	76(100)#
^{165}Gd	^{171}Yb	-59306.810(13)	1.058 489 243(23) ^b	-56522(4)	-56450(120)#	-72(120)#
^{166}Gd	^{136}Xe	-86429.159(7)	1.220 992 828(29)	-54387(4)	-54530(200)#	143(200)#
^{164}Tb	^{171}Yb	-59306.810(13)	0.959 031 473(21)	-62090(4)	-62080(100)	-10(100)

^aAssuming the measured state is the isomer at 137.8 keV [51], the ground-state mass is -61338(4) keV.

^bMeasured as $^{165}\text{Gd}^{16}\text{O}$.

agree within 1σ , they deviate considerably in the case of ^{163}Gd . Interestingly, a new long-lived [$T_{1/2} = 23.5(10)$ s] isomeric state at 137.8 keV in ^{163}Gd was recently discovered [51]. The unusually large discrepancy between this work and the *CPT* [50] could be understood if the proton-induced fission on $^{\text{nat}}\text{U}$ at IGISOL had predominantly populated the isomeric state of ^{163}Gd . Assuming we measured the first isomeric state, our corrected mass-excess value differs from the *CPT* by 24(9) keV. If we use the 15 keV uncertainty quoted in Ref. [50] rather than AME16, it results in an even better agreement.

Nuclear structure far from stability can be probed via two-neutron separation energies S_{2n} [68]. They usually exhibit smooth trends except at shell closures or when there is a change in the nuclear structure, such as the onset of a strong prolate deformation at around $N = 90$ seen as a bump in Fig. 2. This is also observed as a sharp increase in experimental $E(4^+)/E(2^+)$ ratios reaching ≈ 3.3 in the region $N = 92\text{--}102$ compatible with a rigid rotor. The strong deformation is also predicted by theoretical models; e.g., FRDM12 yields a maximum deformation ($\beta_2 \approx 0.31$ [33]) for the Gd isotopes at around $N = 101\text{--}103$. The new S_{2n} values determined in this work show a change in the slope after $N = 100$ for the Gd isotopes ($Z = 64$). A similar effect is also observed for Tb at $N = 100$ and after $N = 96$ for the Nd ($Z = 60$) chain. Incidentally, a small local maximum is seen in the $E(2^+)$ energies at $N = 100$ for Gd and Dy. However, the two-neutron shell-gap energies for $N = 100$ are rather low (< 1 MeV) down to Gd and do not support the proposed subshell gap at $N = 100$ [46,69,70].

We compared the experimental S_{2n} values to the predictions from various mass models commonly used in *r*-process calculations, such as FRDM12 [33], Duflo-Zuker [35], and HFB-24 [34]. These models predict a rather

smooth behavior for the S_{2n} values in the region of interest but overestimate them at $N = 99$ and 100 by around 0.3 MeV for the studied isotopic chains. None of them suggest changes in the slope, in contrast to those observed in this work. Among the other mass models, WS4+ [71] yields the smallest root-mean-square (rms) error for the studied isotopic S_{2n} chains, 0.12 MeV. UNEDF0 [72] results in a similar rms error as HFB-24 and FRDM12, ≈ 0.4 MeV, which is much smaller than for SkM and SLy4 also used in the *r*-process calculations in Ref. [7]. To further explore the evolution of the nuclear structure, we studied neutron pairing energy metrics $D_n(N) = (-1)^{N+1}[S_n(Z, N+1) - S_n(Z, N)]$ [73], which is directly related to the empirical neutron pairing gap $\Delta^3(N) = D_n(N)/2$ [74] also known as the odd-even staggering

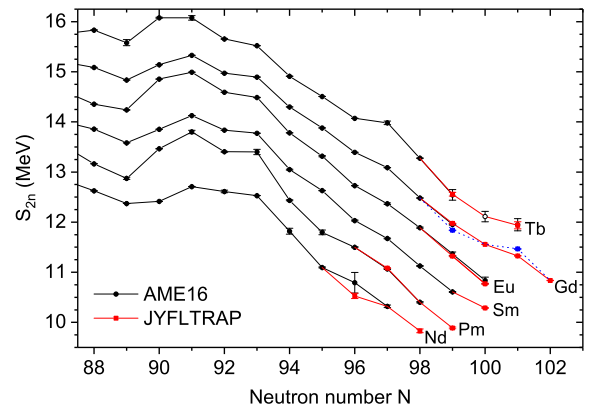


FIG. 2. Two-neutron separation energies S_{2n} from this work (red lines) together with the experimental (solid black circles) values and an extrapolated value for ^{165}Tb (open black circle) from AME16 [64]. The dashed blue lines indicate the values assuming the ground state of ^{163}Gd was measured in this work.

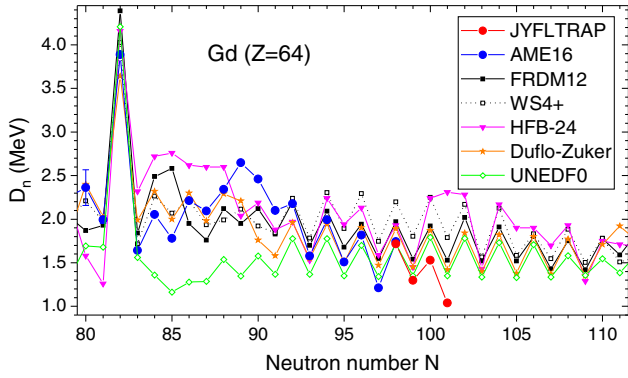


FIG. 3. Neutron pairing energies from this work (red circles) and AME16 (blue line) in comparison with various theoretical predictions for the Gd isotopes.

parameter. These are very sensitive to changes in the nuclear structure; see, e.g., [75]. To highlight such a change, Fig. 3 shows the impact of our new mass values on D_n for neutron-rich Gd isotopes, an isotopic chain extensively studied [45–48] for its possible change in nuclear structure. Whereas $N = 82$ presents as a clear peak, nothing is observed at $N = 100$ to support the existence of a subshell closure. More interestingly, neutron pairing is much weaker than predicted by theoretical models when approaching the midshell. The same can be observed for the other isotopic chains as well: The experimental neutron separation energies are systematically lower at $N = 98, 100$, and 102 , leading to smaller odd-even staggering than predicted by the theoretical models. While there were already some indications of overestimated even- N S_n values from previous measurements in the Tb, Gd, and Sm chains, these were single cases in their respective chains. The new data presented in this Letter establish this as a trend, and also extend it to the Pm and Nd chains.

We studied the impact of the new masses on the r process for astrophysical conditions of a neutron-star merger. The r -process simulations proceed as in Ref. [29]. Masses and relevant Q values not measured in this work were supplemented with experimental data from AME16 or calculated values from FRDM12. For consistency, calculated and experimental masses were not combined in the calculation of a given S_n value. Branching ratios and β -decay half-lives were taken from NUBASE 2016 [76] or Ref. [77]. The neutron-capture rates were calculated with the commonly used TALYS code [78] with the revised mass data set described above. For fission product distributions, we choose a simple asymmetric split [30] so that fission products fall into the $A \sim 130$ region and the rare-earth peak forms entirely via the dynamical formation mechanism of Refs. [36,37]. The rare-earth region of the final abundance patterns for two different types of merger trajectories, corresponding to conditions expected in the dynamical ejecta and accretion disk wind of the merger environment, appear in Fig. 4.

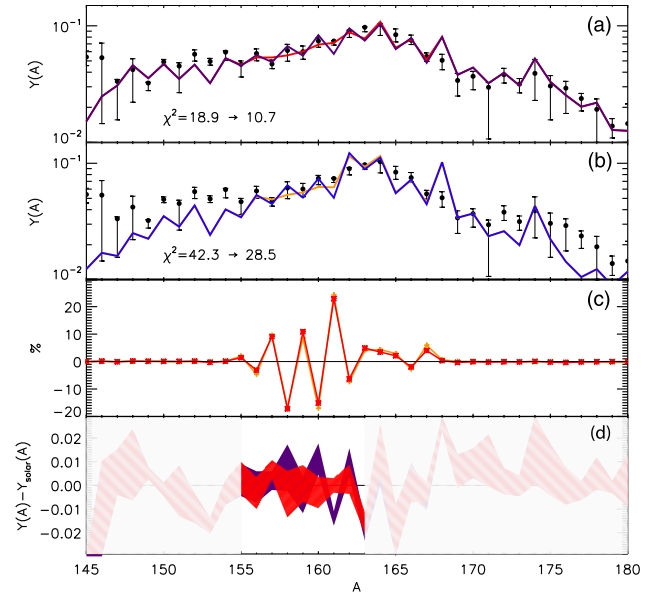


FIG. 4. Solar r -process abundances [3] (black circles) in comparison with the calculations using the experimental AME16 [64] + FRDM12 masses [33] (blue and purple lines, respectively) and the new masses from this work (orange and red lines) for representative trajectories (a) with fission cycling and (b) without fission cycling. (c) Change, in percent, of the abundance pattern as a result of using the masses from this work. (d) Residuals for scenario (a) based on the mass values from this work (red) and the baseline (purple), where the bands represent the solar abundance uncertainties.

Figure 4(a) shows the results from a representative dynamical ejecta trajectory for a 1.35 solar mass neutron-star merger from Ref. [79]. The trajectory initially has a very low electron fraction of $Y_e = 0.016$ and low entropy per baryon $s/k_B \sim 8$, which rises to $s/k_B \sim 100$ due to nuclear reheating. The timescale is initially around 40 ms, after which a homologous expansion is assumed [79]. Up to 90% of the prompt ejected mass may come from these types of reheated, fission-recycling trajectories which all yield very similar abundances with the mass model used and are therefore largely independent of the specific astrophysical conditions as discussed in Ref. [79]. As shown in Figs. 4(a), 4(b), and 4(d), better agreement with the solar abundance pattern is obtained including our new mass values ($\chi^2 = 10.7$) than with the AME16 and FRDM12 values used as a baseline ($\chi^2 = 18.9$). Here, χ^2 is defined as $\chi^2 = \sum \{ [Y(A)_{\text{solar}} - Y(A)_{\text{calc}}] / \sigma[Y(A)_{\text{solar}}] \}^2$, where $\sigma[Y(A)_{\text{solar}}]$ is the uncertainty of the solar abundances [3]. The sum is taken over the mass number range ($A = 154\text{--}168$) affected by the measurements reported in this Letter, and the simulated abundances $Y(A)_{\text{calc}}$ are scaled to solar over the same range. Furthermore, changes of up to 24% in the calculated abundances resulting in a general smoothing of the profile can be seen, as highlighted in Fig. 4(c).

To examine whether these effects are an artifact of fission recycling, we consider a second type of trajectory that is less neutron-rich and does not undergo fission recycling. We choose a low-entropy, hot wind r process, parametrized as in Ref. [80] with values ($s/k_B = 10$, timescale = 70 ms, $Y_e = 0.15$) consistent with those expected for merger accretion disk winds [81]. As seen in Figs. 4(b) and 4(c), the influence of the new masses is notably similar to the fission recycling example.

The nuclei studied in this work are populated at late times in the r process, after $(n, \gamma) - (\gamma, n)$ equilibrium has failed. At this stage, the material is decaying back toward stability, and the fine details of the final abundance pattern are set through a competition between neutron capture and β decay. Although the present work provides more accurate Q_β values relevant for the β decays, they do not affect the β -decay rates, because the half-lives are already experimentally known. Thus, the visible shifts in the abundance distribution are due entirely to the influence of the new masses on the recalculated neutron-capture rates, which changed by 10%–25%. These rates depend on neutron separation energies but also on the choice of the neutron-capture code. Therefore, the calculations done with the TALYS code should be taken as a representative example of the effect of the new mass values on the r -process abundances. However, it can be expected that the effect of the revised neutron separation energies would be rather similar even if a different code was used. The reduced neutron pairing observed in this work, i.e., smaller odd-even staggering in the neutron separation energies, is not predicted by FRDM12 or other mass models typically used for the r -process calculations (see Fig. 3). As a result, the final calculated r -process abundances are smoother than the baseline calculation done with AME16 + FRDM12. More mass measurements are anticipated to test if the seesaw pattern in the abundances at heavier mass numbers is due to the used theoretical mass values.

In this work, we have determined nuclear binding energies for ^{158}Nd , ^{160}Pm , ^{162}Sm , and $^{164-166}\text{Gd}$ for the first time and improved the precisions for ^{156}Nd , ^{158}Pm , $^{162,163}\text{Eu}$, and ^{164}Tb . Neutron pairing in the very neutron-rich isotopes has been found to be weaker than predicted by the theoretical models commonly used in r -process calculations. The data do not support the existence of a subshell closure at $N = 100$. This is in agreement with the conclusions made in Refs. [47,48]. While the changes in the slopes of the S_{2n} values coincide with the observed changes in the $E(2^+)$ energies [45,49], they may also be due to the approaching maximum deformation in the midshell or reduced neutron pairing. Here, further spectroscopic studies would yield valuable information. The impact of the new mass values on the r -process abundance pattern in the rare-earth region has been investigated for two representative neutron-star merger trajectories. Changes of up to 24% and a smoothening of the abundance pattern has been observed for both scenarios. Furthermore, the calculated

abundances are now closer to the solar r -process abundances. The results of this work highlight the need for accurate mass values in the rare-earth region and provide valuable data to improve theoretical mass models needed for experimentally unreachable nuclei in the r process. This is increasingly important in the era of multimessenger observations from neutron-star mergers.

This work has been supported by the Academy of Finland under the Finnish Centre of Excellence Program (Nuclear and Accelerator Based Physics Research at JYFL) and by the National Science Foundation (NSF) Grants No. PHY-1419765 and No. PHY-1713857. A. K., D. A. N., and L. C. acknowledge the support from the Academy of Finland under Projects No. 275389, No. 284516, and No. 312544, and T. E. under Project No. 295207. M. R. M. carried out this work under the auspices of the National Nuclear Security Administration of the U.S. Department of Energy at Los Alamos National Laboratory under Contract No. DE-AC52-06NA25396. R. S.'s work is funded in part by the DOE Office of Science under Contract No. DE-SC0013039.

Note added in proof.—The rare-earth region has recently been studied also with the Canadian Penning Trap, see the following Letter [82].

* markus.k.vilen@student.jyu.fi

† jkelly27@nd.edu

- [1] E. M. Burbidge, G. R. Burbidge, W. A. Fowler, and F. Hoyle, *Rev. Mod. Phys.* **29**, 547 (1957).
- [2] A. Cameron, Chalk River Report No. CLR-41, Atomic Energy of Canada Limited, 1957.
- [3] M. Arnould, S. Goriely, and K. Takahashi, *Phys. Rep.* **450**, 97 (2007).
- [4] B. Pfeiffer, K.-L. Kratz, F.-K. Thielemann, and W. Walters, *Nucl. Phys.* **A693**, 282 (2001).
- [5] O. Sorlin and M.-G. Porquet, *Prog. Part. Nucl. Phys.* **61**, 602 (2008).
- [6] J. Erler, N. Birge, M. Kortelainen, W. Nazarewicz, E. Olsen, A. M. Perhac, and M. Stoitsov, *Nature (London)* **486**, 509 (2012).
- [7] D. Martin, A. Arcones, W. Nazarewicz, and E. Olsen, *Phys. Rev. Lett.* **116**, 121101 (2016).
- [8] A. Wallner, T. Faestermann, J. Feige, C. Feldstein, K. Knie, G. Korschinek, W. Kutschera, A. Ofan, M. Paul, F. Quinto, G. Rugel, and P. Steier, *Nat. Commun.* **6**, 5956 (2015).
- [9] A. P. Ji, A. Frebel, A. Chiti, and J. D. Simon, *Nature (London)* **531**, 610 (2016).
- [10] I. U. Roederer, M. Mateo, J. I. B. III, Y. Song, E. F. Bell, J. D. Crane, S. Loebman, D. L. Nidever, E. W. Olszewski, S. A. Shectman, I. B. Thompson, M. Valluri, and M. G. Walker, *Astron. J.* **151**, 82 (2016).
- [11] A. Arcones and F.-K. Thielemann, *J. Phys. G* **40**, 013201 (2013).
- [12] P. Mösta, C. D. Ott, D. Radice, L. F. Roberts, E. Schnetter, and R. Haas, *Nature (London)* **528**, 376 (2015).

- [13] J. M. Lattimer and D. N. Schramm, *Astrophys. J. Lett.* **192**, L145 (1974).
- [14] D. Argast, M. Samland, F.-K. Thielemann, and Y.-Z. Qian, *Astron. Astrophys.* **416**, 997 (2004).
- [15] C. Freiburghaus, S. Rosswog, and F.-K. Thielemann, *Astrophys. J. Lett.* **525**, L121 (1999).
- [16] S. Goriely, A. Bauswein, and H.-T. Janka, *Astrophys. J. Lett.* **738**, L32 (2011).
- [17] S. Goriely, J.-L. Sida, J.-F. Lemaître, S. Panebianco, N. Dubray, S. Hilaire, A. Bauswein, and H.-T. Janka, *Phys. Rev. Lett.* **111**, 242502 (2013).
- [18] F.-K. Thielemann, M. Eichler, I. Panov, and B. Wehmeyer, *Annu. Rev. Nucl. Part. Sci.* **67**, 253 (2017).
- [19] D. A. Coulter, R. J. Foley, C. D. Kilpatrick, M. R. Drout, A. L. Piro, B. J. Shappee, M. R. Siebert, J. D. Simon, N. Ulloa, D. Kasen, B. F. Madore, A. Murguía-Berthier, Y.-C. Pan, J. X. Prochaska, E. Ramirez-Ruiz, A. Rest, and C. Rojas-Bravo, *Science* **358**, 1556 (2017).
- [20] B. P. Abbott *et al.*, *Astrophys. J. Lett.* **848**, L12 (2017).
- [21] B. P. Abbott (LIGO Scientific Collaboration and Virgo Collaboration), *Phys. Rev. Lett.* **119**, 161101 (2017).
- [22] I. Arcavi, G. Hosseinzadeh, D. A. Howell, C. McCully, D. Poznanski, D. Kasen, J. Barnes, M. Zaltzman, S. Vasylyev, D. Maoz, and S. Valenti, *Nature* (London) (to be published).
- [23] M. M. Kasliwal, E. Nakar, L. P. Singer, D. L. Kaplan, D. O. Cook, A. Van Sistine, R. M. Lau, C. Fremling, O. Gottlieb, J. E. Jencson, S. M. Adams, U. Feindt, K. Hotokezaka, S. Ghosh, D. A. Perley, P.-C. Yu, T. Piran, J. R. Allison, G. C. Anupama, A. Balasubramanian *et al.*, *Science* **358**, 1559 (2017).
- [24] D. Kasen, B. Metzger, J. Barnes, E. Quataert, and E. Ramirez-Ruiz, *Nature* (London) (to be published).
- [25] N. R. Tanvir, A. J. Levan, C. González-Fernández, O. Korobkin, I. Mandel, S. Rosswog, J. Hjorth, P. D'Avanzo, A. S. Fruchter, C. L. Fryer, T. Kangas, B. Milvang-Jensen, S. Rosetti, D. Steeghs, R. T. Wollaeger, Z. Cano, C. M. Copperwheat, S. Covino, V. D'Elia, A. de Ugarte Postigo *et al.*, *Astrophys. J. Lett.* **848**, L27 (2017).
- [26] P. S. Cowperthwaite, E. Berger, V. A. Villar, B. D. Metzger, M. Nicholl, R. Chornock, P. K. Blanchard, W. Fong, R. Margutti, M. Soares-Santos, K. D. Alexander, S. Allam, J. Annis, D. Brout, D. A. Brown, R. E. Butler, H.-Y. Chen, H. T. Diehl, Z. Doctor, M. R. Drout *et al.*, *Astrophys. J. Lett.* **848**, L17 (2017).
- [27] A. Aprahamian, I. Bentley, M. Mumpower, and R. Surman, *AIP Adv.* **4**, 041101 (2014).
- [28] S. Brett, I. Bentley, N. Paul, R. Surman, and A. Aprahamian, *Eur. Phys. J. A* **48**, 184 (2012).
- [29] M. Mumpower, R. Surman, G. McLaughlin, and A. Aprahamian, *Prog. Part. Nucl. Phys.* **86**, 86 (2016).
- [30] M. R. Mumpower, G. C. McLaughlin, R. Surman, and A. W. Steiner, *J. Phys. G* **44**, 034003 (2017).
- [31] M. R. Mumpower, R. Surman, D.-L. Fang, M. Beard, P. Möller, T. Kawano, and A. Aprahamian, *Phys. Rev. C* **92**, 035807 (2015).
- [32] M. Mumpower, R. Surman, D. L. Fang, M. Beard, and A. Aprahamian, *J. Phys. G* **42**, 034027 (2015).
- [33] P. Möller, A. Sierk, T. Ichikawa, and H. Sagawa, *At. Data Nucl. Data Tables* **109–110**, 1 (2016).
- [34] S. Goriely, N. Chamel, and J. M. Pearson, *Phys. Rev. C* **88**, 024308 (2013).
- [35] J. Duflo and A. P. Zuker, *Phys. Rev. C* **52**, R23 (1995).
- [36] R. Surman, J. Engel, J. R. Bennett, and B. S. Meyer, *Phys. Rev. Lett.* **79**, 1809 (1997).
- [37] M. R. Mumpower, G. C. McLaughlin, and R. Surman, *Phys. Rev. C* **85**, 045801 (2012).
- [38] J. Beun, G. C. McLaughlin, R. Surman, and W. R. Hix, *Phys. Rev. C* **77**, 035804 (2008).
- [39] K. Lodders, H. Palme, and H.-P. Gail, *Abundances of the Elements in the Solar System: Data sheet from Landolt-Börnstein Group VI Astronomy and Astrophysics*, Springer Materials Vol. 4B (Springer, New York, 2009).
- [40] P. Brix, *Z. Phys.* **132**, 579 (1952).
- [41] B. R. Mottelson and S. G. Nilsson, *Phys. Rev.* **99**, 1615 (1955).
- [42] R. F. Casten, D. D. Warner, D. S. Brenner, and R. L. Gill, *Phys. Rev. Lett.* **47**, 1433 (1981).
- [43] D. Bonatsos, S. Karampagia, R. B. Cakirli, R. F. Casten, K. Blaum, and L. A. Susam, *Phys. Rev. C* **88**, 054309 (2013).
- [44] R. Casten, *Nat. Phys.* **2**, 811 (2006).
- [45] E. F. Jones, J. H. Hamilton, P. M. Gore, A. V. Ramayya, J. K. Hwang, and A. P. de Lima, *Eur. Phys. J. A* **25**, 467 (2005).
- [46] S. K. Ghorui, B. B. Sahu, C. R. Praharaj, and S. K. Patra, *Phys. Rev. C* **85**, 064327 (2012).
- [47] J. Wu, S. Nishimura, G. Lorusso, P. Möller, E. Ideguchi, P.-H. Regan, G. S. Simpson, P.-A. Söderström, P. M. Walker, H. Watanabe, Z. Y. Xu, H. Baba, F. Browne, R. Daido, P. Doornenbal, Y. F. Fang, G. Gey, T. Isobe, P. S. Lee, J. J. Liu *et al.*, *Phys. Rev. Lett.* **118**, 072701 (2017).
- [48] R. Yokoyama, S. Go, D. Kameda, T. Kubo, N. Inabe, N. Fukuda, H. Takeda, H. Suzuki, K. Yoshida, K. Kusaka, K. Tanaka, Y. Yanagisawa, M. Ohtake, H. Sato, Y. Shimizu, H. Baba, M. Kurokawa, D. Nishimura, T. Ohnishi, N. Iwasa *et al.*, *Phys. Rev. C* **95**, 034313 (2017).
- [49] Z. Patel, P.-A. Söderström, Z. Podolyák, P. H. Regan, P. M. Walker, H. Watanabe, E. Ideguchi, G. S. Simpson, H. L. Liu, S. Nishimura, Q. Wu, F. R. Xu, F. Browne, P. Doornenbal, G. Lorusso, S. Rice, L. Sinclair, T. Sumikama, J. Wu, Z. Y. Xu *et al.*, *Phys. Rev. Lett.* **113**, 262502 (2014).
- [50] J. Van Schelt, D. Lascar, G. Savard, J. A. Clark, S. Caldwell, A. Chaudhuri, J. Fallis, J. P. Greene, A. F. Levand, G. Li, K. S. Sharma, M. G. Sternberg, T. Sun, and B. J. Zabransky, *Phys. Rev. C* **85**, 045805 (2012).
- [51] H. Hayashi, M. Shibata, M. Asai, A. Osa, T. Sato, M. Koizumi, A. Kimura, and M. Oshima, *Nucl. Instrum. Methods Phys. Res., Sect. A* **747**, 41 (2014).
- [52] J. Äystö, *Nucl. Phys.* **A693**, 477 (2001).
- [53] P. Karvonen, I. Moore, T. Sonoda, T. Kessler, H. Penttilä, K. Peräjärvi, P. Ronkanen, and J. Äystö, *Nucl. Instrum. Methods Phys. Res., Sect. B* **266**, 4794 (2008).
- [54] A. Nieminen, J. Huikari, A. Jokinen, J. Äystö, P. Campbell, and E. Cochrane, *Nucl. Instrum. Methods Phys. Res., Sect. A* **469**, 244 (2001).
- [55] T. Eronen, V. S. Kolhinen, V. V. Elomaa, D. Gorelov, U. Hager, J. Hakala, A. Jokinen, A. Kankainen, P. Karvonen,

- S. Kopecky, I. D. Moore, H. Penttilä, S. Rahaman, S. Rinta-Antila, J. Rissanen, A. Saastamoinen, J. Szerypo, C. Weber, and J. Äystö, *Eur. Phys. J. A* **48**, 46 (2012).
- [56] G. Savard, S. Becker, G. Bollen, H. J. Kluge, R. B. Moore, T. Otto, L. Schweikhard, H. Stolzenberg, and U. Wiess, *Phys. Lett. A* **158**, 247 (1991).
- [57] T. Eronen, V.-V. Elomaa, U. Hager, J. Hakala, A. Jokinen, A. Kankainen, S. Rahaman, J. Rissanen, C. Weber, and J. Äystö, *Nucl. Instrum. Methods Phys. Res., Sect. B* **266**, 4527 (2008).
- [58] G. Gräff, H. Kalinowsky, and J. Traut, *Z. Phys. A* **297**, 35 (1980).
- [59] M. König, G. Bollen, H. J. Kluge, T. Otto, and J. Szerypo, *Int. J. Mass Spectrom. Ion Process.* **142**, 95 (1995).
- [60] M. Kretzschmar, *Int. J. Mass Spectrom.* **264**, 122 (2007).
- [61] S. George, K. Blaum, F. Herfurth, A. Herlert, M. Kretzschmar, S. Nagy, S. Schwarz, L. Schweikhard, and C. Yazidjian, *Int. J. Mass Spectrom.* **264**, 110 (2007).
- [62] C. Weber, V.-V. Elomaa, R. Ferrer, C. Fröhlich, D. Ackermann, J. Äystö, G. Audi, L. Batist, K. Blaum, M. Block, A. Chaudhuri, M. Dworschak, S. Eliseev, T. Eronen, U. Hager, J. Hakala, F. Herfurth, F. P. Heßberger, S. Hofmann, A. Jokinen *et al.*, *Phys. Rev. C* **78**, 054310 (2008).
- [63] L. Canete, A. Kankainen, T. Eronen, D. Gorelov, J. Hakala, A. Jokinen, V. S. Kolhinen, J. Koponen, I. D. Moore, J. Reinikainen, and S. Rinta-Antila, *Eur. Phys. J. A* **52**, 124 (2016).
- [64] M. Wang, G. Audi, F. Kondev, W. Huang, S. Naimi, and X. Xu, *Chin. Phys. C* **41**, 030003 (2017).
- [65] M. Shibata, T. Shindou, K. Kawade, V. Kojima, A. Taniguchi, Y. Kawase, and S. Ichikawa, in *Exotic Nuclei and Atomic Masses. Proceedings of the Third International Conference on Exotic Nuclei and Atomic Masses ENAM 2001 Hämeenlinna, Finland, 2001*, edited by J. Äystö, P. Dendooven, A. Jokinen, and M. Leino (Springer-Verlag, Berlin, 2003), p. 479, ISBN 978-3-540-00101-0.
- [66] S. Gujrathi and J. D'auria, *Nucl. Phys.* **A172**, 353 (1971).
- [67] W. Huang, G. Audi, M. Wang, F. Kondev, S. Naimi, and X. Xu, *Chin. Phys. C* **41**, 030002 (2017).
- [68] D. Lunney, J. M. Pearson, and C. Thibault, *Rev. Mod. Phys.* **75**, 1021 (2003).
- [69] L. Satpathy and S. Patra, *Nucl. Phys.* **A722**, C24 (2003).
- [70] L. Satpathy and S. K. Patra, *J. Phys. G* **30**, 771 (2004).
- [71] N. Wang, M. Liu, X. Wu, and J. Meng, *Phys. Lett. B* **734**, 215 (2014).
- [72] M. Kortelainen, T. Lesinski, J. Moré, W. Nazarewicz, J. Sarich, N. Schunck, M. V. Stoitsov, and S. Wild, *Phys. Rev. C* **82**, 024313 (2010).
- [73] B. A. Brown, *Phys. Rev. Lett.* **111**, 162502 (2013).
- [74] W. Satuła, J. Dobaczewski, and W. Nazarewicz, *Phys. Rev. Lett.* **81**, 3599 (1998).
- [75] J. Hakala, J. Dobaczewski, D. Gorelov, T. Eronen, A. Jokinen, A. Kankainen, V. S. Kolhinen, M. Kortelainen, I. D. Moore, H. Penttilä, S. Rinta-Antila, J. Rissanen, A. Saastamoinen, V. Sonnenschein, and J. Äystö, *Phys. Rev. Lett.* **109**, 032501 (2012).
- [76] G. Audi, F. Kondev, M. Wang, W. Huang, and S. Naimi, *Chin. Phys. C* **41**, 030001 (2017).
- [77] P. Möller, B. Pfeiffer, and K.-L. Kratz, *Phys. Rev. C* **67**, 055802 (2003).
- [78] A. Koning and D. Rochman, *Nucl. Data Sheets* **113**, 2841 (2012), special issue on nuclear reaction data.
- [79] J. J. Mendoza-Temis, M.-R. Wu, K. Langanke, G. Martínez-Pinedo, A. Bauswein, and H.-T. Janka, *Phys. Rev. C* **92**, 055805 (2015).
- [80] B. S. Meyer, *Phys. Rev. Lett.* **89**, 231101 (2002).
- [81] O. Just, A. Bauswein, R. A. Pulpillo, S. Goriely, and H.-T. Janka, *Mon. Not. R. Astron. Soc.* **448**, 541 (2015).
- [82] R. Orford *et al.*, following Letter, *Phys. Rev. Lett.* **120**, 262702 (2018).



II

EXPLORING THE MASS SURFACE NEAR THE RARE-EARTH ABUNDANCE PEAK VIA PRECISION MASS MEASUREMENTS

by

M. Vilén, J.M. Kelly, A. Kankainen, M. Brodeur, A. Aprahamian, L. Canete, R. de Groot, A. de Roubin, T. Eronen, A. Jokinen, I.D. Moore, M.R. Mumpower, D.A. Nesterenko, J. O'Brien, A. Pardo Perdomo, H. Penttilä, M. Reponen, S. Rinta-Antila, R. Surman 2019

Submitted to Physical Review C

Exploring the mass surface near the rare-earth abundance peak via precision mass measurements at JYFLTRAP

M. Vilen,^{1,*} J.M. Kelly,^{2,†} A. Kankainen,¹ M. Brodeur,² A. Aprahamian,² L. Canete,¹ R. de Groot,¹ A. de Roubin,¹ T. Eronen,¹ A. Jokinen,¹ I.D. Moore,¹ M.R. Mumpower,³ D.A. Nesterenko,¹ J. O'Brien,¹ A. Pardo Perdomo,² H. Penttilä,¹ M. Reponen,¹ S. Rinta-Antila,¹ and R. Surman²

¹*University of Jyväskylä, P.O. Box 35, FI-40014 University of Jyväskylä, Finland*

²*University of Notre Dame, Notre Dame, Indiana 46556, USA*

³*Theory Division, Los Alamos National Lab, Los Alamos, New Mexico 87544, USA*

(Dated: September 4, 2019)

The JYFLTRAP double Penning trap at the Ion Guide Isotope Separator On-Line (IGISOL) facility has been used to measure the atomic masses of 13 neutron-rich rare-earth isotopes. Eight of the nuclides, ¹⁶¹Pm, ¹⁶³Sm, ^{164,165}Eu, ¹⁶⁷Gd, and ^{165,167,168}Tb, were measured for the first time. The systematics of the mass surface has been studied via one- and two-neutron separation energies as well as neutron pairing-gap and shell-gap energies. The proton-neutron pairing strength has also been investigated. The impact of the new mass values on the astrophysical rapid neutron capture process has been studied. The calculated abundance distribution results in a better agreement with the solar abundance pattern near the top of the rare-earth abundance peak at around $A \approx 165$.

PACS numbers: 21.10.Dr, 26.30.Hj, 27.70.+q

I. INTRODUCTION

The rare-earth region near $A = 165$ is of interest for both nuclear structure and nuclear astrophysics. With regards to nuclear structure, an onset of strong prolate deformation at $N = 88 - 90$ in these isotopic chains was discovered already in the 1950s [1, 2]. The rapid shape change can also be observed in the excitation energies of the first 2^+ and 4^+ states (see Fig. 1). The 2^+ excitation energies decrease strongly after $N = 88$, and $E(4^+)/E(2^+)$ ratios reach ≈ 3.3 , compatible with a rigid rotor. There are also indications of rapid nuclear shape transitions in Nd isotopes [3] as well as a possible sub-shell gap at $N = 100$ [4–7]. More recently, an unusual change in nuclear structure at $N = 98$ near europium has been identified [8], and interpreted as a deformed sub-shell gap.

Neutron-rich rare-earth isotopes play an important role in the astrophysical rapid neutron capture process, the r process [9–12]. The r process takes place at least in neutron-star mergers as evidenced by the binary neutron star event GW170817 [13, 14] in August 2017 and its afterglow known as a kilonova [15, 16]. During the observational period of a few days, the observed kilonova changed from blue to red. The latter color has been interpreted to be due to lanthanide-rich ejecta with high opacities, i.e. heavier ($A > 140$) r -process nuclides [15, 16]. To understand the produced abundances of lanthanides in different astrophysical conditions, masses of the involved nuclei have to be known for reliable calculations as they are one of the key inputs for the r process.

The r process produces rare-earth nuclei during its

freezeout stage when material is decaying back to stability [17, 18]. Nuclear deformation in the $A = 165$ region is essential in this process as it is reflected in nuclear binding energies and therefore in the behavior of neutron-separation energies. This will consequently affect the neutron-capture and beta-decay rates and steer the reaction flow toward the midshell, creating what is known as the rare-earth abundance peak at around $A = 165$ [17, 18]. Another mechanism producing rare-earth nuclei and its abundance peak in the r process is fission cycling from heavier nuclei [19].

The impact of individual nuclear masses on calculated r -process abundances can be quantified using a so-called F -factor, $F = 100 \sum_i |X(A) - X_b(A)|$, where $X_b(A)$ is the final isobaric mass fraction in the baseline simulation done with the experimental Atomic Mass Evaluation 2016 (AME16) [20] and theoretical FRDM12 [21] mass values, and $X(A)$ is the final isobaric mass fraction of the simulation when all nuclear inputs have been modified based on the change in a single mass in an r -process simulation [22, 23], done using a chosen astrophysical trajectory. Figure 2 shows the impact factors in the rare-earth region of interest.

The advent of new and upgraded radioactive ion beam facilities, such as CARIBU [27] and IGISOL-4 [28], has resulted in a resurgence of mass measurements aimed at characterizing the rare-earth abundance peak [8, 26, 29]. The Canadian Penning Trap (CPT) at CARIBU has measured masses of several Nd, Sm, Pm and Eu isotopes [8, 29, 30]. These masses agreed surprisingly well with the predictions of a reverse-engineering mass model [31] that uses the observed shape of the rare-earth abundance peak to predict masses near $A = 165$. At the new IGISOL-4 facility, the first measurement campaign on the masses of neutron-rich rare-earth isotopes with the JYFLTRAP double Penning trap [32] covered 12 rel-

* markus.k.vilen@student.jyu.fi

† jkelly27@alumni.nd.edu

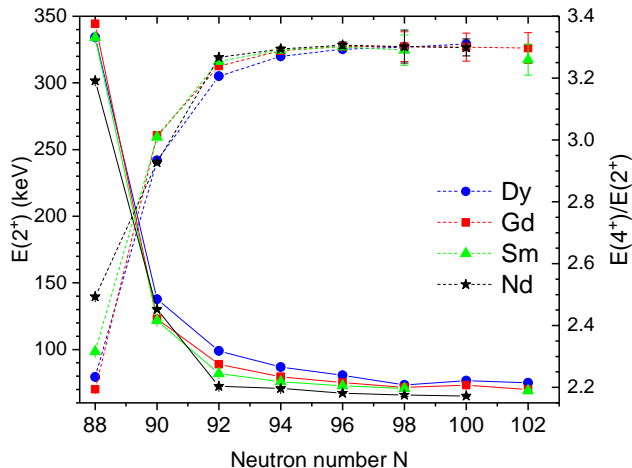


FIG. 1: Experimental excitation energies of the first 2^+ states (solid lines) together with the ratio of the first 4^+ and 2^+ states (dashed lines). The energies have been adopted from ENSDF [24] and [25].

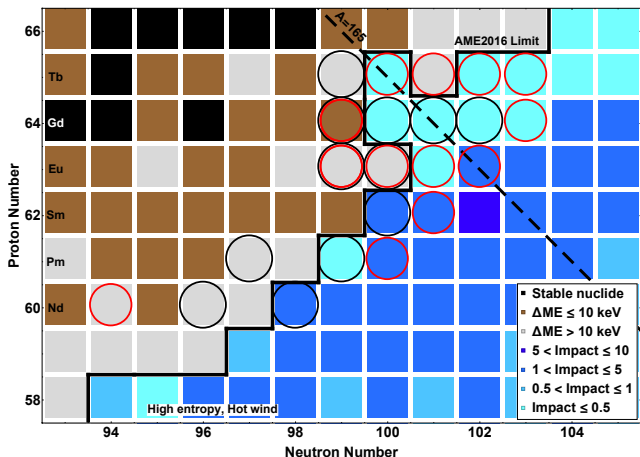


FIG. 2: The r -process impact factors F of masses in the region of interest [22]. Mass measurements from this work are circled in red, while black circles indicate those from an earlier study at JYFLTRAP [26]. In total, 22 ground-state masses and two isomeric states in this region have been measured at JYFLTRAP, of which 14 go beyond the limit of known nuclei in AME16 [20].

actively high-impact masses, 6 of which were measured for the first time [26]. The new JYFLTRAP measurements resulted in a smoothing of the calculated r -process abundance pattern making it closer to the observed solar pattern. After the successful first campaign at JYFLTRAP [26], a second campaign of mass measurements was launched aiming to better understand the formation of the rare-earth abundance peak in the r -process as well as the underlying changes in nuclear structure, in

particular beyond $N = 100$, which has been proposed as a subshell closure by Hartree-Fock calculations [5, 33, 34]. In this article, we report on the results of the second measurement campaign at JYFLTRAP and study the impact of JYFLTRAP measurements on the r process and nuclear structure in this neutron-rich rare-earth region.

II. EXPERIMENTAL METHOD

A. Production of neutron-rich rare-earth isotopes at IGISOL

The JYFLTRAP double Penning trap mass spectrometer [32] is located at the Ion-Guide Isotope Separator On-Line (IGISOL) facility [28, 35] in the JYFL Accelerator Laboratory of the University of Jyväskylä in Finland. The neutron-rich rare-earth nuclei of interest were produced through proton-induced fission on uranium at IGISOL, using 25 MeV, 10-15 μA proton beam from the K-130 cyclotron impinging into a 15 mg/cm² thick ^{nat}U target. This target is sufficiently thin to allow the energetic fission fragments to exit out of the target to the target chamber filled with helium at around 300 mbar, and pass through a nickel separation foil to the stopping and extraction volume of the IGISOL fission ion guide [36, 37]. The thermalized ions are then extracted out of the gas cell by employing a sextupole ion guide [38] and differential pumping. The extracted ion beam is subsequently accelerated to an energy of $30q\text{kV}$, where q is the charge of the ion, and non-isobaric contaminants are separated using a dipole magnet with a mass resolving power ($M/\Delta M$) of about 500. Finally, prior to the injection into JYFLTRAP, the ion beam is decelerated, accumulated, cooled and bunched using a segmented radio-frequency quadrupole ion trap [39].

B. Mass measurements with JYFLTRAP

1. JYFLTRAP double Penning trap mass spectrometer

The JYFLTRAP double Penning trap is comprised of two orthogonalized [40] cylindrical Penning traps located in the common bore of a 7 T superconducting solenoid [32, 41]. The first trap, known as the purification trap, is gas-filled and used to remove isobaric contaminants via the sideband cooling technique [42]. This technique alone can usually provide sufficient cleaning by mass-selectively converting ion motion from magnetron to reduced cyclotron motion. This leads to the centering of the ions in the trap after collisions with the buffer gas. Only the centered ions will be extracted through the 1.5 mm aperture separating the purification and the high-vacuum second trap known as the precision trap. When a sample demands higher resolving power for selecting the ions of interest, then the Ramsey cleaning technique [43] is employed following sideband cooling. Here, the

ions extracted through the aperture to the second trap undergo an additional cleaning step utilizing a dipolar excitation at the reduced cyclotron frequency (ν_+), which selectively increases the cyclotron radius. A subsequent transfer back to the first trap through the aperture leaves contaminants implanted on the diaphragm.

The ion's cyclotron frequency $\nu_c = qB/(2\pi M)$, where B is the magnetic field strength, q is the charge and M the mass of the ion, is determined in the second Penning trap. Conventionally, the time-of-flight ion-cyclotron-resonance (TOF-ICR) [44, 45] technique has been used to determine ν_c with either a single quadrupole excitation or the so-called Ramsey excitation [46, 47]. The latter is comprised of two short excitation pulses separated by a period without excitation. The method can result in a three-fold gain in precision. The TOF-ICR technique has been used exclusively for mass measurements at JYFLTRAP until 2018 when the newer phase-imaging ion-cyclotron-resonance (PI-ICR) technique [48] was successfully commissioned and implemented at JYFLTRAP [49]. The measurements using the two methods in this work are further described in the following subsections IIB 2 and IIB 3.

2. TOF-ICR measurements

In the TOF-ICR technique [44, 45], the ion's initial magnetron motion is converted into cyclotron motion by applying a quadrupole excitation pulse with a fixed duration and amplitude at a frequency around the expected cyclotron frequency. This results in a more-or-less complete conversion of the slow magnetron motion into the fast reduced cyclotron motion depending on the excitation frequency. At the resonance frequency, a maximum conversion is achieved resulting in an increase in the associated radial energy, observed as a much shorter time-of-flight of the ions from the precision trap onto a micro-channel plate (MCP) detector located after the trap.

The choice of employed excitation scheme depends on the half-life, production rates and possible presence of isomeric contamination. The higher-precision two-pulse Ramsey technique was applied when the production rate was sufficient. If the production rate was too low, the conventional one-excitation pulse (referred to as "quadrupolar") was used. Since a Ramsey excitation cannot easily resolve isomeric states, a long, 1600 ms quadrupolar excitation was used for two cases, ^{163}Gd and ^{162}Eu , for which isomeric states have previously been observed [50]. The length of the applied single-pulse quadrupolar excitation varied from 200 ms used for ^{154}Nd , ^{161}Pm , and ^{163}Sm , to 400 ms applied for ^{167}Gd , and 1600 ms for ^{162}Eu , ^{162m}Eu , and ^{163}Gd .

The remaining TOF-ICR measurements utilized the Ramsey method of time-separated oscillatory fields with two excitation pulses, each with a rectangular envelope. A TOF-ICR resonance for ^{165}Eu is presented in Fig. 3. $^{163,165}\text{Eu}$ used an On-Off-On pattern of

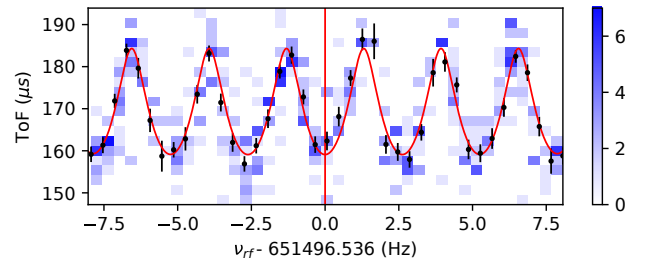


FIG. 3: Time-of-flight spectrum for $^{165}\text{Eu}^+$ using a 25 – 350 – 25 ms (On-Off-On) Ramsey-type excitation pattern. Background shading indicates the total number of ions, where darker shading indicates more ions. The red line is a fit of the lineshape to the data points (in black).

25 – 350 – 25 ms and ^{164}Eu and $^{165-168}\text{Tb}$ used a pattern of 25 – 750 – 25 ms.

3. PI-ICR measurements

In the PI-ICR method, determination of the cyclotron frequency relies on detecting the projections of the ion's radial motions in a trap onto a position-sensitive MCP detector with a delay-line anode. Measurements were performed using the second measurement scheme presented in [48]. In this scheme the cyclotron frequency is determined as a sum of magnetron and modified cyclotron frequencies, $\nu_c = \nu_- + \nu_+$, in such a way that the ion's position is recorded for only one phase (referred to as "phase spot") for each type of motion, in addition to measuring the center position. The cyclotron frequency was then determined using

$$\nu_c = \frac{\alpha + 2\pi(n_+ + n_-)}{2\pi t}, \quad (1)$$

where α is the angle between phase spots of modified cyclotron and magnetron motions, n_+ and n_- are the number of revolutions the ion completed in the precision trap during the respective motion and t is the phase accumulation time ions spent in the precision trap. In this work, the PI-ICR technique was used only for $^{162}\text{Eu}^+$ ions. A phase accumulation time of 600 ms was used for all measurements.

The measurement process was identical to TOF-ICR measurements until the ions were transferred into the precision trap. There, the residual coherent components of axial and radial eigenmotions with frequencies ν_z and ν_- were cooled using dipolar excitation pulses with suitable amplitude, phase and frequency. This was followed by an increase of reduced cyclotron eigenmotion amplitude via a dipolar excitation with the ν_+ frequency. Using the two timing patterns, as described in [48], the ions

were given time to accumulate a phase angle, either with frequency ν_+ or ν_- before being extracted from the precision trap with a non-zero magnetron motion amplitude. This process resulted in at least one spot on the position-sensitive MCP detector for each timing pattern. Additionally, the center of the precision trap was projected onto the detector for determination of the angle between measured spots resulting from the used two timing patterns. In the case of ^{162}Eu , both the ground state and the isomer were injected into the precision trap simultaneously. The two states were distinguished by allowing a sufficiently long phase accumulation time to pass so that the two states produced separate ν_+ spots on the detector. The two states are presented in Fig. 4.

Spot positions on the MCP were averaged over any residual radial eigenmotion after the initial magnetron cooling in the precision trap and following the conversion from reduced cyclotron motion into magnetron motion before extraction of ions onto the detector. This was achieved via scanning the timing pattern over the period of the relevant eigenmotion such that an equal amount of data was gathered with all steps of the scans. Data resulting from this two-dimensional scan was then used in further analysis. This process is highly beneficial since it enables the measurement and data analysis to be performed without a need to do any scanning or fitting, with the exception of unavoidable extrapolation during count rate analysis. The measurement process merely averages results in accounting for residual eigenmotions.

C. Production of stable reference ions

Both the TOF-ICR and PI-ICR methods rely on measuring well-known reference ions before and after the ion of interest in order to calibrate the magnetic field strength. This is done by interpolating the measured reference-ion cyclotron frequencies to the time of the ion-of-interest measurement.

In this work, singly-charged ^{136}Xe and ^{133}Cs ions were used as references. ^{136}Xe was used as a reference for most of the studied nuclides, since its mass is well-known and it is readily available as a fission fragment from IGISOL. However, obtaining the reference as a by-product of fission entails a risk of misidentifying it for another species or molecule with nearly equal mass. In order to eliminate this risk, an offline ion source station [51], completely separate from the IGISOL target chamber, was later added to the beam line. The stable $^{133}\text{Cs}^+$ reference ions were produced at this offline station.

The new off-line ion source station [51] consists of multiple ion sources and a beamline that connects to the existing IGISOL beamline just before the IGISOL dipole magnet. A deflector allows for rapid switching between the off-line ion beams and the radioactive ion beams from the IGISOL target chamber. In this work, a thermal emission alkali metal ion source consisting of ^{39}K , ^{85}Rb , ^{87}Rb , and ^{133}Cs was used. Thanks to the IGISOL dipole

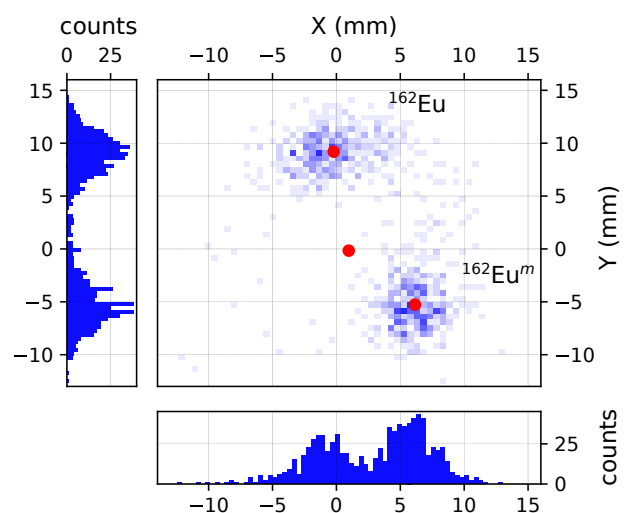


FIG. 4: Projection of cyclotron motion of $^{162}\text{Eu}^+$ ions on the position-sensitive detector using the PI-ICR technique. Two detected ion spots correspond to the ground and isomeric state of ^{162}Eu . In the middle figure background shading indicates the total number of ions, where darker shading indicates more ions. Center point of the two states and the center of the precision trap are marked as red dots. Figures on the left and bottom present projections of the middle figure onto the Y and X axes, respectively.

magnet mass separator, pure beams of $^{133}\text{Cs}^+$ ions were guaranteed.

III. ANALYSIS

A. Determination of the atomic masses

Atomic masses of the measured isotopes were determined using

$$m = \bar{r} \cdot (m_{ref} - m_e) + m_e, \quad (2)$$

where \bar{r} is the weighted mean of the frequency ratios between the reference and the ion of interest ($r = \nu_{c,ref}/\nu_c$), m_{ref} is the atomic mass of the reference ion, and m_e is the mass of the electron. The electron binding energies, all in the eV range, are several orders of magnitude smaller than the statistical uncertainty of the measurements, and can therefore be neglected.

Multiple frequency ratios r were measured. The weighted mean of the frequency ratio \bar{r} was determined together with its internal and external uncertainties. An example is shown for $^{165}\text{Tb}^+$ ions in Fig. 5. Following the procedure of the Particle Data Group [52], the statistical uncertainty of any \bar{r} has been inflated by the ratio of the

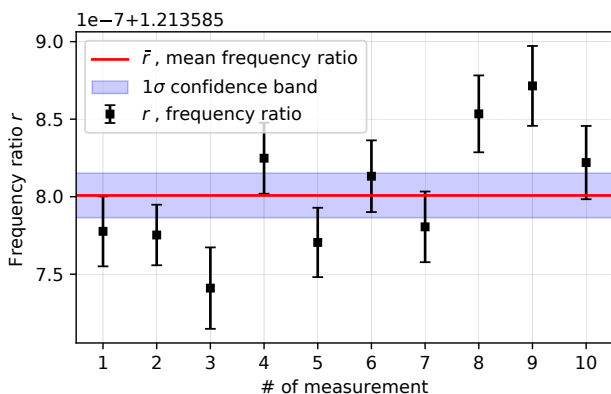


FIG. 5: (Color online) Measured frequency ratios $r = \nu_c(^{136}\text{Xe}^+)/\nu_c(^{165}\text{Tb}^+)$ for ^{165}Tb (black data points) together with the weighted mean (solid red line) and its error band (dashed blue lines). The Birge ratio for ^{165}Tb measurements was 1.05.

external-to-internal uncertainty (so-called Birge ratio) if its value is greater than one. This practice ensures that possible systematic effects bringing the Birge ratio above the statistically-expected value of one are taken into account. Systematic uncertainties were taken into account and added quadratically to the measured frequency ratios as described in the following section, Sect. III B.

B. Systematic uncertainties

1. Uncertainties due to geometry and B field fluctuations

Multiple systematic effects can be present in Penning-trap measurements. These can be due to e.g. misalignment of the trap with respect to the magnetic field, inhomogeneous magnetic field, harmonic and non-harmonic distortion of the trapping potential, and other unavoidable geometric irregularities [53]. The above effects can cause a so-called mass-dependent systematic error on the frequency ratio that ultimately leads to cyclotron frequency determinations away from the expected $\nu_c \propto 1/m$ relationship. At JYFLTRAP, the mass-dependent error has been determined to be equal to $(2.2 \times 10^{-10}/u) \times \Delta m$ [26], where Δm is the mass difference between the ion of interest and the reference ion. This leads to uncertainties of less than 1 keV for $\Delta m \approx 30 u$ in the studied mass region. Another sub-keV systematic error is due to relativistic effects [54], which are minimal for heavier nuclei such as the ones measured in this work. The mass-dependent uncertainties were added in quadrature to the final frequency ratio uncertainty.

An additional systematic effect lies in non-linear temporal fluctuations of the magnetic field on top of its slow linear drift over time. This means that even the

very shortest linear interpolations between successive reference measurements to determine the magnetic field strength at the time of the interposed ion-of-interest measurement are subject to an error. For JYFLTRAP, these uncertainties have been measured to be $8.18(19) \times 10^{-12} \text{ min}^{-1} \times \Delta t$ [55], where Δt is the time between consecutive reference measurements. The effect of these fluctuations on the measured frequencies is, however, negligible over the typical time spans between successive reference measurements for this work.

2. Uncertainties due to ion-ion interactions

The ions are injected into the precision Penning trap as bunches containing typically a few ions. One of the main effects that has to be considered in the data analysis is the ion-ion interactions when multiple ions are simultaneously trapped [56]. The effect is especially significant if more than one ion species are trapped but it can also be present when trapping multiple ions of a single species. Most of the measured isotopes had insufficient ion count rates to correct the result for the effect of having multiple ions in the trap. All data measured with the TOF-ICR technique were limited to 1-3 ions per bunch in the analysis phase, and processed without taking the ion-ion interactions into account. An additional systematic uncertainty was added to all obtained frequency ratios to account for any possible ion-ion interactions.

The magnitude of the correction due to ion-ion interactions was determined by analyzing the ^{165}Tb dataset both with and without taking the ion-ion interactions into account. The ion-ion interaction effects were studied by dividing the data into classes of one, two or three detected ions per bunch. The three classes were analyzed separately and the number of ions in each class was corrected with the detection efficiency. The resulting ν_c frequencies were then extrapolated to the ideal case with only one ion in the trap. A weighted mean was calculated and the larger of the internal and external uncertainties was chosen as the error of the mean. The comparison between the results obtained with and without the count-rate class analysis for the data limited to 1-3 ions per bunch, yielded a small shift of $\delta r/r = (2.2 \pm 3.0) \cdot 10^{-8}$ between the results. Since the shift is compatible with zero within 1σ , we also report the values without this additional systematic contribution in Table I. The additional systematic uncertainty due to the ion-ion interactions was added quadratically to all TOF-ICR results, and is included in the total uncertainty δr_{tot} given in Table I. In the case of PI-ICR measurements, the ion count rate was sufficient to take the ion-ion interactions into account. There, the presence of different ion species (ground and isomeric states) simultaneously in the trap turned out to produce a clear shift in the results.

A detailed characterization of the efficiency of the position sensitive MCP detector and related data acquisition system was conducted in order to minimize any resid-

ual systematic uncertainties in the count-rate class analysis. The MCP detector was found to suffer from gradually decreasing efficiency with higher number of ions per bunch. An assumption of a linear relationship between the efficiency-corrected number of ions per bunch and the extrapolated quantity, cyclotron frequency ν_c , or spot position, was assumed as in Ref. [57]. The use of higher order polynomials or other functions with a larger number of fitted parameters was considered, but had to be rejected due to the lack of data with large numbers of ions per bunch. More details on the systematic uncertainties and determination of the detection efficiency can be found on Ref. [58].

IV. RESULTS

A. Mass-excess values

The results of this work are summarized in Table I and Fig. 6. Altogether 13 different nuclides were measured, of which eight were measured for the first time (see Fig. 2). In addition, isomeric states in ^{162}Eu and ^{163}Gd were studied. In the following, the eight nuclides measured for the first time are discussed initially. This is followed by a nuclide-by-nuclide discussion for the other measured nuclides.

Nuclides measured for the first time:
 ^{161}Pm , ^{163}Sm , $^{164,165}\text{Eu}$, ^{167}Gd , $^{165,167,168}\text{Tb}$

The mass-excess values for eight studied nuclides, ^{161}Pm , ^{163}Sm , $^{164,165}\text{Eu}$, ^{167}Gd , $^{165,167,168}\text{Tb}$, were measured for the first time. The measurements were done with the following excitation patterns in the precision trap: ^{161}Pm (200 ms), ^{163}Sm (200 ms), ^{164}Eu (25 – 750 – 25 ms On-Off-On), ^{165}Eu (25 – 350 – 25 ms On-Off-On), ^{167}Gd (400 ms), and $^{165-168}\text{Tb}$ (25 – 750 – 25 ms On-Off-On). All new mass-excess values agree within 1.5σ with the extrapolated value from AME16 [20]. The largest deviations to AME16 extrapolation occur for the lightest studied nuclides, ^{161}Pm , ^{163}Sm and ^{164}Eu , all being around 150 keV higher than the AME16 extrapolation (see Fig. 6).

^{154}Nd

The determined mass-excess value of ^{154}Nd , $-65601(25)$ keV, is based on three consistent individual frequency ratios measured with 200 ms quadrupolar excitation in the precision trap. In AME16, the mass of ^{154}Nd is based on beta-decay end-point energies of ^{154}Nd [60] and ^{154}Pm [61–63] connecting the isobaric chain to ^{154}Sm for which the mass has been directly measured [64]. The mass-excess value obtained in this work for ^{154}Nd is 225 keV higher than the AME16

value [20]. This is understandable since the beta-decay studies often suffer from the pandemonium effect [65]. It means that transitions from higher-lying states have been missed, leading to too low beta-decay Q -values. More recently, CPT has also measured ^{154}Nd [29]. The JYFLTRAP value agrees well with this recent Penning-trap measurement (see Fig. 6).

$^{162,162m}\text{Eu}$

^{162}Eu was measured already in the first JYFLTRAP campaign on neutron-rich rare-earth nuclides [26]. The measurement done with the TOF-ICR method using a Ramsey excitation pattern 25 – 350 – 25 ms (On-Off-On) resulted in a mass-excess value of $-58658(4)$ keV [26]. Around the same time, the CPT measured ^{162}Eu using the PI-ICR method [8]. They discovered an isomeric state at 160.2(24) keV above the ground state for which a mass-excess of $-58723.9(15)$ keV was determined [8]. The JYFLTRAP mass-excess value for the measured state was around 60 keV above the ground state and 100 keV below the isomer determined at CPT, implying that a mixture of states had been measured at JYFLTRAP. Hence, a remeasurement was performed in this work. It was done both with the TOF-ICR and PI-ICR techniques. For the TOF-ICR measurements, a long, 1600 ms quadrupolar excitation sufficient to separate the two states, was employed. Figure 7 shows TOF-ICR spectra for ^{162}Eu from the first JYFLTRAP campaign [26] and from this work. Clearly, the first JYFLTRAP campaign could not have easily identified the isomeric state, unknown at the time, due to the shorter excitation time (leading to worse resolution) and the used Ramsey pattern with several strong minima.

The PI-ICR measurements of ^{162}Eu and $^{162}\text{Eu}^m$ were performed as described in Sect. II B 3 with a 600-ms phase accumulation time. As can be seen from Fig. 4, abundances of the two states were similar, with 53.5(1.8)% of the detected ions being in the ground state. This supports the fact that a mixture of states was measured during the first JYFLTRAP campaign. The new TOF-ICR and PI-ICR results for the ground and isomeric state of ^{162}Eu (see Table II) are now consistent, confirming that the recently commissioned PI-ICR method works at JYFLTRAP. Both the ground-state and isomeric-state values agree with the CPT results, and with the AME16 value based on a beta-decay study [50]. The excitation energy obtained for the isomer at JYFLTRAP is 156.0(2.8) keV which is somewhat lower than obtained at CPT.

The weighted means presented in Table II were calculated between the two measurement techniques. Internal and external uncertainties were calculated and the larger one was accepted as the uncertainty of the mean. In the case of $^{162}\text{Eu}^m$, the larger error of the two individual results was adopted to account for the difference in results between the techniques.

TABLE I: Frequency ratios ($r = \nu_{c,ref}/\nu_c$) based on N_{meas} measurements together with the mass-excess values (ME) determined in this work. For the JYFLTRAP values, the uncertainties for r and ME are given both without and with the added systematic uncertainty due to ion-ion interactions, see Sect. III B 2. Comparison to AME16 [20] is given, and a # sign indicates extrapolated values therein. The isomeric-state mass values were adopted from NUBASE16 [59]. All measurements were done with singly-charged ions. The masses for the reference ions $^{136}\text{Xe}^+$ and $^{133}\text{Cs}^+$ were adopted from AME16 [20]. For comparison, the recent CPT measurements are also tabulated.

Isotope	Reference	N_{meas}	r	$ME(\text{keV})$			
				JYFL	AME16	ΔME^a	CPT
^{154}Nd	^{133}Cs	3	1.158 189 215(201)(203)	-65601.2(24.9)(25.1)	-65825(53)	224(59)	-65579.6(1.0)[29]
^{161}Pm	^{136}Xe	5	1.184 236 679(468)(468)	-50107.6(59.2)(59.3)	-50235(298)#	127(304)#	N/A
^{163}Sm	^{136}Xe	4	1.198 949 148(285)(286)	-50552.3(36.0)(36.2)	-50720(298)#	168(301)#	-50599.6(7.3)[29]
$^{162}\text{Eu}^b$	N/A ^b	5	N/A ^b	-58720.4(3.1) ^b	-58703(35)	-14(36)	-58723.9(1.5)[8]
$^{162}\text{Eu}^{mb}$	^{133}Cs	5	1.218 439 459(13) ^b	-58565.7(7.6) ^b	-58540(40)	-20(50)	-58563.7(1.9)[8]
^{163}Eu	^{133}Cs	5	1.225 979 710(14)(30)	-56575.7(1.8)(3.8)	-56485(66)	-91(66)	N/A
^{164}Eu	^{136}Xe	4	1.206 285 979(12)(29)	-53231.1(1.6)(3.7)	-53381(114)#	150(115)#	N/A
^{165}Eu	^{136}Xe	3	1.213 663 750(39)(48)	-50726.9(5.0)(6.0)	-50724(138)#	-3(139)#	N/A
^{163}Gd	^{136}Xe	5	1.198 863 600(76)(81)	-61382.4(9.6)(10.2)	-61314(8)	-68(14)	-61316.0(15.0)[30]
$^{163}\text{Gd}^m$	^{136}Xe	5	1.198 864 872(102)(106)	-61221.3(13.0)(13.4)	-61176(8)	-45(16)	N/A
^{167}Gd	^{136}Xe	5	1.228 379 286(93)(97)	-50783.4(11.8)(12.3)	-50813(298)#	30(299)#	N/A
^{165}Tb	^{136}Xe	10	1.213 585 800(15)(31)	-60595.1(2.0)(3.9)	-60566(102)#	-29(103)#	N/A
^{166}Tb	^{136}Xe	6	1.220 965 810(11)(30)	-57807.6(1.6)(3.7)	-57885(70)	77(71)	N/A
^{167}Tb	^{136}Xe	5	1.228 338 998(13)(30)	-55883.7(1.7)(3.8)	-55927(196)#	43(197)#	N/A
^{168}Tb	^{136}Xe	5	1.235 721 496(17)(33)	-52781.2(2.3)(4.1)	-52723(298)#	-58(299)#	N/A

^a JYFL – AME16

^b Measured using both TOF-ICR and PI-ICR techniques, see Table II.

TABLE II: Frequency ratios (r) and mass-excess values (ME) determined in this work for ^{162}Eu and $^{162}\text{Eu}^m$ with the PI-ICR and TOF-ICR measurement techniques. The excitation energy E_x for the isomer is also given. The reference mass values were adopted from AME16 [20].

Isotope	Reference	Method	$r(\delta r_{stat})(\delta r_{tot})$	$ME(\delta ME_{tot})(\text{keV})$	E_x (keV)
^{162}Eu	^{162m}Eu	PI-ICR	0.999 998 966(19)	-58721.8(3.7)	155.9(3.0)
		TOF-ICR	1.218 438 235(35)(45)	-58717.2(4.4)(5.5)	N/A
	Weighted mean	Difference	N/A	-4.7(6.6)	N/A
		Weighted mean	N/A	-58720.4(3.1)	N/A
^{162m}Eu	^{133}Cs	PI-ICR	1.218 439 457(18)	-58566.0(2.2)	N/A
		TOF-ICR	1.218 439 502(55)(61)	-58560.3(6.8)(7.6)	156.8(9.4)
	Weighted mean	Difference	-0.000 000 045(63)	-5.6(7.9)	0.9(9.8)
		Weighted mean	1.218 439 459(61)	-58565.7(7.6)	156.0(2.8)

$^{163,163m}\text{Gd}$, and ^{163}Eu

Both ^{163}Gd and ^{163}Eu were measured already in the previous campaign at JYFLTRAP [26]. There, Ramsey excitation with a pattern 25 – 350 – 25 ms (On-Off-On) was used together with a reference from the same isobaric mass chain, ^{163}Dy . The resulting ^{163}Gd mass-excess value was $-61200(4)$ keV. Surprisingly, this deviated from the AME16 value, based on a CPT measurement [30], by 114(9) keV. Since the difference was very close to the first isomeric state energy, 137.8 keV [50], it was suggested that JYFLTRAP had measured the isomer, which could be predominantly populated in the proton-induced fission of ^{238}U used at IGISOL. The

spontaneous fission of ^{252}Cf used for the production at CPT could, in turn, populate predominantly the ground state.

To confirm whether an isomeric state had been measured in [26], ^{163}Gd was remeasured at JYFLTRAP using the TOF-ICR technique with a long, 1600 ms quadrupolar excitation, which is sufficient to separate the two states. In addition, a more accurate reference, ^{136}Xe , was used. A total of five consistent frequency ratio measurements were done, yielding a ground-state mass-excess of $-61382.4(10.2)$ keV, and an excitation energy of 161(17) keV for the isomer. The new value still disagrees with the CPT value ($-61316.0(15.0)$ [30]) and is not consistent with the excitation energy (137.8 keV) from [50].

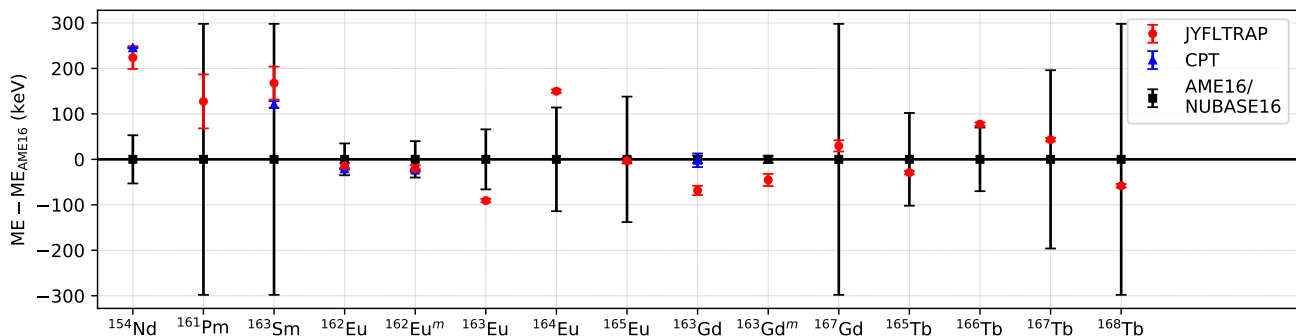


FIG. 6: (Color online) Comparison to AME16 mass-excess values for each measured nuclide. The results from CPT [8, 29, 30] are also shown. The values for the isomeric states were adopted from NUBASE16 [59].

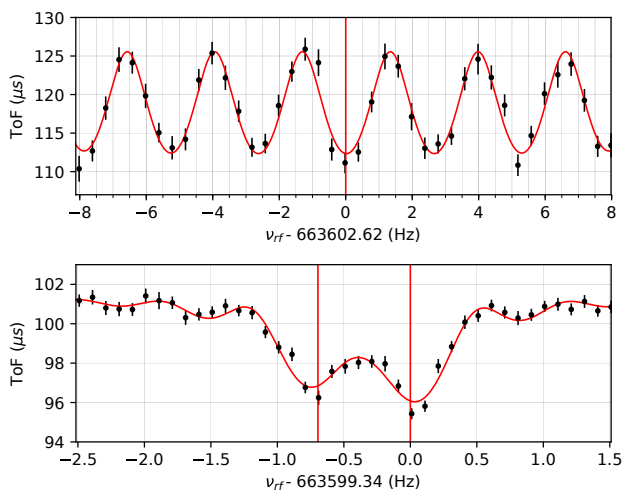


FIG. 7: (Color online) Time-of-flight spectra for $^{162}\text{Eu}^+$ from campaign I using 25 – 350 – 25 ms (On-Off-On) excitation pattern (top), and from this work with a 1600 ms excitation (bottom). Fitted theoretical line shapes and ν_c frequencies are plotted in red.

Counter to the hypothesis, the re-measurement showed that the ground state was dominant. Based on a PI-ICR yield measurement of ^{163}Gd , the yield ratio was 72.5(5.0)% for the ground state at the MCP detector. Hence, the first ^{163}Gd measurement at JYFLTRAP should have produced a mass-excess value close to the ground-state value obtained in the re-measurement. The 180 keV difference between the two ^{163}Gd measurements casts doubt on the reference used in the first measurement, ^{163}Dy . This reference was chosen at the time because the mass-excess value of ^{163}Dy is well known, with a precision of 0.8 keV [20], based on a recent Penning-trap measurement at TRIGA-TRAP [66]. Using a refer-

ence from the same isobaric mass chain is also preferential since it cancels out any mass-dependent uncertainties. Since the ^{163}Eu measurement from [26] had used the same reference, it was decided to remeasure also ^{163}Eu , this time with an unambiguous reference, $^{133}\text{Cs}^+$, from the off-line ion source station. A total of five consistent frequency ratios with a Ramsey excitation pattern of 25 – 350 – 25 ms (On-Off-On) were performed, resulting in a mass-excess value of $-56575.7(3.8)$ keV. This differs by 156 keV from the previous value, $-56420(4)$ keV, reported in [26]. The similar systematic shift as for the remeasured ^{163}Gd confirms the suspicion that the ^{163}Dy reference had been wrongly identified.

In order to correctly identify the $A = 163$ reference ion used in the first campaign [26], we used the software SCM_Qt (Search for Contaminant Masses) [67] which lists all possible molecular combinations of a specified list of elements and maximum number of atoms of those elements that would yield the same frequency ratio. For the calculations, we used the average cyclotron frequency of $^{171}\text{Yb}^+$ (628665.80 Hz) as a reference since it was the closest reference measurement before the use of the to-be-identified $A = 163$ ion (659564.18 Hz). We allowed SCM to form molecules of up to three different elements and up to 10 atoms of the same elements chosen from H, C, O, N, and fission products. We also only kept the isotopes with a half-life greater than 100 ms. As a result, the closest reasonable candidate found was $^{146}\text{La}^{16}\text{O}^1\text{H}^+$. ^{146}La is produced with a large cross section in proton-induced fission, with an estimated rate of around 6.5×10^4 particles/s.

When using $^{146}\text{La}^{16}\text{O}^1\text{H}^+$ as reference for the initial measurement of ^{163}Eu [26], we obtain a mass-excess value of $-56539(37)$ keV. Most of the uncertainty stems from the 30 keV uncertainty in the mass excess of ^{146}La , which is based on a Penning-trap measurement at CPT [68] and several β -decay end-point energy measurements [20]. This result is within one standard deviation from the new measurement presented in Table I.

Similarly, using $^{146}\text{La}^{16}\text{O}^1\text{H}^+$ as a reference for the

initial measurement of ^{163}Gd [26], we obtain a mass-excess value of $-61319(37)$ keV, which is 1.7σ higher than the new measurement presented in Table I. Such a discrepancy is not unexpected, since the initial measurement from [26] was performed using a Ramsey pattern $25 - 350 - 25$ ms (On-Off-On), which is not sufficient to distinguish between the ground and isomeric states. As such, the measured mixture of states in [26] is expected to produce a value in between the two states as in the case of ^{162}Eu . The CPT measurement from [30], which was done with a too short excitation time (500 ms) to resolve the two states, yields a similar mass-excess value of $-61316(15)$ keV. It should also be noted that the frequency difference between $^{146}\text{La}^{16}\text{O}^1\text{H}^+$ and $^{163}\text{Dy}^+$ is less than 1 Hz in JYFLTRAP, and hence, those cannot be resolved in the purification trap and would have been difficult to identify with the used Ramsey-type excitation in the precision trap. Therefore, it is possible that the reference was a mixture of $^{146}\text{La}^{16}\text{O}^1\text{H}^+$ and $^{163}\text{Dy}^+$.

^{166}Tb

The mass of ^{166}Tb was determined based on six individual frequency ratio measurements done with a Ramsey excitation pattern $25 - 750 - 25$ ms (On-Off-On). The resulting mass-excess value is $77(71)$ keV above the AME16 value stemming from a β -decay endpoint energy measurement [69]. The precision of the mass-excess value was improved by a factor of almost 20.

V. IMPACT ON THE MASS SURFACE AND ITS DERIVATIVES

By plotting atomic masses as a function of neutron (N) and proton (Z) numbers, a surface in a three-dimensional space is obtained. If we neglect the pairing effect, i.e. by selecting only even-even, odd-odd, odd-even or even-odd nuclei, the surface is rather regular and smooth. Sudden changes or irregularities on the surface can be caused e.g. by shell closures at magic nucleon numbers or changes in the shape of the ground state. To reveal possible changes in nuclear structure and interactions, it is very useful to study different derivatives of the mass surface, such as one- and two-neutron separation energies (S_n and S_{2n}), neutron pairing gap energies D_n , two-neutron shell gap energies D_{2n} , and proton-neutron pairing strength metrics δV_{pn} . In the following sections, the data presented in Table I were used to study these mass derivatives. Each of the studied quantities is sensitive to some aspect of nuclear structure and offers valuable feedback for theoretical mass models needed e.g. for the unknown neutron-rich nuclei in the abundance calculations of the r process.

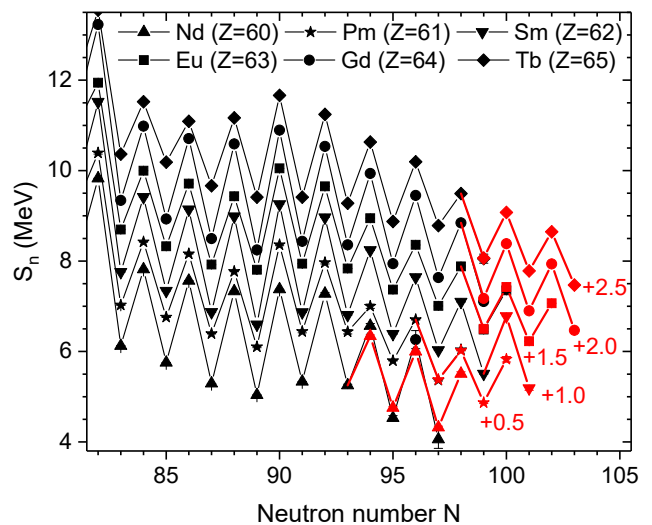


FIG. 8: Experimental neutron separation energies, S_n , from AME16 [20] (in black), and supplemented with the JYFLTRAP results from [26] and this work (in red). Each isotopic chain has been shifted by 0.5 MeV relative to the previous chain for clarity, with the Nd chain remaining unchanged.

A. Neutron separation energies

Neutron separation energies are one of the most influential inputs needed for the r -process modeling, and indeed the primary means by which mass measurements influence the calculated rare-earth abundances in the r process. The neutron separation energy, S_n , is determined as

$$S_n(Z, N) = [m(Z, N - 1) + m_n - m(Z, N)]c^2, \quad (3)$$

where m denotes the masses for the nuclides (Z, N) , $(Z, N - 1)$ and the neutron, and c is the speed of light in vacuum. The neutron separation energy appears directly in neutron-capture rates, which for radioactive nuclides of the type presented, are largely unmeasured, and therefore must be calculated via statistical models [22]. It also appears exponentially in photo-dissociation rates, which are perhaps the most important factors shaping the r -process path, highlighting the direct impact mass measurements have on r -process calculations.

Figure 8 shows the experimental neutron separation energies for isotopic chains from the element neodymium ($Z = 60$) to terbium ($Z = 65$) in the region involving our new measurements. When comparing to AME16 [20], the new S_n values do not immediately reveal any radical changes to the previously known trends. However, the new neodymium measurements supplant four existing, successive literature values from $N = 94$ to $N = 97$, and a notable reduction in odd-even staggering is clearly seen. Similarly to the high precision measurements of Nd,

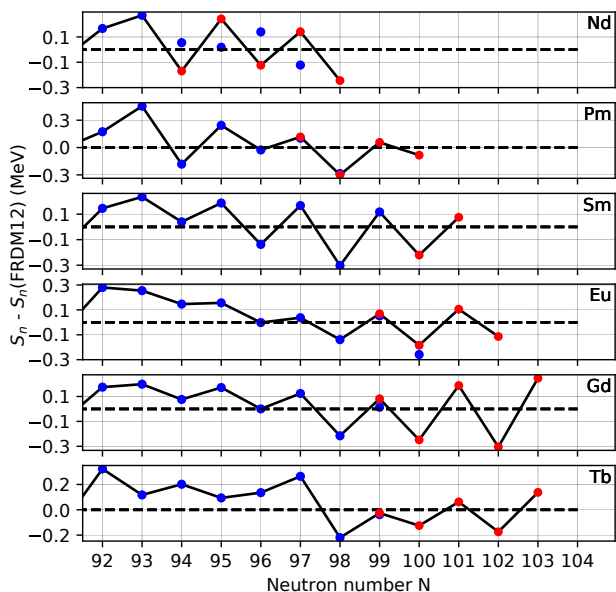


FIG. 9: Experimental neutron separation energies S_n compared to the FRDM12 mass model. The S_n values affected by the JYFLTRAP measurements of this work and [26] are shown in red and AME16 values in blue. Dashed line indicates energies from FRDM12.

TABLE III: Root mean square errors, δ_{RMS} (see Equation 4), between the measured and theoretical S_n values, as well as the over-prediction of the neutron pairing gap, δD_n (see Equation 6) over $60 \leq Z \leq 65$ with $N \geq 94$.

Mass Model	δ_{RMS} (MeV)	δD_n (MeV)
HFB-24	0.356	26.9
FRDM12	0.168	11.2
Duflo-Zuker	0.141	6.5
WS3	0.186	13.9
WS3+	0.224	16.4
WS4	0.190	14.4
WS4+	0.222	16.8

which show a decrease in odd-even staggering relative to existing experimental data, there is also a tendency for the theoretical models to overestimate this effect. This is illustrated in Fig. 9 for FRDM12 [21]. The new experimental S_n values are higher (lower) than in FRDM12 for odd (even) N , decreasing the odd-even staggering for the most neutron-rich isotopes.

In addition to FRDM12 [21], experimental S_n values were compared to other theoretical mass models typically used in astrophysical r process calculations, including HFB24 [70], Duflo-Zuker [71], WS3 [72], WS3+ [73], WS4 [74], and WS4+ [74]. In order to facilitate the com-

parison, root-mean-square (RMS) errors were calculated for the models according to

$$\delta_{RMS} = \sqrt{\frac{1}{N_{tot}} \sum_{Z,N} (S_n(Z,N)_{th.} - S_n(Z,N)_{exp.})^2}, \quad (4)$$

where N_{tot} is the total number of isotopes in the chain, and the sum is over the differences between the theoretical (*th.*) and experimental (*exp.*) values of S_n across all isotopes of each chain, and Z and N are the proton and neutron numbers, respectively. Table III indicates that the calculated RMS errors range from 141 to 356 keV, with any given isotopic chain being within $\delta_{RMS} = 483$ keV from the JYFLTRAP values. Although the S_n values from FRDM12 deviated from the experimental values more than Duflo-Zuker in this mass region, FRDM12 still remains a benchmark against which to compare our measurements. As discussed in [31], this is because r -process simulations using FRDM12 yield isotopic abundances that more closely match the solar data in this region.

B. Neutron pairing gaps

The odd-even staggering of neutron separation energies is a strong signature of neutron pairing. The neutron pairing can be quantified in terms of the differences between the neutron separation energies S_n of successive isotopes:

$$D_n(Z, N) = (-1)^{N+1} [S_n(Z, N+1) - S_n(Z, N)]. \quad (5)$$

This neutron pairing energy metric [75] is twice the odd-even staggering parameter $\Delta_n(N)$, also commonly used to describe the pairing gap, see e.g. [76]. Figure 10 shows the D_n values for the various isotopic chains affected by our new atomic mass measurements. It presents several main features: first a large increase in pairing energy when the closed neutron shell at $N = 82$ is reached. After $N = 82$ there is a sharp drop followed by a gradual increase, peaking at $N = 89$, which corresponds to the well-known region with an onset of deformation. Finally, a steady decrease in the D_n values toward the neutron midshell at $N = 104$ is observed in the region covered by our measurements.

Previously, a sub-shell gap has been predicted at $N = 100$ [5, 33, 34]. With our new mass measurements going beyond the $N = 100$ closure (see Fig. 10), no unusual increase in the D_n values (as seen at $N = 82$) is present at $N = 100$, negating the presence of a sub-shell closure or onset of deformation (as seen at $N = 89$).

To see the effect of the new measurements on the pairing gaps relative to theoretical mass models, Fig. 11 shows the difference in the $D_n(N)$ values between the FRDM12 mass model [77] (which tends to be more accurate than other models at predicting rare-earth abundances that match solar data) and the AME16 [20], supplemented by the previous [26] and new JYFLTRAP

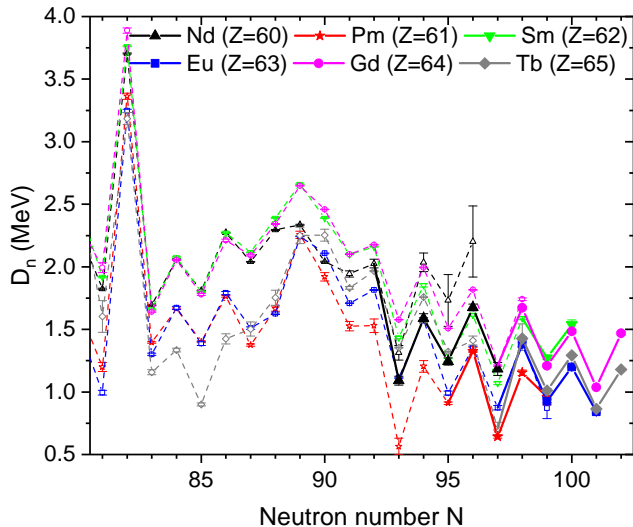


FIG. 10: Pairing-gap energies D_n for the studied isotopic chains based on the experimental AME16 [20] mass values (dashed lines, open symbols) and the JYFLTRAP measurements from this work and [26] (solid thick lines, full symbols)

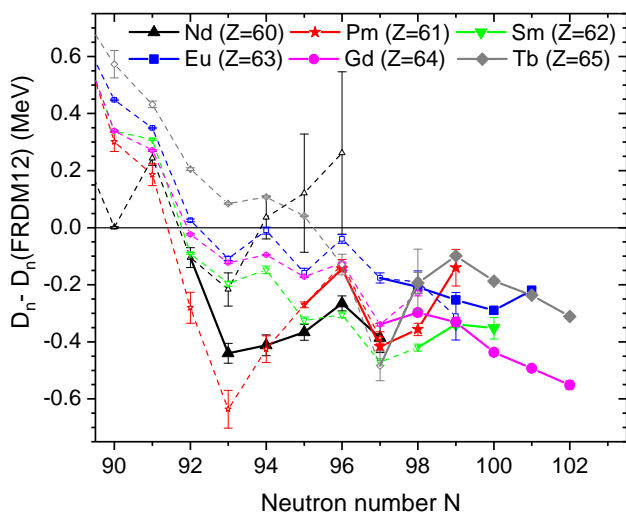


FIG. 11: Differences in pairing-gap energies, D_n , between the experimental values taken from AME16 [20] (dashed lines, open symbols) and the JYFLTRAP measurements from this work and [26] (thick solid lines, full symbols), and the FRDM12 mass model [77] (baseline). JYFLTRAP measurements extend the AME16 trend in showing that FRDM12 consistently over-estimates the effect of pairing for neutron-rich nuclei.

mass measurements. Relative to FRDM12, a consistent trend of smaller pairing gaps for increasing N emerges (negative values in the plot). This stems from the measured nuclei being generally less tightly bound, and translates to the effect of pairing being weaker than FRDM12 predicts.

Finally, we investigated whether the over-estimation in the D_n values near $N = 100$ is also present in other mass models by calculating the following metric:

$$\delta D_n = \sum_{Z,N} (D_n(Z, N)_{th.} - D_n(Z, N)_{exp.}). \quad (6)$$

The δD_n values are given for commonly used mass models in Table III. They show that FRDM12's overprediction of the D_n is not an isolated case since most mass models tend to overpredict this quantity for the studied mass region, $N \geq 94$. The overprediction of neutron pairing energies by Duflo-Zuker was the lowest of the models examined, probably because of its featureless, uniform odd-even staggering across the measured isotopic chains. Meanwhile, HFB-24, the strongest over-predictor of D_n , is consistently high relative to the values calculated using AME16 even for $N < 94$.

C. Two-neutron separation energies

Changes in nuclear structure far from stability can be probed via two-neutron separation energies [78], S_{2n} :

$$S_{2n}(Z, N) = [m(Z, N - 2) + 2m_n - m(Z, N)]c^2. \quad (7)$$

The main advantage of looking at S_{2n} values is that it removes the large odd-even staggering seen in the S_n values, resulting in a smoother pattern that will highlight features that would have been hidden by the effect of pairing.

Two-neutron separation energies for the neutron-rich rare-earth nuclides are plotted in Fig. 12. The magic shell closure at $N = 82$ is seen as a sudden drop in the S_{2n} values whereas the onset of strong prolate deformation at $N = 89$ produces a kink in the energies. On the other hand, the S_{2n} values in the region affected by our measurements follow a rather smooth behavior except for a sudden change in the slope at $N = 97$, strongly present only in the Tb chain. This effect will be investigated further by calculating differences in the S_{2n} values.

D. Two-Neutron shell gap energies

Changes in the slope of S_{2n} values with the number of neutrons can be investigated by calculating the two-neutron shell-gap energies, D_{2n} :

$$D_{2n}(Z, N) = S_{2n}(Z, N) - S_{2n}(Z, N + 2). \quad (8)$$

Figure 13 shows the D_{2n} values for all isotopic chains affected by our measurements. At magic shell closures,

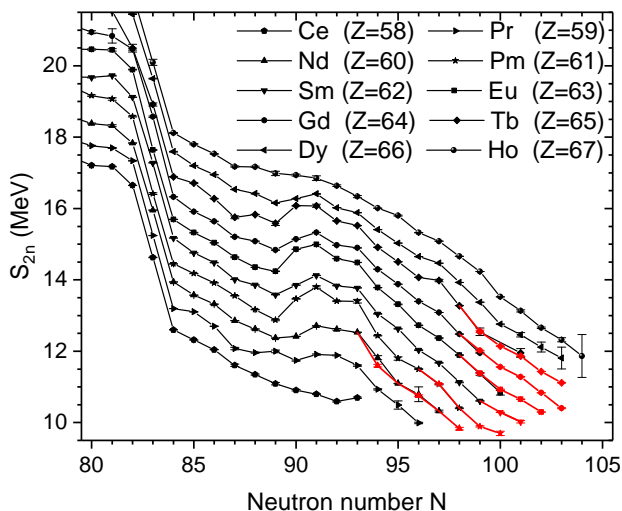


FIG. 12: Two-neutron separation energies, S_{2n} , based on the AME16 [20] experimental mass values (in black) and the JYFLTRAP mass measurements from this work and [26] (in red).

such as at $N = 82$, the two-neutron shell-gap energies increase rapidly. At the proposed subshell gap at $N = 100$, no increase is observed. Hence, the mass measurement data do not support such a subshell closure. It must be noted, however, that based on the 2^+ and 4^+ excitation energies (see Fig. 1), the nuclei in this region are not spherical and deformation can affect the two-neutron separation energies, and consequently the shell-gap energies.

Figure 13 indicates the presence of two smaller peaks at $N = 93$ and 97 . These peaks are particularly interesting as they are strongest for two odd-odd nuclei, ^{154}Pm and ^{162}Tb . Typically such an enhancement is expected only for even-even nuclei. Interestingly, both ^{154}Pm and ^{162}Tb have an equal number of valence nucleons above the magic shell closures at $Z = 50$ and $N = 82$, 11 and 15, respectively. This feature was further investigated by comparing the experimental D_{2n} values with various mass models, such as FRDM12 [77], Duflo-Zuker [71], and HFB-24 [70], for the Tb chain. Figure 14 shows that none of these models predicts the observed unusual peak at $N=97$.

Bonatsos et al. [79] have proposed that neutron-rich rare-earth nuclei show enhanced proton-neutron interactions for nuclei with equal numbers of valence protons and neutrons above the closed proton and neutron shells at $Z = 50$ and $N = 82$. This is in analogy with the nuclei close to the $Z = N$ line, which exhibit peaks in the proton-neutron interactions for nuclides with maximal spatial-spin overlaps of proton and neutron wave functions [80]. It should be further investigated why the peaks in the rare-earth region happen at odd-odd nuclei

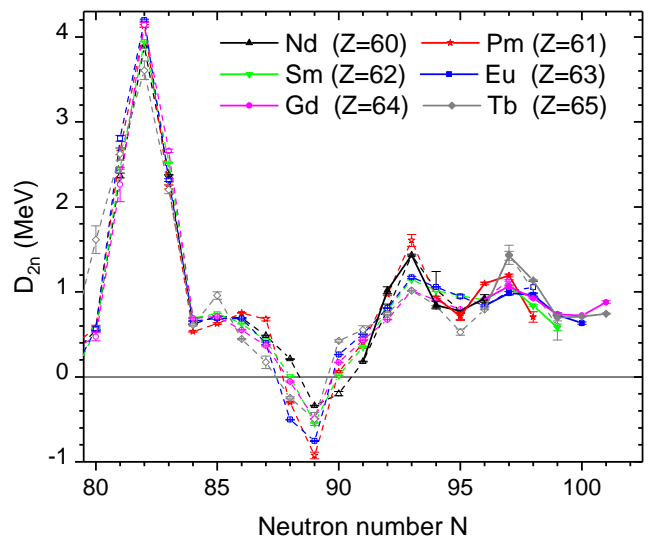


FIG. 13: D_{2n} values based on the AME16 [20] experimental mass values (dashed lines and open symbols) and the JYFLTRAP mass measurements from this work and [26] (thick solid lines and full symbols). No subshell at $N = 100$ is apparent but two peculiar peaks appear at $N = 93$ and $N = 97$.

with $Z_{val} = N_{val} = 11$ and $Z_{val} = N_{val} = 15$.

E. Proton-neutron pairing strength via the δV_{pn} values

Since the unusually large D_{2n} values, at $N = 93$ and 97 , are present for two nuclei with unpaired nucleons, the next natural step was to investigate the proton-neutron ($p-n$) interaction observed in the studied region of nuclei. The unique role of the $p-n$ interaction in nuclear structure has long been known [80, 82], presenting itself in shell effects, the onset of deformation, and many other nuclear shape transitions [79, 83]. A simple way to study the $p-n$ interaction is to calculate a double difference of binding energies across isotopic chains, called δV_{pn} . This quantity is defined for odd-odd nuclei as

$$\delta V_{pn}(Z_{odd}, N_{odd}) = S_n(Z, N) - S_n(Z-1, N). \quad (9)$$

Typically, δV_{pn} values show large singularities for light $Z = N$ nuclei which are linked to maximal spatial-spin overlaps of proton and neutron wave functions [80]. While there are no $Z = N$ nuclei past $A \approx 100$, this feature is present for heavy neutron-rich nuclei where the number of valence neutrons, N_{val} , and valence protons Z_{val} above the magic shell closures at $Z = 50$ and $N = 82$, are equal or, late in the shells, when N_{val} slightly exceeds Z_{val} [79].

Figures 15 and 16 show odd-odd δV_{pn} values over the measured isotopic ranges. The odd-odd nuclei where the

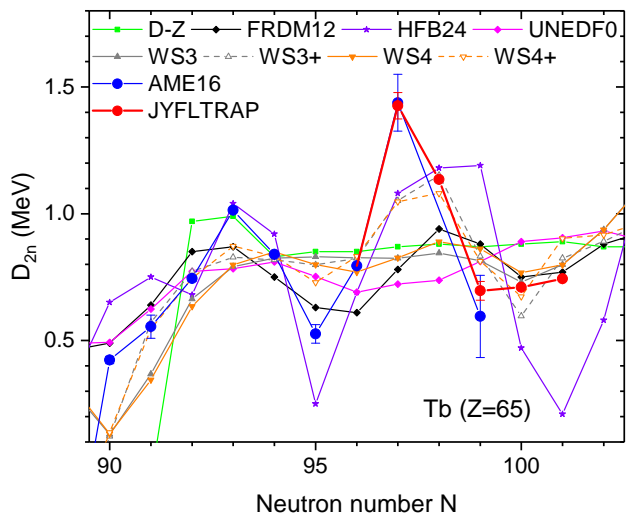


FIG. 14: Experimental D_{2n} values for the Tb isotopic chain, based on AME16 [20] (in blue) and the JYFLTRAP measurements from this work and [26] (in red), and comparison to various commonly used mass models, such as Duflo-Zuker (D-Z) [71], FRDM12 [21], HFB24 [70], UNEDF0 [81], WS3 [72], WS3+ [73], WS4 [74], and WS4+ [74]. None of these models predict the enhancement seen at $N = 97$.

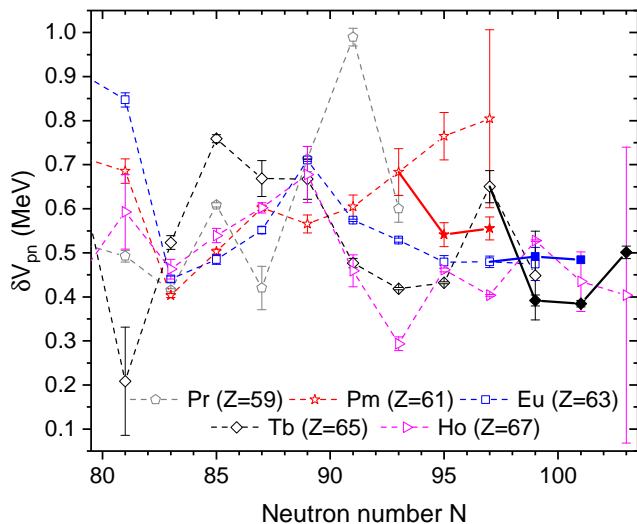


FIG. 15: A measure of the average $p - n$ interaction of valence nucleons in odd-odd nuclei according to Eq. 9. Calculations were done using the experimental mass values from AME16 [20] (dashed lines and open symbols) and supplemented by the JYFLTRAP measurements from this work and [26] (solid lines and full symbols).

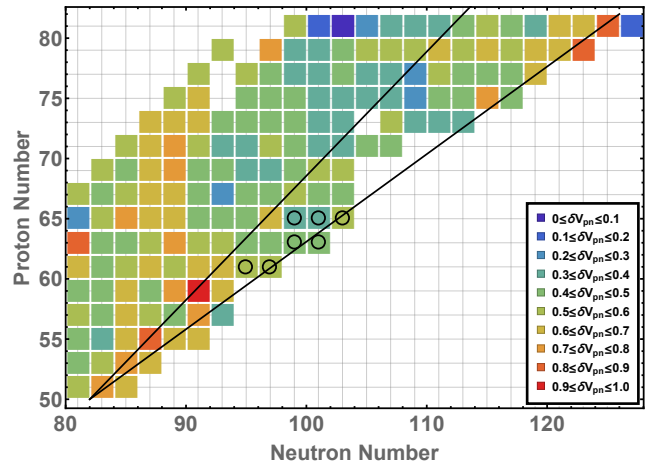


FIG. 16: Odd-odd δV_{pn} values for $80 \leq N \leq 126$ and $50 \leq Z \leq 82$ according to Eq. 9, as in [79]. Values affected by JYFLTRAP measurements are circled, and black lines indicate $N_{val} = Z_{val}$ (upper) and equal fractions of the N and Z shells filled (lower).

last protons and neutrons occupy specific single orbits offer a clearer perspective on the valence $p - n$ interactions. Namely, the orbital part of the many-body wave function determines the degree of spatial overlap between the nucleons. Since the ground states of even-even nuclei have wave functions which are spread out over several orbits due to the pairing force, these cases are poor choices for examining the $p - n$ interaction. For the odd-odd nuclei the singularities in the δV_{pn} values are further enhanced, again at $Z_{val} \approx N_{val}$.

The Pm isotopes ($Z = 61$) have 11 valence protons, and hence one would expect an enhancement in δV_{pn} values for $N_{val} = 11$, corresponding to $N = 93$. Figure 15 indicates that indeed the new measurements unveil the presence of a small peak for the Pm chain at $N = 93$. For the Eu ($Z = 63$, $Z_{val} = 13$) on the other hand, no peak can be seen near the expected $N_{val} = 13$, $N = 95$. However, a peak reappears at $N = 97$ for Tb ($Z = 65$, $Z_{val} = 15$), which matches the expected $N_{val} = 15$. In summary, the singularities seen in [79] are getting weaker and intermittent in the the observed region (see Fig. 16).

VI. IMPACT ON THE RARE-EARTH ABUNDANCE PEAK

The rare-earth abundance peak at around $A = 165$ gives us essential information on the r process and related nuclear structure effects. Namely, deformation in this midshell region close to $Z = 66$, $N = 104$ can funnel the reaction flow toward $A \approx 165$ when matter is decaying toward stability at later stages of the process

when it is running out of neutrons [17, 18]. On the other hand, these lanthanide nuclei can also be populated via fission cycling from asymmetric fission of heavy nuclei in the $A \approx 280$ region [70]. The lanthanides play a key role in the emergence of the red kilonova after GW170817 [16, 84] due to their much higher opacity than lighter elements. In order to provide accurate r -process calculations to interpret multimessenger observational data from neutron star mergers, it is essential to have precise mass values of the lanthanide nuclides in the rare-earth region. It should be noted that the observed solar system abundances of lanthanides are one of the most well known [85]. Europium, for instance, is the standard representative element for the r -process in stellar observations (see e.g. [86, 87]).

In this work, the impact of the new atomic mass values has been studied for a binary neutron star merger scenario. The impact on the calculated r -process abundances is illustrated here by a representative dynamical ejecta trajectory for a 1.35 solar mass neutron-star merger from Ref. [88], with a very low initial electron fraction $Y_e = 0.016$ and low entropy per baryon $s/k_B = 8$. Most of the prompt ejected mass (up to 90%) is assumed to originate from these types of reheated, fission-recycling trajectories which all yield very similar abundances with the mass model used. Thus, the results are largely independent of the specific astrophysical conditions.

The r -process simulation followed the procedure outlined in [23]. In the simulations, the entropy per baryon increased to $s/k_B \approx 100$ due to nuclear reheating. The initial timescale was around 40 ms, after which a homologous expansion was assumed [88]. The baseline calculations were done with the experimental mass values from AME16 [20] supplemented by theoretical FRDM12 [77] mass model values where no experimental data existed. The second calculation included the JYFLTRAP mass values from the first measurement campaign [26]. Finally, the third set included all JYFLTRAP measurements performed in this region ([26] and this work). To be consistent, calculated and experimental mass values were not combined in the calculation of a given S_n value. The neutron-capture rates were calculated with the commonly used TALYS code [89] with the three different mass datasets described above. For fission product distributions, a simple asymmetric split [31] was assumed. This ensured that the produced fission fragments fall into the $A = 130$ region and the rare-earth peak forms entirely via the dynamical formation mechanism of Refs. [17, 18]. The branching ratios and β -decay half-lives were taken from NUBASE16 [59] or Ref. [90].

Figure 17 shows the impact of the masses determined in this work and [26] on the calculated r -process abundances. The masses from [26] were shown to severely affect the abundance pattern, resulting in a smoothening and better agreement with the solar abundances. The new masses from this work still affect the abundance pattern resulting in less staggering and a smoother pro-

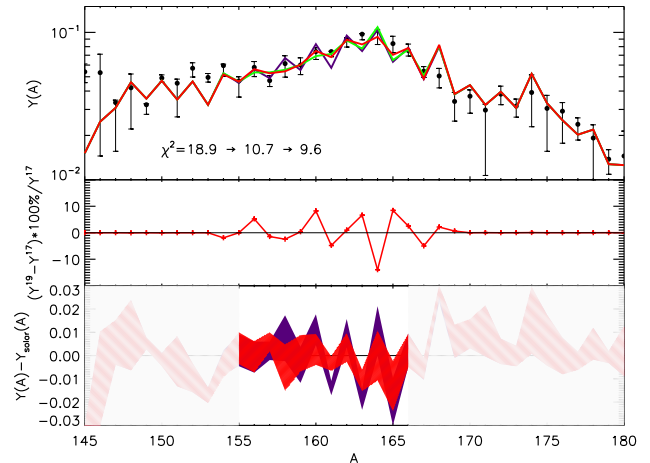


FIG. 17: (Color on-line) Top: Solar r -process abundances Y as a function of the mass number A (black data points) together with the calculated abundances using the AME16 [20] and FRDM12 [77] mass-excess values (purple), and with the addition of the values from the first experimental campaign at JYFLTRAP (green) [26], and with the masses from this work (red). Middle: Difference between the calculated abundances from this work (Y^{19}) and (Y^{17}) [26]. Bottom: Residuals based on the mass values from this work (red) and the baseline (purple), where the bands represent the solar abundance uncertainties.

file at the top of the abundance peak. The reduced staggering at the summit of the peak might be caused by the reduced odd-even staggering in the S_n values, now clearly seen in Fig. 10 for the various chains measured. Such a reduced staggering reveals an increasing over-prediction by the FRDM mass model, especially for the Tb and Gd isotopic chains (see Fig. 11). Furthermore, the small reduction in the following metric $\chi^2 = \sum \{[Y(A)_{solar} - Y(A)_{calc}]/\sigma[Y(A)_{solar}]\}^2$ from 10.7 to 9.6 indicates that the new masses further improved the matching with solar abundance data. The bottom panel of Fig. 17 shows the dramatic improvement in the matching between the solar abundance and the calculated abundance once the new JYFLTRAP masses from this work and [26] are included. Finally, the middle panel shows that the new JYFLTRAP mass measurements change the calculated abundances up to 10% as compared to the results from [26].

VII. CONCLUSIONS

The masses of 13 nuclides in the rare-earth region have been measured using the JYFLTRAP Penning trap facility. This second campaign of measurements adds to the 12 masses previously measured in this sensitive region

by JYFLTRAP [26] and the 10 masses measured by the CPT [8, 29]. In this second JYFLTRAP campaign, the masses of eight isotopes, namely ^{161}Pm , ^{163}Sm , $^{164,165}\text{Eu}$, ^{167}Gd , and $^{165,167,168}\text{Tb}$ were measured for the first time. The mass of ^{166}Tb was found to be consistent with the AME16 value, while being 54 times more precise. The result for ^{154}Nd agreed well with the recent PI-ICR measurement from CPT [29]. Due to previous disagreements and inconsistencies, the masses of $^{162,163}\text{Eu}$ and ^{163}Gd have been remeasured. We confirm both the ground-state mass and the isomeric-state energy of ^{162}Eu measured by the CPT. The re-measurement of ^{163}Gd and ^{163}Eu using calibrant ions ^{136}Xe and ^{133}Cs , respectively, indicates that the reference ion used for these isotopes in the first JYFLTRAP campaign [26] was incorrectly assigned, and was most likely $^{146}\text{La}^{16}\text{O}^+\text{H}^+$, or its mixture with $^{163}\text{Dy}^+$. Using the mass of this molecule as a calibrant leads to mass-excess values consistent with the CPT measurements for ^{163}Gd and ^{163}Eu .

The impact of the new mass values on nuclear structure was studied via different parameters and derivatives of the mass surface. All mass models, including FRDM, were found to over-predict the odd-even staggering in S_n values. The new mass values reveal an unusual enhancement in two-neutron shell-gap energies at $N = 97$ for the odd-odd nuclei ^{162}Tb . Such an enhancement is also seen at $N = 93$ for ^{154}Pm , but is absent at $N = 95$ for ^{158}Eu . Finally, a similar enhancement in the δV_{pn} values is also seen for ^{154}Pm and ^{162}Tb , while being muted for ^{158}Eu . Further studies are needed to understand the nature of the unusual enhancement in D_{2n} value for the odd-odd nuclei ^{154}Pm and ^{162}Tb and for the sudden quenching in δV_{pn} values for ^{158}Eu .

The mass measurements presented in this work provide essential nuclear data for the r -process calculations, complementing the knowledge of the rare-earth region together with the recent beta-decay half-life measurements from the Radioactive Isotope Beam Factory [6]. While the new mass-excess values are shown to further reduce the staggering at the top of the rare-earth abundance peak in the r -process, the effect is more modest than previously seen [26]. In the future, the isomeric states in the region can be further explored with the PI-ICR technique which has been demonstrated to work well for ^{162}Eu in this work. More mass measurements in this region are warranted to refine theoretical mass models used for the r -process calculations as well as to better understand this region with rapid changes in nuclear structure.

ACKNOWLEDGMENTS

This work has been supported by the Academy of Finland under the Finnish Centre of Excellence Programme 2012-2017 (Nuclear and Accelerator Based Physics Research at JYFL) and by the National Science Foundation (NSF) Grants No. PHY-1713857. A.K., D.N., L.C., and T.E. acknowledge support from the Academy of Finland under projects No. 275389 and 295207. M.M. carried out this work under the auspices of the National Nuclear Security Administration of the U.S. Department of Energy at Los Alamos National Laboratory under Contract No. DE-AC52-06NA25396. R.S. work is funded in part by the DOE Office of Science under contract DE-SC0013039. The authors would like thank S. Frauendorf and I. Bentley for fruitful discussions.

-
- [1] P. Brix, *Z. Phys.* **132**, 579 (1952).
 [2] B. R. Mottelson and S. G. Nilsson, *Phys. Rev.* **99**, 1615 (1955).
 [3] J. B. Gupta, *Phys. Rev. C* **92**, 044316 (2015).
 [4] E. F. Jones, J. H. Hamilton, P. M. Gore, A. V. Ramayya, J. K. Hwang, and A. P. de Lima, *Eur. Phys. J. A* **25**, 467 (2005).
 [5] S. K. Ghorui, B. B. Sahu, C. R. Prahara, and S. K. Patra, *Phys. Rev. C* **85**, 064327 (2012).
 [6] J. Wu, S. Nishimura, G. Lorusso, P. Möller, E. Ideguchi, P.-H. Regan, G. S. Simpson, P.-A. Söderström, P. M. Walker, H. Watanabe, Z. Y. Xu, H. Baba, F. Browne, R. Daido, P. Doornenbal, Y. F. Fang, G. Gey, T. Isobe, P. S. Lee, J. J. Liu, Z. Li, Z. Korkulu, Z. Patel, V. Phong, S. Rice, H. Sakurai, L. Sinclair, T. Sumikama, M. Tanaka, A. Yagi, Y. L. Ye, R. Yokoyama, G. X. Zhang, T. Alharbi, N. Aoi, F. L. Bello Garrote, G. Benzoni, A. M. Bruce, R. J. Carroll, K. Y. Chae, Z. Dombradi, A. Estrade, A. Gottardo, C. J. Griffin, H. Kanaoka, I. Kojouharov, F. G. Kondev, S. Kubono, N. Kurz, I. Kuti, S. Lalkovski, G. J. Lane, E. J. Lee, T. Lokotko, G. Lotay, C.-B. Moon, H. Nishibata, Y. Nishizuka, C. R. Nita, A. Odahara, Z. Podolyák, O. J. Roberts, H. Schaffner, C. Shand, J. Taprogge, S. Terashima, Z. Vajta, and S. Yoshida, *Phys. Rev. Lett.* **118**, 072701 (2017).
 [7] R. Yokoyama, S. Go, D. Kameda, T. Kubo, N. Inabe, N. Fukuda, H. Takeda, H. Suzuki, K. Yoshida, K. Kusaka, K. Tanaka, Y. Yanagisawa, M. Ohtake, H. Sato, Y. Shimizu, H. Baba, M. Kurokawa, D. Nishimura, T. Ohnishi, N. Iwasa, A. Chiba, T. Yamada, E. Ideguchi, T. Fujii, H. Nishibata, K. Ieki, D. Murai, S. Momota, Y. Sato, J. W. Hwang, S. Kim, O. B. Tarasov, D. J. Morrissey, B. M. Sherrill, G. Simpson, and C. R. Prahara, *Phys. Rev. C* **95**, 034313 (2017).
 [8] D. J. Hartley, F. G. Kondev, R. Orford, J. A. Clark, G. Savard, A. D. Ayangeakaa, S. Bottoni, F. Buchinger, M. T. Burkey, M. P. Carpenter, P. Copp, D. A. Gorelov, K. Hicks, C. R. Hoffman, C. Hu, R. V. F. Janssens, J. W. Klimes, T. Lauritsen, J. Sethi, D. Seweryniak, K. S. Sharma, H. Zhang, S. Zhu, and Y. Zhu, *Phys. Rev. Lett.* **120**, 182502 (2018).
 [9] E. M. Burbidge, G. R. Burbidge, W. A. Fowler, and F. Hoyle, *Rev. Mod. Phys.* **29**, 547 (1957).
 [10] A. Cameron, "Stellar evolution, nuclear astrophysics, and nucleogenesis," (1957), Chalk River Report CLR-41. Publisher: Atomic Energy of Canada Limited.

- [11] M. Arnould, S. Goriely, and K. Takahashi, *Phys. Rep.* **450**, 97 (2007).
- [12] C. J. Horowitz, A. Arcones, B. Côté, I. Dillmann, W. Nazarewicz, I. U. Roederer, H. Schatz, A. Aprahamian, D. Atanasov, A. Bauswein, T. C. Beers, J. Bliss, M. Brodeur, J. A. Clark, A. Frebel, F. Foucart, C. J. Hansen, O. Just, A. Kankainen, G. C. McLaughlin, J. M. Kelly, S. N. Liddick, D. M. Lee, J. Lippuner, D. Martin, J. Mendoza-Temis, B. D. Metzger, M. R. Mumpower, G. Perdikakis, J. Pereira, B. W. O'Shea, R. Reifarh, A. M. Rogers, D. M. Siegel, A. Spyrou, R. Surman, X. Tang, T. Uesaka, and M. Wang, *J. Phys. G: Nucl. Part. Phys.* **46**, 083001 (2019).
- [13] B. P. Abbott (LIGO Scientific Collaboration and Virgo Collaboration), *Phys. Rev. Lett.* **119**, 161101 (2017).
- [14] B. P. Abbott *et al.*, *Astrophys. J. Lett.* **848**, L12 (2017).
- [15] N. R. Tanvir, A. J. Levan, C. González-Fernández, O. Korobkin, I. Mandel, S. Rosswog, J. Hjorth, P. D'Avanzo, A. S. Fruchter, C. L. Fryer, T. Kangas, B. Milvang-Jensen, S. Rosetti, D. Steeghs, R. T. Wollaeger, Z. Cano, C. M. Copperwheat, S. Covino, V. D'Elia, A. de Ugarte Postigo, P. A. Evans, W. P. Even, S. Fairhurst, R. F. Jaimes, C. J. Fontes, Y. I. Fujii, J. P. U. Fynbo, B. P. Gompertz, J. Greiner, G. Hodosan, M. J. Irwin, P. Jakobsson, U. G. Jørgensen, D. A. Kann, J. D. Lyman, D. Malesani, R. G. McMahon, A. Melandri, P. T. O'Brien, J. P. Osborne, E. Palazzi, D. A. Perley, E. Pian, S. Piranomonte, M. Rabus, E. Rol, A. Rowlinson, S. Schulze, P. Sutton, C. C. Thöne, K. Ulaczyk, D. Watson, K. Wiersema, and R. A. M. J. Wijers, *Astrophys. J. Lett.* **848**, L27 (2017).
- [16] D. Kasen, B. Metzger, J. Barnes, E. Quataert, and E. Ramirez-Ruiz, *Nature* **551**, 80 (2017).
- [17] R. Surman, J. Engel, J. R. Bennett, and B. S. Meyer, *Phys. Rev. Lett.* **79**, 1809 (1997).
- [18] M. R. Mumpower, G. C. McLaughlin, and R. Surman, *Phys. Rev. C* **85**, 045801 (2012).
- [19] S. Goriely, J.-L. Sida, J.-F. Lemaître, S. Panebianco, N. Dubray, S. Hilaire, A. Bauswein, and H.-T. Janka, *Phys. Rev. Lett.* **111**, 242502 (2013).
- [20] M. Wang, G. Audi, F. Kondev, W. Huang, S. Naimi, and X. Xu, *Chin. Phys. C* **41**, 030003 (2017).
- [21] P. Möller, A. Sierk, T. Ichikawa, and H. Sagawa, *At. Data Nucl. Data Tables* **109–110**, 1 (2016).
- [22] M. R. Mumpower, R. Surman, D.-L. Fang, M. Beard, P. Möller, T. Kawano, and A. Aprahamian, *Phys. Rev. C* **92**, 035807 (2015).
- [23] M. Mumpower, R. Surman, G. McLaughlin, and A. Aprahamian, *Progr. Part. Nucl. Phys.* **86**, 86 (2016).
- [24] <https://www.nndc.bnl.gov/ensdf/>.
- [25] Z. Patel, P.-A. Söderström, Z. Podolyák, P. H. Regan, P. M. Walker, H. Watanabe, E. Ideguchi, G. S. Simpson, H. L. Liu, S. Nishimura, Q. Wu, F. R. Xu, F. Browne, P. Doornenbal, G. Lorusso, S. Rice, L. Sinclair, T. Sumikama, J. Wu, Z. Y. Xu, N. Aoi, H. Baba, F. L. Bello Garrote, G. Benzoni, R. Daido, Y. Fang, N. Fukuda, G. Gey, S. Go, A. Gottardo, N. Inabe, T. Isobe, D. Kameda, K. Kobayashi, M. Kobayashi, T. Komatsubara, I. Kojouharov, T. Kubo, N. Kurz, I. Kuti, Z. Li, M. Matsushita, S. Michimasa, C.-B. Moon, H. Nishibata, I. Nishizuka, A. Odahara, E. Şahin, H. Sakurai, H. Schaffner, H. Suzuki, H. Takeda, M. Tanaka, J. Taprogge, Z. Vajta, A. Yagi, and R. Yokoyama, *Phys. Rev. Lett.* **113**, 262502 (2014).
- [26] M. Vilen, J. M. Kelly, A. Kankainen, M. Brodeur, A. Aprahamian, L. Canete, T. Eronen, A. Jokinen, T. Kuta, I. D. Moore, M. R. Mumpower, D. A. Nesterenko, H. Penttilä, I. Pohjalainen, W. S. Porter, S. Rinta-Antila, R. Surman, A. Voss, and J. Äystö, *Phys. Rev. Lett.* **120**, 262701 (2018).
- [27] G. Savard, S. Baker, C. Davids, A. Levand, E. Moore, R. Pardo, R. Vondrasek, B. Zabransky, and G. Zinkann, *Nucl. Instr. Meth. Phys. Res. Sect. B* **266**, 4086 (2008), proceedings of the XVth International Conference on Electromagnetic Isotope Separators and Techniques Related to their Applications.
- [28] I. Moore, T. Eronen, D. Gorelov, J. Hakala, A. Jokinen, A. Kankainen, V. Kolhinen, J. Koponen, H. Penttilä, I. Pohjalainen, M. Reponen, J. Rissanen, A. Saastamoinen, S. Rinta-Antila, V. Sonnenschein, and J. Äystö, *Nucl. Instr. Meth. Phys. Res. Sect. B* **317**, 208 (2013), xVIth International Conference on ElectroMagnetic Isotope Separators and Techniques Related to their Applications, December 2–7, 2012 at Matsue, Japan.
- [29] R. Orford, N. Vassh, J. A. Clark, G. C. McLaughlin, M. R. Mumpower, G. Savard, R. Surman, A. Aprahamian, F. Buchinger, M. T. Burkey, D. A. Gorelov, T. Y. Hirsh, J. W. Klimes, G. E. Morgan, A. Nystrom, and K. S. Sharma, *Phys. Rev. Lett.* **120**, 262702 (2018).
- [30] J. Van Schelt, D. Lascar, G. Savard, J. A. Clark, S. Caldwell, A. Chaudhuri, J. Fallis, J. P. Greene, A. F. Levand, G. Li, K. S. Sharma, M. G. Sternberg, T. Sun, and B. J. Zabransky, *Phys. Rev. C* **85**, 045805 (2012).
- [31] M. R. Mumpower, G. C. McLaughlin, R. Surman, and A. W. Steiner, *J. Phys. G: Nucl. Part. Phys.* **44**, 034003 (2017).
- [32] T. Eronen, V. S. Kolhinen, V. V. Elomaa, D. Gorelov, U. Hager, J. Hakala, A. Jokinen, A. Kankainen, P. Karvonen, S. Kopecky, I. D. Moore, H. Penttilä, S. Rahaman, S. Rinta-Antila, J. Rissanen, A. Saastamoinen, J. Szerypo, C. Weber, and J. Äystö, *Eur. Phys. J. A* **48**, 46 (2012).
- [33] L. Satpathy and S. Patra, *Nucl. Phys. A* **722**, C24 (2003).
- [34] L. Satpathy and S. K. Patra, *J. Phys. G: Nucl. Part. Phys.* **30**, 771 (2004).
- [35] J. Äystö, *Nucl. Phys. A* **693**, 477 (2001).
- [36] H. Penttilä, V. V. Elomaa, T. Eronen, J. Hakala, A. Jokinen, A. Kankainen, I. D. Moore, S. Rahaman, S. Rinta-Antila, J. Rissanen, V. Rubchenya, A. Saastamoinen, C. Weber, and J. Äystö, *Eur. Phys. J. A* **48**, 43 (2012).
- [37] Al-Adili, A., Jansson, K., Lantz, M., Solders, A., Gorelov, D., Gustavsson, C., Mattera, A., Moore, I., Prokofiev, A. V., Rakopoulos, V., Penttilä, H., Tarrío, D., Wiberg, S., Österlund, M., and Pomp, S., *Eur. Phys. J. A* **51**, 59 (2015).
- [38] P. Karvonen, I. Moore, T. Sonoda, T. Kessler, H. Penttilä, K. Peräjärvi, P. Ronkanen, and J. Äystö, *Nucl. Instr. Methods Phys. Res. Sect. B* **266**, 4794 (2008).
- [39] A. Nieminen, J. Huikari, A. Jokinen, J. Äystö, P. Campbell, and E. Cochrane, *Nucl. Instr. Methods Phys. Res. Sect. A* **469**, 244 (2001).
- [40] G. Gabrielse and F. Mackintosh, *Int. J. Mass Spectrom. Ion Proc.* **57**, 1 (1984).
- [41] V. Kolhinen, S. Kopecky, T. Eronen, U. Hager, J. Hakala, J. Huikari, A. Jokinen, A. Nieminen, S. Rinta-Antila, J. Szerypo, and J. Äystö, *Nucl. Instr. Meth. Phys. Res. Sect. A* **528**, 776 (2004).

- [42] G. Savard, S. Becker, G. Bollen, H. J. Kluge, R. B. Moore, T. Otto, L. Schweikhard, H. Stolzenberg, and U. Wiess, *Phys. Lett. A* **158**, 247 (1991).
- [43] T. Eronen, V.-V. Elomaa, U. Hager, J. Hakala, A. Jokinen, A. Kankainen, S. Rahaman, J. Rissanen, C. Weber, and J. Äystö, *Nucl. Instr. Methods Phys. Res. Sect. B* **266**, 4527 (2008).
- [44] G. Gräff, H. Kalinowsky, and J. Traut, *Z. Phys. A* **297**, 35 (1980).
- [45] M. König, G. Bollen, H. J. Kluge, T. Otto, and J. Szerypo, *Int. J. Mass Spectrom. Ion Proc.* **142**, 95 (1995).
- [46] S. George, K. Blaum, F. Herfurth, A. Herlert, M. Kretzschmar, S. Nagy, S. Schwarz, L. Schweikhard, and C. Yazidjian, *Int. J. Mass Spectrom.* **264**, 110 (2007).
- [47] M. Kretzschmar, *Int. J. Mass Spectrom.* **264**, 122 (2007).
- [48] S. Eliseev, K. Blaum, M. Block, A. Dörr, C. Droese, T. Eronen, M. Goncharov, M. Höcker, J. Ketter, E. M. Ramirez, D. A. Nesterenko, Y. N. Novikov, and L. Schweikhard, *Appl. Phys. B* **114**, 107 (2014).
- [49] D. A. Nesterenko, T. Eronen, A. Kankainen, L. Canete, A. Jokinen, I. D. Moore, H. Penttilä, S. Rinta-Antila, A. de Roubin, and M. Vilen, *Eur. Phys. J. A* **54**, 154 (2018).
- [50] H. Hayashi, M. Shibata, M. Asai, A. Osa, T. Sato, M. Koizumi, A. Kimura, and M. Oshima, *Nucl. Instr. Methods Phys. Res. Sect. A* **747**, 41 (2014).
- [51] M. Vilén, L. Canete, B. Cheal, A. Giatzoglou, R. de Groote, A. de Roubin, T. Eronen, S. Geldhof, A. Jokinen, A. Kankainen, I. Moore, D. Nesterenko, H. Penttiä, I. Pohjalainen, M. Reponen, and S. Rinta-Antila, *Nucl. Instr. Meth. Phys. Res. Sect. B* (2019), <https://doi.org/10.1016/j.nimb.2019.04.051>.
- [52] J. Beringer *et al.* (Particle Data Group), *Phys. Rev. D* **86**, 010001 (2012).
- [53] L. S. Brown and G. Gabrielse, *Rev. Mod. Phys.* **58**, 233 (1986).
- [54] M. Brodeur, T. Brunner, C. Champagne, S. Ettenauer, M. Smith, A. Lapierre, R. Ringle, V. L. Ryjkov, G. Audi, P. Delheij, D. Lunney, and J. Dilling, *Phys. Rev. C* **80**, 044318 (2009).
- [55] L. Canete, A. Kankainen, T. Eronen, D. Gorelov, J. Hakala, A. Jokinen, V. S. Kolhinen, J. Koponen, I. D. Moore, J. Reinikainen, and S. Rinta-Antila, *Eur. Phys. J. A* **52**, 124 (2016).
- [56] G. Bollen, H.-J. Kluge, M. König, T. Otto, G. Savard, H. Stolzenberg, R. B. Moore, G. Rouleau, G. Audi, and ISOLDE Collaboration, *Phys. Rev. C* **46**, R2140 (1992).
- [57] A. Kellerbauer, K. Blaum, G. Bollen, F. Herfurth, H.-J. Kluge, M. Kuckein, E. Sauvan, C. Scheidenberger, and L. Schweikhard, *Eur. Phys. J. D* **22**, 53 (2003).
- [58] M. Vilén, D. A. Nesterenko, T. Eronen, and A. Kankainen, To be submitted (2019).
- [59] G. Audi, F. Kondev, M. Wang, W. Huang, and S. Naimi, *Chin. Phys. C* **41**, 030001 (2017).
- [60] R. Greenwood and M. Putnam, *Nucl. Instr. Meth. Phys. Res. Sect. A* **337**, 106 (1993).
- [61] J. D'auria, D. Ostrom, and S. Gujrathi, *Nucl. Phys. A* **178**, 172 (1971).
- [62] O. Tannila and J. Kantele, *Z. Phys. A* **251**, 87 (1972).
- [63] H. Yamamoto, K. Kawade, H. Fukaya, and T. Katoh, *J. Phys. Soc. Japan* **37**, 10 (1974), <https://doi.org/10.1143/JPSJ.37.10>.
- [64] D. C. Kayser and W. H. Johnson, *Phys. Rev. C* **12**, 1054 (1975).
- [65] J. Hardy, L. Carraz, B. Jonson, and P. Hansen, *Phys. Lett. B* **71**, 307 (1977).
- [66] F. Schneider, T. Beyer, K. Blaum, M. Block, S. Chenmarev, H. Dorrer, C. E. Düllmann, K. Eberhardt, M. Eibach, S. Eliseev, J. Grund, U. Köster, S. Nagy, Y. N. Novikov, D. Renisch, A. Türler, and K. Wendt, *Eur. Phys. J. A* **51**, 89 (2015).
- [67] R. Ringle, *High-Precision Mass Measurement of ^{38}Ca and Development of the LEBIT 9.4-T Penning Trap System*, Ph.D. thesis, Michigan State University (2006).
- [68] G. Savard, J. Wang, K. Sharma, H. Sharma, J. Clark, C. Boudreau, F. Buchinger, J. Crawford, J. Greene, S. Gulick, A. Hecht, J. Lee, A. Levand, N. Scielzo, W. Trimble, J. Vaz, and B. Zabransky, *Int. J. Mass Spectrom.* **251**, 252 (2006).
- [69] H. Hayashi, Y. Kojima, M. Shibata, and K. Kawade, *Nucl. Instr. Meth. Phys. Res. Sect. A* **613**, 79 (2010).
- [70] S. Goriely, N. Chamel, and J. M. Pearson, *Phys. Rev. C* **88**, 024308 (2013).
- [71] J. Dufflo and A. Zuker, *Phys. Rev. C* **52**, R23 (1995).
- [72] N. Wang and M. Liu, *Journal of Physics: Conference Series* **420**, 012057 (2013).
- [73] N. Wang and M. Liu, *Phys. Rev. C* **84**, 051303 (2011).
- [74] N. Wang, M. Liu, X. Wu, and J. Meng, *Phys. Lett. B* **734**, 215 (2014).
- [75] B. A. Brown, *Phys. Rev. Lett.* **111**, 162502 (2013).
- [76] J. Hakala, J. Dobaczewski, D. Gorelov, T. Eronen, A. Jokinen, A. Kankainen, V. S. Kolhinen, M. Kortelainen, I. D. Moore, H. Penttilä, S. Rinta-Antila, J. Rissanen, A. Saastamoinen, V. Sonnenschein, and J. Äystö, *Phys. Rev. Lett.* **109**, 032501 (2012).
- [77] P. Möller, W. D. Myers, H. Sagawa, and S. Yoshida, *Phys. Rev. Lett.* **108**, 052501 (2012).
- [78] D. Lunney, J. M. Pearson, and C. Thibault, *Rev. Mod. Phys.* **75**, 1021 (2003).
- [79] D. Bonatsos, S. Karampagia, R. B. Cakirli, R. F. Casten, K. Blaum, and L. A. Susam, *Phys. Rev. C* **88**, 054309 (2013).
- [80] P. Van Isacker, D. D. Warner, and D. S. Brenner, *Phys. Rev. Lett.* **74**, 4607 (1995).
- [81] M. Kortelainen, T. Lesinski, J. Moré, W. Nazarewicz, J. Sarich, N. Schunck, M. V. Stoitsov, and S. Wild, *Phys. Rev. C* **82**, 024313 (2010).
- [82] I. Talmi, *Rev. Mod. Phys.* **34**, 704 (1962).
- [83] D. Brenner, C. Wesselborg, R. Casten, D. Warner, and J.-Y. Zhang, *Phys. Lett. B* **243**, 1 (1990).
- [84] S. J. Smartt *et al.*, *Nature* **551**, 75 (2017).
- [85] K. Lodders, H. Palme, and H.-P. Gail, “4.4 Abundances of the elements in the Solar System: Datasheet from Landolt-Börnstein - Group VI Astronomy and Astrophysics - Volume 4B: “Solar System” in SpringerMaterials (http://dx.doi.org/10.1007/978-3-540-88055-4_34),” (2009), accessed 2017-07-18.
- [86] Christlieb, N., Beers, T. C., Barklem, P. S., Bessell, M., Hill, V., Holmberg, J., Korn, A. J., Marsteller, B., Mashonkina, L., Qian, Y.-Z., Rossi, S., Wasserburg, G. J., Zickgraf, F.-J., Kratz, K.-L., Nordström, B., Pfeiffer, B., Rhee, J., and Ryan, S. G., *A&A* **428**, 1027 (2004).
- [87] A. Frebel and T. Beers, *Phys. Today* **71**, 30 (2018).
- [88] J. d. J. Mendoza-Temis, M.-R. Wu, K. Langanke, G. Martínez-Pinedo, A. Bauswein, and H.-T. Janka, *Phys. Rev. C* **92**, 055805 (2015).
- [89] A. Koning and D. Rochman, *Nucl. Data Sheets* **113**, 2841 (2012), special Issue on Nuclear Reaction Data.

- [90] P. Möller, B. Pfeiffer, and K.-L. Kratz, *Phys. Rev. C* **67**, 055802 (2003).



III

HIGH-PRECISION MASS MEASUREMENTS AND PRODUCTION OF NEUTRON-DEFICIENT ISOTOPES USING HEAVY-ION BEAMS AT IGISOL

by

M. Vilén, A. Kankainen, P. Ba_łczyk, L. Canete, J. Dobaczewski, T. Eronen, S. Geldhof, A. Jokinen, M. Konieczka, J. Kostensalo, I.D. Moore, D.A. Nesterenko, H. Penttilä, I. Pohjalainen, M. Reponen, S. Rinta-Antila, A. de Roubin, W. Satuła, J. Suhonen

Submitted to Physical Review C

High-precision mass measurements and production of neutron-deficient isotopes using heavy-ion beams at IGISOL

M. Vilén,^{1,*} A. Kankainen,¹ P. Bączyk,² L. Canete,¹ J. Dobaczewski,^{2,3,4} T. Eronen,¹ S. Geldhof,¹
 A. Jokinen,¹ M. Konieczka,² J. Kostensalo,¹ I.D. Moore,¹ D.A. Nesterenko,¹ H. Penttilä,¹
 I. Pohjalainen,¹ M. Reponen,¹ S. Rinta-Antila,¹ A. de Roubin,¹ W. Satuła,^{2,4} and J. Suhonen¹

¹*University of Jyväskylä, P.O. Box 35, FI-40014 University of Jyväskylä, Finland*

²*Institute of Theoretical Physics, Faculty of Physics,*

University of Warsaw, ul. Pasteura 5, PL-02-093 Warsaw, Poland

³*Department of Physics, University of York, Heslington, York YO10 5DD, United Kingdom*

⁴*Helsinki Institute of Physics, University of Helsinki, P.O. Box 64, FI-00014 Helsinki, Finland*

(Dated: September 5, 2019)

An upgraded ion-guide system for the production of neutron-deficient isotopes with heavy-ion beams has been commissioned at the IGISOL facility with an ^{36}Ar beam on a ^{nat}Ni target. It was used together with the JYFLTRAP double Penning trap to measure the masses of ^{82}Zr , ^{84}Nb , ^{86}Mo , ^{88}Tc , ^{89}Ru ground states and the isomeric state $^{88}\text{Tc}^m$. Of these, ^{89}Ru and $^{88}\text{Tc}^m$ were measured for the first time. The precisions of ^{82}Zr , ^{84}Nb and ^{88}Tc were significantly improved. The literature value for ^{86}Mo was verified. The measured states in ^{88}Tc were compared to shell-model calculations and additional constraints on the spins and level scheme were obtained. The masses of ^{82}Mo and ^{86}Ru have been predicted using the measured masses of their mirror partners and theoretical mirror displacement energies, resulting in more tightly bound nuclei with smaller atomic mass uncertainties than reported in literature.

I. INTRODUCTION

Neutron-deficient nuclei in the mass region $A \approx 80 - 100$ provide invaluable data for understanding basic nuclear interactions. Being close to the $Z = N$ line, the protons and neutrons are filling the same orbitals, mainly the high spin $1g_{9/2}$ orbital above the subshell closure at $N = Z = 40$. This opens an interesting playground to investigate proton-neutron pairing [1, 2] as well as isospin symmetry [3, 4] in nuclei. Recent theoretical calculations for mirror (MDE) or triplet displacement energies (TDE) using extended Skyrme energy density functionals with proton-neutron-mixed densities and isospin-symmetry breaking terms have yielded a good agreement with experimental data in the lower mass region [3, 4]. For example, with next-to-leading order isospin-symmetry breaking terms included, the root mean square deviation (RMSD) to experimental data for $T = 1$ MDEs is 180 keV, and only around 65 keV for TDEs [4]. Above $A \approx 70$, the available experimental data for MDEs or TDEs is rather limited. There, these new calculations can provide predictions for the more exotic mirror partners in the isobaric doublets or triplets.

The neutron-deficient region close to $A \approx 80$ is known for shape coexistence and deformation. For example, the $N = Z = 40$ nucleus ^{80}Zr is one of the most deformed nuclei known so far with a quadrupole deformation of $\beta_2 \approx 0.4$ [5]. Total-Routhian-surface calculations have indicated that the $g_{9/2}$ shell plays an important role in the shape evolution, with spherical, prolate, oblate and triaxial shapes predicted [6]. Even possible tetrahedral

deformation has been proposed to exist in the region [7]. The onset of deformation is reflected in nuclear binding energies [8], and therefore new precision mass measurements can shed light on the shape changes in the $A = 80 - 100$ region.

The masses of neutron-deficient nuclei are also relevant for the astrophysical rapid proton (rp) capture process occurring in type I x-ray bursts [9, 10]. For reliable calculations of the produced light curves and burst ashes, the masses should be known with a precision of around 10 keV [9]. Previous mass measurements at JYFLTRAP [11–13] and SHIPTRAP [12, 14] have revealed large deviations up to 1 MeV to the earlier literature values. Before the Penning trap era, the masses were mainly based on beta-decay endpoint energies which are prone to underestimations of the Q values, and hence the masses.

Neutron-deficient nuclei in the $A = 80 - 100$ region are rich in long-living isomeric states. Nucleons in the high spin $1g_{9/2}$ orbital can pair up from low to high spins, and odd nucleons can also occupy the low spin $2p_{1/2}$ orbital below, creating plenty of opportunities for spin-trap isomers. If a measured state is wrongly assigned as the ground state when in reality it is the isomer or a mixture of states, it can cause a substantial offset and lead to biased rp -process calculations. The excitation energies for low-lying, beta-decaying isomeric states have been very difficult to measure due to the lack of resolving power in available mass-measurement techniques. Recently, the Phase-Imaging Ion Cyclotron Resonance (PI-ICR) technique [15, 16] has made it possible to measure isomers with very low excitation energies ($E_x \geq 10$ keV), providing valuable data for understanding nucleon-nucleon interactions and single-particle properties in nuclei.

Many neutron-deficient nuclei in the $A = 80 - 100$ region have been challenging to produce at conventional

* markus.k.vilen@student.jyu.fi

ISOL facilities due to their refractory nature. One solution to the problem is the Ion Guide Isotope Separator On-Line (IGISOL) technique, which is a fast (sub-ms) and chemically insensitive method for the production of low-energy radioactive ion beams for nuclear physics experiments [17–19]. Although the IGISOL technique has proven to be a valuable tool in producing a great variety of rare isotope beams covering a large portion of the nuclear chart, heavy neutron-deficient nuclei lying further away from stability have been more difficult to access. The most commonly used ion-guide types at IGISOL have been optimized for either light-ion induced fusion or proton-induced fission reactions [18]. There, the target foil is mounted in direct contact with the buffer gas and the primary beam traverses through the gas cell. For heavy ion beams this is not possible because the primary beam would create a substantial number of buffer-gas ion-electron pairs which are detrimental to the overall efficiency. To tackle this problem, a Heavy-ion Ion Guide Isotope Separator On-Line (HIGISOL) method [19–21] employing a shadow gas-cell technique [22] was developed at IGISOL. In this method, the target is located in front of the ion guide and the primary beam is stopped before entering the gas cell. The reaction products are emitted at sufficiently large angles to bypass the beam dump and enter the gas cell through a thin window. Recently, the HIGISOL ion guide was upgraded and used in an on-line experiment for the first time. In this article, we report on this commissioning experiment which was used to produce neutron-deficient refractory isotopes for precision mass measurements improving the knowledge of the mass surface in the mass region $A \approx 80 - 90$.

II. EXPERIMENTAL METHODS

A. Production using the upgraded HIGISOL

The heavy neutron-deficient nuclei were produced employing a 260 pnA, 222 MeV $^{36}\text{Ar}^{8+}$ beam impinging on a ^{nat}Ni target with a thickness of $4\ \mu\text{m}$ at the IGISOL facility [18, 24]. The upgraded HIGISOL system (see FIG 1) houses two degrader foils that can be used to fine-tune the primary beam energy. However, in this work the full beam energy was used. The target was located outside the gas cell next to the degrader foils. The primary beam was stopped right after the target using a small cylindrical graphite beam dump mounted in front of the gas cell. This shielded the buffer gas from excessive ionization. In the new HIGISOL system the target is mounted on a rotating wheel and the degrader foils on frames that can be moved back and forth in order to allow the thermal power of the primary beam to be dissipated over a larger surface area. The electronics for the platform were upgraded and a new control system was constructed utilizing a combination of a Raspberry Pi computer and an Arduino microcontroller. The rotational frequency of the target wheel as well as the position of the target wheel

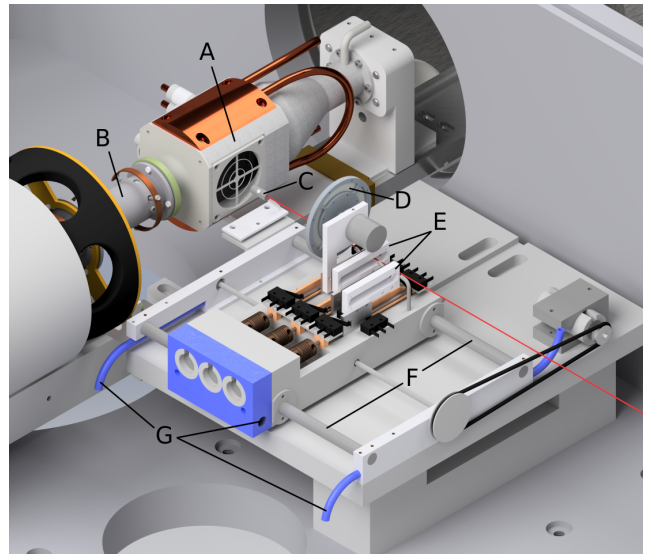


FIG. 1: The new HIGISOL system: A: Ion guide gas cell, B: SPIG [23], C: Beam dump, D: Target wheel, E: Degrader holder, F: Rails for distance adjustment, G: Coolant line.

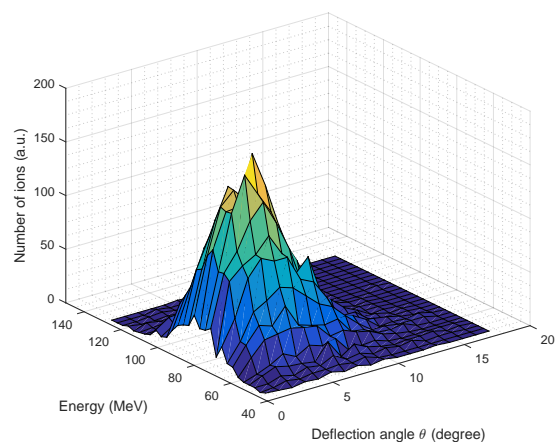


FIG. 2: Yield distribution (in arbitrary units) as a function of recoiling energy E_r and angle θ for a 228.60 MeV ^{36}Ar beam on a ^{nat}Ni target summed over all reaction products using the PACE4 program.

and degrader foils can now be remotely controlled using a Java-based software. Additionally, the whole platform can be remotely moved closer or further away from the gas cell, in parallel to the primary beam axis, based on the position information provided by the system. This production method has been utilized at IGISOL in the past using two mechanical designs. For further details, the reader is referred to [20] for the original design and to [21] for the second iteration of the system design.

The choice of primary beam energy was made based on fusion-evaporation cross-section simulations using

PACE4 [25], HIVAP [26] and NRV [27] codes. An example of an ion yield contour for an $^{36}\text{Ar}^{8+}$ beam on a ^{nat}Ni target obtained with the PACE4 [25] code is presented in FIG. 2. The position of the yield maximum changes as a function of primary beam energy in (E_r, θ) space, where E_r is the energy of recoiling reaction products and θ is the deflection angle. Reaction products have their yield maxima at slightly different, non-zero angles. Therefore, the distance between the gas cell and the target wheel needs to be optimized for each ion of interest so that the recoiling reaction products can enter the ion guide gas cell through its entrance window and are not implanted into the beam dump. In addition to the angle of the products, the kinetic energy of the reaction products has to be taken into account. Ions-of-interest must have enough energy after the target to go through the $2.17\mu\text{m}$ -thick Havar window and then be stopped and thermalized within the buffer gas (helium) volume of the HIGISOL ion guide. Therefore, the pressure (stopping power) of the buffer gas needs to be adjusted so that the range of the ions does not exceed the inner diameter of the HIGISOL gas cell (approximately 6 cm). In order to accommodate different recoil energies and angular distributions resulting from the choice of primary beam energy and target, both the distance between the target and the gas cell, as well as buffer gas pressure, can be adjusted in the new system. These degrees of freedom are sufficient for optimizing the system for different primary beam energies for a variety of reaction channels. In this experiment, the helium pressure was typically around 240 mbar.

Reaction products stopped and evacuated from the ion guide gas cell were collected and guided towards the high vacuum region of the mass separator using a radio-frequency sextupole ion guide (SPIG) [23], with a typical charge-state being $q = +e$. The ions were accelerated to 30 keV and mass-separated using a dipole magnet before stopping, cooling and bunching in the radio-frequency quadrupole cooler-buncher (RFQ) [28]. The ion bunches from the RFQ were injected into the double Penning trap mass spectrometer, JYFLTRAP [29].

B. Mass measurement techniques

Masses of the nuclides of interest were measured utilizing Time-of-Flight Ion-Cyclotron Resonance (TOF-ICR) [30, 31] and Phase-Imaging Ion-Cyclotron Resonance (PI-ICR) [15] techniques. Measured ions were prepared in the purification trap via the mass-selective buffer gas cooling method [32], capable of providing isobarically purified ion samples. Masses were determined in the precision trap by measuring the ion's cyclotron frequency $\nu_c = qB/(2\pi m)$, where q and m are the charge and mass of the ion, respectively, and B is the magnetic field strength. The magnetic field strength was acquired by interleaving measurements of ions with well-known masses ($\nu_{c,ref}$) before and after each measurement of the

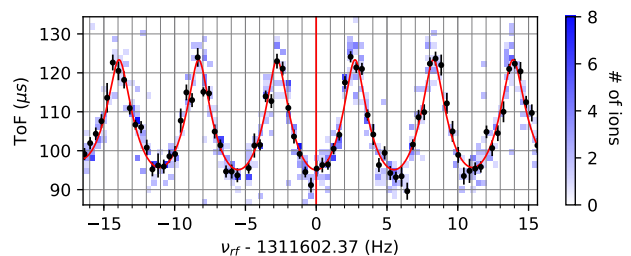


FIG. 3: A typical time-of-flight resonance of $^{82}\text{Zr}^+$ using Ramsey excitation pattern 25-150-25 ms (On-Off-On). The black points with error bars represent the mean time-of-flight for each scanned quadrupolar excitation frequency ν_{rf} . Background shading indicates the total number of ions in each time-of-flight bin. The red solid line is a fit of the theoretical curve [35] on the data points.

ion-of-interest (ν_c) and interpolating the field strength at the time of the ion-of-interest measurement. Identical excitation patterns were applied in the precision trap for the ion-of-interest and the reference ion in order to minimize the magnitude of any systematic errors due to different ion species. In this work, $^{85,87}\text{Rb}^+$ ions were used as references.

Two excitation schemes were utilized in the TOF-ICR measurements. A 200 ms quadrupole excitation pulse was used for ^{86}Mo and ^{88}Tc whereas the remaining masses were determined using the method of time-separated oscillatory fields [33, 34] with 25-750-25 ms (On-Off-On) excitation pattern for ^{84}Nb and 25-150-25 ms (On-Off-On) for ^{82}Zr and ^{89}Ru . For these cases, the position of the centre fringe was first verified via a measurement with a single conversion pulse. An example of a time-of-flight resonance of ^{82}Zr is presented in FIG. 3.

^{88}Tc was first measured using the TOF-ICR technique in order to improve the precision of the literature value of its ground-state mass. This was followed by a PI-ICR measurement in which the energy separation between the ground state and presumed first isomeric state was measured. The mass difference between the two states is too low to result in two separate peaks in the TOF-ICR measurement with 200 ms quadrupolar excitation.

In the PI-ICR measurements ion samples were prepared in the purification trap in the same way as with the TOF-ICR measurements. Ions were injected into the precision trap and the amplitude of residual coherent magnetron and axial motion was damped using RF fields of suitable frequency, phase and amplitude in preparation for the actual measurement. As ions are injected into the precision trap they acquire a non-zero amplitude for the magnetron and axial eigenmotions. If not addressed, the non-zero amplitudes would adversely affect the measurement precision. Therefore, for each eigenmotion, a dipole pulse with a suitable amplitude π rad out of phase with

the motion is applied in order to reduce the motion amplitude.

After the residual eigenmotion amplitudes were damped, a dipole excitation pulse at the modified cyclotron frequency ν_+ was applied followed by a phase accumulation time of 200 ms and a conversion pulse to convert the ion motion into magnetron motion. Finally, the ions were extracted out of the trap towards a position-sensitive delay-line MCP detector. This measurement cycle was followed by one with slightly modified timings. The second cycle was identical to the first one with the exception of the phase accumulation time being after the conversion pulse rather than before. Additionally, the center point of the precision trap was projected onto the detector. These three measurement cycles allowed us to calculate the mass difference between the ground and isomeric state of ^{88}Tc and $^{88}\text{Tc}^m$. For a more detailed discussion on this measurement technique the reader is referred to [15, 16], where the excitation scheme used in this work is presented as scheme 2.

C. Data analysis

In the case of the TOF-ICR method, the cyclotron frequency ν_c was measured multiple times for each nuclide. Each cyclotron frequency measurement was corrected, whenever possible, for shifts due to having multiple ions in the precision trap at the same time, as described in [36]. Data available for ions of interest were not sufficient to allow for this kind of corrections to be made. However, all reference ion species were sufficiently abundant for applying the correction. Additionally, a correction due to B -field fluctuations, $\delta_B(\nu_{c,ref})/\nu_{c,ref} = \Delta t \cdot 8.18 \cdot 10^{-12} / \text{min}$ [37], was applied to each interpolated reference ion frequency, where Δt is the time between consecutive reference measurements, followed by calculation of frequency ratio (r) for each measurement. Atomic masses were calculated according to

$$r = \frac{\nu_{c,ref}}{\nu_c} = \frac{m_{ion-of-interest}}{m_{reference\ ion}} \quad (1)$$

$$m = \frac{\nu_{c,ref}}{\nu_c} \cdot (m_{ref} - m_e) + m_e, \quad (2)$$

where the cyclotron frequencies ν_c are for the studied singly-charged ions and the masses are expressed as atomic masses unless stated otherwise in subscripts. Electron binding energies were neglected as such corrections are beyond the precision of our measurements.

A weighted mean of frequency ratios along with internal and external errors [38] were calculated, and the larger of the two was chosen as the uncertainty of the mean. In most cases the Birge ratios were smaller than one, indicating that statistical uncertainties of individual measurements were conservative. Finally, a mass-dependent uncertainty $\delta_m(r)/r = \Delta m \cdot 2.2(6) \cdot 10^{-10} / \text{u}$ [37] was added to the frequency ratio error, where Δm

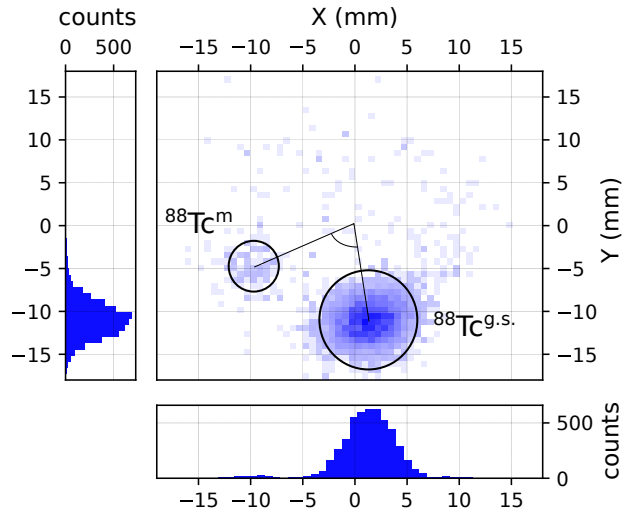


FIG. 4: Projection of reduced cyclotron motion of $^{88}\text{Tc}^+$ ions on the position-sensitive detector using the PI-ICR technique. The ground state and isomer are clearly separated using 200 ms phase accumulation time.

is the mass difference of the ion-of-interest and the reference ion. The applied data analysis process takes into account all systematic uncertainties that had been quantified at the time of the measurements. A detailed discussion on the different sources of systematic uncertainties at JYFLTRAP is to follow this article [39].

Data measured using the PI-ICR technique was used to determine the energy difference between the ground and the presumed first isomeric state of ^{88}Tc (see FIG. 4). The angle between the accumulated phases of magnetron and reduced cyclotron radial motions was calculated from multiple measurements for both the ground and isomeric state, followed by the calculation of the cyclotron frequency using

$$\nu_c = \frac{\phi + 2\pi(n_+ + n_-)}{2\pi t}, \quad (3)$$

where ϕ is the angle between the positions of the accumulated magnetron and cyclotron phase spots projected on the detector, n_+ and n_- the number of full revolutions ions completed in corresponding timing patterns within the phase accumulation time t . A frequency ratio between the isomeric and ground state, $r = \nu_{c,gs}/\nu_{c,is}$, was calculated for each measurement. A weighted mean of the frequency ratios was used to determine the mass difference Δm between the two states, i.e. the excitation energy of the isomer E_x , using

$$E_x = \Delta m = (r - 1)(m_{gs} - m_e), \quad (4)$$

where m_{gs} is the mass of the ground state determined in this work using the TOF-ICR technique. Inner and outer errors were determined, and the larger one was chosen as the error of the mean. Systematic uncertainties of the PI-ICR measurements with JYFLTRAP were

studied in [16]. Systematic uncertainties discussed in [16] were found to be insignificant compared to the statistical uncertainty of this work.

One additional systematic uncertainty that was accounted for in this work is the shift of measured frequency as a function of the angle between the accumulated phase spots in the PI-ICR method due to distortions of ion-motion projection onto the detector. As shown in FIG. 4, there was a non-zero angle between the isomeric and ground states. For the purpose of characterizing the effect of the angle another measurement was performed with stable ^{87}Rb ions where the ν_c frequency was determined using ^{87}Rb as a reference. The positions of the phase spots on the detector were tuned to match the ^{88}Tc measurement. In an ideal case a measurement like this would result in a frequency ratio $r = 1$. However, the measurement resulted in

$$r - 1 = -3.7(2) \cdot 10^{-8}. \quad (5)$$

This systematic shift was corrected for in the results and, additionally, added quadratically as a systematic uncertainty. In the case of the PI-ICR measurement between ^{88}Tc and $^{88}\text{Tc}^m$ the effect of having multiple ion species in the precision trap could not be accounted for due to the low production rate of the isomeric state.

III. RESULTS AND DISCUSSION

A. Results and comparison to literature

In this work a total of six masses were measured: ^{82}Zr , ^{84}Nb , ^{86}Mo , ^{88}Tc , $^{88}\text{Tc}^m$, and ^{89}Ru . Of these, $^{88}\text{Tc}^m$ and ^{89}Ru were measured for the first time. The mass-excess value for ^{89}Ru is 14 times more precise and 112(299) keV lower than the AME16 extrapolation. A more detailed study of the mass surface and separation energies is presented in Sect. III C. The excitation energy of the isomeric state in $^{88}\text{Tc}^m$ was also determined for the first time and it is discussed in Sect. III B. Precisions for the masses of ^{82}Zr , ^{84}Nb and ^{88}Tc were significantly improved and the mass of ^{86}Mo was verified in this work. The resulting mass-excess values along with frequency ratios and literature values for the reference ions are presented in Table I.

The mass values determined for ^{86}Mo and ^{88}Tc in this work agree well with the previous literature values from Penning-trap measurements. The mass-excess value of ^{86}Mo , $-64109(3)$ keV, agrees almost perfectly with the SHIPTRAP Penning trap measurement $-64110(4)$ keV [14]. Also the mass excess value determined in this work for ^{88}Tc , $-61669(2)$ keV, is in a good agreement with AME16. The AME16 value, $-61681(149)$ keV [40], is mainly based on an earlier measurement at JYFLTRAP [12] where the authors measured an unidentified state at $-61679.1(3.8)$ keV. The isomeric state could not be separated with the TOF-ICR technique used at that time,

which led the authors to assign the measured state as the high-spin ground state with an increased uncertainty of 87 keV based on analogy with the neighboring odd-odd nuclide ^{90}Tc .

Of the studied nuclides, ^{82}Zr and ^{84}Nb have both been measured at the CSRe storage ring [42] using isochronous mass spectrometry, and were already included in AME16 [40] as private communications. Our more precise measurements suggest that ^{82}Zr is 17(12) keV and ^{84}Nb 25(13) keV less bound than in AME16, resulting in a disagreement of more than one sigma in both cases. Since the AME16 values were based on the CSRe storage ring measurements [42], we decided to do a more thorough comparison between the Penning-trap and storage-ring measurements to find out if there is a systematic deviation between the two methods.

Firstly, we gathered all published CSRe results and checked which nuclides had been measured also with a Penning trap. All in all, there were 17 nuclides available for the comparison with the CSRe publications [42–46]. These include publications on ^{37}K [47] and ^{39}Ca [48] from ISOLTRAP, ^{42}Ti [49], ^{45}V [50], ^{49}Mn [50], ^{52}Co [51], $^{52}\text{Co}^m$ [51], ^{53}Co [52], ^{55}Ni [52], ^{57}Cu [52], ^{59}Zn [52], ^{82}Zr (this work), ^{84}Nb (this work) from JYFLTRAP, ^{56}Cu [53] from LEBIT and ^{90}Ru [12, 54] from CPT, SHIPTRAP and JYFLTRAP. As can be seen from FIG. 5, Penning-trap measurements seem to give on the average around 20 keV higher mass values than CSRe. It is also noteworthy that only 4 out of 17 measurements give lower mass values than CSRe.

The obtained χ_n value between the two methods, calculated according to

$$\chi_n = \sqrt{\frac{1}{N} \sum_{i=1}^N \frac{(ME_{trap,i} - ME_{CSRe,i})^2}{\delta ME_{trap,i}^2 + \delta ME_{CSRe,i}^2}} \quad (6)$$

is $\chi_n = 1.54$ without the revised CSRe values for ^{45}V and ^{49}Mn [46], and $\chi_n = 1.47$ using the revised values. In both cases, the χ_n value is above the limit $\chi_n = 1 + 1/\sqrt{2N} = 1.18$. Therefore, the deviation between the trap and CSRe measurements cannot be explained solely by statistical fluctuations of the two datasets. Note that here only the JYFLTRAP measurement for ^{90}Ru was taken into account in order not to triple count the CSRe measurement.

In addition to the above mentioned measurements, estimations for ^{63}Ge , ^{65}As , ^{67}Se and ^{71}Kr can be obtained from the mirror displacement energies (MDE) and precise Penning-trap measurements of ^{63}Ga [55] at ISOLTRAP as well as ^{63}Ga [56], ^{65}Ge [56], ^{67}As [56] and ^{71}Br [57] at LEBIT. These are shown as open circles in Fig. 5. Above $A = 63$, all the Penning-trap values are clearly higher than what the CSRe measurements yield.

TABLE I: Frequency ratios (r) and mass-excess values (ME_{JYFL}) determined in this work with JYFLTRAP and compared with AME16 [40]. All measurements were done with singly-charged ions. The reference masses, ^{85}Rb ($ME = -82167.331(5)$ [40]) and ^{87}Rb ($ME = -84597.791(6)$ [40]) were adopted from AME16, and # signs indicate extrapolated values therein. The differences between the this work and AME16 are listed in the last column. The excitation energy for $^{88}\text{Tc}^m$, $E_x = 70.4(31)$ keV, was determined for the first time, see text for details.

Nuclide	Reference	$r = \nu_{c,ref}/\nu_c$	$ME_{JYFL}(\text{keV})$	$ME_{AME16}(\text{keV})$	$\Delta ME_{JYFL-AME16}(\text{keV})$
^{82}Zr	^{85}Rb	0.964 903 56(2)	-63613(2)	-63631(12)	17(12)
^{84}Nb	^{85}Rb	0.988 488 167(5)	-61193.8(4)	-61219(13)	25(13)
^{86}Mo	^{85}Rb	1.012 005 28(6)	-64112(5)	-64113(5)	-2(6)
^{88}Tc	^{87}Rb	1.011 789 55(5)	-61670(4)	-61681(149)	11(149)
$^{88}\text{Tc}^m$	^{88}Tc	1.000 000 86(4) ^a	-61600(5)	-61680(340)# [41]	-80(340)#
^{89}Ru	^{85}Rb	1.047 408 9(3)	-58372(21)	-58260(298)#	-112(299)#

^a Measured using the PI-ICR technique.

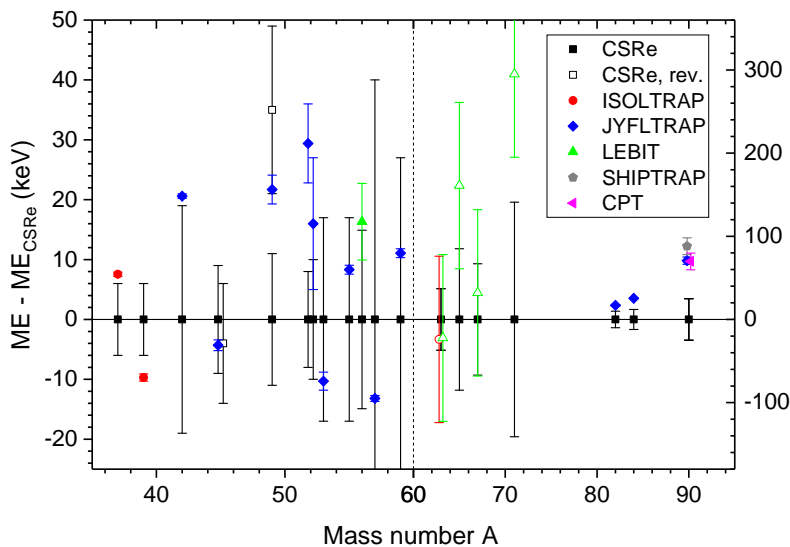


FIG. 5: Comparison of Penning-trap measurements performed at ISOLTRAP, JYFLTRAP, LEBIT, SHIPTRAP and CPT to the results from CSRe. The open circle and triangles denote the masses estimated based on the masses of ^{63}Ga , ^{65}Ge , ^{67}As and ^{71}Br and mirror displacement energies. The revised CSRe values for ^{45}V and ^{49}Mn are shown by an open square. Note the different y-axis scale after $A = 60$ (shown on the right-hand side).

B. Isomeric state in ^{88}Tc

In this work, we determined the excitation energy and the mass-excess value for the isomeric state in ^{88}Tc for the first time using the recently implemented PI-ICR technique at JYFLTRAP. Moreover, this enabled us to remove the uncertainty regarding the isomeric contamination, and therefore considerably improve the precision of the ground-state mass. The mass excess of $^{88}\text{Tc}^m$ was determined using a combination of two measurements. Firstly, the dominantly produced ground state was measured using the TOF-ICR technique. Secondly, the less-populated isomeric state was successfully separated from the dominant state using the PI-ICR technique. The latter was used to measure the excitation energy of the

isomeric state and to determine the relative abundance of the two states. It was found that the ground state accounted for 97(1)% of ions detected after the Penning traps. The excitation energy of the isomeric state was measured to be 70.4(31) keV.

Based on the yield ratio and the excitation energy of the isomeric state, i.e. frequency ratio of the two states, a correction was made for the TOF-ICR measurement of ^{88}Tc to account for the presence of the weakly populated isomeric state. The applied correction was calculated using

$$\nu_{c,measured} = a\nu_{c,gs} + (1-a)\nu_{c,is}, \quad (7)$$

leading to

$$\frac{\nu_{c,measured}}{\nu_{c,gs}} = a + (1 - a) \frac{\nu_{c,is}}{\nu_{c,gs}}, \quad (8)$$

where a is the fraction of ions in the ground state. Using frequency ratio $\nu_{c,is}/\nu_{c,gs}$ from the PI-ICR measurement, we get

$$\nu_{c,measured} = (1 - 25.7 \cdot 10^{-9}) \nu_{c,gs}. \quad (9)$$

Applying this correction to all TOF-ICR measurements of ^{88}Tc resulted in a shift of -2.1 keV to the ground-state mass excess. In order to be conservative with our results, the error of the ground-state mass excess was increased by the same amount. The mass excess and frequency ratio values of ^{88}Tc and $^{88}\text{Tc}^m$ presented in Table I have this correction included.

In addition to the states measured in this work, there is a second isomeric state with a very short half-life, $T_{1/2} = 146$ ns, listed in the latest NUBASE16 evaluation of nuclear properties [41]. The half-life of the state is several orders of magnitude below what is reachable via Penning-trap mass measurements. Therefore, we conclude that our results correspond to states listed as the ground state and the longer-lived isomeric state in [41], with half-lives 6.4 s and 5.8 s, respectively.

The order of the three lowest states in ^{88}Tc has remained unclear. The presumed ground state of ^{88}Tc was observed for the first time in 1991, and assigned as $7, 8^+$ due to observed feeding of 8^+ and 7^- states in ^{88}Mo [61]. The beta-decay study of Odahara et al. [62] suggested spins of 3^+ and 6^+ for the detected states with half-lives of 5.8(2) s and 6.4(8) s, respectively. The isomeric states of ^{88}Tc were further studied by Garnsworthy et al. [63]. Based on the observed 95-keV transition, which they assign tentatively as $4^+ \rightarrow 2^+$, and by comparing with the shell-model calculations using the Gross-Frenkel interaction [64] in a $1g_{9/2} - 2p_{1/2}$ model space, they suggest that the $(5^+, 6^+, 7^+)$ state listed as the ground state in [41] would in reality be the first isomeric state with spin 6^+ . The ground state would then be 2^+ fed by the observed 95-keV transition.

The excitation energy measured in this work, $E_x = 70.4(31)$ keV, is lower than the observed 95 keV transition energy for the $4^+ \rightarrow 2^+$ (or $2^+ \rightarrow 4^+$) transition in [63]. Therefore, either the 4^+ or 2^+ state should lie above the isomeric state observed in this work. We studied possible options for the order of the states: (i) 6^+ ($E_x = 0$ keV), 2^+ ($E_x = 70$ keV), 4^+ ($E_x = 165$ keV), (ii) 6^+ ($E_x = 0$ keV), 4^+ ($E_x = 70$ keV), 2^+ ($E_x = 165$ keV), (iii) 2^+ ($E_x = 0$ keV), 6^+ ($E_x = 70$ keV), 4^+ ($E_x = 95$ keV), or (iv) 4^+ ($E_x = 0$ keV), 6^+ ($E_x = 70$ keV), 2^+ ($E_x = 95$ keV). We calculated half-lives for the isomeric states using Weisskopf estimates. Option (i) is not plausible since the 165-keV $E2$ transition from 4^+ to 6^+ should be faster and more intense than the 95-keV transition observed clearly in [63], and therefore should have been detected in the earlier works [61, 63]. The fact that

no other gamma rays than the 95-keV transition was observed from the 146(12)-ns isomeric state in [63] is revealing: the energy difference between the states has to be so small that it was below the detection threshold in [63].

For option (ii), the 70-keV $E2$ transition would be too fast for the state to be detected with a Penning trap. The same is true for option (iv), and it can be excluded. Therefore, the most likely option is (iii), with 2^+ as the ground state and 6^+ as the isomeric state just below the 4^+ state (see Fig. 6). This result is somewhat surprising because 97(1)% of the ions detected after the Penning traps belonged to the ground state of ^{88}Tc . Heavy-ion fusion-evaporation reactions tend to predominantly populate higher-spin states. As such, the production ratio of the states would favor 6^+ as the ground state, i.e. option (i). Note that the half-lives of the ground and isomeric states are roughly similar [62] and long compared to the trap cycles, and cannot therefore explain the dominance of the ground-state ions.

Shell-model calculations were performed in order to compare our experimental results with theoretical models. Three nuclear interactions were employed, slgt0 [58], jun45 [59] and jj44b [60], using the same model space as in [63], $1p_{1/2} - 0g_{9/2}$. Acquired level schemes, presented in FIG. 6, do not give a consistent picture of the order of the states and, additionally, significantly overestimate excitation energies. It is interesting to note, however, that jj44b in the smaller model space (FIG. 6.(d)) would agree well with the level ordering of option (i), i.e. 6^+ ground state and 2^+ isomer. This would also be compatible with the production argument that higher-spin states are favored in heavy-ion fusion-evaporation reactions.

Shell-model calculations were repeated using a larger model space, $0f_{5/2} - 1p - 0g_{9/2}$, with jun45 and jj44b interactions, see Fig. 6. The larger model space changed the order of the states as well as produced energy levels closer to experimental results. However, spins of the states are still not in agreement with expectations based on experimental results. Discrepancies between the experimental and theoretical level schemes, as well as between the level schemes obtained with different theoretical model spaces, show that theoretical approaches for this particular nuclide are highly sensitive and cannot offer additional support for the spin assignments.

C. Mass surface in the region

The effect of this work on the mass surface was studied via two-neutron (S_{2n}) and two-proton (S_{2p}) separation energies, and neutron pairing-gap energies D_n . Two-neutron and two-proton separation energies are sensitive to trends in nuclear structure irrespective of odd-even staggering, making them a useful tool in searching for changes in nuclear deformation and onset of shell-closures. Neutron pairing gap energies D_n were used as a complementary tool to S_{2n} and S_{2p} energies since it is

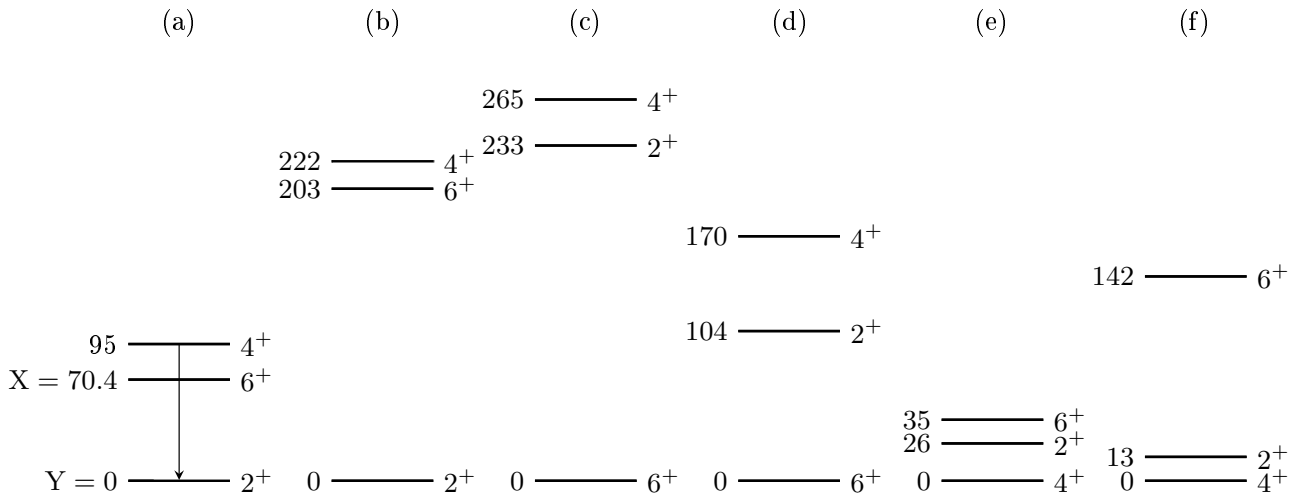


FIG. 6: Experimental (a) and theoretical excitation energies (b-f) for ^{88}Tc . Based on this work, the ground state is most likely 2^+ and the first isomeric state 6^+ . The theoretical calculations employed the $1p_{1/2}-0g_{9/2}$ model space with the interactions (b) *slgt0* [58], (c) *jun45* [59] and (d) *jj44b* [60], and the $0f_{5/2}-1p-0g_{9/2}$ model space with the interactions (e) *jun45* [59] and (f) *jj44b* [60].

a quantity highly sensitive to pairing of single neutrons.

Two-neutron separation energies in the region of this work are presented in FIG. 7. The new data introduces minor changes to Zr, Nb, Mo and Tc isotopic chains. The new values offer improved precision compared to [40] and follow the trend set by the literature values. This work extends the Ru isotopic chain by one isotope, revealing an over-estimation of S_{2n} energy by extrapolated theoretical values.

Two-proton separation energies S_{2p} , see FIG. 8, largely mirror the changes seen in two-neutron separation energies. Similarly as with the S_{2n} values, minor changes are introduced to Zr, Nb, Mo and Tc isotopic chains by the new results. Also, the Ru chain is again extended by one additional isotope, revealing an under-estimation of S_{2p} energy by extrapolated theoretical values.

The new S_{2n} and S_{2p} results suggest minor changes compared to theoretical values in the case of the Ru chain, but do not reveal any major changes in the case of previously experimentally-known masses.

Neutron pairing-gap energies

$$D_n = (-1)^{N+1}[S_n(Z, N+1) - S_n(Z, N)] \quad (10)$$

[65], where S_n are neutron separation energies, were also studied. D_n energies, contrary to S_{2n} and S_{2p} , are an effective indicator of changes in pairing of individual valence neutrons. This is highlighted by the fact that the neutron pairing gap energy can be expressed using the empirical neutron pairing gap $\Delta^3(N) = D_n(N)/2$ which is also known as the odd-even staggering parameter [66]. Neutron pairing gap energies affected by this work are presented in FIG. 9.

Similarly to S_{2n} and S_{2p} energies, the neutron pairing gap energies of this work produce only minor changes

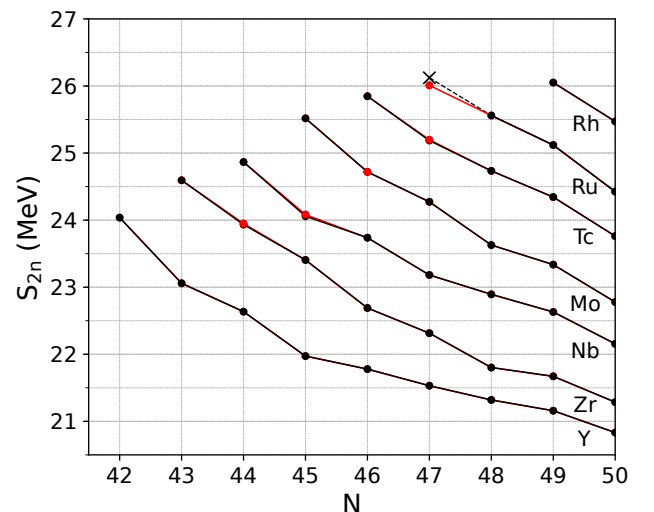


FIG. 7: Two-neutron separation energies S_{2n} . Experimental AME16 [40] values are presented with black dots and results affected by this work with red dots. An extrapolated value for ^{91}Ru adopted from [40] is presented with an X.

in Zr, Nb, Mo and Tc isotopic chains. In the case of ^{90}Ru , this work shows a clear over-estimation of odd-even staggering by extrapolated values of [40].

TABLE II: Mass-excess values (ME_{JYFL}) determined in this work, using the measured mass-excess values of ^{82}Zr and ^{86}Mo and the theoretical MDEs, compared with the AME16 [40] values (ME_{AME16}), where # indicates extrapolated values therein. The uncertainties given in brackets are deduced from the errors of fitted parameters and RMSD, respectively. The differences between the two data sets are listed in the last column.

Nuclide	T_z	MDE(keV)	ME_{JYFL} (keV)	ME_{AME16} (keV)	$\Delta ME_{JYFL-AME16}$ (keV)
^{86}Ru	-1	25370(50)(180)	-40310(190)	-39770(400)#	-540(450)
^{82}Mo	-1	24290(50)(180)	-40910(190)	-40370(400)#	-540(450)

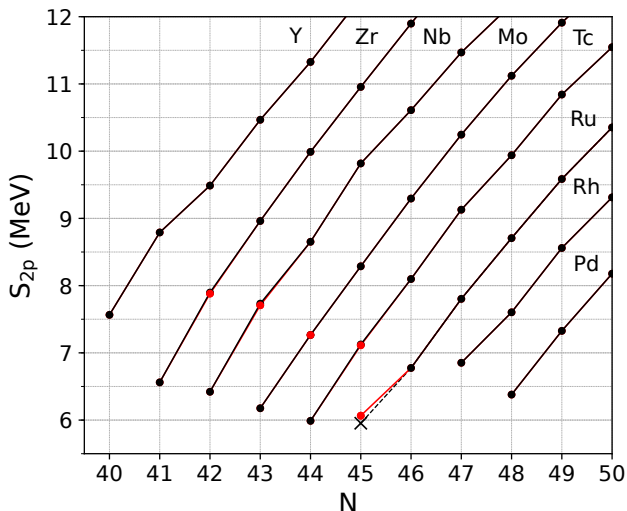


FIG. 8: Two-proton separation energies S_{2p} . Experimental AME16 [40] values are presented with black dots and results affected by this work with red dots. An extrapolated value for ^{89}Ru adopted from [40] is presented with an X.

D. Mass predictions using mirror displacement energies

In this work, we measured the ground-state mass of ^{89}Ru for the first time. Our result, $-58372(21)$ keV, indicated that it is somewhat (by $112(299)$ keV) more bound than the extrapolated literature value, $-58260(298)$ keV [40]. Since we measured many isospin projection $T_z = (N - Z)/2 = +1$ nuclei, we decided to investigate what kind of mass predictions we obtain for the $T_z = -1$ mirror partners by combining our precise mass measurements of $T_z = +1$ nuclei with the state-of-the-art theoretical calculations for mirror displacement energies (MDE) [3, 4]. Such a method was proved to provide accurate predictions for lower mass numbers, such as $A = 52$ [3]. The theoretical calculations presented in this work employ extended Skyrme energy density functional $SV_{\text{T:NLO}}^{\text{ISB}}$ with proton-neutron-mixed densities and isospin-symmetry-breaking terms in next-to-leading order [4].

The calculations yield mirror displacement energies of $24290(50)(180)$ keV for $A = 82$ and $25370(50)(180)$ keV for $A = 86$. The uncertainties given in brackets are de-

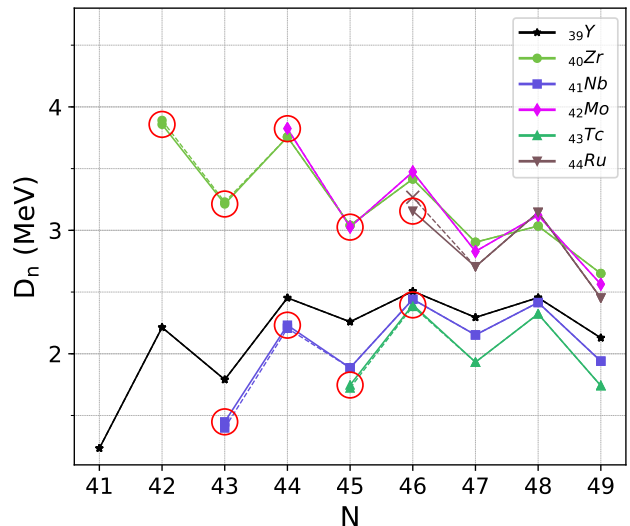


FIG. 9: Neutron pairing-gap energies D_n . Experimental AME16 [40] values are presented with dashed lines and AME16 values together with results from this work with solid lines. An extrapolated value for ^{90}Ru adopted from [40] is presented with an X. Results affected by this work are highlighted with red circles.

duced from the errors of fitted parameters and RMSD, respectively. Predictions for $A = 84$ and $A = 88$ were not presented since $T_z = -1$ partners in these triplets are most likely proton-unbound and the model is not suitable for performing calculations of such nuclei. For the same reason, the $T = 1/2$ doublet at $A = 89$ was not studied. The mass excesses of $T_z = -1$ isotopes ^{86}Ru and ^{82}Mo were calculated utilizing the results from this work for respective $T_z = +1$ mirror nuclei ^{86}Mo and ^{82}Zr (see Table II). The results from this work consistently predict more bound nuclei than literature [40], and also decrease the uncertainty of the predicted mass-excess values.

IV. CONCLUSIONS

An upgraded system for the production of neutron-deficient isotopes using heavy-ion beams has been successfully commissioned at IGISOL. The new system was used in its first on-line experiment where a total of six

masses were measured, ^{82}Zr , ^{84}Nb , ^{86}Mo , ^{88}Tc , $^{88}\text{Tc}^m$ and ^{89}Ru . The precisions of ^{82}Zr , ^{84}Nb and ^{88}Tc were improved and the literature value of ^{86}Mo was verified. $^{88}\text{Tc}^m$ and ^{89}Ru were measured for the first time.

The new results for ^{82}Zr and ^{84}Nb do not fully agree with the literature values based on the measurements at the CSRe storage ring in Lanzhou [42]. A thorough comparison between the results from the CSRe and several Penning traps was performed, and a deviation larger than what can be explained by statistical fluctuations alone was discovered. The comparison suggests that Penning trap measurement seem to produce on average about 20 keV higher mass values. The impact on the astrophysical rp -process was already studied in [42]. A systematic shift of around 10 keV will not have a huge impact on the calculated abundances and light curves as it will be partly cancelled out in the proton separation energies used as an input for the rp -process calculations.

The excitation energy for the long-living isomer in ^{88}Tc , 70.4(31) keV, was determined for the first time in this work. The order of the lowest three levels in ^{88}Tc was studied based on the excitation energy together with known and expected half-lives for the states. Based on the new limitations, 2^+ is most likely the ground state and 6^+ the first isomer in ^{88}Tc . This is somewhat unexpected since the ground state was dominantly produced, contrary to the expectation of better production for the higher-spin state.

Masses of ^{82}Zr and ^{86}Mo measured in this campaign were used to study corresponding mirror nuclei ^{82}Mo and ^{86}Ru via theoretical MDE's. The resulting mass-excess values are more precise than predicted in the most recent atomic mass evaluation for ^{82}Mo and ^{86}Ru [40]. The new values suggest that the studied nuclei are more tightly bound than expected from extrapolations of the mass

surface [40]. This is consistent with the observation that the mass of ^{89}Ru measured in this work for the first time was lower than the AME16 extrapolation.

In conclusion, we have improved the knowledge of the mass surface in the neutron-deficient mass region $A = 82 - 89$ by precise Penning-trap measurements. The results indicate that the extrapolated masses might be somewhat overpredicted in this region. Future precision measurements aiming toward $N = Z$ nuclei or beyond, are anticipated to shed more light on the evolution of the mass surface in this region rich in isomeric states and structural changes. The recently commissioned PI-ICR technique will be an invaluable tool for revealing and identifying longer-living isomeric states as demonstrated with ^{88}Tc in this work.

ACKNOWLEDGMENTS

This work has been supported by the Academy of Finland under the Finnish Centre of Excellence Programme 2012-2017 (Nuclear and Accelerator Based Physics Research at JYFL). A.K., D.N., L.C., and T.E. acknowledge support from the Academy of Finland under projects No. 275389, 284516, 312544, 295207, and 306980. This project has also received funding from the European Union's Horizon 2020 research and innovation program under grant agreement No. 771036 (ERC CoG MAIDEN). This work was supported in part by the Polish National Science Centre under Contract Nos. 2015/17/N/ST2/04025, 2017/24/T/ST2/00159 and No. 2018/31/B/ST2/02220. We acknowledge the CIŚ Świerk Computing Center, Poland, for the allocation of computational resources. J.D. acknowledges support by the STFC Grants No. ST/M006433/1 and No. ST/P003885/1.

-
- [1] B. Cederwall, F. G. Moradi, T. Bäck, A. Johnson, J. Blomqvist, E. Clément, G. de France, R. Wadsworth, K. Andgren, K. Lagergren, A. Dijon, G. Jaworski, R. Liotta, C. Qi, B. M. Nyakó, J. Nyberg, M. Palacz, H. Al-Azri, A. Algora, G. de Angelis, A. Ataç, S. Bhattacharyya, T. Brock, J. R. Brown, P. Davies, A. D. Nitto, Z. Dombrádi, A. Gadea, J. Gál, B. Hadinia, F. Johnston-Theasby, P. Joshi, K. Juhász, R. Julin, A. Jungclaus, G. Kalinka, S. O. Kara, A. Khaplanov, J. Kownacki, G. L. Rana, S. M. Lenzi, J. Molnár, R. Moro, D. R. Napoli, B. S. N. Singh, A. Persson, F. Recchia, M. Sandzelius, J.-N. Scheurer, G. Sletten, D. Sohler, P.-A. Söderström, M. J. Taylor, J. Timár, J. J. Valiente-Dobón, E. Vardaci, and S. Williams, *Nature* **469**, 68 (2011).
- [2] S. Frauendorf and A. Macchiavelli, *Progr. Part. Nucl. Phys.* **78**, 24 (2014).
- [3] P. Bączyk, J. Dobaczewski, M. Konieczka, W. Satuła, T. Nakatsukasa, and K. Sato, *Phys. Lett. B* **778**, 178 (2018).
- [4] P. Bączyk, W. Satuła, J. Dobaczewski, and M. Konieczka, *J. Phys. G: Nucl. Part. Phys.* **46**, 03LT01 (2019).
- [5] C. J. Lister, M. Campbell, A. A. Chishti, W. Gelletly, L. Goettig, R. Moscrop, B. J. Varley, A. N. James, T. Morrison, H. G. Price, J. Simpson, K. Connel, and O. Skeppstedt, *Phys. Rev. Lett.* **59**, 1270 (1987).
- [6] S. J. Zheng, F. R. Xu, S. F. Shen, H. L. Liu, R. Wyss, and Y. P. Yan, *Phys. Rev. C* **90**, 064309 (2014).
- [7] J. Dudek, A. Goźdz, N. Schunck, and M. Miśkiewicz, *Phys. Rev. Lett.* **88**, 252502 (2002).
- [8] D. Lunney, J. M. Pearson, and C. Thibault, *Rev. Mod. Phys.* **75**, 1021 (2003).
- [9] H. Schatz, *Int. J. Mass Spectrom.* **251**, 293 (2006).
- [10] H. Schatz and W.-J. Ong, *Astrophys. J.* **844**, 139 (2017).
- [11] A. Kankainen, S. A. Eliseev, T. Eronen, S. P. Fox, U. Hager, J. Hakala, W. Huang, J. Huikari, D. Jenkins, A. Jokinen, S. Kopecky, I. Moore, A. Nieminen, Y. N. Novikov, H. Penttilä, A. V. Popov, S. Rinta-Antila, H. Schatz, D. M. Seliverstov, G. K. Vorobjev, Y. Wang,

- J. Äystö, and the IS403 Collaboration, *Eur. Phys. J. A* **25**, 129 (2005).
- [12] C. Weber, V.-V. Elomaa, R. Ferrer, C. Fröhlich, D. Ackermann, J. Äystö, G. Audi, L. Batist, K. Blaum, M. Block, A. Chaudhuri, M. Dworschak, S. Eliseev, T. Eronen, U. Hager, J. Hakala, F. Herfurth, F. P. Heßberger, S. Hofmann, A. Jokinen, A. Kankainen, H.-J. Kluge, K. Langanke, A. Martín, G. Martínez-Pinedo, M. Mazzocco, I. D. Moore, J. B. Neumayr, Y. N. Novikov, H. Penttilä, W. R. Plaß, A. V. Popov, S. Rahaman, T. Rauscher, C. Rauth, J. Rissanen, D. Rodríguez, A. Saastamoinen, C. Scheidenberger, L. Schweikhard, D. M. Seliverstov, T. Sonoda, F.-K. Thielemann, P. G. Thirolf, and G. K. Vorobjev, *Phys. Rev. C* **78**, 054310 (2008).
- [13] V.-V. Elomaa, G. K. Vorobjev, A. Kankainen, L. Batist, S. Eliseev, T. Eronen, J. Hakala, A. Jokinen, I. D. Moore, Y. N. Novikov, H. Penttilä, A. Popov, S. Rahaman, J. Rissanen, A. Saastamoinen, H. Schatz, D. M. Seliverstov, C. Weber, and J. Äystö, *Phys. Rev. Lett.* **102**, 252501 (2009).
- [14] E. Haettner, D. Ackermann, G. Audi, K. Blaum, M. Block, S. Eliseev, T. Fleckenstein, F. Herfurth, F. P. Heßberger, S. Hofmann, J. Ketelaer, J. Ketter, H.-J. Kluge, G. Marx, M. Mazzocco, Y. N. Novikov, W. R. Plaß, S. Rahaman, T. Rauscher, D. Rodríguez, H. Schatz, C. Scheidenberger, L. Schweikhard, B. Sun, P. G. Thirolf, G. Vorobjev, M. Wang, and C. Weber, *Phys. Rev. Lett.* **106**, 122501 (2011).
- [15] S. Eliseev, K. Blaum, M. Block, A. Dörr, C. Droese, T. Eronen, M. Goncharov, M. Höcker, J. Ketter, E. M. Ramirez, D. A. Nesterenko, Y. N. Novikov, and L. Schweikhard, *Appl. Phys. B* **114**, 107 (2014).
- [16] D. A. Nesterenko, T. Eronen, A. Kankainen, L. Canete, A. Jokinen, I. D. Moore, H. Penttilä, S. Rinta-Antila, A. de Roubin, and M. Vilen, *Eur. Phys. J. A* **54**, 154 (2018).
- [17] J. Ärje, J. Äystö, H. Hyvönen, P. Taskinen, V. Koponen, J. Honkanen, A. Hautojärvi, and K. Vierinen, *Phys. Rev. Lett.* **54**, 99 (1985).
- [18] J. Äystö, *Nucl. Phys. A* **693**, 477 (2001).
- [19] I. D. Moore, P. Dendooven, and J. Ärje, *Hyperfine Int.* **223**, 17 (2013).
- [20] J. Huikari, P. Dendooven, A. Jokinen, A. Nieminen, H. Penttilä, K. Peräjärvi, A. Popov, S. Rinta-Antila, and J. Äystö, *Nucl. Instrum. Meth. Phys. Res. B* **222**, 632 (2004).
- [21] V.-V. Elomaa, *Mass measurements for explosive nucleosynthesis in stars*, *Ph.D. thesis*, University of Jyväskylä (2009).
- [22] R. Béraud, A. Emsallem, A. Astier, R. Bouvier, R. Dufait, Y. L. Coz, S. Morier, A. Wojtasiewicz, Y. Lazarev, I. Shirokovsky, I. Izosimov, D. Barnéoud, J. Genevey, A. Gizon, R. Guglielmini, G. Margotton, and J. Vieux-Rochaz, *Nucl. Instrum. Meth. Phys. Res. A* **346**, 196 (1994).
- [23] P. Karvonen, I. Moore, T. Sonoda, T. Kessler, H. Penttilä, K. Peräjärvi, P. Ronkanen, and J. Äystö, *Nucl. Instrum. Meth. Phys. Res. B* **266**, 4794 (2008).
- [24] I. Moore, T. Eronen, D. Gorelov, J. Hakala, A. Jokinen, A. Kankainen, V. Kolhinen, J. Koponen, H. Penttilä, I. Pohjalainen, M. Reponen, J. Rissanen, A. Saastamoinen, S. Rinta-Antila, V. Sonnenschein, and J. Äystö, *Nucl. Instrum. Meth. Phys. Res. B* **317**, 208 (2013).
- [25] O. Tarasov and D. Bazin, *Nucl. Instrum. Meth. Phys. Res. B* **266**, 4657 (2008).
- [26] N. Wang and W. Scheid, *Phys. Rev. C* **78**, 014607 (2008).
- [27] V. I. Zagrebaev, A. S. Denikin, A. V. Karpov, A. P. Alekseev, M. A. Naumenko, V. A. Rachkov, V. V. Samarin, and V. V. Saiko, “NRV web knowledge base on low-energy nuclear physics,” (1999).
- [28] A. Nieminen, J. Huikari, A. Jokinen, J. Äystö, P. Campbell, and E. Cochrane, *Nucl. Instrum. Meth. Phys. Res. A* **469**, 244 (2001).
- [29] T. Eronen, V. S. Kolhinen, V. V. Elomaa, D. Gorelov, U. Hager, J. Hakala, A. Jokinen, A. Kankainen, P. Karvonen, S. Kopecky, I. D. Moore, H. Penttilä, S. Rahaman, S. Rinta-Antila, J. Rissanen, A. Saastamoinen, J. Szerypo, C. Weber, and J. Äystö, *Eur. Phys. J. A* **48**, 46 (2012).
- [30] G. Gräff, H. Kalinowsky, and J. Traut, *Z. Phys. A* **297**, 35 (1980).
- [31] M. König, G. Bollen, H.-J. Kluge, T. Otto, and J. Szerypo, *Int. J. Mass Spectrom. Ion Proc.* **142**, 95 (1995).
- [32] G. Savard, S. Becker, G. Bollen, H.-J. Kluge, R. Moore, T. Otto, L. Schweikhard, H. Stolzenberg, and U. Wiess, *Phys. Lett. A* **158**, 247 (1991).
- [33] M. Kretzschmar, *Int. J. Mass Spectrom.* **264**, 122 (2007).
- [34] S. George, K. Blaum, F. Herfurth, A. Herlert, M. Kretzschmar, S. Nagy, S. Schwarz, L. Schweikhard, and C. Yazidjian, *Int. J. Mass Spectrom.* **264**, 110 (2007).
- [35] M. Kretzschmar, *Int. J. Mass Spectrom.* **264**, 122 (2007).
- [36] A. Kellerbauer, K. Blaum, G. Bollen, F. Herfurth, H.-J. Kluge, M. Kuckein, E. Sauvan, C. Scheidenberger, and L. Schweikhard, *Eur. Phys. J. D* **22**, 53 (2003).
- [37] L. Canete, *High precision mass measurements for nuclear astrophysics*, *Ph.D. thesis*, Jyväskylä (2019).
- [38] R. T. Birge, *Phys. Rev.* **40**, 207 (1932).
- [39] D. Nesterenko, M. Vilén, T. Eronen, A. Kankainen, *et al.*, To be submitted (2019).
- [40] M. Wang, G. Audi, F. Kondev, W. Huang, S. Naimi, and X. Xu, *Chin. Phys. C* **41**, 030003 (2017).
- [41] G. Audi, F. G. Kondev, M. Wang, W. Huang, and S. Naimi, *Chin. Phys. C* **41**, 030001 (2017).
- [42] Y. Xing, K. Li, Y. Zhang, X. Zhou, M. Wang, Y. Litvinov, K. Blaum, S. Wanajo, S. Kubono, G. Martínez-Pinedo, A. Sieverding, R. Chen, P. Shuai, C. Fu, X. Yan, W. Huang, X. Xu, X. Tang, H. Xu, T. Bao, X. Chen, B. Gao, J. He, Y. Lam, H. Li, J. Liu, X. Ma, R. Mao, M. Si, M. Sun, X. Tu, Q. Wang, J. Yang, Y. Yuan, Q. Zeng, P. Zhang, X. Zhou, W. Zhan, S. Litvinov, G. Audi, T. Uesaka, Y. Yamaguchi, T. Yamaguchi, A. Ozawa, C. Fröhlich, T. Rauscher, F.-K. Thielemann, B. Sun, Y. Sun, A. Dai, and F. Xu, *Phys. Lett. B* **781**, 358 (2018).
- [43] X. Tu, M. Wang, Y. Litvinov, Y. Zhang, H. Xu, Z. Sun, G. Audi, K. Blaum, C. Du, W. Huang, Z. Hu, P. Geng, S. Jin, L. Liu, Y. Liu, B. Mei, R. Mao, X. Ma, H. Suzuki, P. Shuai, Y. Sun, S. Tang, J. Wang, S. Wang, G. Xiao, X. Xu, J. Xia, J. Yang, R. Ye, T. Yamaguchi, X. Yan, Y. Yuan, Y. Yamaguchi, Y. Zhang, H. Zhao, T. Zhao, X. Zhang, X. Zhou, and W. Zhan, *Nucl. Instrum. Meth. Phys. Res. A* **654**, 213 (2011).
- [44] X. Xu, P. Zhang, P. Shuai, R. J. Chen, X. L. Yan, Y. H. Zhang, M. Wang, Y. A. Litvinov, H. S. Xu, T. Bao, X. C. Chen, H. Chen, C. Y. Fu, S. Kubono, Y. H. Lam, D. W. Liu, R. S. Mao, X. W. Ma, M. Z. Sun, X. L. Tu, Y. M. Xing, J. C. Yang, Y. J. Yuan, Q. Zeng, X. Zhou, X. H.

- Zhou, W. L. Zhan, S. Litvinov, K. Blaum, G. Audi, T. Uesaka, Y. Yamaguchi, T. Yamaguchi, A. Ozawa, B. H. Sun, Y. Sun, A. C. Dai, and F. R. Xu, *Phys. Rev. Lett.* **117**, 182503 (2016).
- [45] P. Zhang, X. Xu, P. Shuai, R. Chen, X. Yan, Y. Zhang, M. Wang, Y. Litvinov, K. Blaum, H. Xu, T. Bao, X. Chen, H. Chen, C. Fu, J. He, S. Kubono, Y. Lam, D. Liu, R. Mao, X. Ma, M. Sun, X. Tu, Y. Xing, J. Yang, Y. Yuan, Q. Zeng, X. Zhou, X. Zhou, W. Zhan, S. Litvinov, G. Audi, T. Uesaka, Y. Yamaguchi, T. Yamaguchi, A. Ozawa, B. Sun, Y. Sun, and F. Xu, *Phys. Lett. B* **767**, 20 (2017).
- [46] Y. H. Zhang, P. Zhang, X. H. Zhou, M. Wang, Y. A. Litvinov, H. S. Xu, X. Xu, P. Shuai, Y. H. Lam, R. J. Chen, X. L. Yan, T. Bao, X. C. Chen, H. Chen, C. Y. Fu, J. J. He, S. Kubono, D. W. Liu, R. S. Mao, X. W. Ma, M. Z. Sun, X. L. Tu, Y. M. Xing, Q. Zeng, X. Zhou, W. L. Zhan, S. Litvinov, K. Blaum, G. Audi, T. Uesaka, Y. Yamaguchi, T. Yamaguchi, A. Ozawa, B. H. Sun, Y. Sun, and F. R. Xu, *Phys. Rev. C* **98**, 014319 (2018).
- [47] C. Yazidjian, G. Audi, D. Beck, K. Blaum, S. George, C. Guénaut, F. Herfurth, A. Herlert, A. Kellerbauer, H.-J. Kluge, D. Lunney, and L. Schweikhard, *Phys. Rev. C* **76**, 024308 (2007).
- [48] S. George, G. Audi, B. Blank, K. Blaum, M. Breitenfeldt, U. Hager, F. Herfurth, A. Herlert, A. Kellerbauer, H.-J. Kluge, M. Kretzschmar, D. Lunney, R. Savreux, S. Schwarz, L. Schweikhard, and C. Yazidjian, *EPL (Europhysics Letters)* **82**, 50005 (2008).
- [49] T. K. Nieto, J. Souin, T. Eronen, L. Audirac, J. Äystö, B. Blank, V. V. Elomaa, J. Giovinazzo, U. Hager, J. Hakala, A. Jokinen, A. Kankainen, P. Karvonen, T. Kessler, I. D. Moore, H. Penttilä, S. Rahaman, M. Reponen, S. Rinta-Antila, J. Rissanen, A. Saastamoinen, T. Sonoda, and C. Weber, *Phys. Rev. C* **80**, 035502 (2009).
- [50] A. Kankainen, T. Eronen, D. Gorelov, J. Hakala, A. Jokinen, V. S. Kolhinen, M. Reponen, J. Rissanen, A. Saastamoinen, V. Sonnenschein, and J. Äystö, *Phys. Rev. C* **89**, 051302 (2014).
- [51] D. A. Nesterenko, A. Kankainen, L. Canete, M. Block, D. Cox, T. Eronen, C. Fahlander, U. Forsberg, J. Gerl, P. Golubev, J. Hakala, A. Jokinen, V. S. Kolhinen, J. Koponen, N. Lalović, C. Lorenz, I. D. Moore, P. Papadakis, J. Reinikainen, S. Rinta-Antila, D. Rudolph, L. G. Sarmiento, A. Voss, and J. Äystö, *J. Phys. G: Nucl. Part. Phys.* **44**, 065103 (2017).
- [52] A. Kankainen, V.-V. Elomaa, T. Eronen, D. Gorelov, J. Hakala, A. Jokinen, T. Kessler, V. S. Kolhinen, I. D. Moore, S. Rahaman, M. Reponen, J. Rissanen, A. Saastamoinen, C. Weber, and J. Äystö, *Phys. Rev. C* **82**, 034311 (2010).
- [53] A. A. Valverde, M. Brodeur, G. Bollen, M. Eibach, K. Gulyuz, A. Hamaker, C. Izzo, W.-J. Ong, D. Puentes, M. Redshaw, R. Ringle, R. Sandler, S. Schwarz, C. S. Sumithrarachchi, J. Surbrook, A. C. C. Villari, and I. T. Yandow, *Phys. Rev. Lett.* **120**, 032701 (2018).
- [54] J. Fallis, J. A. Clark, K. S. Sharma, G. Savard, F. Buchinger, S. Caldwell, A. Chaudhuri, J. E. Crawford, C. M. Deibel, S. Gulick, A. A. Hecht, D. Lascar, J. K. P. Lee, A. F. Levand, G. Li, B. F. Lundgren, A. Parikh, S. Russell, M. Scholte-van de Vorst, N. D. Scielzo, R. E. Segel, H. Sharma, S. Sinha, M. G. Sternberg, T. Sun, I. Tanihata, J. Van Schelt, J. C. Wang, Y. Wang, C. Wrede, and Z. Zhou, *Phys. Rev. C* **84**, 045807 (2011).
- [55] C. Guénaut, G. Audi, D. Beck, K. Blaum, G. Bollen, P. Delahaye, F. Herfurth, A. Kellerbauer, H.-J. Kluge, J. Libert, D. Lunney, S. Schwarz, L. Schweikhard, and C. Yazidjian, *Phys. Rev. C* **75**, 044303 (2007).
- [56] P. Schury, C. Bachelet, M. Block, G. Bollen, D. A. Davies, M. Facina, C. M. Folden III, C. Guénaut, J. Huikari, E. Kwan, A. Kwiatkowski, D. J. Morrissey, R. Ringle, G. K. Pang, A. Prinke, J. Savory, H. Schatz, S. Schwarz, C. S. Sumithrarachchi, and T. Sun, *Phys. Rev. C* **75**, 055801 (2007).
- [57] J. Savory, P. Schury, C. Bachelet, M. Block, G. Bollen, M. Facina, C. M. Folden, C. Guénaut, E. Kwan, A. A. Kwiatkowski, D. J. Morrissey, G. K. Pang, A. Prinke, R. Ringle, H. Schatz, S. Schwarz, and C. S. Sumithrarachchi, *Phys. Rev. Lett.* **102**, 132501 (2009).
- [58] H. Herndl and B. Brown, *Nucl. Phys. A* **627**, 35 (1997).
- [59] M. Honma, T. Otsuka, T. Mizusaki, and M. Hjorth-Jensen, *Phys. Rev. C* **80**, 064323 (2009).
- [60] B. A. Brown and A. F. Lisetskiy, (unpublished) see also endnote (28) in B. Cheal et al., *Phys. Rev. Lett.* **104**, 252502 (2010).
- [61] D. Rudolph, F. Cristancho, C. J. Gross, A. Jungclaus, K. P. Lieb, M. A. Bentley, W. Gelletly, J. Simpson, H. Grawe, J. Heese, K. H. Maier, J. Eberth, S. Skoda, J. L. Durell, B. J. Varley, D. J. Blumenthal, C. J. Lister, and S. Rastikerdar, *J. Phys. G: Nucl. Part. Phys.* **17**, L113 (1991).
- [62] A. Odahara, Y. Gono, S. Mitarai, T. Shizuma, E. Ideguchi, J. Mukai, H. Tomura, B. J. Min, S. Sue-matsu, T. Kuroyanagi, K. Heiguchi, T. Komatsubara, and K. Furuno, *Z. Phys. A* **354**, 231 (1996).
- [63] A. B. Garnsworthy, P. H. Regan, S. Pietri, Y. Sun, F. R. Xu, D. Rudolph, M. Górska, L. Cáceres, Z. Podolyák, S. J. Steer, R. Hoischen, A. Heinz, F. Becker, P. Bednarczyk, P. Doornenbal, H. Geissel, J. Gerl, H. Grawe, J. Grębosz, A. Kelic, I. Kojouharov, N. Kurz, F. Montes, W. Prokopwicz, T. Saito, H. Schaffner, S. Tachenov, E. Werner-Malento, H. J. Wollersheim, G. Benzoni, B. Blank, C. Brandau, A. M. Bruce, F. Camera, W. N. Catford, I. J. Cullen, Z. Dombrádi, E. Estevez, W. Gelletly, G. Ilie, J. Jolie, G. A. Jones, A. Jungclaus, M. Kmiecik, F. G. Kondev, T. Kurtukian-Nieto, S. Lalkovski, Z. Liu, A. Maj, S. Myalski, M. Pfützner, S. Schwertel, T. Shizuma, A. J. Simons, P. M. Walker, and O. Wieland, *Phys. Rev. C* **80** (2009), 10.1103/physrevc.80.064303.
- [64] R. Gross and A. Frenkel, *Nucl. Phys. A* **267**, 85 (1976).
- [65] B. A. Brown, *Phys. Rev. Lett.* **111**, 162502 (2013).
- [66] W. Satuła, J. Dobaczewski, and W. Nazarewicz, *Phys. Rev. Lett.* **81**, 3599 (1998).



IV

A NEW OFF-LINE ION SOURCE FACILITY AT IGISOL

by

M. Vilén, L. Canete, B. Cheal, A. Giatzoglou, R. de Groote, A. de Roubin, T. Eronen, S. Geldhof, A. Jokinen, A. Kankainen, I.D. Moore, D.A. Nesterenko, H. Penttilä, I. Pohjalainen, M. Reponen, S. Rinta-Antila, J. Äystö

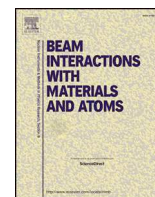
Accepted for publication in Nuclear Instruments and Methods in Physics
Research Section B: Beam Interactions with Materials and Atoms
(DOI:10.1016/j.nimb.2019.04.051)



ELSEVIER

Contents lists available at ScienceDirect

Nuclear Inst. and Methods in Physics Research B

journal homepage: www.elsevier.com/locate/nimb

A new off-line ion source facility at IGISOL

M. Vilén^{a,*}, L. Canete^a, B. Cheal^b, A. Giatzoglou^c, R. de Groot^a, A. de Roubin^a, T. Eronen^a, S. Geldhof^a, A. Jokinen^a, A. Kankainen^a, I.D. Moore^a, D.A. Nesterenko^a, H. Penttilä^a, I. Pohjalainen^a, M. Reponen^a, S. Rinta-Antila^a

^a University of Jyväskylä, P.O. Box 35, FI-40014 University of Jyväskylä, Finland

^b Department of Physics, University of Liverpool, Liverpool L69 7ZE, United Kingdom

^c Department of Physics and Astronomy, University College London, Gower Street, London WC1E 6BT, United Kingdom

ARTICLE INFO

Keywords:

Discharge ion source

Surface ion source

IGISOL

ABSTRACT

An off-line ion source station has been commissioned at the IGISOL (Ion Guide Isotope Separator On-Line) facility. It offers the infrastructure needed to produce stable ion beams from three off-line ion sources in parallel with the radioactive ion beams produced from the IGISOL target chamber. This has resulted in improved feasibility for new experiments by offering reference ions for Penning-trap mass measurements, laser spectroscopy and atom trap experiments.

1. A new ion source facility at IGISOL-4

In this contribution, we present the latest addition to the IGISOL-4 (Ion Guide Isotope Separator On-Line) facility [1], a new off-line ion source station, see Fig. 1. The new ion source infrastructure consists of an ion source setup located on the second floor of the experimental hall and a beamline connecting the new system to the main IGISOL mass separator. The ion source station is designed to accommodate three ion sources simultaneously, two sources in the horizontal branches of the vacuum system and one vertically mounted.

The new station houses electrostatic ion optics that can accept a beam from each of the three directions. Both ion sources presented in Fig. 1 utilize a skimmer electrode to form an ion beam which is injected into the quadrupole bender. The beam is focused with an Einzel lens, situated immediately after the quadrupole bender, and its alignment is adjusted using a set of steering electrodes. The ions have $800q$ eV of energy, q being the charge state of the ions, before entering the extractor electrode which further accelerates them to $30q$ keV.

Subsequently, ions are transported to the lower floor of the IGISOL facility, deflected by 90° into the horizontal beamline and separated based on their m/q ratio using a dipole magnet. The deflector system consists of two sets of parallel plates, one curved set of plates that deflects the ions by 65° and another set with straight plates that can be used to deflect the ions by the remaining 25° . The system can accept beam from either the off-line ion source station or the IGISOL target chamber. Switching between these two sources is achieved by

alternating a voltage on the latter set of parallel plates.

In its present configuration, the ion source station houses two types of ion source, a surface ion source based on resistive heating and a glow discharge ion source. The former ionizes a mixture of potassium, rubidium and cesium, whereas the latter source is a more flexible device that ionizes its cathode material via electric discharge through helium buffer gas. The ion source station is equipped with a cryogenic buffer gas purification system in order to provide beams with higher concentrations of the cathode material. Commissioning of a third ion source, a laser ablation ion source, is being planned.

2. Commissioning of the ion source station

After the first commissioning runs with ^{63}Cu and ^{133}Cs , the new ion source station has been employed in many experiments at IGISOL. The station was used to provide ion samples in parallel to the IGISOL system. This enabled the laser spectroscopy work [2] by making $^{89}\text{Y}^{2+}$ ions available where they would not have been previously and made possible the Penning trap mass measurement campaign [3] conducted fully off-line using both the vertical and horizontal beamlines. Additionally, the ion source station has been used to provide well-known and identified reference ions for the on-line Penning trap mass measurements [4] and to provide $^{133}\text{Cs}^+$ for demonstrating the operation of a new laser cooling and trapping facility for the production of ultra-cold atomic samples of caesium [5]. The new station has been proven to be a useful tool in preparing for on-line experiments through allowing initial

* Corresponding author.

E-mail address: markus.k.vilen@student.jyu.fi (M. Vilén).

<https://doi.org/10.1016/j.nimb.2019.04.051>

Received 14 January 2019; Received in revised form 5 April 2019; Accepted 18 April 2019

0168-583X/© 2019 Published by Elsevier B.V.

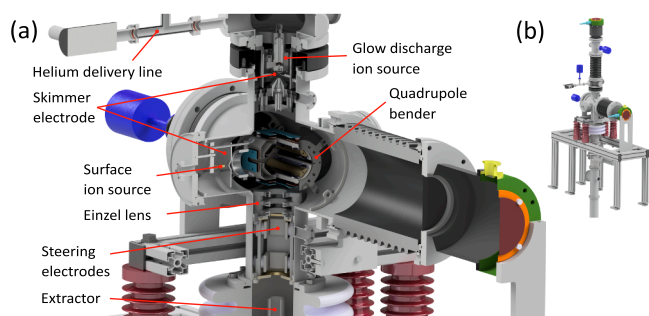


Fig. 1. Internal structure of the new off-line ion source station (a) and the full station (b).

tuning of both Penning trap and collinear laser systems without disrupting preparation of the IGISOL front end.

Operating parameters of the system were mostly the same during these experiments, with the exception of ion source settings. Typical values for the glow discharge ion source were 5–10 mbar helium pressure and 800–1400 V source voltage. Current used to heat the surface ion source was adjusted based on the amount of beam needed, typically being 1.5–1.8 A.

3. Conclusions

The new ion source infrastructure has been used in several experiments demonstrating additional flexibility in the operating modes of the IGISOL facility, enabling novel experiments, such as [2], and the possibility to conduct Penning trap mass measurement campaigns in a

fully off-line operating mode. The off-line ion source station, with its two commissioned ion sources, provides a large variety of mass separated ion beams to experiments. Commissioning of a third ion source based on laser ablation would not only provide an increased number of ion species for experiments, but also a possibility to explore carbon cluster formation which would be of interest as reference ions for mass measurements.

References

- [1] I. Moore, T. Eronen, D. Gorelov, J. Hakala, A. Jokinen, A. Kankainen, V. Kolhinen, J. Koponen, H. Penttilä, I. Pohjalainen, M. Reponen, J. Rissanen, A. Saastamoinen, S. Rinta-Antila, V. Sonnenschein, J. Äystö, Towards commissioning the new IGISOL-4 facility, *Nucl. Instrum. Methods Phys. Res., Sect. B* 317 (2013) 208–213, <https://doi.org/10.1016/j.nimb.2013.06.036> xVIth International Conference on ElectroMagnetic Isotope Separators and Techniques Related to their Applications, December 27, 2012 at Matsue, Japan (2013).<http://www.sciencedirect.com/science/article/pii/S0168583X13007143> ..
- [2] L.J. Vormawah, M. Vilén, R. Beerwerth, P. Campbell, B. Cheal, A. Dicker, T. Eronen, S. Fritzsche, S. Geldhof, A. Jokinen, S. Kelly, I.D. Moore, M. Reponen, S. Rinta-Antila, S.O. Stock, A. Voss, Isotope shifts from collinear laser spectroscopy of doubly charged yttrium isotopes, *Phys. Rev. A* 97 (2018) (Apr 2018) 042504, <https://doi.org/10.1103/PhysRevA.97.042504>.
- [3] D. Nesterenko, L. Canete, T. Eronen, A. Jokinen, A. Kankainen, Y. Novikov, S. Rinta-Antila, A. de Roubin, M. Vilén, High-precision measurement of the mass difference between ^{102}Pd and ^{102}Ru , *Int. J. Mass Spectrom.* 435 (2019) 204–208, <https://doi.org/10.1016/j.ijms.2018.10.038> URL<http://www.sciencedirect.com/science/article/pii/S1387380618303257>.
- [4] M. Vilén, J.M. Kelly, A. Kankainen, M. Brodeur, et al., Exploring the mass surface near the rare-earth abundance peak via precision mass measurements, to be submitted.
- [5] A. Giatzoglou, T. Poomaradee, I. Pohjalainen, S. Rinta-Antila, I.D. Moore, P.M. Walker, L. Marmugi, F. Renzoni, A facility for production and laser cooling of cesium isotopes and isomers, *Nucl. Instrum. Methods Phys. Res., Sect. A* 908 (2018) 367–375, <https://doi.org/10.1016/j.nima.2018.08.095> URL<http://www.sciencedirect.com/science/article/pii/S0168900218310532>.